Structural Investigations of Ionizable Lipid Nanoparticles for mRNA Delivery

Julian Philipp

SIGILL. UNIVERSITAT. LUDOVIC. MAXIM.

Munich 2026

Structural Investigations of Ionizable Lipid Nanoparticles for mRNA Delivery

Julian Philipp

Dissertation
an der Fakultät für Physik
der Ludwig-Maximilians-Universität
München

vorgelegt von
Julian Philipp
aus München

München, den 22.01.2026

Erstgutachter: Prof. Dr. Joachim O. Rädler
Zweitgutachter: Prof. Dr. Nadine Schwierz
Tag der mündlichen Prüfung: 06.03.2026

Zusammenfassung

Lipid Nanopartikel (LNPs) sind etwa 100 nm große, synthetische Partikel mit einem flüssigkristallinen Lipid Kern und einer Lipid Hülle. Die Eigenschaften der Lipide spielen eine zentrale Rolle bei der Effizienz dieser Partikel als Transportsystem für mRNA-basierte Impfstoffe und Medikamente. LNPs bestehen typischerweise aus ionisierbaren kationischen Lipiden, Helferlipiden, Cholesterin, und PEG-Lipiden. Diese ermöglichen eine effiziente Komplexierung der negativ geladenen mRNA und die anschließende Abgabe in Zellen. Trotz ihrer erfolgreichen Anwendung während der globalen SARS-CoV-2-Pandemie stellt ein vollständiges Verständnis des Zusammenhangs zwischen der LNP Zusammensetzung, der internen Nanostruktur und der anschließenden biologischen Wirksamkeit weiterhin einen kritischen Engpass für ein rationales Arzneimitteldesign dar. Insbesondere der Mechanismus der entscheidenden endosomalen mRNA Freisetzung ist bisher nur unzureichend verstanden.

Diese kumulative Dissertation präsentiert eine strukturelle und biophysikalische Untersuchung von Lipid-Mesophasen mit dem Ziel, Zusammenhänge zwischen Struktur und Funktion in LNPs zu etablieren. Wir nutzten Kleinwinkel-Röntgenstreuung (SAXS) um verschiedene ionisierbare Lipide systematisch zu vergleichen und den Einfluss von pH-Wert, Puffer und Temperatur auf die interne Struktur der LNPs aufzuklären. In meiner Arbeit wurden erstmals Phasenübergänge zwischen Mesophasen von ionisierbaren Lipiden (inverse mizellar, hexagonal, kubisch) beschrieben und deren Existenz in LNPs nachgewiesen (Philipp et al., PNAS 2023). Insbesondere der Phasenübergang von invers-mizellar zu invers-hexagonal, der bei allen gemessenen ionisierbaren Lipiden auftritt, wird als entscheidend für eine erfolgreiche Transfektion der mRNA ins Zellplasma vermutet. Es wurde zudem beobachtet, dass der pH-Wert dieses Phasenübergangs vom Lipid, der Temperatur und der Wertigkeit der Gegenionen abhängt. In-vitro Experimente mit LNPs, die mit verschiedenen Puffern hergestellt wurden, zeigten eine klare Korrelation zwischen der Transfektionseffizienz, der Startzeit der kodierten Proteinexpression und dem pH-Wert des Phasenübergangs (Carucci, Philipp, et al., ACS Nano 2025). Eine tiefergehende Analyse der Elektronendichteverteilung lieferte Einblicke in die interne Struktur der LNPs, insbesondere dem Wassergehalt der Mesophasen (Philipp et al., Soft Matter 2025). Die Kombination unserer SAXS-Analyse mit Molekulardynamik (MD) Simulationen ermöglichte es uns in Zusammenarbeit mit AstraZeneca ein Kontinuum-Modell zu erstellen und zu validieren, das den Wassergehalt invers-hexagonaler Phasen unter Verwendung der gemessenen SAXS-Streuprofile berechnet. Beim Vergleich der Hydratation von LNPs mit verschiedenen ionisierbaren Lipiden beobachteten wir eine Korrelation zwischen dem Wassergehalt und der Wirksamkeit des Gentransfers. Aus den hier erarbeiteten Zusammenhängen zwischen Hydratation, Phasenübergängen und der Effizienz des Gentransfers von LNPs lassen sich grundlegende rationale Designprinzipien ableiten, die wertvoll für die Optimierung der therapeutischen Wirksamkeit zukünftiger LNP Formulierungen sind.

Abstract

Lipid nanoparticles are synthetic particles with sizes in the order of 100 nm, that consist of a liquid crystal core and a lipid shell. The lipid properties play a central role in the efficiency of those particles as transport system for mRNA-based vaccines and drugs. Their intricate design, typically comprising an ionizable cationic lipid, a helper lipid, cholesterol, and a PEG-lipid, allows for efficient complexation of the negatively charged mRNA and subsequent delivery into target cells. Despite their successful application during the global SARS-CoV-2 pandemic, a complete understanding of the correlation between LNP composition, internal nanoscale structure, and subsequent biological efficacy, remains a critical bottleneck for rational drug design. Particularly the mechanism of crucial endosomal escape is only poorly understood so far.

This cumulative dissertation presents a structural and biophysical investigation of lipid mesophases, aiming to establish structure-function relationships of LNPs. We utilized small-angle X-ray scattering (SAXS) to systematically compare different ionizable lipids and to clarify the influence of the environment (pH, buffer, temperature) on the LNP's internal structure. During my PhD research, specific mesophases of ionizable lipids (inverse micellar, hexagonal, cubic) were identified for the first time and their existence in LNPs was demonstrated (Philipp et al., PNAS 2023). Especially the phase transition from inverse micellar to inverse hexagonal, which occurs in all measured ionizable lipids, is suspected to be crucial for a successful transfection of mRNA into cell plasma. The pH of this phase transition was observed to be dependent on the lipid, temperature, and valency of counterions. In-vitro experiments with LNPs prepared with different buffers have shown a clear correlation between the transfection efficiency, the onset time of its encoded protein expression, and the phase transition pH (Carucci, Philipp, et al., ACS Nano 2025). An in-depth analysis of the electron density profiles provided insights into the LNP's internal structure, particularly the water content of the mesophases (Philipp et al., Soft Matter 2025). The combination of our SAXS analysis with molecular dynamics (MD) simulation enabled us to create and validate a continuum model in cooperation with AstraZeneca, that calculates the water content of inverse-hexagonal phases using the measured SAXS scattering profiles. When we compared the hydration of LNPs with different ionizable lipids, we observed a correlation between the water content and efficiency of gene transfer. From the relationships developed here between hydration, phase transitions, and the efficiency of gene transfer by LNPs, it is possible to derive fundamental rational design principles that are valuable for optimizing the therapeutic efficacy of future LNP formulations.

Contents

1 Introduction to mRNA-based Therapeutics and Lipid Nanoparticles

Over the last century, medicine has gradually evolved from treading symptoms to curing the underlying causes of disease. That transformation became possible only because extensive research has enabled a profound understanding of biological mechanisms. In modern medicine, nucleic acid-based therapeutics, particularly messenger ribonucleic acid (mRNA), represent the forefront of pharmaceutical innovation. The ability of mRNA to act as a temporary genetic blueprint, harnessing the cell's own machinery to produce a specific protein, represents a fundamental shift in how drugs are conceived and deployed against diseases ranging from infectious threats to cancer and genetic disorders. Although this potential is immense, overcoming significant biophysical hurdles has proven difficult, as these delicate therapeutic molecules must be shielded from degradation and efficiently ferried into target cells. Consequently, the field of effective drug delivery has become one of the main topics of pharmaceutical research today.

1.1 Evolution of RNA-based Therapeutics: From Concept to Clinical Reality

The first conceptualization of RNA as a therapeutic agent started in 1988, before foundational research in 1990 demonstrated that administered mRNA could directly induce protein production within living cells.[1,2,3] Although this laid the groundwork for a new and revolutionary class of medicines, the field of RNA therapeutics encountered substantial skepticism and formidable developmental hurdles that significantly stalled its progress for several decades.

A primary hurdle in the development of RNA drugs was the disappointment caused by the performance of DNA vaccines in the 1990s, particularly within the context of human immunodeficiency virus (HIV) research.[4,5] Early attempts with DNA vaccines, including those using viral vectors, largely failed to live up to their initial promise and hindered funding and sustained research efforts across all nucleic acid-based therapeutic modalities. Additionally, the inherent instability of RNA molecules presented another critical challenge. RNA is very fragile and sensitive to environmental factors like heat, making it difficult to handle, impractical for mass manufacturing, and challenging to deliver effectively in-vivo. Viruses evolved for billions of years trying to inject their genome in cells and in the meantime all living organisms developed mechanisms to prevent this transfection. But the barriers were not only scientific or technological limitations. There was also a negative perception influenced by the failures of related technologies and economic disincentives within the pharmaceutical industry, which historically viewed vaccines as an unprofitable research area due to unpredictable demand, low margins, and high development costs. This combination of factors effectively deferred the progress of nucleic acid based therapeutics.[1]

The first RNA-based drug to achieve approval was Vitravene (Fomivirsen) in 1998. This antisense oligonucleotide (ASO) was introduced for the treatment of cytomegalovirus retinitis, an infection of the retina that could rapidly lead to blindness in individuals with

HIV. Despite Vitravene's effectiveness, its market presence only lasted for a short time. The success of antiretroviral therapies which significantly reduced the incidence of infections in HIV-positive individuals quickly made Vitravene redundant. For the following two decades, the RNA therapeutic market remained mostly stagnant, with only very few new product approvals. This finally changed in 2018 with the approval of Onpattro (Patisiran), which was the first small interfering RNA (siRNA) therapy to enter the market.[6,7,8]

The global SARS-CoV-2 pandemic served as a pivotal catalyst in accelerating the development and deployment of mRNA vaccines.[1] Their success did not exactly come as a sudden surprise but was the culmination of decades of fundamental research, particularly in the development of delivery nanotechnology.[9] An important breakthrough was the research on nucleoside base modifications by Dr. Katalin Karikó and Dr. Drew Weissman, for which they were awarded the 2023 Nobel Prize in Medicine and Physiology. Their joint discovery, published in 2005, demonstrated that modifying uridine in mRNA allowed it to be introduced into cells without triggering a robust innate immune response, thereby overcoming a key immunological barrier that had hampered previous mRNA applications.[10] The widespread deployment and high efficacy (95% for Pfizer/BioNTech and 94.1% for Moderna) of mRNA vaccines during the pandemic demonstrated that mRNA technology was safe, efficacious and could be produced on a global scale.[6] This success reignited research interest and caused a significant increase in RNA therapy trial initiations, with a 53% increase in the last quarter of 2024 alone.[6] Government initiatives, such as the US Operation Warp Speed, provided substantial upfront funding and accelerated clinical trials and manufacturing scale-up. This proved that many perceived limitations were primarily a matter of funding rather than fundamental scientific or technological barriers. The COVID-19 pandemic effectively acted as an extraordinary market corrector and accelerator as the global health crisis created an urgent demand for rapid vaccine development. This unprecedented urgency and the massive public funding effectively bypassed or eliminated the economic disincentives that had previously stifled investment. This caused pharmaceutical companies to heavily invest in the resolution of practical challenges related to mRNA's perceived fragility and manufacturing scalability, pushing the technology past its theoretical potential into practical, large-scale application. This shows how a global crisis can help to overcome economic hurdles, allowing a scientifically mature but commercially undervalued technology to finally flourish.[1]

1.2 The Expanding Landscape of RNA in Modern Medicine

RNA has rapidly emerged as one of the most important topics in modern medicine, offering a versatile platform for precise treatments across a wide spectrum of diseases. In contrast to DNA, which serves as a stable library of genetic information, RNA functions as a short-lived blueprint to translate genetic instructions into proteins and regulate gene expression.[11] This dynamic nature allows RNA molecules to directly influence and modulate a wide array of cellular processes without causing permanent changes to the DNA. One of the most profound advantages of RNA-based therapeutics is their theoretical capacity to target virtually any gene of interest. This capability opens up unprecedented possibilities for treating rare genetic conditions and addressing a vast landscape of proteins that were previously out of reach. This is particularly important as conventional small molecule and antibody drugs have historically only targeted approximately 0.05% of the human genome, and an estimated 85% of proteins lack the specific binding pockets or clefts that make them accessible to small molecule interaction.[6] The ability of RNA to directly interact with gene expression at various levels, such as mRNA degradation or splicing modification, fundamentally bypasses the need for specific protein binding pockets, which are often absent in disease-relevant targets. This positions RNA therapeutics not just as a new alternative, but as an enabling technology that can address a vast and previously inaccessible therapeutic space. RNA therapeutics have the potential for treating a wide array of diseases, including complex genetic disorders, cancers, and infectious diseases, that were once considered intractable.[6,11]

The success of mRNA vaccines in combating infectious diseases, most notably SARS-CoV-2, has unequivocally demonstrated RNA's potential for rapid, adaptable, and targeted vaccine development. These vaccines ingeniously harness the body's own cellular machinery to produce specific antigens, thereby causing robust and protective immune responses. Beyond infectious disease prevention, RNA-based therapeutics hold immense promise for gene therapy, offering treatments for a wide range of genetic disorders.[12] Unlike traditional gene therapies that may involve altering the host genome, RNA-based approaches can directly modulate gene expression without permanent genomic integration, reducing risks such as insertional mutagenesis.[13] The field is also actively expanding into personalized cancer immunotherapy, where mRNA can be engineered to encode patient-specific tumor antigens, effectively training the immune system to recognize and attack cancer cells. Furthermore, RNA therapies are being explored in regenerative medicine.[12,13]

The current landscape of RNA therapeutics is rich and diverse, operating through different mechanisms to influence cellular processes. Antisense Oligonucleotides (ASOs) are short, synthetic nucleic acid sequences designed to bind to specific mRNA targets, thereby interfering with gene expression through mechanisms such as inhibiting translation or modulating RNA splicing, as exemplified by Vitravene and Spinraza. Small Interfering RNAs (siRNAs) uses the natural RNA interference (RNAi) pathway to silence disease-causing genes by promoting the degradation of their corresponding mRNA transcripts, with Onpattro being the first FDA-approved siRNA therapy. Messenger RNA (mRNA) is primarily utilized for rapid in-vivo production of specific proteins, such as antigens for vaccines or therapeutic proteins for therapies.[6] MicroRNAs (miRNAs) are endogenous non-coding RNAs that play crucial roles in post-transcriptional gene regulation. Therapeutic strategies involve either introducing miRNA mimics to restore downregulated miRNAs or using inhibitors to suppress overactive ones.[9] Circular RNA (circRNA), characterized by its closed loop structure, exhibits enhanced stability compared to linear RNAs and holds potential as miRNA sponges, regulators of protein translation, or even as templates for protein synthesis in gene therapy and vaccine development. Self-amplifying RNA (saRNA) incorporates replication machinery, typically from alphaviruses, enabling prolonged intracellular expression at lower doses through RNA amplification, which enhances potency and durability. RNA Aptamers are synthetic RNA molecules engineered to bind specific molecular targets, such as proteins or small molecules, with high affinity and specificity, finding use in targeted drug delivery and diagnostics. Finally, emerging

RNA-Editing Technologies, such as those utilizing adenosine deaminases acting on RNA (ADAR), offer a reversible method to correct genetic mutations directly at the RNA level without permanently altering the DNA genome.[11]

This huge diversity of RNA therapeutics is not just a list of different RNA types but represents a sophisticated toolkit for precise intervention at virtually every stage of biological information flow, from gene expression to protein function. Each one offers a distinct mechanism to either silence, activate, replace, or modify specific biological instructions. This positions RNA as an unparalleled “information drug” that can be programmed to fine-tune complex cellular networks, offering a level of control and specificity previously unattainable with conventional therapeutics.

1.3 Lipid Nanoparticles: Essential Delivery Vehicles for RNA Therapeutics

Despite their immense therapeutic potential, RNA molecules face significant challenges in reaching their targets in-vivo. Naked RNA is highly unstable, prone to rapid degradation by endogenous RNases, and quickly cleared from extracellular circulation. Furthermore, their large size and polyanionic nature prevent passive diffusion across the cellular membranes, necessitating specialized active transport mechanisms for cellular entry. These fundamental biophysical barriers severely limit the utility of RNA therapeutics without an effective delivery system.[14]

Lipid nanoparticles have emerged as the most successful, optimized, and clinically validated delivery vehicles capable of overcoming these challenges. They effectively encapsulate and protect sensitive RNA payloads from enzymatic degradation, facilitate their efficient uptake into target cells, and enable the release of RNA from endosomal compartments into the cytosol, where it can exert its therapeutic function. Beyond protection and cellular delivery, LNPs also contribute to reducing undesired immunotoxicity that might be triggered by naked RNA. Long polyethylene glycol (PEG) molecules on the LNP surface help extend the circulation half-life of the therapeutic cargo by avoiding renal clearance via steric repulsion.[14]

The journey of lipid-based nanocarriers began with the discovery of liposomes in the 1960s, which were the first nanomedicine delivery platform to successfully transition from concept to clinical application. An early example is Doxil, an LNP formulation of the antitumor agent doxorubicin, used for ovarian cancer treatment. Liposomes demonstrated the versatility of lipid vesicles in encapsulating both hydrophobic and hydrophilic molecules. While groundbreaking, liposomes had limitations such as complex production methods involving organic solvents, low drug encapsulation efficiency, and difficulties in large-scale manufacturing. This led to the development of subsequent generations of LNPs, including solid lipid nanoparticles, nanostructured lipid carriers, and nonlamellar lipid nanoparticles, which were designed to address the shortcomings of earlier liposomal formulations. These newer platforms offered enhanced physical stability, higher loading capacities, easier large-scale production, and more precise control over the drug release.[15] The development of ionizable lipid nanoparticles marked a critical advancement, specifically engineered to overcome the unique challenges associated with nucleic acid delivery. Their pH-responsive nature was designed to avoid the systemic toxicity of permanently charged lipids while facilitating efficient nucleic acid encapsulation and endosomal escape.[16] The LNP compositions utilized in the highly successful COVID-19 mRNA vaccines (Pfizer/BioNTech, Moderna) represent the culmination of decades of research and iterative improvements in lipid chemistry and formulation science. This historical progression of LNPs, from basic liposomes to increasingly complex and specialized nanocarriers, exemplifies a continuous process of iterative innovation. Each successive generation was developed in direct response to specific limitations or unmet needs of its predecessors, such as improving stability, increasing encapsulation efficiency, reducing toxicity, or enabling the transport of specific cargo like mRNA.

1.4 Functions of Lipid Components in Lipid Nanoparticles

Lipid nanoparticles are typically composed of four main lipid components, each meticulously designed to contribute uniquely to the LNP's overall stability, transfection efficacy, and safety profile (Fig. 1).

Table 1: Lipid Components and their Functions in Lipid Nanoparticles[14,16]

Component	**Typical Molar Percentage**	**Primary Function(s)**
Ionizable Lipids	∼50%	RNA encapsulation, endosomal escape
Cholesterol	∼38.5%	Formation of liquid-ordered phase
Phospholipids (e.g. DSPC)	∼10%	Formation of outer membrane, prevents RNA leakage
PEGylated Lipids	∼1.5%	Prolonged circulation, anti-aggregation

Ionizable lipids are considered the most crucial component of LNP formulations. Their functionality hinges on their unique pH-responsive properties. At physiological pH (approximately 7.4), these lipids remain predominantly neutral, which significantly minimizes their systemic toxicity and prevents non-specific interactions with proteins. In the acidic environment of endosomes (pH typically ranging down to 5), the ionizable lipids become protonated, acquiring a positive charge. This charge switch is essential for two primary functions: efficient electrostatic encapsulation of the negatively charged RNA payload during formulation, and facilitating the critical process of endosomal escape.[14,16,17] Although the process of endosomal escape is not perfectly understood so far, there are indications that a combination of pH reduction and subsequent charge of the ionizable lipids play a major role. Section 1.5 describes different theories as well as our own research on this topic.

The design of ionizable lipids represents a sophisticated exploit of natural pH gradients that exist within the cellular environment. This pH-responsive behavior allows the LNP

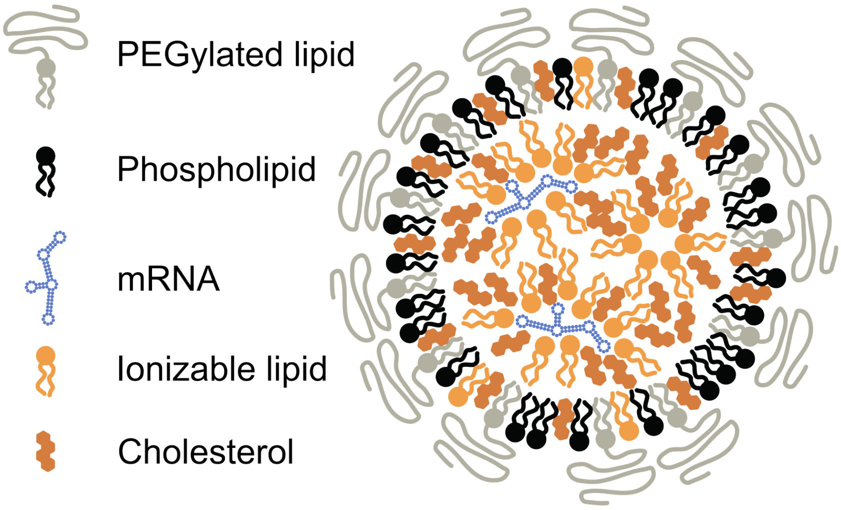

Figure 1: Schematic of a typical lipid nanoparticle. The spherical particle has an outer lipid monolayer including a PEGylated lipid. The inner lipid phase consists of the ionizable lipid, cholesterol and the RNA payload.

to maintain low toxicity during systemic circulation due to its neutral charge, and then actively engage in cargo release only when it reaches the acidic pH in endosomes, where it becomes positively charged. This highly controlled, localized release mechanism is a significant advancement over earlier, permanently charged cationic lipids, which exhibited high systemic toxicity due to indiscriminate interactions.[18]

The first ionizable lipid used in the context of LNPs was 1,2-dioleoyl-3-dimethylammonium propane (DODAP), described by a group around Pieter Cullis in 2001. By rapidly mixing DODAP with other lipids and oligonucleotides in ethanol, LNPs made with this lipid already achieved RNA encapsulation efficiencies of up to 70%.[19] But this only marked the beginning of the rapid development of improved ionizable lipids. During the following years, researchers uncovered that polyunsaturated lipids improved the transfection efficiency further and in 2006 1,2-dilinoleyl-N,N-dimethyl-3-aminopropane (DLinDMA or DD) was synthesized and tested in animal studies.[20,21] This was then followed by 2,2-dilinoleyl-4-dimethylaminoethyl-[1,3]-dioxolane (DLin-KC2-DMA or KC2) in 2010[22] and in 2012 a study was published in which researchers already compared over 50 different lipids in mice. One of the most notable ionizable lipids in this study was dilinoleylmethyl-4-dimethylaminobutyrate (DLin-MC3-DMA or MC3).[23]

A crucial parameter of ionizable lipids is the acid dissociation constant (pK_a), which is described by the Henderson-Hasselbalch equation (Eq. 1) and states the pH of the turning point at which half of the lipids are charged. Another important finding of the mice study was the optimal acid dissociation constant (pK_a) range of ionizable lipids: pH 6.2 - 6.5.[23] But in general the optimal pK_a of ionizable lipids for LNPs can vary depending on the target cell type and the route of administration, adding complexity to universal LNP design.[24,25]

$$pH = pK_a + \log_{10}\left(\frac{[A^-]}{[HA]}\right) \tag{1}$$

In 2018, the U.S. Food and Drug Administration (FDA) approved Onpattro, the first drug to utilize a combination of an siRNA therapeutic and the newly developed ionizable lipid MC3 encapsulated within a lipid nanoparticle.[8] Shortly afterwards the global COVID-19 pandemic led to newly developed mRNA vaccines using the ionizable lipids SM-102 (Moderna) and ALC-0315 (Pfizer/BioNTech).[16] The ongoing refinement of their chemical structure, including their ionizable heads, linker groups, and hydrophobic tails, is aimed at precisely tuning this pH-responsiveness for optimal potency, reduced off-target effects, and improved safety.[26]

Cholesterol is an indispensable component of LNP formulations, contributing significantly to the formation of its inner liquid-ordered phase and overall nanoparticle stability.[16] In our publication "Combining SAXS Analysis and MD Simulation to Determine Structure and Hydration of Ionizable Lipid Hexagonal Phases" (Section 5), MD simulations have shown that cholesterol accumulates in the edges between three channels within the inverse hexagonal H_{II} phase. There it fills a crucial gap in the structure, stabilizing it in the process. Recent research has also highlighted the important role of cholesterol, indicating that its concentration can directly influence the nanoparticle's transfection efficiency.[27]

Phospholipids are structural helper lipids with a hydrophilic head and hydrophobic tails. This amphiphilic nature causes phospholipids to spontaneously organize into lipid bilayers. In LNPs, phospholipids form the outer membrane of the LNP. 1,2-distearoyl-sn-glycero-3-phosphocholine (DSPC), with its saturated 18-carbon tails, is a commonly used structural lipid found in LNPs for siRNA therapy (e.g. Onpattro) and SARS-CoV-2 mRNA vaccines. Its higher phase transition temperature compared to 1,2-dioleoyl-sn-glycero-3-phosphoethanolamine (DOPE) enhances the overall membrane stability of the LNPs.[16]

PEGylated lipids, despite typically constituting the smallest molar percentage (around 1.5 mol%) of the lipid components in LNPs, exert significant influence on the nanoparticles' properties and in-vivo behavior. Their primary function is to provide steric hindrance for surrounding proteins, effectively cloaking the LNP. This stealth effect protects LNPs from rapid uptake by the mononuclear phagocyte system (MPS) and reduces antibody association by serum proteins, thereby extending their circulation time in the bloodstream and preventing premature aggregation.[14] Depending on the medical application, a prolonged systemic circulation can be crucial for achieving optimal biodistribution and reaching target tissues. An example for this is PEG-1,2-distearoyl-sn-glycero-3-phosphorylethanolamine (PEG-DSPE), which is used in the anti-cancer drug Doxil, boosting the accumulation at the tumor site. In contrast to PEG-DSPE, PEG-c-DMG is designed to dissociate from the LNP upon administration, to allow for rapid cellular uptake in the liver. This balance between extended circulation time and efficient cellular uptake is often referred to as the "PEG dilemma".[16]

Despite their critical benefits, PEGylated lipids present notable safety challenges. These include the accelerated blood clearance (ABC) phenomenon, where repeated administration can provoke an immune response leading to the production of anti-PEG antibodies, resulting in rapid clearance and reduced efficacy of subsequent doses.[16] PEG lipids can also be found in a wide range of cosmetic products. Experiments with mice demonstrated that frequent application of cosmetics containing PEG can induce the production of anti-PEG antibodies.[28] Therefore excessive usage of these cosmetics could reduce the efficacy of PEGylated LNPs.

1.5 Cellular Uptake and the Critical Process of Endosomal Escape

For LNPs to deliver their RNA payload, they must first enter target cells. This internalization primarily occurs through various endocytosis pathways. These mechanisms include both clathrin-dependent and clathrin-independent processes, such as macropinocytosis, with the predominant pathway often depending on the LNP's size and surface characteristics. Once internalized, the LNPs become encapsulated within membrane-bound vesicles known as endosomes, which serve as intracellular sorting compartments.[29]

The endosomal pathway is a dynamic intracellular trafficking route that begins with early endosomes, characterized by a slightly acidic pH of approximately 6.5. These early endosomes then progressively mature into late endosomes, where the pH further drops to pH $\approx$ 5.5, and eventually fuse with lysosomes, which are highly acidic (pH $\approx$ 4.5) and serve as the primary sites of enzymatic degradation within the cell.[18] For the RNA payload to exert its therapeutic effect, it must successfully escape from these endosomal compartments into the cytosol before the maturation of late endosomes to lysosomes, where the highly acidic environment and hydrolytic enzymes would rapidly degrade the RNA.[29] This progressive acidification and eventual fusion with lysosomes reveals it as a sophisticated cellular defense mechanism designed to process and degrade foreign materials. For LNPs, this pathway represents a major challenge that the RNA payload must navigate and escape from. The inherent inefficiency of this escape, with estimates suggesting less than 3% success rate,[26] underscores the formidable nature of this cellular barrier, which is a result of billions of years of cellular evolution to prevent foreign constructs from entering cells. Therefore, the endosomal escape is not only a simple delivery step but a critical battle against deeply ingrained cellular defense systems.

Although there is no perfect consensus on the exact process of endosomal escape yet, it is agreed upon that the primary mechanism is the pH-responsive nature of the ionizable lipids within the LNP.[29] As LNPs are trafficked within the progressively acidifying endosomes, the ionizable lipids become protonated, acquiring a positive charge. Recent publication like our own named "pH-dependent structural transitions in cationic ionizable lipid mesophases are critical for lipid nanoparticle function" (Section 4) try to shed light on this crucial step. We showed in-vitro that the protonation of the ionizable lipids is capable to trigger a phase transition of the LNP's inner structure from an inverse micellar L_{II} phase to an inverse hexagonal H_{II} phase. This internal phase transition could then influence the LNP surface, which goes hand in hand with another recently suggested mechanism driving endosomal escape. Positively charged ionizable lipids in the LNP surface could be able to electrostatically interact with the negatively charged phospholipids present on the inner leaflet of the endosomal membrane. This interaction of oppositely charged lipids could promote the formation of H_{II} structures at the endosomal membrane, leading to endosomal rupture or fusion and the subsequent release of the nucleic acid payload into the cytoplasm.[26] An alternative or complementary theory, the "proton sponge effect", suggests that the buffering capacity of lipid nanoparticles within the acidic endosomes leads to an increased activation of the endosomal proton pumps. This increased proton accumulation, accompanied by chloride ion influx to maintain charge neutrality, could result in increased osmotic pressure within the endosome, causing it to swell and eventually burst, thereby releasing the cargo.[30,29]

Despite significant advancements, endosomal escape remains a major bottleneck in LNP-mediated therapeutics. Estimates suggest that less than 3% of internalized nucleic acids successfully transfer their cargo from the endosomal pathway into the cytosol.[26] The vast majority of LNPs are either degraded within lysosomes or recycled out of the cell, rendering their payload therapeutically inert.[18] The field still grapples with limited and contradicting data regarding the precise mechanism of endosomal escape, and there is no consensus on the exact endosomal compartment from which escape predominantly occurs. Furthermore, robust, quantitative, and high-throughput methods to accurately detect and study endosomal escape in-vivo are currently lacking, hindering rational LNP design.[29]

Strategies to enhance the escape efficiency include the continued rational design of ionizable lipids, focusing on their ionizable heads, linker groups, and hydrophobic tails. But this necessitates a deeper understanding of how these structural features influence pH-dependent protonation and subsequent mesophase transitions.[18] A novel and promising strategy involves actively modulating the intracellular transport of RNA-based drugs. Research has shown that slowing down the transport of those drugs from early endosomes to lysosomes, for example by selectively inhibiting genes like AP1M1 which regulates this transport, can significantly increase the residence time in endosomes. This prolonged residence time enhances the opportunity for endosomal escape, thereby improving therapeutic efficacy without the need to increase drug dosage.[31] Additionally, the judicious selection and optimization of helper lipids, such as cholesterol and phospholipids, can also contribute to enhancing the overall endosomal escape efficiency. The persistent challenge of endosomal escape highlights that overcoming this bottleneck requires more than just incremental improvements in LNP chemistry. It necessitates a truly multidisciplinary approach that integrates deep understandings from lipid chemistry for rational design of ionizable lipids that fine-tune pH-responsiveness and membrane-disrupting properties, cell biology to understand the intricate dynamics of endosomal trafficking, pH gradients, and cellular defense mechanisms, and drug delivery engineering to develop novel strategies that actively manipulate cellular processes, such as modulating intracellular transport kinetics. This integrated approach, moving beyond passive delivery to active cellular intervention, represents the cutting edge of research aimed at unlocking the full therapeutic potential of RNA-based medicines.

1.6 Motivation and Research Questions

The journey of RNA-based therapeutics from a concept to a clinical reality has been remarkable, underscoring the important role of LNPs as delivery vehicles. Despite the unprecedented success of mRNA-LNPs, particularly during the SARS-CoV-2 pandemic, the precise molecular and biophysical mechanisms governing their intracellular function, especially the critical process of endosomal escape, remain incompletely understood. This knowledge gap represents a significant bottleneck in the rational design and optimization of next-generation RNA therapeutics. The inherent inefficiency of endosomal escape, with estimates suggesting less than 3% success rate,[26] is mostly caused by an effective cellular barrier. This barrier is a testament to billions of years of cellular evolution designed to prevent foreign constructs from entering the cytoplasm. This lack of precise knowledge about the cellular pathway creates a significant barrier to rational LNP design, making predictive optimization mostly impossible. Small molecular variations in chemical structure have unexpectedly large effects on LNP efficiency, underscoring the complexity of these systems.

The current state of LNP optimization largely proceeds through a trial-and-error methodology, driven by the absence of a comprehensive understanding regarding endosomal escape and the subsequent release of mRNA in the cytosol. This empirical approach is inherently challenging because of the sheer amount of possible combinations, even when focusing solely on different head-, linker- and tail-groups of the ionizable lipid.[32] This immense experimental landscape, coupled with the high cost of critical materials such as RNA, makes LNP development economically challenging and exceedingly time-consuming.

A significant consequence of this predominantly empirical approach is the frequent necessity of conducting extensive in-vivo experiments with animals. In-vitro data often fails to adequately predict the behavior of LNPs in-vivo, as demonstrated by variable in-vitro efficacy not consistently correlating with in-vivo outcomes for different LNP formulations.[33] The inherent limitations of empirical optimization underscore the urgent need for a paradigm shift towards a rational design approach in LNP development. This strategic shift aims to significantly reduce the amount of animal experimentation required and accelerate the development of superior LNPs. The objective is to establish a deeper understanding of lipid structures and formulations that can consistently lead to higher endosomal escape efficiency. This represents a proactive, knowledge-driven approach that moves beyond simply observing outcomes to understanding why certain lipid designs are effective.

This dissertation, through the integration of three distinct but interconnected research publications, investigates different fundamental properties of LNPs. The first one, "pH-dependent structural transitions in cationic ionizable lipid mesophases are critical for lipid nanoparticle function" (Section 4), explores the pH-dependent response of ionizable lipids and its influence on endosomal release and transfection efficiencies. We systematically studied the pH response of three ionizable lipids (MC3, KC2, and DD) and identified pH-dependent structural transitions in their bulk phases. Particularly the transition from the inverse micellar to inverse hexagonal phase was suspected to play a major role during endosomal escape. Additionally, a correlation between their varying in-vivo efficacy and delayed protein expression onset has been observed.

The second publication, “Buffer Specificity of Ionizable Lipid Nanoparticle Transfection Efficiency and Bulk Phase Transition” (Section 5), delves into how the chemical identity of buffer ions, beyond just the pH, influences LNP transfection efficiency by modulating these critical pH-dependent structural transitions within the LNP core. We demonstrated that specific ion adsorption at the lipid-water interface altered the area per headgroup, thereby shifting the transition pH and impacting endosomal release efficiency.

Finally, the third publication, “Combining SAXS Analysis and MD Simulation to Determine Structure and Hydration of Ionizable Lipid Hexagonal Phases” (Section 6), presents an integrated approach utilizing small-angle X-ray scattering (SAXS) experiments, molecular dynamics (MD) simulations, and a continuum model to elucidate lipid distribution and water content within inverse hexagonal (H_{II}) phases. We established a link between the hydration properties of ionizable lipid mesophases and their transfection efficiency, providing a powerful tool for the rational design and optimization of LNPs by predicting performance based on structural characteristics.

2 Theoretical Principles of Small-Angle X-ray Scattering (SAXS)

Small-angle X-ray scattering (SAXS) is a powerful technique used for the structural investigation of materials at the nanoscale. This method relies on the elastic scattering of X-rays by a sample, with the scattered radiation recorded at very small angles, typically between 0.1° and 10°. At typical SAXS wavelengths of 0.07-0.2 nm, this small-angle scattering provides information on structural features with dimensions ranging from approximately 1 to 100 nm. The technique is a standard tool across a wide range of fields, including condensed matter physics, molecular biology, and materials science.[34]

The X-ray beam is scattered by the sample and forms a shallow cone around the unscattered beam before it is recorded by the detector. As long as the structures inside the sample are small compared to the beam size, the random orientation of those structures will cause the scattered X-rays to form isotropic patterns. If the contrast is high enough and the sample shows sufficient ordering, the recorded images show concentric circles around the unscattered beam.

The fundamental principle underlying the SAXS signal is the difference in electron density between a scattering object and its surrounding medium. X-rays interact with the electrons of the material and the resulting scattering pattern arises from the interference of X-ray waves scattered by these electrons. For biological systems, the electron density contrast is often subtle. For instance, the average electron density of a protein (~ 0.43 electrons/Å^3) is only slightly higher than that of water (~ 0.33 electrons/Å^3), which makes the scattering signal inherently weak.[35] Consequently, high-quality SAXS measurements require instruments with a high X-ray flux and sensitive detector to capture a clear signal above the background noise.

2.1 SAXS Instruments

The inherent weakness of the SAXS signal, particularly for systems with subtle electron density contrast, presents the primary engineering challenge for all SAXS instruments. The design and evolution of every component in a SAXS system, whether a compact laboratory setup or at a large-scale synchrotron, are a direct response to this foundational problem. Each element is meticulously engineered to either maximize the flux of the incident beam to increase the signal or to minimize background noise and parasitic scattering to improve the signal to noise ratio.

The X-ray source is the starting point of the SAXS beamline, generating the radiation used to probe the sample. Its characteristics, specifically brilliance, flux, and beam diameter, are critical determinants of overall instrument performance. In a typical in-house setup, the source is a microfocus X-ray tube. Inside this tube, a heated cathode emits high-energy electrons that are accelerated toward a metal anode (often Copper or Molybdenum). The collision of those high-energy electrons with the metal generates X-rays through two distinct mechanisms: Bremsstrahlung radiation and Characteristic radiation.

Bremsstrahlung radiation is caused by the deceleration of electrons, causing their kinetic energy to be emitted as electromagnetic radiation. With sufficient kinetic energy, this radiation will be X-rays, but emission is a continuous spectrum. Characteristic radiation, on the other hand, is discrete and caused by the accelerated electrons knocking specific electrons from the metal anode's atoms. Knocked-out electrons are then replaced by electrons from higher-energy shells within the same atom, which emit the energy difference as Characteristic radiation. The most intense Characteristic radiation is caused by electrons from the 2nd shell (L shell) replacing holes in the inner-most shell (K shell) and is called Kα radiation. The wavelength of this Kα radiation depends on the material, being 0.154 nm for copper and 0.071 nm for molybdenum.

In contrast to a laboratory source, the X-ray source for a synchrotron SAXS setup is fundamentally different, offering vastly superior performance. In this case, the X-rays are generated by an electron storage ring, where electrons are accelerated to near the speed of light and forced to change direction by powerful magnets (undulators). This process produces extremely intense, highly collimated, and naturally brilliant synchrotron radiation at a far greater flux than any laboratory tube can achieve.

After generation, the raw X-ray beam in both setups is shaped and prepared by a series of optical components. These optics serve two crucial functions. First, they provide monochromatization, filtering the X-ray spectrum to a narrow wavelength to ensure accurate scattering analysis. Second, they are responsible for collimation and focusing, creating a highly parallel or precisely focused beam to illuminate the sample. This is achieved using a combination of pinholes, slits, and advanced mirrors. To combat the issue of parasitic scattering from the collimating slits, modern instruments employ sophisticated designs, such as scatterless blades.

The thin X-ray beam is then directed at the sample and scattered at shallow angles between 0.1° and 10° creating a cone around the unscattered beam. To be able to record the scattering even at small angles, the detector is usually located up to several meters behind the sample. Detectors used in SAXS are typically 2-dimensional X-ray area detectors to detect the 2D scattering pattern, similar to normal cameras but with sensor chip areas of several hundred cm^2.[36] High-end versions are sensitive enough to count the X-ray photons directly, but the unscattered beam has to be blocked before it reaches the detector to prevent the sensor chip from being damaged by its high flux.

To minimize background noise from air molecules in the beam path, the source, sample, and detector are usually separated by vacuum tubes. Those tubes are sealed by thin, low-scattering materials such as Kapton foil. A standard approach for correcting background scattering is to perform a separate measurement of an empty sample holder, such as a quartz capillary, and subtract its scattering signal from the sample data. The angular calibration of the detector is typically performed by using a standard reference material like silver behenate, which produces a large number of well-defined diffraction peaks at known positions.

Although advances in laboratory X-ray sources and detection systems have made in-house instruments increasingly versatile, synchrotron radiation is essential for certain, more challenging studies due to its exceptionally high X-ray flux. The high flux of a synchrotron allows for rapid data acquisition, enabling the measurement of dozens of samples in a matter of hours instead of weeks. High-end synchrotron instruments can also achieve higher angular resolutions which makes it possible to differentiate between individual peaks in close proximity that are otherwise indistinguishable. On the other hand, in-house instruments usually offer better accessibility and are therefore a crucial and complementary tool for performing preliminary work, testing different samples and sample holders, and optimizing preparation techniques before using the limited and highly competitive synchrotron beamtime, which requires a formal proposal. The complementary nature of these two types of instruments allows researchers to promptly understand the general structure of samples in the lab, while reserving the high-resolution experiments for the limited time at the synchrotron.

2.2 SAXS Data Analysis

For isotropic samples with sufficient ordering, the data recorded by the detector is a 2D scattering pattern of concentric circles around the unscattered beam, which is usually blocked to protect the detector from its high intensity. To analyze the data further, the recorded experimental data is analyzed in reciprocal space, a mathematical construct that simplifies the interpretation of scattering patterns. The analysis is achieved by integrating the 2D detector data radially with the unscattered beam position at the center. This integration converts the 2D pattern into a one-dimensional scattering curve with the scattered intensity I on the y axis. For the x axis, the scattering angle (2θ) is converted into a scattering vector q, which is defined by the equation $q = \frac{4\pi}{\lambda} sin(\theta)$, where λ is the X-ray wavelength.

The conversion allows the rings from the 2D pattern to be shown as humps in the 1D plot, which can then be analyzed further to determine structural properties. In highly ordered materials like liquid crystals, the scattering creates sharp, distinct rings which lead to sharp Bragg peaks, reflecting the periodicity and symmetry of the arrangement. For less ordered systems, the rings are more diffuse and the peaks broader. Following the Bragg condition for constructive interference $n\lambda = 2d\, sin(\theta)$, peaks in the q space correspond to recurrent spacings (d) between diffraction planes via $d = \frac{2\pi}{q}$.[34] This relationship establishes a crucial inverse correlation between the scattering vector and the real-space dimensions of the structure, where larger structures correspond to smaller q values and vice versa.

Lipids, as amphiphilic molecules, possess a remarkable capacity to self-assemble into a wide variety of ordered structures known as liquid crystalline mesophases. SAXS is the ideal technique for identifying and characterizing these mesophases, as each has a unique structural “fingerprint” defined by a set of distinct Bragg reflections. The positions of these Bragg peaks are directly related to the periodic distances between planes of a crystal lattice, which are indexed by a set of integers known as Miller indices (h,k,l). Position ratios of peaks can be calculated by comparing their miller indices and using phase-specific equations that are listed in Table S1 and S2 inside the Supporting Information of our first publication (Section 4). By analyzing the ratios of these peak positions, it is possible to identify the specific liquid crystalline phase present in the sample.

For example, the two-dimensional inverse hexagonal (H_{II}) phase, which is composed of a hexagonal lattice of inverse cylindrical micelles, is characterized by a specific series of sharp Bragg peaks with relative positions following the ratio $1{:}\sqrt{3}{:}\sqrt{4}$ for the first three peaks. Common inverse mesophases relevant to lipid systems include:

- L_{II} (Inverse Micellar, disordered): A disordered fluid of inverse micelles, characterized by a single, broad peak, indicating a lack of long-range order.[37]
- $P6_3/mmc$ (Inverse Micellar, hexagonal): A hexagonal packing of inverse micelles.[38,39] Relative peak positions: $\sqrt{4/3}{:}\sqrt{3/2}{:}\sqrt{41/24}{:}\sqrt{17/6}{:}\sqrt{16}{:}...$
- Fd3m (Inverse Micellar, cubic): A cubic packing of inverse micelles.[37,40] Relative peak positions: $\sqrt{3}{:}\sqrt{8}{:}\sqrt{11}{:}\sqrt{12}{:}\sqrt{16}{:}...$
- H_{II} (Inverse Hexagonal): A hexagonal lattice of inverse cylinders.[37] Relative peak positions: $1{:}\sqrt{3}{:}\sqrt{4}{:}\sqrt{7}{:}\sqrt{9}{:}...$
- Pn3m (Bicontinuous Cubic): A complex network of interconnected channels.[37] Relative peak positions: $\sqrt{2}{:}\sqrt{3}{:}\sqrt{4}{:}\sqrt{6}{:}\sqrt{8}{:}...$

SAXS plots of those five lipid phases can be found in the forementioned Supporting Information as Figure S1.

To get even more information about the sample, the usual analytical approach in SAXS is the deconvolution of the total scattering intensity I(q) into two distinct components: the form factor P(q) and the structure factor S(q). This separation is mathematically represented as $I(q) \sim P(q) \cdot S(q)$. The form factor P(q) describes the scattering from isolated particles or repeating structural units, encapsulating information about their size, shape, and internal composition. In contrast, the structure factor S(q) describes the spatial organization and arrangement of these particles relative to one another. It accounts for the interference of scattered waves from different particles, revealing how the constituents are organized. In our latest publication, we instead conducted a Fourier analysis of the peak intensities to create 2D electron density maps following a procedure described by Michael Rappolt and his colleagues.[41] This method and our adjustments to it are explained in detail in Section 6.

3 Experimental Methodology

3.1 Sample Preparation Techniques for the Ionizable Lipid Bulk Phase

The preparation of the ionizable lipid bulk phase used the procedure developed by Marianna Yanez Arteta and her colleagues[42] as reference. In this procedure, the best comparability of bulk phase samples and lipid nanoparticles is achieved by mimicking their different environments with multiple dialysis steps. For our synchrotron measurements, the original procedure was adjusted to decrease the volume per sample. In order to improve sample consistency and reduce inter-sample variability, we standardized the procedure with small, commercially available dialysis cups and clearly defined step-by-step instructions. After a lot of trial and error, we found a reliable way to preserve most of our sample material during crucial steps as outlined below.

The revised procedure started with dissolving cholesterol and the cationic ionizable lipid (CIL) at a molar ratio of 1:3 in ethanol. 9.35 mg/mL cholesterol was mixed with either 46.5 mg/mL MC3/KC2 or 46.1 mg/mL DD in ethanol. Samples with polyA or mRNA had their lipid amount adjusted to get the same amount of sample material in the end. For this reason, the polyA/mRNA samples were prepared with only 6.98 mg/mL cholesterol and 40.7 mg/mL MC3/KC2 or 40.2 mg/mL DD in ethanol. Adding the right amount of CIL proved itself tricky since it is usually in a pure, oily form and if pipetted, a certain amount was always left behind in the pipette tip. Therefore, it was preferable to use a scale and measure how much CIL was exactly added to the sample. It was also easier to add the CIL before the ethanol since at those scales the ethanol evaporated quick enough to hampered the weight measurements.

The polyA or mRNA was dissolved in pure water (MilliQ) to a concentration of 42.2 mg/mL. Additional 2.5 mM HCl helped dissolving the polyA. The samples were then mixed directly inside small dialysis cups with one cup per sample. In our case the Slide-A-Lyzer™ MINI Dialysis Devices from Thermo Scientific™ had proven to be the most reliable option. Their dialysis membranes had a molecular weight cut-off of 3.5 kDa and although the cups were indicated to be optimal for a sample volume of 100 µL, up to 500 µL fitted inside. For the synchrotron measurements about 12 mg of material per sample resulted in a good signal to noise ratio. Therefore 215 µL of lipid-ethanol mixture and 40.5 µL polyA/mRNA-water was added to each dialysis cup. For samples without polyA or mRNA, the same amount of MilliQ was added instead. Additionally, 44.5 µL of 100 mM citric acid at pH 3 was added to each sample, which causes the mixed samples to become slightly opaque. To avoid any contamination, the dialysis cups were sealed once all components were inside. The Slide-A-Lyzer™ MINI Dialysis Devices came with tiny lids that were used for this purpose. At this point it was also advisable to label each cup.

For the following dialysis steps, the cups were put in swimmers to keep them afloat in the buffer, which was slowly stirred with magnetic stir bars during the whole procedure (Fig. 2). The first dialysis was conducted in a 500 mL reservoir of dialysis buffer consisting of 50 mM citrate buffer pH 3 and ethanol at a 3:1 volume ratio for two days. This slowly

Figure 2: Dialysis of the lipid bulk samples in preparation for SAXS measurements. The samples are inside pink dialysis cups with dialysis membranes at the bottom. Yellow, custom made swimmers keep the cups afloat while white magnet stir bars slowly mix the different buffers.

reduced the amount of ethanol which caused the lipids to precipitate in the water phase. At pH 3 the head groups of the CIL were positively charged, causing them to bind to the negative charges of polyA and mRNA.

After two days the dialysis reservoir was exchanged with PBS buffer consisting of 1 mM KH_2PO_4, 155 mM NaCl, and 3 mM Na_2HPO_4 at pH 7.4 for another two days. During this step, the ethanol was dialyzed out of the sample and the PBS mimicked the environment that lipid nanoparticles experience after their medical application. In the end the dialysis reservoir was exchanged for a last dialysis towards the desired pH. McIlvaine buffer was used for the last dialysis, which is a citrate-phosphate buffer consisting of Na_2HPO_4 and citric acid. Depending on the ratio of both chemicals the pH is adjustable from 2.2 to 8.0.

The next step was the extraction of the samples from the dialysis cups and transfer to the quartz capillaries. This part was the most crucial since it was easy to lose significant amounts of the prepared sample if not handled with the upmost care. The goal here was to have the samples at the bottom of capillaries, sandwiched between layers of buffer on both sides to prevent the samples from drying out. This was achieved by first pipetting about half a centimeter of the final dialysis buffer inside the capillaries. The exact amount depends on the capillary diameter. The capillaries were then put into conical centrifuge tubes with a volume of approximately 15 mL. Only one capillary per tube is allowed, otherwise the capillaries crush each other during the following centrifugation. Although quartz capillaries are not cheap, it was helpful to sacrifice one or two in order to determine the maximum centrifugal force they could withstand. A slightly lower force is then used to centrifuge the buffer to the bottom of the capillaries. This way, capillaries with defects broke before the precious sample material was inserted.

After preparing the capillaries with buffer, the sample material was carefully scooped from the dialysis cups and squeezed inside the capillaries. The consistency of our sample material was highly dependent on the pH of the last dialysis buffer. Below pH 6, the sample precipitated as white and sticky blobs. Using a small, clean and blunt rod (like the blunt end of a metal inculation loop), it was possible to fish the precipitates out without losing much sticking to the rod. Some of it also stuck to the walls of the dialysis

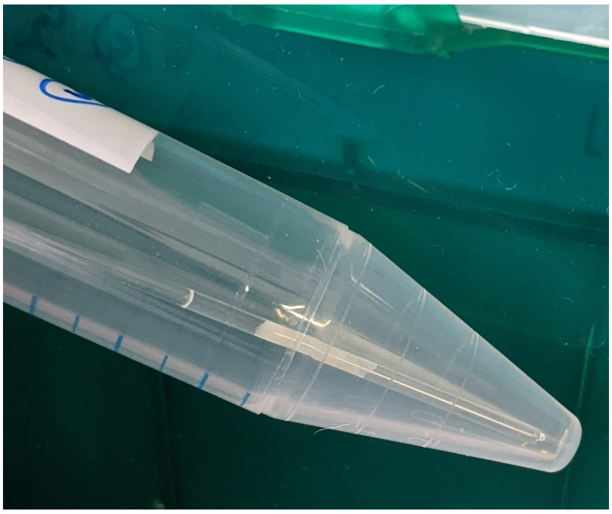

Figure 3: The thin quartz capillary contains white lipid bulk material, layered between buffer on both sides.

cups, so it was necessary to carefully scrape it off the dialysis cup walls and inside the capillaries. Above pH 6, the sample material formed an greasy, liquid film at the top of the dialysis cups, making it impossible to fish or scrape it out. To still achieve a high sample concentration, the sample was instead carefully pipetted out, trying to take the least possible amount of buffer with it.

The sample material was then centrifuged down, forming a distinct layer on top of the buffer that was inserted before. A second layer of buffer was then pipetted on top. This second buffer layer was only centrifuged slowly, to prevent it from being pushed below the sample material. If everything was performed correctly, the result was a capillary with a layer of sample material between two layers of buffer (Fig. 3). In the end, the capillaries were sealed using hot wax, forming an airtight seal. The samples were then stored in the dark and at 4°C for several weeks or even months before being measured. Although these samples probably cannot be preserved indefinitely, extended storage time gave the lipid structure time to equilibrate. When remeasuring samples that were stored in the dark and at room temperature for one year, their signal quality even improved compared to them being measured after only one month. In any case, the samples were always warmed to at least room temperature before being measured.

3.2 SAXS Measurement Protocols and Data Acquisition

While adjusting our preparation protocol, we used our in-house SAXS device to compare sample qualities and to check which pH range to focus on subsequently. But due to its superior resolution and measuring speed, we exclusively used synchrotron data for our publications. In total we prepared samples for four beam times at the P12 EMBL beam line at DESY in Hamburg between 2021 and 2023. At this point I have to thank their beam line scientist Clement E. Blanchet, who helped us measure about 500 different capillaries. Each capillary was measured at up to 20 different positions and at each position 20-40 individual frames were recorded by the detector with a exposure period of

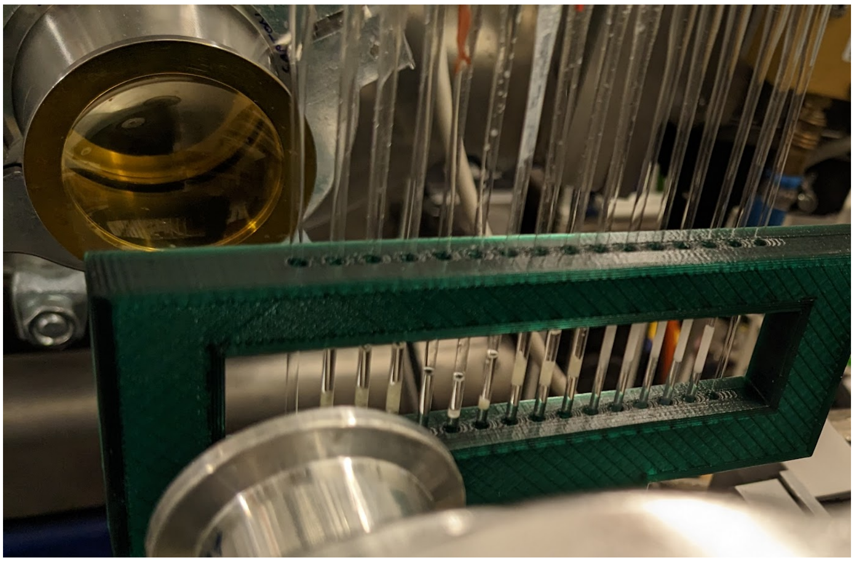

Figure 4: This 3D printed sample holder contains 16 capillaries with lipid bulk samples and is mounted on a motorized stage. During the measurement, the X-ray beam is directed through the upper vacuum tube and the brown Kapton foil before it scatters at the sample and enters the lower vacuum tube to reach the detector.

100 ms per frame. The capillaries were placed side by side in a 3D printed capillary holder on a motorized stage, that made it possible to automatically measure up to 16 capillaries per run (Fig. 4). For our publication "Buffer Specificity of Ionizable Lipid Nanoparticle Transfection Efficiency and Bulk Phase Transition" (Section 5) we additionally measured samples at an increased temperature of 37°C by heating them externally for at least three hours to give the lipid mesophases time to equilibrate.

3.3 SAXS Data Analysis and Interpretation

The recorded SAXS data showed concentric circles around the direct beam, which is usually blocked to protect the detector from its high intensity. Looking at these circles, we could already indicate two different types of circles: isotropic and non-isotropic (Fig. 5). Most of the circles were isotropic, indicating that the alignment of the source of these circles was isotropic at the scale of the beam size. The non-isotropic circles on the other hand came from crystals that were large enough to create X-ray diffraction into certain preferred directions. In our lipid bulk phase samples, these non-isotropic circles were created by cholesterol monohydrate crystals, which can grow large enough to be visible via conventional light microscopy (Fig. 6).

In order to analyze the measurements further, the 2D detector images was integrated radially and plotted versus the absolute scattering vector q. In this depiction, the rings, both isotropic and non-isotropic, were presented as peaks. In order to increase the signal-to-noise ratio, the background was measured by using empty capillaries and subtracted from the sample measurement. Most of the undesired scattering came from the Kapton foils at the end of the vacuum tubes with only little contribution by the air between the tubes and from the capillaries. Since the Kapton scattering always occurred at the same

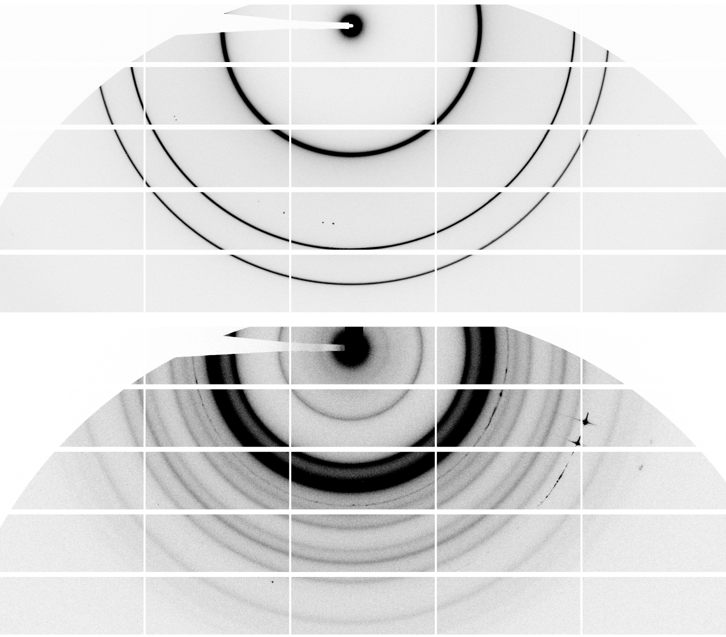

Figure 5: Inverted SAXS detector images of lipid bulk phases. The upper scattering pattern shows an inverse hexagonal structure with its characteristic ratio of $1{:}\sqrt{3}{:}2$ around the mostly blocked direct beam. The lower scattering pattern shows the much more complex inverse micellar Fd3m structure. Most of the rings are isotropic but two distinct rings contain several radiant spots. Those non-isotropic rings are caused by large cholesterol monohydrate crystals formed by an excess of cholesterol inside our samples.

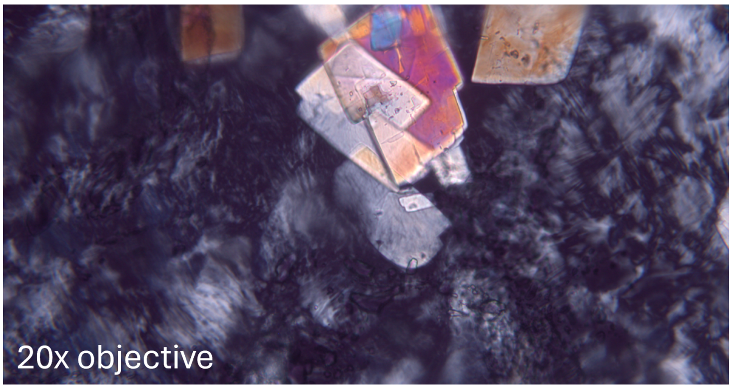

Figure 6: An excess of cholesterol during the lipid bulk phase preparation causes large cholesterol monohydrate crystals, which are visible through crossed polarizers in a light microscope. This microscopy image shows the H_{II} phase and was recorded by Dorothea Hofer during her Master Thesis.

positions, it was relatively easy to subtract them properly. The resulting SAXS plots are displayed in Fig. 2 of our first publication in Section 4 and Fig. 3a of our second publication in Section 5.

The following analysis of the SAXS data was conducted via custom scripts, that were either entirely written by myself or derived from scripts by Gerome Vancuylenberg and Michael Rappolt[41] (2D electron density maps), and Jan Westergren (continuum model). The whole procedure is described in detail in our publication "Combining SAXS Analysis and MD Simulation to Determine Structure and Hydration of Ionizable Lipid Hexagonal Phases" (Section 6) and its Supplementary Information.

4 Publication 1: pH-dependent structural transitions in cationic ionizable lipid mesophases are critical for lipid nanoparticle function

Our first major publication compared different cationic ionizable lipids (CILs) used in lipid nanoparticle (LNP) formulation and analyzed their structural behaviour in response to the pH of the environment. In collaboration with Lennart Lindfors and his collegues (AstraZeneca in Gothenburg), who conducted in-vivo experiments, as well as Nadine Schwierz and Akhil Sudarsan (University of Augsburg) for molecular dynamics (MD) simulations, we analyzed three common CILs: DLin-MC3-DMA (MC3), DLin-KC2-DMA (KC2), and DLinDMA (DD). In-vivo analysis in the mouse liver demonstrated a ranking of eGFP protein expression (MC3 $\geq$ KC2 $>$ DD), despite all three CIL-LNPs showing similar mRNA delivery to the target cells.

This key finding led to the conjecture that the difference in efficacy is entirely caused by the subsequent endosomal escape and mRNA release efficiency. To confirm this hypothesis, Anita Reiser conducted in-vitro experiments which showed that DD-based LNPs exhibited a delayed onset and reduced level of protein expression compared to MC3 and KC2, directly mirroring the in-vivo ranking.

To find the structural root of this difference, we used synchrotron small-angle X-ray scattering (SAXS) to systematically study bulk phases consisting only of the CIL and cholesterol as a simplified model of the LNP core. Upon lowering the pH, we observed a sequence of ordered mesophases, including inverse micellar (L_{II}, $P6_3/mmc$, and $Fd3m$), inverse hexagonal (H_{II}), and inverse bicontinuous cubic ($Pn3m$) phases. We identified the pH-driven transition from the inverse micellar to the inverse hexagonal phase, occurring around pH 6, to be the critical event, that is likely responsible for endosomal membrane disruption and mRNA release. The same transition was also observed in molecular dynamics (MD) simulations, which was accompanied by the relocation of the MC3 head groups into the water phase.

Crucially, the SAXS data revealed that while all three CILs underwent the critical inverse micellar to inverse hexagonal phase transition, the excess lipid phase in DD models exhibited a considerably larger nearest-neighbor distance, which probably also led to a higher degree of hydration compared to MC3 and KC2. The DD phase also uniquely exhibited the $Pn3m$ phase at the lowest pH, posing as a possible hindrance during endosomal escape and subsequent release of the mRNA in the cell plasma. This increased spacing and hydration correlated with our in-vitro and in-vivo findings of the delayed onset and reduced level of protein expression for DD-based LNPs. We picked up this link in our latest publication (Section 6) and extended our analysis of SAXS data and MD simulations.

PNAS RESEARCH ARTICLE | BIOPHYSICS AND COMPUTATIONAL BIOLOGY
PHARMACOLOGY
OPEN ACCESS

pH-dependent structural transitions in cationic ionizable lipid mesophases are critical for lipid nanoparticle function

Julian Philipp[a], Aleksandra Dabkowska[b], Anita Reiser[a], Kilian Frank[a], Rafał Krzysztoń[a], Christiane Brummer[a], Bert Nickel[a], Clement E. Blanchet[c], Akhil Sudarsan[d], Mohd Ibrahim[d], Svante Johansson[b], Pia Skantze[b], Urban Skantze[b], Sofia Östman[e], Marie Johansson[e], Neil Henderson[f], Kjetil Elvevold[g], Bård Smedsrød[h], Nadine Schwierz[d], Lennart Lindfors[b], and Joachim O. Rädler[a,1]

Edited by David Weitz, Harvard University, Cambridge, MA; received June 25, 2023; accepted October 28, 2023

Lipid nanoparticles (LNPs) are advanced core-shell particles for messenger RNA (mRNA) based therapies that are made of polyethylene glycol (PEG) lipid, distearoylphosphatidylcholine (DSPC), cationic ionizable lipid (CIL), cholesterol (chol), and mRNA. Yet the mechanism of pH-dependent response that is believed to cause endosomal release of LNPs is not well understood. Here, we show that eGFP (enhanced green fluorescent protein) protein expression in the mouse liver mediated by the ionizable lipids DLin-MC3-DMA (MC3), DLin-KC2-DMA (KC2), and DLinDMA (DD) ranks MC3 ≥ KC2 > DD despite similar delivery of mRNA per cell in all cell fractions isolated. We hypothesize that the three CIL-LNPs react differently to pH changes and hence study the structure of CIL/chol bulk phases in water. Using synchrotron X-ray scattering a sequence of ordered CIL/chol mesophases with lowering pH values are observed. These phases show isotropic inverse micellar, cubic Fd3m inverse micellar, inverse hexagonal H_{II} and bicontinuous cubic Pn3m symmetry. If polyadenylic acid, as mRNA surrogate, is added to CIL/chol, excess lipid coexists with a condensed nucleic acid lipid H_{II}^{c} phase. The next-neighbor distance in the excess phase shows a discontinuity at the Fd3m inverse micellar to inverse hexagonal H_{II} transition occurring at pH 6 with distinctly larger spacing and hydration for DD vs. MC3 and KC2. In mRNA LNPs, DD showed larger internal spacing, as well as retarded onset and reduced level of DD-LNP-mediated eGFP expression in vitro compared to MC3 and KC2. Our data suggest that the pH-driven Fd3m-H_{II} transition in bulk phases is a hallmark of CIL-specific differences in mRNA LNP efficacy.

lipid nanoparticles | mRNA delivery | ionizable lipid | lyotropic mesophases | SAXS

Significance

The pH-dependent response of CIL-LNPs (Cationic ionizable lipid-Lipid nanoparticles) is key to endosomal release and subsequently improved clinical outcome. We provide a systematic study of lyotropic order of three ionizable lipids and determine pH-dependent structural transitions in terms of crystal symmetry and spacings. The findings result in a refined perception of mode of action. Supported by molecular dynamics (MD) simulations, it stands to reason that the inverse micellar to inverse hexagonal transition of the excess CIL phase is the limiting step associated with release and less efficient in DD (DLin-DMA). This hypothesis is substantiated by delayed protein expression onset in DD-LNP-mediated transfection compared to MC3 and KC2. Our data suggest that not structure but structural transitions cause fusogenic activity.

Decades of research, based on rational design and screening approaches, resulted in the achievement of lipid nanoparticles (LNPs), which have improved efficiency and safety of nucleic acid delivery over several orders of magnitude (1–3). First formulations based on LNP technology have been approved by the US Food and Drug Administration, including Onpattro, the first LNP-based drug delivering small interference RNA (siRNA) (4), as well as Moderna's and Pfizer/BioNTech's mRNA LNP-based vaccines against SARS-CoV-2 (5, 6). It is expected that LNPs will play a vital role in future mRNA-based vaccines for cancer immunotherapy (6), chimeric antigen receptor T cell–based immunotherapies (7), and gene editing using CRISPR (8). LNPs exhibit favorable properties such as defined size, colloidal stability, and surface inertness. Efficient condensation and encapsulation of negatively charged nucleic acid cargo in LNPs is enabled via cationic lipid charge and rapid microfluidic mixing during the self-assembly process (9, 10). The choice of ionizable and biodegradable lipids reduces cytotoxicity and enables rapid elimination from plasma and tissue (11). Finally, LNPs efficiently mediate cellular uptake via plasma proteins and subsequent release of nucleic acid to the cytosol (12). It is understood that these properties come about by optimal choice of four lipid components including cholesterol (chol) that self-assemble into a well-defined core-shell architecture which distinguishes LNPs from other gene delivery particles. Typically, PEG-lipid and a structural helper lipid are employed to form a surface monolayer that stabilizes LNP size, while cationic ionizable lipid (CIL) and chol represent the components that condense and encapsulate nucleic acid in the LNP core. Cryo-TEM imaging provides some insight into LNP size and morphology (13–16). For LNPs formulated from ionizable lipid and siRNA, spherical morphology is observed with relatively homogeneous size and core textures indicating dense hexagonal or lamellar order (13, 15). The picture is in agreement with coarse-grained simulations of siRNA-LNPs reproducing core-shell particles with PEG-lipid segregated at the surface and a disordered, densely packed core phase (10, 17). The mRNA LNPs discussed here show spherical shapes with dense, homogenous cores in cryo-TEM images (14).

Author contributions: L.L. and J.O.R. designed research; J.P., A.D., A.R., R.K., C.B., C.E.B., A.S., M.I., P.S., U.S., S.Ö., M.J., N.H., K.E., and B.S. performed research; J.P., A.D., A.R., K.F., B.N., and S.J. analyzed data; A.S., M.I., and N.S. performed simulations; S.Ö., M.J., N.H., K.E., and B.S. carried out animal study; and J.P., N.S., L.L., and J.O.R. wrote the paper.

Competing interest statement: A.D., P.S., U.S., S.Ö., M.J., N.H., K.E., B.S., and L.L. are employed by AstraZeneca R&D Gothenburg.

This article is a PNAS Direct Submission.

[1] To whom correspondence may be addressed. Email: raedler@lmu.de.

This article contains supporting information online at https://www.pnas.org/lookup/suppl/doi:10.1073/pnas.2310491120/-/DCSupplemental.

Despite clinical success, the mechanism of how LNPs mediate release of mRNA from endosomes into the cytosol is still not fully resolved. As a result of this, we are not yet in the position to design predictable nanomedicine from the bottom up. Small molecular variations in chemical structure have unexpectedly large effects on efficiency. While transport and biodistribution in the extracellular space as well as adhesion and uptake by target cells is controlled by surface properties, it is generally believed that the core structure and pH-dependent properties of the fusogenic ionizable lipid components enable endosomal release. Specifically, the claim was made that for optimal siRNA-mediated gene silencing, the effective pK_a of ionizable lipids, as determined using the anionic fluorescent dye 2-(p-toluidino)-6-naphthalenesulfonic acid binding assay, should be in the range between 6.2 and 6.5 (18). The ionizable lipids DLin-DMA (DD), DLin-KC2-DMA (KC2) (19), and DLin-MC3-DMA (MC3) (18) have been a showcase of ionizable lipid optimization featuring dramatically improved in vivo activity (Fig. 1 *A* and *B*). However, despite the use of the same ionizable dimethylamino group and tail length, DD, KC2, and MC3 perform differently. It appears that the pH-dependent response of ionizable lipids is key to understand endosomal release, but the choice of an optimal ionizable lipid headgroup alone is not the full answer (13, 20).

It has been argued for long that lipid polymorphism, i.e., the properties of lipids to aggregate into various liquid crystalline symmetries, plays a role in lipid-mediated delivery of nucleic acid (19, 21, 22). In the past, cationic lipid complexed with negatively charged DNA has been shown to form distinct mesophases with lyotropic lipid order and DNA superlattices (22–26). These condensed lipid phases are indexed with a superscribed “c” for complexed and constitute electrostatically neutral thermodynamic phases with defined DNA spacings. With increasing nitrogen–phosphate (N/P) ratio, complexed nucleic acid lipid phases coexist with excess cationic lipid. Phase behavior depends on composition, temperature, and salt conditions. Recently, lamellar CIL phases mixed with mRNA were studied and shown to be pH responsive (27–29). It has been shown that inverse hexagonal and cubic symmetries of complexed phases lead to increased nucleic acid delivery compared to lamellar order, a structure–activity relation that seems to hold both for lipoplexes (22–24) as well as LNPs (15, 16). In contrast to lipoplexes, that can be perceived as dispersed complexed mesophases without dedicated surface component, LNPs are core-shell particles with distinct surface and core composition. In fact, as shown in recent neutron scattering studies, the surface-active components PEG-lipid and DSPC are phase separated, for the most part, from ionizable lipid–chol that predominantly form the core phase (14). This finding is of fundamental value since it allows to study and improve surface and core properties separately. In this spirit, it is insightful to study phase behavior of macroscopic bulk samples that mimic the LNP core moiety. Yet, studies on CIL/chol bulk phases with and without nucleic acid are missing.

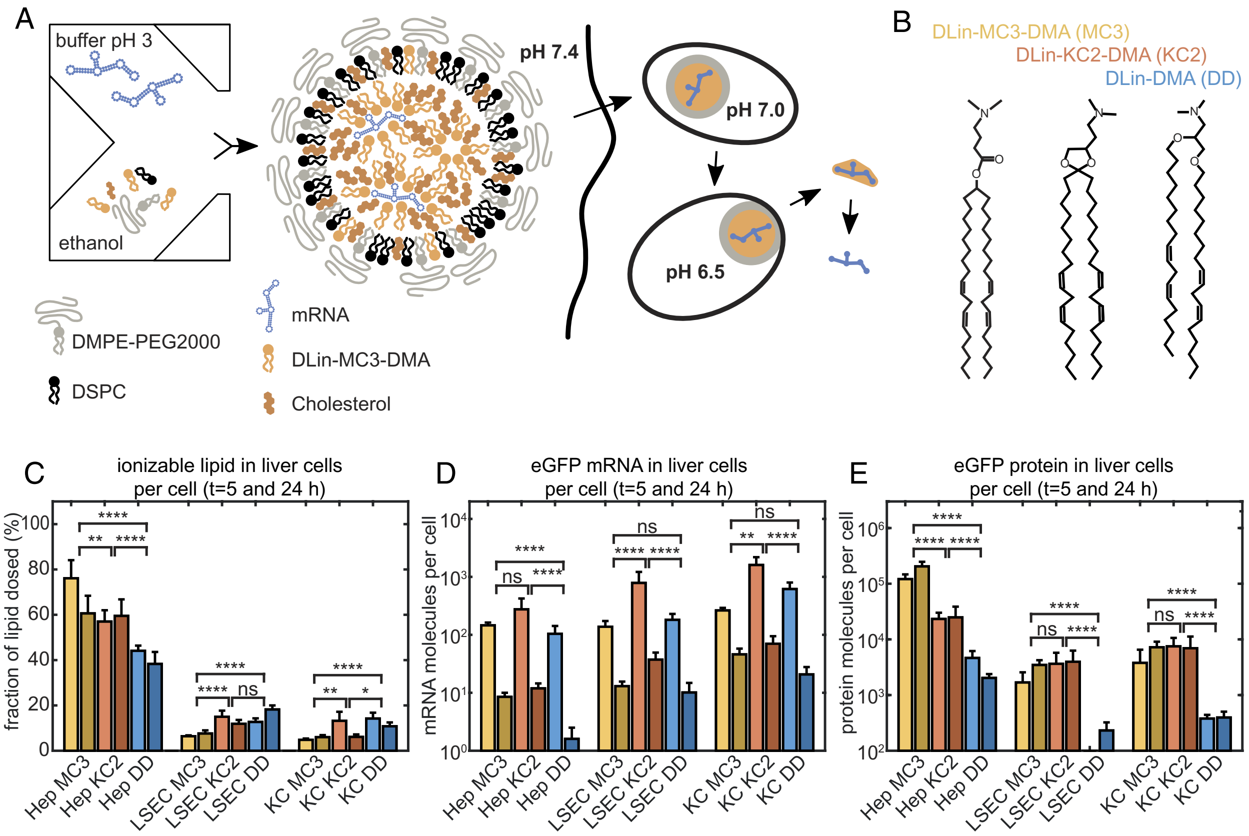

Fig. 1. LNP-mediated mRNA delivery and protein expression in vivo. (*A*) Schematic drawing of production, internalization via endocytosis, and pH-dependent maturation of LNPs preceding endosomal release. mRNA LNP particles exhibit a core-shell structure consisting of a condensed core phase composed of mRNA, CIL, and chol, with an outer shell enriched in DSPC and a PEG corona. (*B*) The ionizable lipids MC3, KC2, and DD differ in head group area while sharing the same lipid tails and ionizable dimethylamino-group. (*C*) Mice study of ionizable lipid uptake in liver cells, (*D*) mRNA uptake in liver cells, and (*E*) in vivo protein expression per cell type showing same uptake yet unexplained order of protein expression efficacy MC ≥ KC2 > DD. Four mice in each group were used with an mRNA dose of 0.5 mg/kg. Error bars in figures (*C*–*E*) are the SEM. Significance levels are based on the Mann–Whitney method.

Here, we explore the in vivo delivery of eGFP (enhanced green fluorescent protein) mRNA LNPs based on MC3, KC2, and DD and quantify the cell-specific lipid and mRNA delivery as well as the consecutive protein expression. To rationalize these in vivo observations, we systematically study the mesophases of the core-forming LNP components, i.e., the CIL, MC3, KC2, and DD and chol. Using high-resolution synchrotron X-ray scattering, we identify lyotropic structures as a function of pH in pure CIL/chol/buffer phases and phases of CIL/chol/buffer and nucleic acid. We pursue the hypothesis that structures found in reconstituted bulk phases are meaningful for the clarification of LNP response inside endosomes. Throughout this manuscript, we will distinguish macroscopic "bulk phases" with defined lipid composition, from "LNP core phases", which represent the inner lipid moiety of LNPs. We find for the three ionizable lipids, MC3, KC2, and DD, that first the pure lipid/chol phases exhibit ordered mesophases in the following order of appearance: L_{II}, cubic micellar Fd3m, inverse hexagonal H_{II}, and bicontinuous cubic Pn3m, when lowering pH from pH7 to pH5. Second, if polyA (polyadenylic acid) as linear mRNA model is added to the bulk phases, coexistence of pure lipid phases and a complexed nucleic acid lipid H_{II}^{c} phase is evidenced by separate sets of Bragg reflections. We show that the observed structures are consistent with SAXS (Small angle X-ray scattering) data from less ordered phases containing eGFP-mRNA as well as from LNPs. We find that the excess lipid phase for all three CIL studied undergoes an Fd3m-H_{II} transition at about pH 6. However, DD exhibits considerably larger micellar nearest-neighbor distances in the transition region. Likewise, we observe that in LNPs, both spatial order and lipid mobility undergo a pronounced transition with pH. This finding goes hand in hand with a distinctly delayed onset and reduced level of eGFP expression in DD-meditated compared to MC3- and KC2-mediated mRNA LNP transfection. We discuss how the pH-sensitive transition from inverse spherical micellar to inverse hexagonal lipid structures in lipid excess phases explains the observed CIL-dependent difference in LNP endosomal release.

Results

In Vivo eGFP-mRNA LNP Dosing Experiment in Mice. The LNPs studied here are prepared at pH 3 by rapid mixing of an aqueous mRNA citrate buffer phase and lipid/chol components dissolved in ethanol phase. The resulting particles are dialyzed against phosphate-buffered saline (PBS, pH 7.4) in order to adjust the pH and remove residual ethanol (*Materials and Methods*). LNPs are composed of ionizable lipid, DSPC, Chol and PEGylated lipid (DMPE-PEG2000) forming core-shell particles as schematically depicted in Fig. 1*A*. The N/P ratio of nitrogen atoms on the ionizable lipid and phosphor atoms on the mRNA chain was 3:1. In the following, we compare the three ionizable lipids DLin-MC3-DMA (MC3), DLin-KC2-DMA (KC2), and DD, which are outfitted with the same ionizable (dimethyl)-amino group and the identical (dilinoleyl) tail moiety as shown in Fig. 1*B* (*Materials*). However, the ionizable lipids differ in their linker group, and it has been noticed earlier that also the siRNA knockdown efficiency of the three lipids vastly differ both in vitro as well as in vivo (18). LNPs are internalized by cells via receptor-mediated endocytosis. Inside endosomes, pH is lowered over time and pH-induced structural changes are believed to induce LNP-endosomal membrane fusion and subsequent release of mRNA from LNPs (Fig. 1*A*). The different efficiency of the three ionizable lipids is believed to be routed in the endosomal release mechanism. In order to verify that this hypothesis is valid for mRNA delivery in vivo and furthermore that the mechanism is independent of cell type, we designed a comparative LNP dosing experiment in CD1 mice. Specifically, we measure uptake of the ionizable lipid component and the eGFP-mRNA via MC3-, KC2- and DD-based LNP formulations and compare relative uptake to protein expression. To this end, mice were injected with eGFP encoding mRNA LNPs, and the resulting mRNA and eGFP level in liver cells was analyzed. In order to quantify uptake into various types of liver cells in an unbiased way, cells from the liver were carefully isolated, thus removing extracellular components containing unsuccessful LNP material. Subsequently, cells were sorted to yield insight into possible cell type dependence. Specifically, hepatocytes, liver sinusoidal endothelial cells (LSECs), and Kupffer cells (KCs) were isolated from mouse liver. Hepatocytes make up 90% of the liver volume, LSECs account for most of the liver endothelial interface, and KCs comprise tissue-resident macrophages (30). There is a distinct dual blood clearance functionality between LSECs, which are specialized on uptake of macromolecules and nanoparticles <approx. 200 nm, and KCs, which are specialized on uptake of particles >approx. 200 nm (31). All three cell types are then subject to analysis of mRNA, eGFP, and ionizable lipid content. As shown in Fig. 1 *C* and *D*, the uptake of both ionizable lipid and mRNA in liver cells is similar between MC3-, KC2-, and DD-mediated delivery. In control mice given only PBS, analytical measurements of either the ionizable lipid, the mRNA or the protein was below the lower limit of quantification. A significant fraction of the lipid dose for all three LNPs is found in hepatocytes, likely because by both number and volume, these cells constitute the major part of the liver. Note that the study was designed with animals randomized in pairs as diagramed by two bars in the plot representing samples taken at 5 and 24h, respectively. Protein expression was most pronounced in the hepatocyte fraction vs LSECs and KCs. Furthermore, in the hepatocytes, eGFP expression varied in the order MC3 > KC2 > DD (Fig. 1*E*), despite similar lipid and mRNA uptake at the cellular lever (per cell). It should be noted that for LSEC and KC fractions, LNPs of MC3 and KC2 gave similar but higher expression vs DD LNPs. Furthermore, the order of expression level follows the same trend, albeit less pronounced, as for siRNA-LNP-mediated hepatic gene silencing (18, 19). Hence, the quest to search for difference in the pH-dependent response of the three different CIL-LNPs during endosomal release is of immediate importance for clinical applications.

Bulk CIL/Chol Mixtures Exhibit Sequence of Lyotropic Phases as a Function of pH. In order to understand structural transitions that occur in the core of LNPs, we study macroscopic bulk phases of CIL/chol/water with and without nucleic acid as a function of pH. An overview of the high-resolution synchrotron SAXS data is given in Fig. 2. *SI Appendix*, Fig. S1 shows an overview of these SAXS measurements at a higher resolution. Adenoside monophosphate homopolymer, polyA, was selected as a model for mRNA because of similar biophysical properties. The experiments follow the investigations done in previous work (14) exploring bulk phase properties as proxies for LNP core phase behavior. In their study as well as in ours, the bulk phases were produced in a way that was as analogous to LNP production as possible. CILs, chol, and polyA were mixed and dialyzed against the same buffer used in the microfluidic mixer during the formation of LNPs (50 mM citrate pH 3 and ethanol, in a 3 to 1 volume ratio (*SI Appendix*, Fig. S2). Afterward, to simulate the process of LNP production, the bulk phases were dialyzed against PBS pH 7.4. Finally, a third dialysis step was used to bring the bulk phases to the required pH. The chosen pH range (pH 4.5 to pH 7.4) was adjusted to match the pH conditions experienced by LNPs within the cellular endosome (32) to capture the entire gamut of interactions of polyA with the

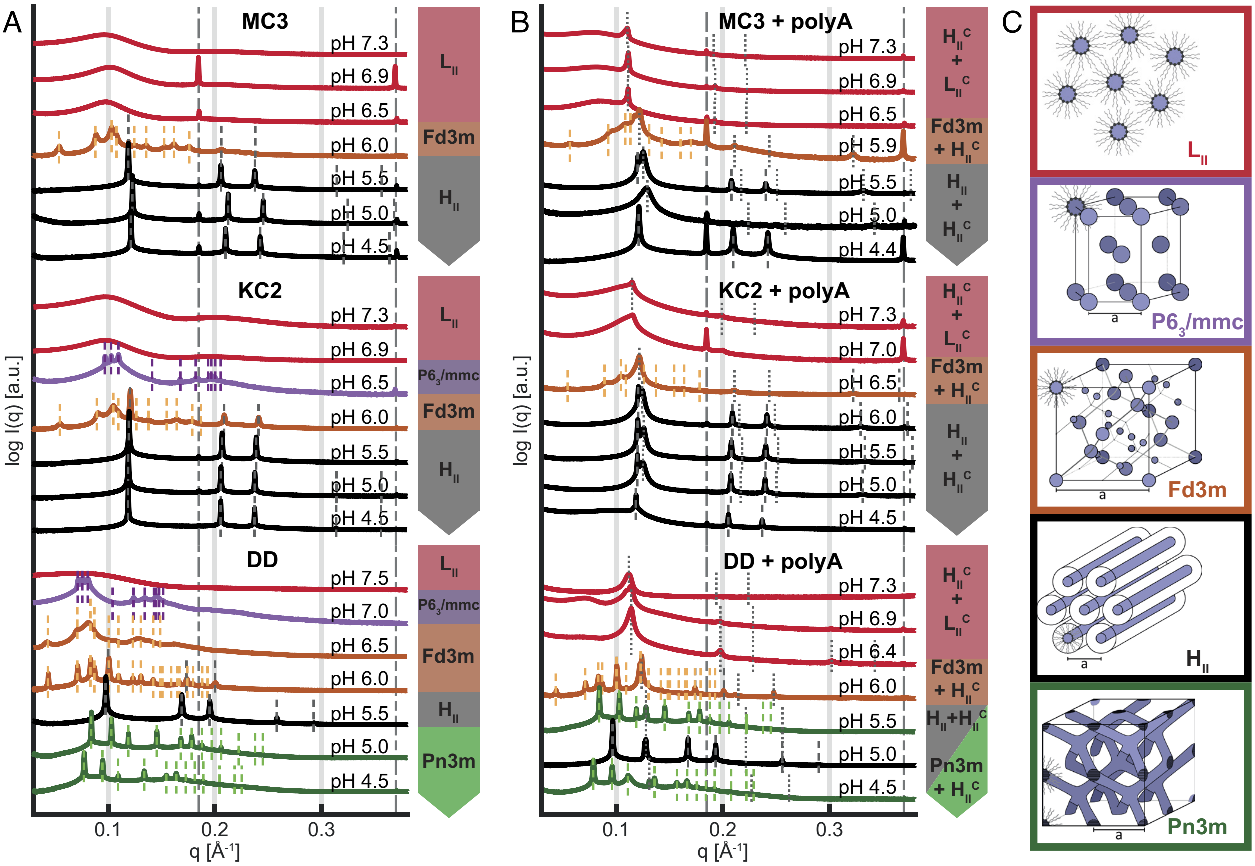

Fig. 2. SAXS-based identification of pH-dependent mesophase transitions. (*A*) Ionizable lipid, chol, and buffer and (*B*) ionizable lipid, chol, buffer, and polyA. Data show the three ionizable lipids, MC3, KC2, and DD, for comparison. (*C*) Schematic representation of lipid phases with decreasing pH from top to bottom showing a trend from negative curvature toward zero curvature with increasing headgroup protonation: Inverse micellar fluid isotropic L_{II}, inverse micellar cubic with P6$_3$/mmc symmetry, inverse micellar cubic with Fd3m symmetry, inverse hexagonal H_{II}, and bicontinuous cubic Pn3m. In the presence of polyA (panel *B*), coexistence of lipid mesophases with a complexed, nucleic acid containing, phase is observed. In the pH range from 5.0 to 6.0 typically H_{II} and H_{II}^{c} coexist. See main text for further information.

lipids. Samples were equilibrated over 1 to 4 wk. The long dialysis and equilibration time are required to ensure the formation of equilibrated homogeneous phases as also seen in the evolution of SAXS data with time (*SI Appendix*). Note that according to the preparation protocol, water is added in excess and CIL/chol/buffer phases typically swim above supernatant buffer due to their lower density. Fig. 2*A* shows the scattering data of CIL/chol/buffer bulk phases dialyzed to a range of pH conditions for the three CILs, MC3, KC2, and DD. Sharp Bragg reflections emerge at pH values lower than about 6.5, indicating the formation of ordered phases. The crystal symmetries of the ordered phases are identified according to the relative peak positions (Fig. 2*C* and *Methods*). The overall progression of structures exhibits a general trend for all three CIL/chol/buffer phases: At neutral pH, the bulk phase is a disordered inverse micellar L_{II} phase with one main structural peak (in the region of 0.1 Å^{-1}) and a weak second-order peak at about 0.2 Å^{-1}. As the conditions become more acidic, at a pH of around 6.0 to 6.5, an isotropic cubic inverse micellar phase (Fd3m) appears, which is followed by a transition to an inverse hexagonal H_{II} phase. In the case of DD/chol/buffer, one additional phase, a bicontinuous cubic phase Pn3m, appears at very low pH values below pH 5.0. In rare cases, we observe an inverse hexagonal micellar phase with P6$_3$/mmc symmetry (33) preceding the Fd3m cubic phase at pH 7.0. All core phases, in all pH conditions, also showed two characteristic peaks at q values of 0.186 Å^{-1} and 0.368 Å^{-1} (Bragg spacings of 33.8 Å and 17.0 Å, respectively), which were noted previously (14) as chol monohydrate crystals (34). The chol crystals are already present during the preparation steps of the bulk phases. These crystals are not expected to be present in the LNPs due to the nano-sized precipitates rapidly formed by microfluidic mixing. The overall sequence of CIL mesophases observed in Fig. 2*A* follows well-known behavior in lyotropic liquid crystalline phase formation which are driven by the molecular shape factor, also known as critical packing parameter (CPP) (35). This interpretation suggests that at neutral pH the effectively charge neutral CIL monolayer possesses negative curvature favoring inverse micelles. Increasing protonation of the CIL headgroup will increase the headgroup area and hence shifts the spontaneous curvature of the CIL monolayer toward less negative values. In summary, the lipid bulk phases of the three CIL/chol/buffer mixtures show almost identical order of distinct mesophases following a trend from negative curvature toward zero curvature structure with decreasing pH.

polyA-Complexed CIL Phase Coexistence with Excess CIL. If polyA is added to CIL/chol/buffer phases (Fig. 2*B*), we observe additional peaks in the SAXS data which correspond to nucleic acid complexed phases. The additional peaks appear on top of the phases without polyA, hence showing coexistence of an excess CIL phase with polyA-CIL complexed phases (*SI Appendix*). Most prominently, coexistence is observed in the pH range 5.5 to 6.5, where a complexed inverse hexagonal H_{II}^c and the inverse lipid H_{II} phases are seen by two closely spaced first-order reflections. Higher-order reflection with spacings 1:√3:√4 is found in some cases. At pH values above pH 6.5, when the ordered lipid phases turn into the disordered L_{II} phase, the complexed phase H_{II}^c seems to continue to exist as seen by the sharp peak on top of the L_{II} phase signature. However, over periods of weeks, this peak broadens, shrinks, and eventually disappears (*SI Appendix*, Fig. S3). We investigated whether polyA was released from the bulk phase during this process but did not find increased nucleic acid content in the supernatant (*SI Appendix*, Fig. S4). Hence, we interpret the disappearance of the H_{II}^c as unbundling of the hexagonal bundles into dispersed polyA filled inverse cylindrical micelles dissolved in the excess micellar lipid phase. As this equilibrated phase is stable over long time and SAXS pattern at long time scales do not show signs of phase coexistence, we term this isotropic complexed L_{II}^c for a nucleic acid complexed micellar phase. Taken together, the addition of polyA to CIL/chol/buffer systems leads to complexation of polyA and CIL as indicated by the appearance of an additional inverse hexagonal condensed H_{II}^c phase. At high pH values (pH 6 to pH 7), a less defined isotropic complexed L_{II}^c phase forms.

Electron Density Profiles and Water Content of Inverse Phases for MC3. Next, we study the electron density distribution and molecular conformations within the MC3/chol/buffer phases. We combine experiments and all-atom MD simulations by incorporating the experimental lattice symmetry and distances as constraints to the simulations and yield an accurate form factor from MD to model the SAXS intensities. Using this approach, the simulations provide detailed molecular insights into the lyotropic phases H_{II} and L_{II} and resolve the individual contributions to the scattering intensities. The measured Bragg peak intensities show that the lipid phases contain a water core surrounded by MC3 lipids with headgroups facing the water core and chol and MC3 lipid tails forming an outer oil-like moiety. We performed MD simulations of MC3/chol/water using our recently developed force fields for uncharged and charged MC3, which were validated based on neutron reflectometry data of MC3 lipid bilayers (36). Fig. 3*A* shows the inverse hexagonal structure with fully protonated MC3 obtained from the simulations. In the simulation, we assumed that MC3 at pH 5.5 is fully charged. Note that the exact degree of protonation of MC3 as a function of pH is difficult to determine and remains a matter of ongoing research. For the two extreme cases, we find that the hexagonal assembly with protonated headgroup is stable over the course of the simulation, while the corresponding simulation with uncharged MC3 headgroup is not. In the MD simulation, the water content is a free variable described by the molar ratio n_W of water to CIL molecules. In order to determine the correct water content in the H_{II} phase, we performed simulations with varying molar ratios n_W. During the simulations, the box size and hence the lattice constant adapts to the external conditions. From these simulations, we selected the ratio that reproduced

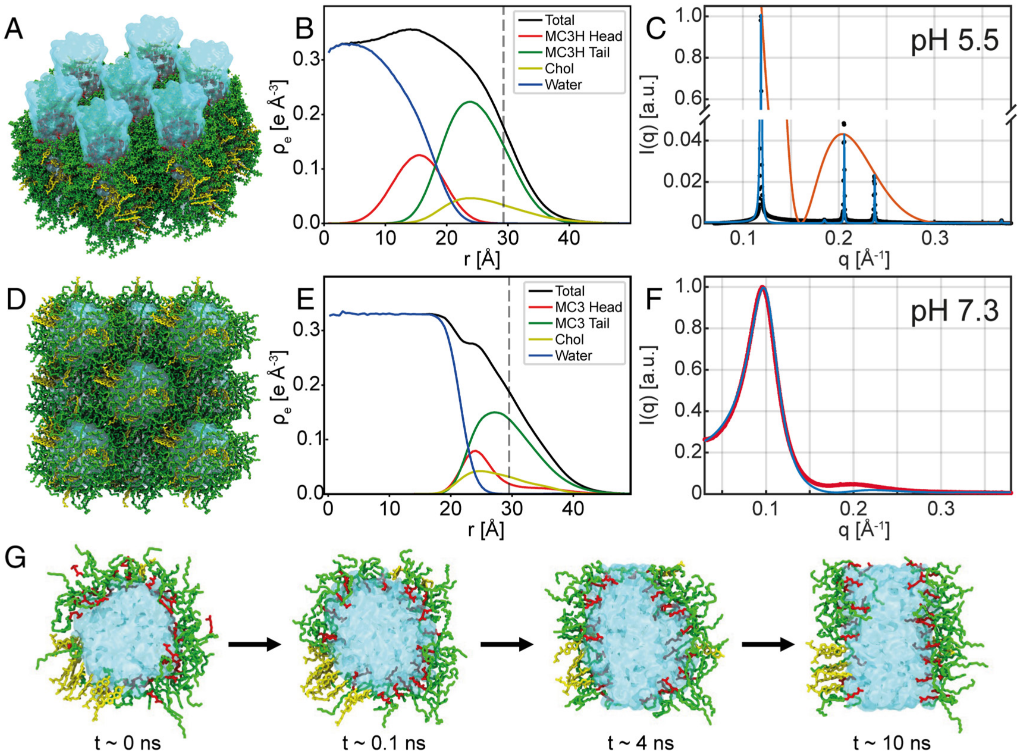

Fig. 3. MD simulations and electron density profiles of inverse phases for MC3. (*A*) Snapshot from an all-atom MD simulation of the H_{II} phase for fully charged MC3 and chol. Water is shown in blue; cationic headgroup and tail of MC3 are shown in red and green, respectively. Chol is shown in yellow. (*B*) corresponding radial electron density profile for the individual components of a single cylindrical micelle from MD simulations. The black line indicates the total electron density; the vertical dash line is the half nearest neighbor distance (*C*) SAXS data are plotted as black dots, the fitted SAXS profile in blue and the form factor obtained from MD in orange. (*D*) Simulation of tightly packed inverse micelles for uncharged MC3 and (*E*) electron density profile. (*F*) Scattering of L_{II} phase in red fitted in blue with the structure factor for densely packed spheres multiplied by the form factor obtained from MD. (*G*) Time series showing a cross-sectional view of an inverse-spherical to inverse-cylindrical micellar transition after charging the MC3 ionizable group at time t = 0. First, the MC3 headgroups swing into the water phase. Subsequently, a slower rearrangement from an inverse spherical to inverse cylindrical micelle takes place.

the experimentally measured lattice distance (*SI Appendix*, Fig. S5). Fig. 3*B* shows the electron density profile of an isolated inverse cylindrical micelle, i.e., a water channel surrounded by a monolayer of ionizable lipid and chol. The electron density profiles can be converted into effective volume fractions of the water and lipid components (see details in *SI Appendix*, Fig. S6). We obtain a water volume fraction $\phi_W = 24\%$ for $n_W = 12$ in the H_{II} phase in good agreement with earlier experimental work for the core phase MC3 LNPs at neutral pH using neutron scattering. (14). Next, we calculated the scattering form factor from the radial MD electron density profile of an H_{II} cylinder considering also neighboring cylinders (*SI Appendix*, Fig. S6*C*) and compared the result with the experimentally observed peak intensities. Fig. 3*C* shows a direct comparison of the SAXS data with a H_{II} structure factor including Lorentzian line shapes and peak intensity given by the form factor from MD data with $n_W = 12$ (orange line). The model agrees without any parameter adjustment, besides a global scaling factor, indicating that MD simulations reliably reproduce the H_{II} structure. In the simulations, the electron density profiles of water, lipid headgroup, lipid tails, and chol can be calculated separately. In order to approach simulation of the disordered inverse micellar phase L_{II}, we performed MD simulations of inverse spherical micelles with face-centered cubic symmetry providing periodic boundary conditions with twelve neighboring micelles. As before, the water content of the micelles was varied in multiple MD simulations (*SI Appendix*, Fig. S4 *C* and *D*). Note that the inverse spherical shape of the micelles is well reproduced by MD simulation even though the packing order of the simulation (fcc) and the more random packing in experiment differ. In particular, the simulations show that inverse micelles are stable if the MC3 head is uncharged, but unstable if the headgroup is charged. Moreover, we find a dramatic difference in the MC3 headgroup conformations in H_{II} compared to L_{II} phase. As the electron density profiles show, the charged MC3 headgroup sticks into the H_{II} water column (Fig. 3*B*), while in case of L_{II} spherical micelles, the uncharged MC3 headgroup hides within the hydrophobic lipid tail region (Fig. 3*E*). A cross-sectional view of the two phases clearly displays the different headgroup conformations (*SI Appendix*, Fig. S7). The experimental scattering data were fitted by the so-called Percus-Yevick structure factor with two free parameters for densely packed spheres and employing the form factor from MD simulations (Fig. 3*F*, red line). Moreover, the MD simulations are able to reproduce the L_{II} to H_{II} phase transition. As pH decreases, MC3 headgroups get charged. This is simulated by introducing charge to the MC3 headgroups at time $t = 0$ starting from an equilibrated conformation with uncharged MC3 headgroups (Fig. 3*G*). Within the first 120 ps, the headgroups swing out from an in-plane conformation toward a straight conformation that sticks into the water phase. Following this process on a time scale of 10 ns, we then see the transition of an inverse spherical to inverse cylindrical micelle, which is the basic local rearrangement in a transition from a disordered spherical water-in-oil microemulsion (L_{II}) to an ordered anisotropic inverse hexagonal phase (H_{II}) (Movie S1). To summarize, the MD simulations confirm the stability of the proposed liquid crystalline order for uncharged and fully charged MC3 headgroup. In addition, the combined approach allows us to assign the water content to the H_{II} phase and to provide quantitative comparison with SAXS data by including the form factor from the all-atom simulations in the model fits.

SAXS Signal of LNPs Is Broader but Retains Hallmarks of pH-Dependent Structural Changes. Additionally, we demonstrate that the structural hallmarks, which are clearly visible in reconstituted macroscopic bulk phases, persist in LNP core phases. To this end, we directly compare the SAXS scattering profiles of CIL+polyA against bulk CIL+mRNA and mRNA containing LNPs at both pH 5 and pH 7 (Fig. 4*A*). Here, we observe two effects. First, exchanging polyA with mRNA, in this case mRNA encoding for eGFP, the sharp peaks of the polyA containing complexed H_{II}^c phase disappear. We attribute this finding to secondary mRNA structure, which is incompatible with long range inverse hexagonal order. We also see that the order of the lipid-only H_{II} is disturbed, even though the 2nd- and 3rd-order peaks remain visible. In the course of this, the signatures of polyA-filled H_{II}^c phase and the lipid-only H_{II} phase become indistinguishable. Second, when we compare CIL-mRNA bulk phase with scattering from dispersed 100 nm-size mRNA LNPs we see an additional broadening of the remaining peak together with a small shift of the q_{max} position toward smaller q-values. We attribute this behavior to a finite size effect, which reduces long-range order of the inverse hexagonal phase even further. The fact that the real-space spacing increases is likely caused by the fact that the LNP core phase composition might slightly differ from the reconstituted CIL bulk phase, since small amounts of both CIL as well as chol are also present in the surface monolayer. Overall, we can state that the SAXS data from bulk phases are consistent with the observed LNP scattering. Most importantly CIL+mRNA bulk phases exhibit scattering that closely resembled the signal from LNPs suggesting that the main CIL transition from high pH L_{II} to low pH H_{II} phase also takes place in the LNP core phase. However, the highly ordered polyA condensed H_{II}^c appears to be a special feature of the linear homopolymer polyA. At pH 6.5, the H_{II}^c phase becomes metastable and dissolves into a disordered isotropic phase L_{II}^c. We graphically depict the H_{II}^c to L_{II}^c transition in Fig. 4*B* showing an order hexagonal arrangement loosening into dispersed inverse wormlike micelles containing linear polyA molecules (37). If mRNA is mixed into CIL bulk phases, no H_{II}^c is observed at any pH. We expect that mRNA retains secondary structure and that cylindrical CIL structures will cover the mRNA contours as shown as $L_{II}^c(mRNA)$ in Fig. 4*B*. Hence, the highly ordered CIL+polyA H_{II}^c phases represent a rather artificial case. However, we show in the following that we can derive some general insights about nucleic acid-CIL complexes from the ordered H_{II}^c phases.

pH-Induced Transitions in CIL Phases and LNPs. Furthermore, we study the evolution of real-space distances as a function of pH. We define the nearest neighbor distance, d_{NN}, as a figure of merit which can be deduced for all liquid crystalline phases shown in Fig. 2. In Fig. 4, the nearest neighbor distances are shown for all three CIL/chol/buffer mesophases Fig. 4*C* as well as for the condensed CIL/chol/polyA/buffer phases, Fig. 4*D*. At first glance, we note that MC3 and KC2 exhibit remarkably similar trends and spacings. The nearest neighbor distance in the inverse micellar phase L_{II} increases with decreasing pH. This can be interpreted as protonation of the ionizable lipid headgroup concomitant with water uptake and swelling of the micelles. With increasing size, the degree of packing order increases, which ends up in cubic liquid crystalline phases at pH values around 6.5. In this pH regime, we almost always see coexistence with an inverse hexagonal phase H_{II}, with considerably smaller nearest neighbor spacing of 60 Å. Interestingly, the nearest neighbor spacing does not change as pH values decrease further. In mesophases containing the ionizable lipid DD, the nearest neighbor distances are considerably larger, showing d_{NN}, of about 85 to 89 Å for inverse micellar and inverse

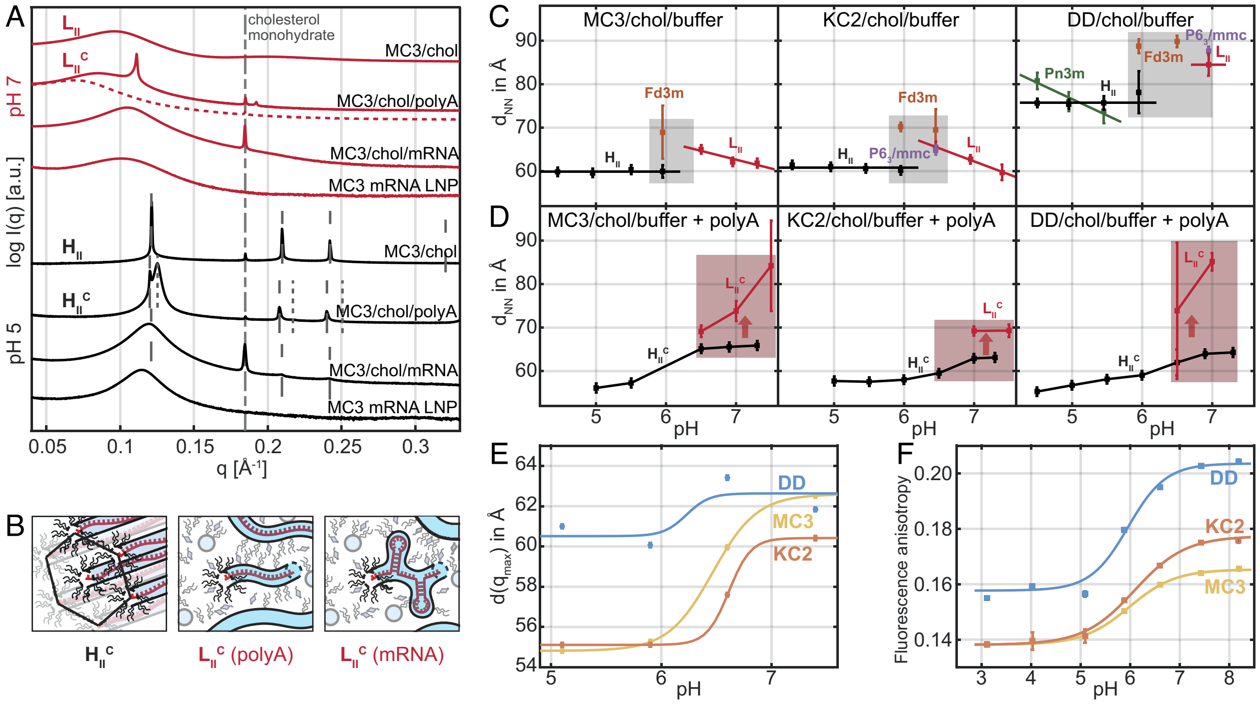

Fig. 4. Scattering signature and pH-induced transitions in CIL bulk vs. LNP core phase. (*A*) SAXS scattering at pH 7 (red curves) of MC3/chol/water L_{II} bulk phase, MC3/chol/water/polyA L_{II}^{C} bulk phase, MC3/chol/water/mRNA L_{II}^{C} bulk phase, and mRNA LNPs and corresponding SAXS data at pH 5 (black curves). The MC3/chol/water/polyA preparation at pH 7 showed time dependence with the H_{II}^{C} peak dissolving over weeks. We denote the dashed line as micellar isotropic L_{II}^{C} phase. The mRNA filled bulk phases and LNPs exhibit less long-range order due to mRNA secondary structure. (*B*) Schematic drawing of the polyA condensed H_{II}^{C} phase at pH 5, the polyA condensed L_{II}^{C} (polyA) phase at pH 7, and an mRNA condensed L_{II}^{C} (mRNA) phase. mRNA is assumed to retain secondary structure in a disordered L_{II}—micellar-like lipidic phase. (*C*) Next nearest neighbor distances as a function of pH showing pH-induced transitions in CIL bulk phases and (*D*) in polyA containing complexed phases. The gray area indicates the transition region with cubic phases. The reddish area indicates metastability of H_{II}^{c}. (*E*) pH-dependent correlation distance in LNPs derived from SAXS data (*F*) Fluorescence anisotropy of a hydrophobic probe (DPH) as a function of pH for MC3-, KC2-, and DD-LNPs, respectively. Increasing anisotropy indicates decreasing mobility. The critical pH values of half-maximum are 6.0, 6.1, and 6.0 for MC3-, KC2-, and DD, respectively. Data shown in (*C* and *D*) are measured at room temperature, (*E* and *F*) at 37 °C.

micellar cubic phase and d_{NN} of 77 Å for the corresponding inverse hexagonal phase H_{II}. Another peculiarity of DD is the coexistence of a bicontinuous cubic and an H_{II} phase with the $Pn3m$ d_{NN} spacing swelling with decreasing pH value. Hence, DD clearly shows features that are distinct from MC3 and KC2. At the same time, there is the common feature of all three ionizable lipid CIL/chol mesophases that the micellar-to-inverse hexagonal $Fd3m \rightarrow H_{II}$ transition occurs at around the same pH value of 6.5 and in a regime, when the inverse micellar phase is most tightly packed with cubic order (highlighted as gray area in Fig. 4*C*). It is remarkable that the transition regime with coexistence of Fd3m and H_{II} occurs at almost the same pH values for the three CILs. Fig. 4*D* shows the nearest neighbor spacing in polyA complexed H_{II}^{c} phases to increase with increasing pH. At pH 6.5, the H_{II}^{c} becomes metastable and dissolves into a disordered isotropic L_{II}^{c} phase (metastable region highlighted in red). Before we discuss how these features possibly link to mechanistic action, we show that this feature and the distinction of DD are present in LNP SAXS data. Fig. 4*E* shows the $2\pi / q_{max}$ spacing derived from LNP SAXS measurements that exhibit one maximum (*SI Appendix*, Fig. S8). We find that the characteristic internal spacing of MC3 and KC2 clearly exhibits the signature of a transition around the same pH value at which the $Fd3m \rightarrow H_{II}$ transition occurs in the MC3 and KC2 mesophases. Strikingly, the spacing of DD-based LNPs does not exhibit a characteristic jump as d_{NN} values in the bulk phases.

In order to further substantiate the existence of a structural pH-dependent transition in the LNP core phase, we carried out fluorescence anisotropy measurements using the hydrophobic tracer diphenylhexatriene (*SI Appendix*). Fluorescence anisotropy is inversely proportional to the tracer mobility in the lipid tail region (38). We find that fluorescence anisotropy, with increasing pH, exhibits a transition toward larger values around pH 6.0 for all three ionizable lipids. Again, MC3 and KC2 show closer agreement in absolute numbers, while DD exhibits the same trend but larger fluorescence anisotropy values indicating lower mobility in DD LNPs over the entire pH range. At the same time, the spherical to cylindrical transition does not significantly change the characteristic spacing in DD LNPs while it does in MC3 and KC2 LNPs.

DD-Mediated Transfection Exhibits Delayed Expression Kinetics vs. MC3 and KC2. Finally, we explore the kinetics of endosomal fusion and mRNA release in transfection experiments. As the endosome matures, its pH lowers and CILs become positively charged. The structural changes discussed above provide a reasonable basis to assume that LNP core phases become more fusogenic. However, little is known when endosomal fusion events occur and if MC3, KC2, and DD differ in expression kinetics. For this reason, we pursue single-cell eGFP transfection experiments using Cy5-labeled eGFP mRNA. Cells are seeded on micropatterned arrays with fibronectin coated squares in otherwise PEGylated, nonadhesive area (*SI Appendix*, Fig. S9). We monitor the Cy5 fluorescence of the Cy5-labeled mRNA and the onset of eGFP expression after LNP transfection (Fig. 5*A*). Typically, 12 view fields per channel are sequentially imaged in 10-min

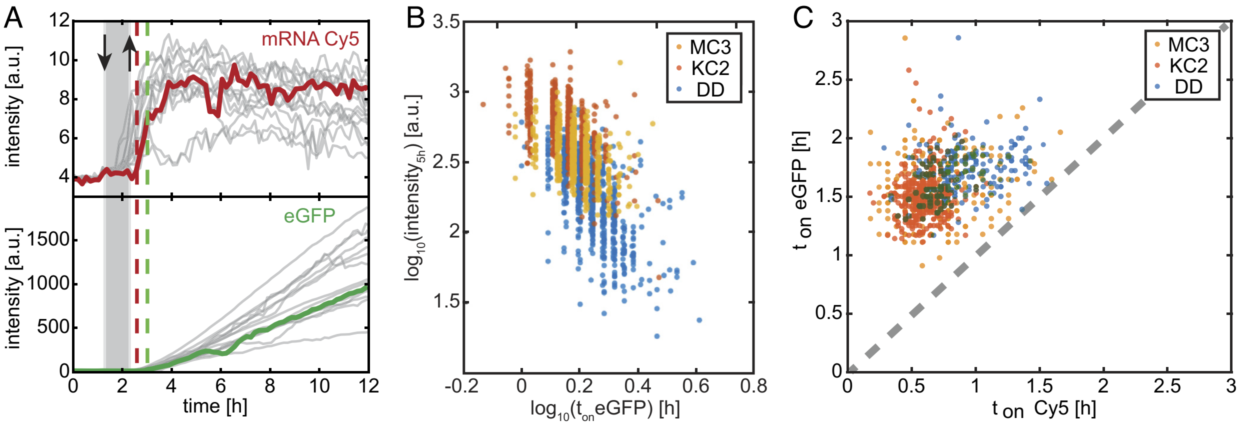

Fig. 5. Expression kinetics after eGFP-mRNA LNP transfection in vitro. (*A*) Exemplary single-cell fluorescence time courses of mRNA-Cy5 and eGFP (*B*) Correlation of transfection efficiency and onset time of single cells reveals delayed and less efficient expression for DD vs. MC3 and KC2. (*C*) eGFP-onset typically occurs 0.9 h after the event of Cy5-signal increase.

intervals. In total about 1,000 fluorescence time courses of single cells are recorded. LNPs were prepared as described in the *Methods* section. Microscopy channel slides are used to infuse cells with LNP transfection medium (dose 5 ng/μL mRNA) for a defined period of 1 h (gray bar in Fig. 5*A*). After the incubation period, the channels were washed with fresh medium. Setup and protocol has been described in the *Methods* section and previous work (39). We determine the time points of fluorescence onset, t_{on}, after incubation, as well as the eGFP fluorescence intensity 5 h after t_{on} for each single-cell trajectory. The fluorescence increase over the first 5 h is taken as a measure for the initial expression rate k_{CIL} (32). Fig. 5*B* shows the single-cell scatter plot of eGFP onset time and expression rate, k_{CIL} for MC3, KC2 and DD respectively. The mean eGFP onset times (see distribution functions *SI Appendix*, Fig. S10) show the order $t_{KC2} < t_{MC3} < t_{DD}$ while the initial expression rates show opposite order $k_{KC2} > k_{MC3} > k_{DD}$ (*SI Appendix*, Fig. S9). This inverse relation states that on average, early expression onset is likely to lead to larger expression levels. This finding agrees with the notion that endosomal release is associated with a window of opportunity (40). We also observe that the Cy5 fluorescence signal of the labeled Cy5-mRNA exhibits an abrupt increase over time (Fig. 5*A*). We attribute this signal to an dequenching of the Cy5 quantum efficiency as a result of an abrupt change in the environmental conditions. It stands to reason that this transition is associated with mRNA release from LNPs. Plotting Cy5 onset vs. onset of the eGFP signal exhibits similar timing for MC3 and KC2, while both Cy5 onset as well as eGFP onset are delayed for DD with respect to MC3 and KC2 (Fig. 5*C*). Hence, we conclude that endosomal fusion of DD-mediated transfection is delayed with respect to MC3 and KC2 and likely as a consequence of this, DD-mediated eGFP initial expression rate is reduced.

Discussion

We showed that LNP-mediated delivery in mice experiments results in different protein expression of the three CILs DD, KC2 and MC3, while the lipid and mRNA uptake was similar for the three LNPs. From this finding, we concluded that there must be distinct differences in the behavior of LNPs inside endosomes that affects escape from endosomes and hence expression efficiency. To this end, we studied reconstituted mixtures of CIL and chol as proxy for the LNP core phase and explored the structural evolution of these model systems as a function of pH. We find ordered mesophases that appear in a distinct sequence. These observations are unique for the ionizable lipids MC3, KC2, and DD but fall in line with lyotropic phase behavior of binary or ternary lipid–water mixtures in general. Many amphiphilic liquid crystals display lyotropic order from inverse micellar (L_{II}), isotropic cubic inverse micellar (I), inverse hexagonal (H_{II}), and bicontinuous cubic (Q) toward lamellar (L_α) lipid order depending on the preferred curvature of the amphiphiles (35, 41). In lyotropic liquid crystals, the CPP, which describes the ratio of headgroup to tail volume and hence the preferred curvature, predicts the observed sequence of mesophases. Applied to CILs the CPP will continuously increase with protonation of the ionizable lipid headgroups due to electrostatic headgroup repulsion explaining the sequence of all three ionizable lipids. In the specific case of MC3, all-atom MD simulations reveal that protonation of the lipid headgroup goes along with a remarkable relocation of the charged amine group from the hydrophobic part of the membrane into the aqueous phase. However, we notice CIL-specific differences in the SAXS data showing that first the nearest neighbor spacing is about 30% larger for DD vs. MC3 and KC2 phases and second that only DD exhibits a bicontinuous Pn3m phase coexisting with H_{II} at low pH values. Both phenomena indicate a larger water content in DD compared to MC3 and KC2 for CIL/chol/water phases without polyA. When polyA is added to these phases at N/P ratio of three, we find coexistence of pure lipidic structures and polyA complexed structures. At pH above 6.5, the complexed inverse hexagonal structure H_{II}^c dominates and decomposes at high pH into a disordered condensed phase L_{II}^c over time periods of weeks. The H_{II}^c phase agrees with previous work on DNA-lipoplexes (22) and general conjectures about a critical role of inverse hexagonal structures in LNP activity (19). However, the coexistence of two inverse hexagonal phases, a polyA filled one and an empty one, raises the question, which of the two phases relates to endosomal fusion. The data presented here support the notion that a structural transition in excess lipid is causal for fusion as key features of the lipid bulk phase transition seem to prevail in the LNP core phase. First, the curvature-driven transition from inverse spherical to inverse cylindrical structures is likely fusogenic as topological rearrangements include defects and fusogenic intermediates. In contrast, the polyA-condensed H_{II}^c phase shows no abrupt transition at pH 6 rather coexistence of

H_{II}^c with a hypothetic isotropic wormlike L_{II}^c phase at pH above 7. Second, the highest efficacy is observed at N/P ratio larger than one (42) demonstrating that excess lipid is adjuvant. Third, it is the Fd3m-H_{II} transition that shows the biggest difference between DD and MC3 and KC2, namely increased spacing and degree of hydration. Larger spacing and hydration will lower the Gaussian curvature energies involved in the cubic-to-hexagonal transition possibly turning DD less fusogenic. It is striking that the pH-dependent shift of the one broad SAXS peak observed in nanoscopic mRNA LNPs occurs around pH 6 as the transition in excess lipid bulk phase. However, it remains an open question whether a phase-separated lipidic phase exists in the LNP core. While phase-separated structures have been recently observed in TEM images and SAXS data of oligonucleotide-loaded LNPs (15) and GMO-based LNPs (16), there is no direct evidence of phase separation in the mRNA LNPs presented here. This is most likely due to the fact that mRNA secondary structures obscure long ranged order. Our MD simulations show that excess lipid regions should at least locally favor inverse spherical micellar geometry and is likely to undergo a topological transition analogous to the inverse spherical to cylindrical transition shown in Fig. 3*G*. Such mechanism could possibly trigger LNP fusion with the endosomal membrane. This is in line with our finding that DD-LNP-mediated mRNA delivery showed delayed release compared to MC3 and KC2. Delayed release is closely connected to loss of LNPs and reduced delivery. Our work also suggests that "fusion" and "mRNA release" should be discerned as two distinct and deferred processes. If mRNA is embedded in an electrostatically neutral, salt-like nucleic acid lipid H_{II}^c phase then endosomal membrane disruption will not immediately set free mRNA for translation. Little is known about the time it needs to dissolve the condensed ionizable lipid-mRNA state in the cytosol. In fact, our observation of an extremely persistent H_{II}^c phase in macroscopic samples suggests that "unpacking" mRNA should follow endosomal fusion with some delay as evidenced in single-cell fluorescence time courses. A small percentage of internalized mRNA undergoes exocytosis which may impact the overall efficacy (43, 44). Little is known whether this externalization pathway depends on mRNA being associated with ionizable lipid.

In summary, we conclude from macroscopic phase transitions mimicking LNP core composition that pH-dependent response of excess lipid in LNPs is causing endosomal fusion. The observed bulk structures are consistent with SAXS scattering from LNP core phase and LNP cores exhibit hallmarks of pH-driven transitions. Nonetheless, we are aware that the constituents of the LNP core phase are in exchange with the LNP surface. Ionizable lipids, as well as chol molecules, partition in the surface monolayer to some degree. Recent SAXS data show that indeed changes induced by protein adsorption affects LNP core structure (45). Vice versa, a surface-core interrelation implies that pH-induced core phase transition will affect surface composition. In particular, chol partition plays a role, and there is evidence for lateral phase separation in the surface monolayer (46). While most literature strives to elicit structure–activity relations, we show that pronounced phase transitions with impetuous rearrangements might trigger activity. By comparing MC3, KC2, and DD, we conclude that structural changes in the lipidic spherical-to-cylinder transition make a difference. Similar transitions might exist in bulk phases of other ionizable lipids optimized for mRNA delivery, including ALC-0315 and SM-102, which deserve further studies. The objective of our work was to explain the distinct in vivo efficacy of mRNA LNPs made from structurally related ionizable lipids. Intravenous dosing in mice demonstrated the unequal in vivo efficiency of DD-LNPs vs. MC3- and KC2-LNPs which be ascribed to distinct behavior not in LNP uptake but in endosomal mRNA release efficiency. Elucidating further, the determinants of CIL structural transitions, their kinetics, and impact on fusion and release will contribute to rational design of improved mRNA LNP formulations for a broad spectrum of future medical applications.

Materials and Methods

Materials. The three ionizable lipids DLin-MC3-DMA [O-(Z,Z,Z,Z-heptatriaconta-6,9,26,29-tetraem-19-yl)-4-(N,N-dimethylamino)butanoate; $C_{43}H_{79}NO_2$; mw 642.09 g mol^{-1}, >99% purity], DLin-KC2-DMA [DLin-KC2-DMA; 2,2-dilinoleyl-4-(2-dimethylaminoethyl)-[1, 3]-dioxolane; $C_{43}H_{79}NO_2$; mw 642.09 g mol^{-1}, >99% purity], and DD (1,2-dilinoleyloxy-3-dimethylaminopropane; $C_{41}H_{77}NO_2$; mw 616.06 g mol^{-1}, >99% purity) were synthesized at AstraZeneca. 1,2-distearoyl-sn-glycero-3-phosphocholine (DSPC; $C_{44}H_{88}NO_8P$; mw 790.15 g mol^{-1}; 18:0 PC; >99% purity) was purchased from Avanti Polar Lipids; N-(Carbonyl-methoxypolyethyleneglycol 2000)-1,2-dimyristoyl-sn-glycero-3-phosphoethanolamine (DMPE-PEG2000) from NOF Corporation (average molecular weight 2785 g mol^{-1}); Chol ($C_{27}H_{45}OH$; 386.66 g mol^{-1}; >98% purity) was purchased from Sigma-Aldrich. PolyA (600 to 4,000 bases according to the manufacturer) was purchased from Sigma-Aldrich. mRNA encoding for eGFP was purchased from Trilink, in both the unlabelled [Clean Cap eGFP (5 moU)] as well as the fluorescently labelled form (Cyanine 5 eGFP 5 Mec psi mRNA). PBS (1 mM KH_2PO_4, 155 mM NaCl, and 3 mM Na_2HPO_4.7H2O, pH 7.4) was purchased from Gibco (Life Technologies). Citrate buffer was purchased from Teknova. HyClone RNAse-free water was used for all LNP preparations with mRNA and was purchased from GE Healthcare Cell Culture.

Formulation and Characterization of LNPs. DLin-MC3-DMA, DLin-KC2-DMA, and DLinDMA LNPs containing modified CleanCap eGFP mRNA (5-methoxyuridine) (TriLink Biotechnologies) were prepared by precipitating the mRNA with four different lipid components. These components consist of an ionizable lipid, DLin-MC3- DMA, DLin-KC2-DMA or DLinDMA, which are ionizable (cationic) at low pH, two helper lipids (DSPC and Chol) and a PEGylated lipid (DMPE-PEG2000). A solution of eGFP mRNA in water was prepared by mixing mRNA dissolved in HyClone-water, 100 mM citrate buffer pH 3 and HyClone-water to give a solution of 50 mM citrate. For cy5-labeled eGFP mRNA LNPs, the eGFP/cy5-eGFP molar ratio was 9:1. Lipid solutions in ethanol (99.5%) were prepared with a composition of four lipid components [Ionizable Lipid:Chol:DSPC:DMPE-PEG2000] = 50:38.5:10:1.5 mol% and a total lipid content of 12.5 mM. The mRNA and lipid solutions were mixed in a NanoAssemblr (Precision Nanosystems) microfluidic mixing system at a volume mixing ratio of Aq:EtOH = 3:1 and a constant total flow rate of 12 mL/min. At the time of mixing, the ratio between the nitrogen atoms on the ionizable lipid and phosphor atoms on the mRNA chain was 3:1. If "empty" LNPs were prepared, i.e., LNPs without any mRNA, the ethanol phase was mixed with only 50 mM citrate buffer pH 3. The initial 0.25 mL and the last 0.05 mL of the LNP solution prepared were discarded while the rest of the volume was transferred immediately to a Slide-a-lyzer G2 dialysis cassette (10,000 MWCO, Thermo Fisher Scientific Inc.) and dialyzed overnight at 4 °C against PBS (pH7.4). The volume of the PBS buffer was 650 to 800x the sample fraction volume. For some samples, the LNP suspension was concentrated using Amicon Ultra 30K centrifugation filters. For the characterization of formulated LNPs, following preparation, the intensity-averaged particle size (Z-average) was measured using a ZetaSizer Nano (Malvern Instruments Inc.). The final mRNA concentration and encapsulation efficiency were measured by the Quant-it RiboGreen Assay Kit (Thermo Fisher Scientific).

Animals. Female CD1 mice, 10 to 11 wk of age, were purchased from Charles River Laboratory, Germany, and housed in the animal facility at AstraZeneca, Mölndal, Sweden. The mice were left to acclimatize for 5 d prior to study start. Mice were kept in groups of 2 mice per cage under standard conditions (21 °C RT, 12:12 h light–dark cycle, 45 to 55% air humidity) with access to a normal chow diet (R70, Lactamin AB) and water ad libitum. Environmental enrichment was provided (cartons, gnawing stick, and cotton nesting pads). Experimental procedures were approved (ethical application number 83-2015) by the Regional Laboratory Animal Ethics Committee of Gothenburg, Sweden. The care and husbandry of animals was conducted in accordance with the European Directive (no.86/609) and the Swedish Animal Welfare Act and regulations (SJVFS 2012: 26.).

Inclusion and Exclusion Criteria. All mice were in the expected weight range (23 to 26 g) and thereby met the inclusion criteria. Exclusion criteria were predetermined and set for unsuccessful performance of the liver perfusion or Intravenous injection. One mouse was excluded due to unsuccessful liver perfusion.

Study Design. Animals were randomized in pairs, and cages with pairs allocated to dose groups based on body weight (ranged from 23 to 26 g), using an animal randomization tool at 3 d prior to study start. The dosing order was fixed and adapted to fit termination time points. The termination order was randomized and decided prior to the study start. The LNP formulations and Vehicle was coded and kept blinded for the operators during the cause of the study. At study start, eGFP mRNA LNPs (DLin-MC3-DMA, DLin-KC2-DMA, and DD) (0.5 mg/kg) (n = 4 per group) or PBS (n = 3) were intravenously injected in the tail vein of mice. At 5 and 24 h after iv injection, groups of mice were anesthetized using isoflurane (Baxter Medical AB, Kista, Sweden) and killed by cervical dislocation. The animal was placed under the microscope for performance of the liver perfusion.

Liver Cell Isolation. Isolated hepatocytes, LSECs, and KCs were prepared by the following sequential steps (47): After perfusion with collagenase (LiberaseTM Research Grade bought from Roche Diagnostics, Oslo, Norway) through the portal vein, the liver was excised, and connective tissue and gallbladder removed before carefully transferring the liver to a Petri dish for weighing. The liver was then placed in cold albumin solution (1% bovine serum albumin in 10 mM phosphate buffer, pH 7.4) and Glisson's capsule carefully removed with forceps before gently shaking of the liver tissue to generate a single-cell suspension. The dispersed cells were filtered through a 70 μm gauge filter, and the volume was measured. Glisson's capsule and undigested liver residue that did not pass the filter were weighed. After a low-speed centrifugation (50 × g) of the liver cell suspension, the resulting supernatant depleted of hepatocytes and containing the majority of the LSECs and KCs was collected, whereas the pellet containing the majority of the hepatocytes was resuspended in buffer and subjected to four more low-speed centrifugation washing steps for further enrichment. The purity of the hepatocytes (>95%) was easily assessed by inspection in the light microscope, as these cells are readily distinguished from other types of liver cells due to their much larger size. The LSECs and KCs from the supernatants of the first and second low-speed centrifugations were pelleted and mixed into a 20 mL 20% Percoll solution (GE Healthcare, Nydalen, Norway). After centrifugation at 300 × g for 20 min, debris and dead cells moved to the top, whereas LSECs and KCs were pelleted. The pelleted cells were resuspended in MACS isolation buffer (Miltenyi Biotec Norden AB, Lund, Sweden) before being further purified by immunomagnetic cell isolation according to the instructions by the manufacturer. Briefly, 1/3 of the resuspended cells was incubated with magnetic beads (Miltenyi) conjugated with anti-CD146 antibodies for isolation of LSECs; in parallel, the remaining 2/3 of the resuspended cells were incubated with biotin anti-mouse F4/80 (Bio-Rad, Oslo, Norway) antibodies, and then with streptavidin-conjugated magnetic beads (Miltenyi) for isolation of KCs. Separation of the two cell types was achieved by passing the cell-beads complexes over two LS+ QuadroMACSTM separation columns, according to the manufacturer's instructions. Liver cell fractions were stored in cryotubes at -80°C until assessment of the amounts of ionizable lipids, eGFP mRNA and eGFP protein.

Gradient UPLC for the analysis of ionizable lipids in liver cell fractions. Each cell fraction was dissolved in 400 μL of a mixture of Triton X-100 in 0.5% formic acid (1% w/v). The samples were incubated at 37 °C for 30 min, centrifuged at 10,000 rpm for 10 min, and then injected on Acquity Ultra Performance LC coupled to a Single Quad Detector, SQD (Waters, Milford). The analytical column was a Waters Acquity UPLC® CSH C18, 1.7 μm, 2.1 × 100 mm, kept at 60 °C. The flow rate was 0.50 mL/min using a mobile phase of 0.1% formic acid in water (A) and 0.1% formic acid in acetonitrile (B). A gradient run was applied where 5% B at 0.0 min was increased to 83% B at 0.5 to 3.0 min and kept at 83% B to 6.5 min. A washing step of 99% B at 6.6 to 8.5 min was included in the gradient run. Then, 5% B was applied for conditioning from 8.6 min to 11.0 min. The separation between main peak of Triton X-100 and the cationic lipids was good under these conditions. Quantification was made using external standard solutions of DLin-MC3-DMA, DLin-KC2-DMA, and DD dissolved in Triton X-100 in 0.5% formic acid (1% w/v). The SQD was run using electrospray, positive mode and tuned using a solution of DLin-MC3-DMA. Recording of the cationic lipids was made using Single Ion Recording at M + 1 for each cationic lipid.

Branched DNA Analysis of Intact eGFP mRNA in Liver Cell Fractions. Levels of eGFP mRNA were quantified using a commercial kit purchased from ThermoFisher (QuantiGene SinglePlex bDNA assay kit, QS0012). A bDNA probe set (eGFP SF-10526) specific for TriLink eGFP mRNA was designed and supplied by ThermoFisher. Prior to analysis, the cell pellet was lysed in bDNA working lysis buffer mix containing 33% Lysis Mix (QP0522) and 0.3% proteinase K (QS0510) to give a 400 cell/μL final concentration. The cell pellet was incubated for 30 min at 55 °C, after which time, the sample was vortexed for 1 min to ensure optimal lysate viscosity. Processed sample was then stored at −80 °C until analysis. To perform analysis, 60 μL of the working probe mix (33.3 μL Lysis mix, 25.4 μL water, 1.0 μL block reagent, and 0.3 μL eGFP probe set) was added to appropriate wells in the kit-supplied 96-well bDNA plate; following this, 40 μL of all samples and standards were added. The plate was sealed and incubated, without shaking, overnight at 55 °C. After washing the plate three times with washing buffer, 100 μL pre-amplification solution was added to each well, and the sealed plate was incubated, without shaking, for 90 min at 55 °C. The plate was then washed three times with washing buffer, and 100 μL amplification solution was added to each well and incubated without shaking for 90 min at 55 °C. The plate was then washed three times with washing buffer, and 100 μL label solution was added to each well and incubated without shaking for 90 min at 50 °C. The plate was then washed three times with washing buffer, and 100 μL substrate solution was added to each well and incubated in the absence of light and without shaking for 10 min at room temperature. Total luminescence was then measured on a SpectraMax iD3, and the analyte concentration in the samples was backcalculated from the standard curve (4pL fit, 1/y weighting).

Determination of eGFP Protein in Liver Cell Fractions. The eGFP protein levels were quantified using a commercial kit purchased from Abcam (ab171581). An extraction buffer (recommended by the kit vendor) was added to the cell samples, that were spun down and the supernatant stored at −80 °C until analysis. Fifty microliters of all samples and standards were added to appropriate wells in a 96-well plate. Then 50 μL of Antibody Cocktail, containing capture and detection antibodies were added to the wells. The plate was sealed and put on a shaker (400 rpm) for 1 h at room temperature. After washing the plate three times with washing buffer, 100 μL TMB substrate was added to each well, and the plate was put on a plate shaker for 10 min before 100 μL stop solution was added. The absorbance was then measured at 450 nm on a SpectraMax iD3, and the analyte concentration in the samples was backcalculated from the standard curve (4pL fit, 1/y weighting).

Preparation of Ionizable Lipid Bulk Phases. CIL/chol/polyA bulk phases were produced at a range of pH conditions via three dialysis steps. First, the ionizable lipid and chol were dissolved in ethanol and mixed in a molar ratio of 3:1 (CIL:chol) to a total lipid concentration of 56.1 mg/mL. The ethanol mixture was introduced into a dialysis cassette with a molecular weight cutoff of 3.5 kDa (Slide-A-Lyzer™ G2, Thermo Scientific). An aqueous solution of polyA in buffer (20.1 mg/mL polyA in 50 mM citrate buffer at pH 3) was injected rapidly into the ethanol mixture to a final volume that resulted in a 3:1 CIL:nucleotide molar ratio. The dialysis cassette was placed into a beaker containing 500× the volume of dialysis buffer at 22 ± 2 °C. Samples were first dialyzed against 50 mM citrate buffer (pH 3) containing ethanol (at a volume ration of 3:1, buffer: ethanol) for 48 h. In the second dialysis step, the sample was dialyzed against PBS (1 mM KH_2PO_4, 155 mM NaCl, and 3 mM Na_2HPO_4 $0.7H_2O$, pH 7.4) for 48 h. In the third step, the sample was dialyzed against a McIlvaine buffer with the required final pH (4.5, 5, 5.5, 6, 6.5, 7, and 7.5) for 48 h. During the dialysis process, large precipitates were formed from the polyA and lipids. The supernatant was removed from the cassette, and the solid precipitates were extracted for characterization by SAXS. CIL/chol bulk phases were prepared according to the same protocol, except without adding polyA.

SAXS. Synchrotron small-angle X-ray scattering (SAXS) was carried out at the P12 BioSAXS EMBL beamline, PETRA III, DESY (Hamburg, Germany). The beamline instrumentation has been described elsewhere (48). The crystallographic space groups of the liquid crystalline phases were determined from relative peak positions. Corresponding Miller indices, calculation of the lattice constant *a* and nearest neighbor distance d_{NN} are listed in *SI Appendix*, Tables S1 and S2. All measurements at P12 were performed in quartz capillaries (0.01 mm wall thickness, 1.5 mm outer diameter by Hilgenberg) at 10 keV. Scattering data background was subtracted by measuring empty capillaries. Fits of the H_{II} phase (Fig. 4*C*) represent best fits of a rigid cylinder form factor P(q) and a H_{II} structure factor S(q) as P(q)S(q)+bg(q), with bg(q) being a background term including the contribution of chol monohydrate in terms of two Lorentzian peaks at 0.185 Å^{-1} and 0.370 Å^{-1}. The cylinder form factor P(q) is calculated from a radial electron density profile ρ(r) as retrieved from MD simulations. For data analysis, the numerical data were approximated by box model with ten partitions and fitted using the program SasView (49). The structure factor was approximated by Lorentzian profiles with peak spacings as discussed above. The fit of the L_{II} phase (Fig. 4*F*) was obtained using P(q)S(q)+bg(q), with bg(q) being a constant, P(q) the form factor calculated from a radial electron density profile ρ(r) obtained from MD simulations (Fig. 4*E*) and the structure factor S(q). For S(q), the Percus–Yevick structure factor for densely packed spheres with hard core repulsive interaction was chosen (50). It describes the ordering of spheres with radius a and volume fraction ϕ. The nearest neighbor distance was approximated by $d_{NN} \approx a$ assuming that micelles are in close contact as also suggested from MD simulations. Note that this approach agrees within 10% with the approximation $d_{NN} \approx 2\pi/q_{max}$, where q_{max} denotes the peak position with maximum intensity.

MD Simulations. MD simulations are powerful tools to gain insights into the distribution of the various lipids (51). The Gromacs package (v-2019) (52) was used to perform the MD simulations. The AMBER Lipid 17 force field (53) was used to describe the chol. For the uncharged and cationic MC3, we used our recently developed force field parameters (36). These parameters have the advantage that they closely reproduce the structure of MC3 in lipid layers as judged by neutron reflectometry experiments. In addition, the parameters are compatible with the AMBER force field family. Ions were described using the Mamatkulov–Schwierz force field parameters (54), and the TIP3P water model (55) was used. After energy minimization using a gradient descent algorithm and a short equilibration run using the Berendsen thermostat and barostat, the production runs were carried out for 200 ns. The temperature was fixed at 293 K using the Nose–Hoover thermostat with a time constant of 1 ps. The pressure was fixed at 1 bar using semi-isotropic (for inverse hexagonal setup) or isotropic (for inverse micellar setup) Parrinello–Rahman barostat with a 5 ps time constant. Van der Waals interactions were truncated and shifted to zero at 1.2 nm. Short-range electrostatic interactions were cutoff at 1.2 nm, and long-range electrostatic interactions were evaluated using the Particle Mesh Ewald method with a Fourier grid spacing of 0.12 nm. All bonds involving hydrogens were constrained using the LINCS. A time step of 2 fs was used to integrate the equations of motion. A detailed description of the simulation's setup for the inverse hexagonal and inverse micellar phase can be found in *SI Appendix*.

Single-Cell Time-Lapse Imaging. Live-cell imaging on single-cell arrays was carried out as previously described (39, 56). In short, single-cell microarrays with adhesive squares were produced by microscale plasma-induced protein patterning. The adhesion sites are coated with fibronectin, and the interspace is passivated with PLL-g-PEG. Microstructured coverslips were attached to a six-channel slides (ibidi, GmbH Munich). Human hepatocyte-derived carcinoma, HuH7 cells (I.A.Z. Toni Lindl GmbH, Germany) were grown in modified RPMI containing GlutaMax supplemented with 5 mM HEPES, 1 mM sodium pyruvate, and 10% fetal bovine serum (FBS). Cells were seeded in the six-channel slide 4 h prior to the time-lapse measurement at a cell density of 10,000 cells per channel. The slide was connected to a tubing system allowing for transfection and subsequent rinsing during the time-lapse measurement. Scanning time-lapse imaging was performed on a motorized inverted microscope (Eclipse Ti-E; Nikon) with an objective lens (CFI PlanFluor DL-10x, Phase 1, N.A. 0.30; Nikon) equipped with a heating system (Okolab). Fluorescence image stacks with a time resolution of 10 min were acquired using a cooled CMOS camera (pco.edge 4.2; pco), a LED light source (SOLA-SE II, Lumencor), and a suitable filter cube for eGFP (BP450 to 490, FT510, LP 510 to 565; CHROMA Technology Corp.) or Cy5 (filter cube). First, all channels were rinsed with 37 °C warm PBS. Subsequently, LNP containing solution was added to each channel. After 1 h of incubation with the transfection complexes, all channels were washed with L15 medium supplemented with 10% FBS, which remains in the channels for the remaining 12 h of measurement. Analysis of single-cell fluorescence traces was done as described in earlier studies (56–58). The onset times of the Cy5 traces were determined manually, whereas the eGFP traces were determined using a hierarchical cluster analysis approach as described in ref. 39. Per LNP preparation, about 500 cells were evaluated (see scatterplot Fig. 5). At least two technical repeats were carried out.

Data, Materials, and Software Availability. All study data are included in the article and/or supporting information.

ACKNOWLEDGMENTS. This work was supported by the German Federal Ministry of Education and Research through BMBF Project 05K18WMA and 05K18EZA within the framework of the Swedish–German research collaboration Röntgen-Ångström Cluster. A.R. and R.K acknowledge funding from the German Science Foundation through the Graduate School of Quantitative Biosciences (QBM), LMU. We would like to acknowledge Johan Broddefalk (AstraZeneca) for the synthesis of the CILs. This work benefited from the use of the SasView application, originally developed under NSF award DMR-0520547. SasView contains code developed with funding from the European Union's Horizon 2020 research and innovation program under the SINE2020 project, grant agreement no. 654000. The authors gratefully acknowledge the scientific support and HPC resources provided by the Erlangen National High Performance Computing Center (NHR@FAU) of the Friedrich-Alexander-Universität Erlangen-Nürnberg (FAU) under the NHR project b119ee.

Author affiliations: [a]Faculty of Physics and Center for NanoScience, Ludwig Maximilians-University, Munich 80539, Germany; [b]Advanced Drug Delivery, Pharmaceutical Sciences, BioPharmaceuticals Research and Development, AstraZeneca, Gothenburg, Mölndal 431 83, Sweden; [c]European Molecular Biology Laboratory Hamburg Outstation c/o Deutsches Elektronen-Synchrotron, Hamburg 22607, Germany; [d]Institute of Physics, University of Augsburg, Augsburg 86159, Germany; [e]Animal Sciences and Technologies, Clinical Pharmacology & Safety Sciences, BioPharmaceuticals R&D, AstraZeneca, Gothenburg, Mölndal 431 83, Sweden; [f]Integrated Bioanalysis, Clinical Pharmacology & Safety Sciences, BioPharmaceuticals R&D, AstraZeneca, Gothenburg, Mölndal 431 83, Sweden; [g]Marine Biotechnology, Nofima AS, Tromsø 9291, Norway; and [h]Vascular Biology Research Group, Department of Medical Biology, University of Tromsø, Tromsø 9019, Norway

1. C. Wan, T. M. Allen, P. R. Cullis, Lipid nanoparticle delivery systems for siRNA-based therapeutics. *Drug Deliv. Transl. Res.* **4**, 74–83 (2014).
2. H. Yin *et al.*, Non-viral vectors for gene-based therapy. *Nat. Rev. Genet.* **15**, 541–555 (2014).
3. P. R. Cullis, M. J. Hope, Lipid nanoparticle systems for enabling gene therapies. *Mol. Ther.* **25**, 1467–1475 (2017).
4. D. Adams *et al.*, Patisiran, an RNAi therapeutic, for hereditary transthyretin amyloidosis. *N. Engl. J. Med.* **379**, 11–21 (2018).
5. X. Hou, T. Zaks, R. Langer, Y. Dong, Lipid nanoparticles for mRNA delivery. *Nat. Rev. Mater.* **6**, 1078–1094 (2021).
6. L. Miao, Y. Zhang, L. Huang, mRNA vaccine for cancer immunotherapy. *Mol. Cancer* **20**, 41 (2021).
7. J. G. Rurik *et al.*, CAR T cells produced in vivo to treat cardiac injury. *Science* **375**, 91–96 (2022).
8. J. D. Gillmore *et al.*, CRISPR-Cas9 in vivo gene editing for transthyretin amyloidosis. *N. Engl. J. Med.* **385**, 493–502 (2021).
9. N. M. Belliveau *et al.*, Microfluidic synthesis of highly potent limit-size lipid nanoparticles for in vivo delivery of siRNA. *Mol. Ther. Nucleic Acids* **1**, e37 (2012).
10. A. K. K. Leung, Y. Y. C. Tam, S. Chen, I. M. Hafez, P. R. Cullis, Microfluidic mixing: A general method for encapsulating macromolecules in lipid nanoparticle systems. *J. Phys. Chem. B* **119**, 8698–8706 (2015).
11. M. A. Maier *et al.*, Biodegradable lipids enabling rapidly eliminated lipid nanoparticles for systemic delivery of RNAi therapeutics. *Mol. Ther.* **21**, 1570–1578 (2013).
12. V. Francia, R. M. Schiffelers, P. R. Cullis, D. Witzigmann, The biomolecular corona of lipid nanoparticles for gene therapy. *Bioconjug. Chem.* **31**, 2046–2059 (2020).
13. J. A. Kulkarni *et al.*, On the formation and morphology of lipid nanoparticles containing ionizable cationic lipids and siRNA. *ACS Nano* **12**, 4787–4795 (2018).
14. M. Yanez Arteta *et al.*, Successful reprogramming of cellular protein production through mRNA delivered by functionalized lipid nanoparticles. *Proc. Natl. Acad. Sci. U.S.A.* **115**, E3351–E3360 (2018).
15. M. Hammel *et al.*, Correlating the structure and gene silencing activity of oligonucleotide-loaded lipid nanoparticles using small-angle X-ray scattering. *ACS Nano* **17**, 11454–11465 (2023).
16. L. Zheng, S. R. Bandara, Z. Tan, C. Leal, Lipid nanoparticle topology regulates endosomal escape and delivery of RNA to the cytoplasm. *Proc. Natl. Acad. Sci. U.S.A.* **120**, e2301067120 (2023).
17. D. Rozmanov, S. Baoukina, D. P. Tieleman, Density based visualization for molecular simulation. *Faraday Discuss.* **169**, 225–243 (2014).
18. M. Jayaraman *et al.*, Maximizing the potency of siRNA lipid nanoparticles for hepatic gene silencing in vivo*. *Angew. Chem. Int. Ed.* **5**, 8529–8533 (2012).
19. S. C. Semple *et al.*, Rational design of cationic lipids for siRNA delivery. *Nat. Biotechnol.* **28**, 172–176 (2010).
20. M. J. Carrasco *et al.*, Ionization and structural properties of mRNA lipid nanoparticles influence expression in intramuscular and intravascular administration. *Commun. Biol.* **4**, 956 (2021).

21. I. Hafez, N. Maurer, P. Cullis, On the mechanism whereby cationic lipids promote intracellular delivery of polynucleic acids. *Gene Ther.* **8**, 1188–1196 (2001).
22. I. Koltover, T. Salditt, J. O. Rädler, C. R. Safinya, An inverted hexagonal phase of cationic liposome-DNA complexes related to DNA release and delivery. *Science* **281**, 78–81 (1998).
23. C. Leal, N. F. Bouxsein, K. K. Ewert, C. R. Safinya, Highly efficient gene silencing activity of siRNA embedded in a nanostructured gyroid cubic lipid matrix. *J. Am. Chem. Soc.* **132**, 16841–16847 (2010).
24. R. N. Majzoub, K. K. Ewert, C. R. Safinya, Cationic liposome–nucleic acid nanoparticle assemblies with applications in gene delivery and gene silencing. *Philos. Trans. R. Soc. Math. Phys. Eng. Sci.* **374**, 20150129 (2016).
25. J. O. Rädler, I. Koltover, T. Salditt, C. R. Safinya, Structure of DNA-cationic liposome complexes: DNA intercalation in multilamellar membranes in distinct interhelical packing regimes. *Science* **275**, 810–814 (1997).
26. C. R. Safinya, J. O. Rädler, *Handbook of Lipid Membranes: Molecular, Functional, and Materials Aspects* (CRC Press, ed. 1, 2021), 10.1201/9780429194078. (12 April 2023).
27. Z. Li *et al.*, Acidification-induced structure evolution of lipid nanoparticles correlates with their in vitro gene transfections. *ACS Nano* **17**, 979–990 (2023).
28. L. Uebbing *et al.*, Investigation of pH-responsiveness inside lipid nanoparticles for parenteral mRNA application using small-angle X-ray scattering. *Langmuir* **36**, 13331–13341 (2020).
29. G. Settanni, W. Brill, H. Haas, F. Schmid, pH-Dependent behavior of ionizable cationic lipids in mRNA-carrying lipoplexes investigated by molecular dynamics simulations. *Macromol. Rapid Commun.* **43**, 2100683 (2022).
30. H. Pertoft, B. Smedsrød, "Separation and characterization of liver cells" in *Cell Separation: Methods and Selected Applications*, T. G. Pretlow, T. P. Pretlow, Eds. (Academic Press, 1987), pp. 1–24.
31. K. K. Sørensen, B. Smedsrød, "The liver sinusoidal endothelial cell: Basic biology and pathobiology" in *The Liver: Biology and Pathobiology*, I. M. Arias *et al.*, Eds. (John Wiley & Sons Ltd, ed. 34, 2020), pp. 422–434, chap. 6.
32. P. Paramasivam *et al.*, Endosomal escape of delivered mRNA from endosomal recycling tubules visualized at the nanoscale. *J. Cell Biol.* **221**, e202110137 (2022).
33. G. C. Shearman *et al.*, A 3-D hexagonal inverse micellar lyotropic phase. *J. Am. Chem. Soc.* **131**, 1678–1679 (2009).
34. J. Huang, J. T. Buboltz, G. W. Feigenson, Maximum solubility of cholesterol in phosphatidylcholine and phosphatidylethanolamine bilayers. *Biochim. Biophys. Acta* **1417**, 89–100 (1999).
35. A. Yaghmur, M. Rappolt, "The micellar cubic Fd3m phase" in *Advances in Planar Lipid Bilayers and Liposomes* (Elsevier, 2013), pp. 111–145.
36. M. Ibrahim, J. Gilbert, M. Heinz, T. Nylander, N. Schwierz, Structural insights on ionizable Dlin-MC3-DMA lipids in DOPC layers by combining accurate atomistic force fields, molecular dynamics simulations and neutron reflectivity. *Nanoscale* **15**, 11647–11656 (2023), 10.1101/2023.02.28.529897.
37. A. Hohner, J. Bayer, J. O. Rädler, Wormlike lipid/DNA micelles in a non-polar solvent. *Eur. Phys. J. E* **21**, 41–48 (2006).
38. A. M. T. M. do Canto *et al.*, Diphenylhexatriene membrane probes DPH and TMA-DPH: A comparative molecular dynamics simulation study. *Biochim. Biophys. Acta* **1858**, 2647–2661 (2016).
39. A. Reiser *et al.*, Correlation of mRNA delivery timing and protein expression in lipid-based transfection. *Integr. Biol.* **11**, 362–371 (2019).
40. A. Wittrup *et al.*, Visualizing lipid-formulated siRNA release from endosomes and target gene knockdown. *Nat. Biotechnol.* **33**, 870–876 (2015).
41. A. Salonen, S. Guillot, O. Glatter, Determination of water content in internally self-assembled monoglyceride-based dispersions from the bulk phase. *Langmuir* **23**, 9151–9154 (2007).
42. L. Schoenmaker *et al.*, mRNA-lipid nanoparticle COVID-19 vaccines: Structure and stability. *Int. J. Pharm.* **601**, 120586 (2021).
43. M. Maugeri *et al.*, Linkage between endosomal escape of LNP-mRNA and loading into EVs for transport to other cells. *Nat. Commun.* **10**, 4333 (2019).
44. M. Nawaz *et al.*, Lipid nanoparticles deliver the therapeutic VEGFA mRNA in vitro and in vivo and transform extracellular vesicles for their functional extensions. *Adv. Sci.* **10**, 2206187 (2023).
45. F. Sebastiani *et al.*, Apolipoprotein E Binding drives structural and compositional rearrangement of mRNA-containing lipid nanoparticles. *ACS Nano* **15**, 6709–6722 (2021).
46. Y. Eygeris, S. Patel, A. Jozic, G. Sahay, Deconvoluting lipid nanoparticle structure for messenger RNA delivery. *Nano Lett.* **20**, 4543–4549 (2020).
47. K. Elvevold, I. Kyrrestad, B. Smedsrød, "Protocol for isolation and culture of mouse hepatocytes (HCs) in kupffer cells (KCs), and liver sinusoidal endothelial cells (LSECs) in analyses of hepatic drug distribution" in *Antisense RNA Design, Delivery, and Analysis, Methods in Molecular Biology*, V. Arechavala-Gomeza, A. Garanto, Eds. (Springer, US, 2022), pp. 385–402.
48. C. E. Blanchet *et al.*, Versatile sample environments and automation for biological solution X-ray scattering experiments at the P12 beamline (PETRA III, DESY). *J. Appl. Crystallogr.* **48**, 431–443 (2015).
49. SasView, Version 5.0.5. https://github.com/SasView/sasview/releases. Github. Accessed 3 June 2022.
50. R. Botet, S. Kwok, B. Cabane, Percus-Yevick structure factors made simple. *J. Appl. Crystallogr.* **53**, 1570–1582 (2020).
51. S. Park, Y. K. Choi, S. Kim, J. Lee, W. Im, CHARMM-GUI membrane builder for lipid nanoparticles with ionizable cationic lipids and PEGylated lipids. *J. Chem. Inf. Model.* **61**, 5192–5202 (2021).
52. M. J. Abraham *et al.*, GROMACS: High performance molecular simulations through multi-level parallelism from laptops to supercomputers. *SoftwareX* **1–2**, 19–25 (2015).
53. C. J. Dickson *et al.*, Lipid14: The amber lipid force field. *J. Chem. Theory Comput.* **10**, 865–879 (2014).
54. S. Mamatkulov, N. Schwierz, Force fields for monovalent and divalent metal cations in TIP3P water based on thermodynamic and kinetic properties. *J. Chem. Phys.* **148**, 074504 (2018).
55. W. L. Jorgensen, J. Chandrasekhar, J. D. Madura, R. W. Impey, M. L. Klein, Comparison of simple potential functions for simulating liquid water. *J. Chem. Phys.* **79**, 926–935 (1983).
56. R. Krzysztoń *et al.*, Single-cell kinetics of siRNA-mediated mRNA degradation. *Nanomed. Nanotechnol. Biol. Med.* **21**, 102077 (2019).
57. C. Leonhardt *et al.*, Single-cell mRNA transfection studies: Delivery, kinetics and statistics by numbers. *Nanomed. Nanotechnol. Biol. Med.* **10**, 679–688 (2014).
58. M. Ferizi *et al.*, Stability analysis of chemically modified mRNA using micropattern-based single-cell arrays. *Lab. Chip* **15**, 3561–3571 (2015).

PNAS

Supporting Information for

pH-dependent structural transitions in cationic ionizable lipid mesophases and LNP core phases

Julian Philipp[8], Aleksandra Dabkowska[1], Anita Reiser[8], Kilian Frank[8], Rafał Krzysztoń[8], Christiane Brummer[8], Bert Nickel[8], Clement E. Blanchet[6], Akhil Sudarsan[7], Mohd Ibrahim[7], Svante Johansson[1], Pia Skantze[1], Urban Skantze[1], Sofia Östman,[2] Marie Johansson,[2] Neil Henderson,[3] Kjetil Elvevold[4], Bård Smedsrød[5], Nadine Schwierz[7], Lennart Lindfors[1] and Joachim O. Rädler[8*]

*Joachim Oskar Rädler (ORCID ID 0000-0002-5846-1489)
Email: raedler@lmu.de

This PDF file includes:

- Supporting text
- Figures S1 to S10
- Tables S1, S2
- SI References

Symmetry and SAXS indexation of CIL/chol/buffer mesophases

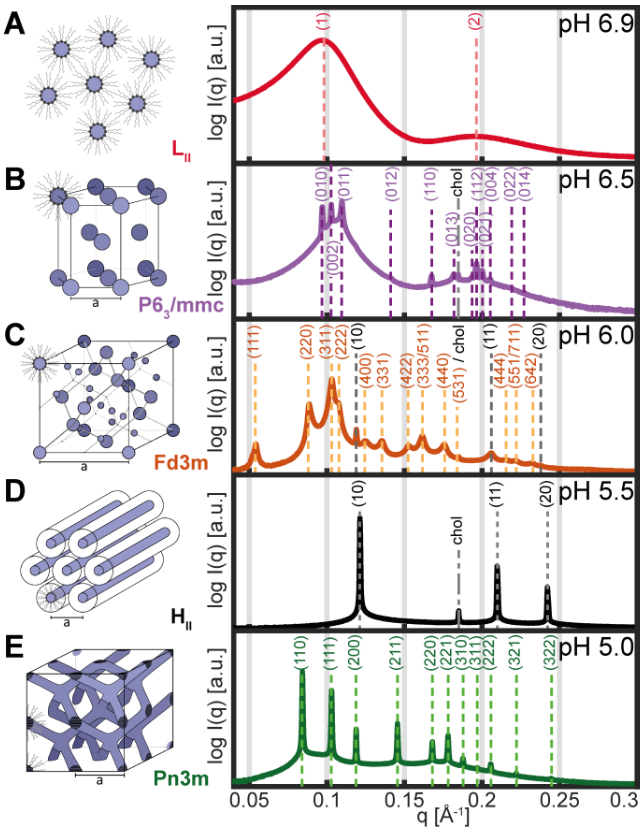

Figure S1. (A) Inverse micellar fluid isotropic, L_{II} (B) inverse micellar hexagonal with P6$_3$/mmc symmetry (C) inverse micellar cubic with Fd3m symmetry (D) inverse hexagonal, H_{II} (E) bicontinuous cubic, Pn3m

Preparation of bulk phases

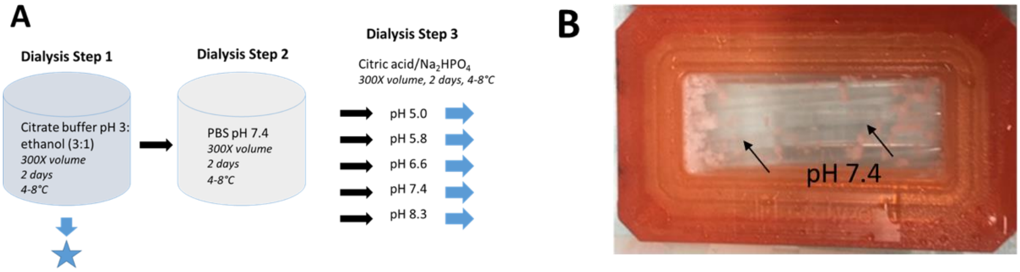

Figure S2. (A) Diagram of the dialysis steps followed for the production of lipid bulk phase. (B) Photograph of dialysis cassette containing precipitated core phases (arrows) in PBS, pH 7.4. The preparation mimics the LNP manufacturing conditions in the microfluidic mixer where the polyA:CIL complex forms. At these low pH conditions, the core phases of all CILs form disordered phases after two days of dialysis.

Reproducibility of bulk phases

While the results are generally consistent with the ordered hexagonal phase disappearing at pH 7.4, the location and amplitude of the broad peaks below 0.1 Å^{-1} are not reproducible between samples and between re-measurements of the same sample. Figure S2 shows one polyA-containing sample (same dialysis cassette) was re-measured in succession. The amplitude of the peak at 0.05 Å^{-1} was found to decrease with re-loading. Also, there appears to be a slight shift in the cholesterol peak.

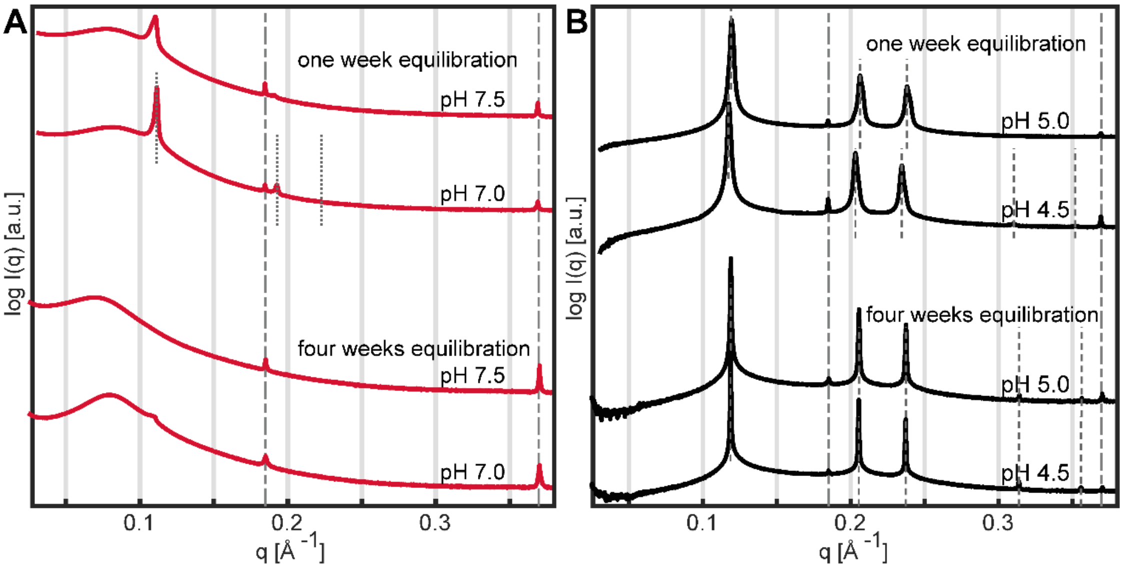

Figure S3. Comparison of bulk phase samples prepared following the same procedure but measured at different times. (A) At neutral pH the H_{II}^{C} phase disappears over time, possibly converting into the more stable L_{II}^{C} phase. (B) At low pH the H_{II} peaks become narrower, indicating an increase in domain size and therefore crystallization.

Encapsulation of polyA in the mesophases

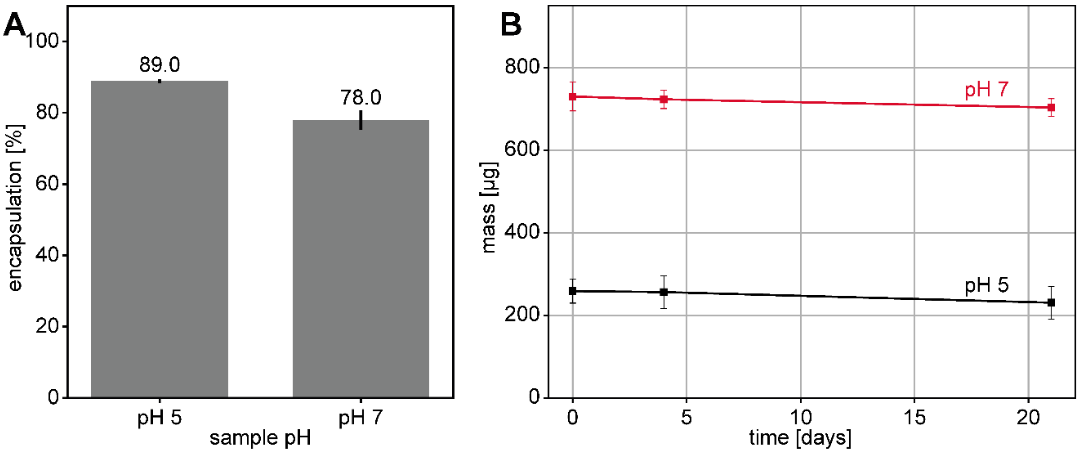

Figure S4. (A) For the bulk samples the polyA encapsulation was measured at pH 7 and pH 5 with two samples each. As expected the polyA encapsulation is higher with charged CIL compared to the encapsulation at neutral pH and therefore neutral charge of the CIL. The measurements were conducted by measuring the polyA content in the remaining supernatant after the dialysis to the respective pH value. (B) By measuring the polyA content in the supernatant at different time points after the dialysis, the release of polyA from the samples after the preparation was examined. Over the course of three weeks, almost no additional polyA was measured which shows that after the preparation only very little polyA diffuses out the bulk phases, regardless of the buffer pH. Each data point consists of five individual measurements of five different probes of the supernatant.

Simulation Methods

Simulation setup of inverse hexagonal (H_{II}) phase

To model the inverse hexagonal phase, we follow the procedure described in (1). A cylindrical water column surrounded by MC3 lipids and cholesterol was initially prepared using the CHARMM-GUI webserver (2). We assume that at the given pH, all MC3 molecules are charged. The mole fractions of MC3 and cholesterol was in the ratio 3:1. The setup so prepared was placed in a triclinic simulation box, which ensures a hexagonal lattice structure of the setup and its periodic images (**Fig. 5A**). To reproduce the experimental hexagonal lattice spacing, several simulations were first run by varying the number of waters per lipid (n_w) (**Fig. S5B**). We used 3 replicas of the system for each lattice spacing and the simulations were 200 ns long, discarding the first 50 ns for equilibration. To confirm that the systems are sufficiently equilibrated, we performed a longer simulation (1 μs) for the final lattice spacings (n_w = 12). The resulting electron density profiles remained unchanged (**Fig. S7E**) and we conclude that 200 ns are sufficient to yield converged results. The concentration of NaCl in the simulations was 150 mM and additional anions were included to neutralize the systems if necessary.

For H_{II}**,** each simulation box contained 150 MC3 lipids and 50 cholesterols. The corresponding number of water molecules were 1200, 2400, 3600 at n_w = 6, 12, 18. n_w = 12, best reproduced the experimental lattice spacing of 60 Å and was therefore used for further analysis and interpretation (see below).

Simulation setup of inverse micellar phase

To model the inverse micellar phase, we use a rhombic dodecahedron box with square faces to mimic a surrounding with twelve nearest neighbors. The Packmol package (3) was used to create a uniform water sphere surrounded by MC3 lipids and cholesterol. Here, we assume that at the given pH all MC3 molecules are uncharged. Similar to the hexagonal phase, we vary the molar ratios of water to CIL molecules (**Fig.S5C,D**). Each simulation box contained 75 MC3 lipids and 25 cholesterols. The corresponding number of water molecules were 600, 1000, 1200, 1600, 1800 at n_w = 6, 10, 12, 16, 18. The inverse micellar system with n_w = 16 was found to reproduce the lattice spacing of 60 Å (see below). Further analysis was performed on this system.

Simulation setup of the inverse micellar to inverse hexagonal transition

To understand the micellar to hexagonal transition with pH change, the equilibrated inverse micelle structure at n_w = 16 was used as starting structure. In a first step, the charge state of the MC3 head groups was changed from unprotonated to fully protonated. Subsequently, the system was energy minimized and equilibrated as described below. During the equilibration, the cationic MC3 head groups swing out into the water phase after a few hundred picoseconds. During the production run, the lipids reorder and the characteristic cylindrical water column of the hexagonal phase is formed after about 10 ns.

Lattice spacing as a function of hydration

In the MD Simulations, we varied the water content by choosing increasing molar ratios of water to CIL molecules (n_w). The results for the inverse hexagonal (H_{II}) phase and the inverse micellar (L_{II}) phase are shown in **Fig. S6A** and **Fig. S6B**, respectively. Based on the experimentally measured lattice spacing of 60 Å, we selected the systems with $n_w = 12$ for inverse hexagonal phase simulations and $n_w = 16$ for inverse micelle simulations.

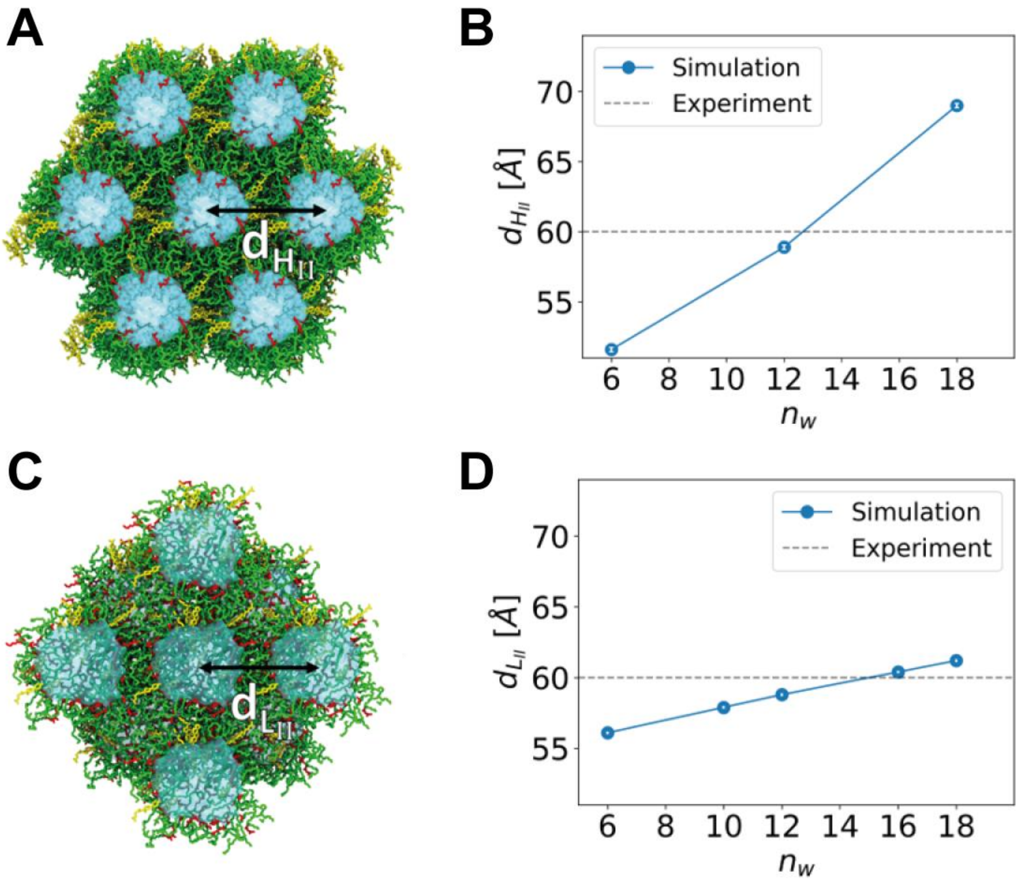

Figure S5. (A) Simulation snapshot of the inverse hexagonal phase in top view. The lattice spacing $d_{H_{II}}$ is given by the distance between the center of neighboring water wires. (B) Lattice spacing with increasing hydration for the H_{II} phase. The horizontal dashed line represents the experimental value of lattice spacing. Errors correspond to the standard deviation obtained from 3 independent simulations. Note that the error bars are smaller than the symbols. (C) Simulation snapshot of the inverse micellar phase. Each inverse micelle is surrounded by 12 neighboring inverse micelles. (D) Lattice spacing $d_{L_{II}}$ with increasing hydration for the L_{II} phase. Similar to B the horizontal dashed line represents the experimental value of lattice spacing and the errors correspond to the standard deviation obtained from 3 independent simulations.

Calculation of the effective volume fraction of water from MD simulations

The volume fraction of water ϕ_W is defined as the ratio of the volume of the water and the total volume of the system. In the MD simulations, the probability density function of finding an atom at a radial distance r is given by $p(r) = \rho_t(r)/\rho_0$ where $\rho_t(r)$ is the number density of the system along r and ρ_0 is the normalizing constant defined by $\int_0^\infty p(r)\, d^3r = 1$. Using the radial symmetry of the inverse hexagonal and micellar phase, the effective water volume fractions $\phi_w^{H_{II}}$ and $\phi_w^{L_{II}}$ were calculated from

$$\phi_w^{H_{II}} = \frac{\int_0^\infty p_w^{H_{II}}(r) d^3r}{\int_0^\infty p_t^{H_{II}}(r) d^3r} = \frac{\int_0^{r_{cut}} r\rho_w^{H_{II}}(r) dr}{\int_0^{r_{cut}} r\rho_t^{H_{II}}(r) dr}$$

$$\phi_w^{L_{II}} = \frac{\int_0^\infty p_w^{L_{II}}(r)d^3r}{\int_0^\infty p_t^{L_{II}}(r)d^3r} = \frac{\int_0^{r_{cut}} r^2\rho_w^{L_{II}}(r)dr}{\int_0^{r_{cut}} r^2\rho_t^{L_{II}}(r)dr}$$

where ρ_w and ρ_t are the number densities of water and the system. The results are shown in **Fig. S6** as function of n_w. Note that the water volume ratio calculated from the integrals becomes constant after a distance larger than r_{cut}. The values obtained by integration of the probability densities are 1-2% smaller compared to the calculation assuming an empirical water volume of 30.5 Å^3.

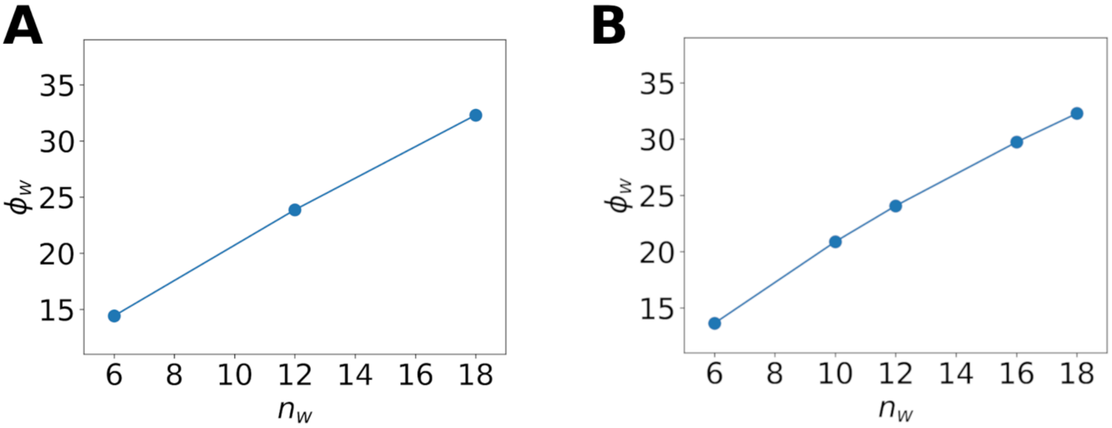

Figure S6. Variation of water volume fraction of the inverse hexagonal phase (A) and inverse micellar phase (B) with increasing hydration. For the H_{II} phase, the water volume fraction for n_w =12 is 23.9% and for the L_{II} phase with n_w =16 the volume fraction is 29.7%.

Electron Density Calculation

The electron density was calculated using custom python scripts based on MDAnalysis (4). For the inverse hexagonal phase, the simulation box was divided into concentric cylindrical shells oriented along the z-axis (i.e. along the water column orientation). The electron density in a given shell at distance r from the cylinder axis is given by

$$\rho_e(r) = \frac{\sum_i n_i z_i}{2\pi h r dr}$$

where n_i is the number of atoms of type i with z_i electrons, h is the box height in z-direction and dr = 0.5 Å is the width of the cylindrical shell. The summation is performed over all the atoms in a given shell.

Similarly, for the micellar phase, the box was divided into concentric spherical shells centered at the center of mass of the micelle. The electron density at a distance r is given by,

$$\rho_e(r) = \frac{\sum_i n_i z_i}{4\pi r^2 dr}$$

To confirm the simulation setup and binning for the electron density profile, we calculated the water density as function of the distance from the water wire (inverse hexagonal phase) or center of water sphere (inverse micelle phase). The value close to the center is identical to the literature value for bulk TIP3P water (5).

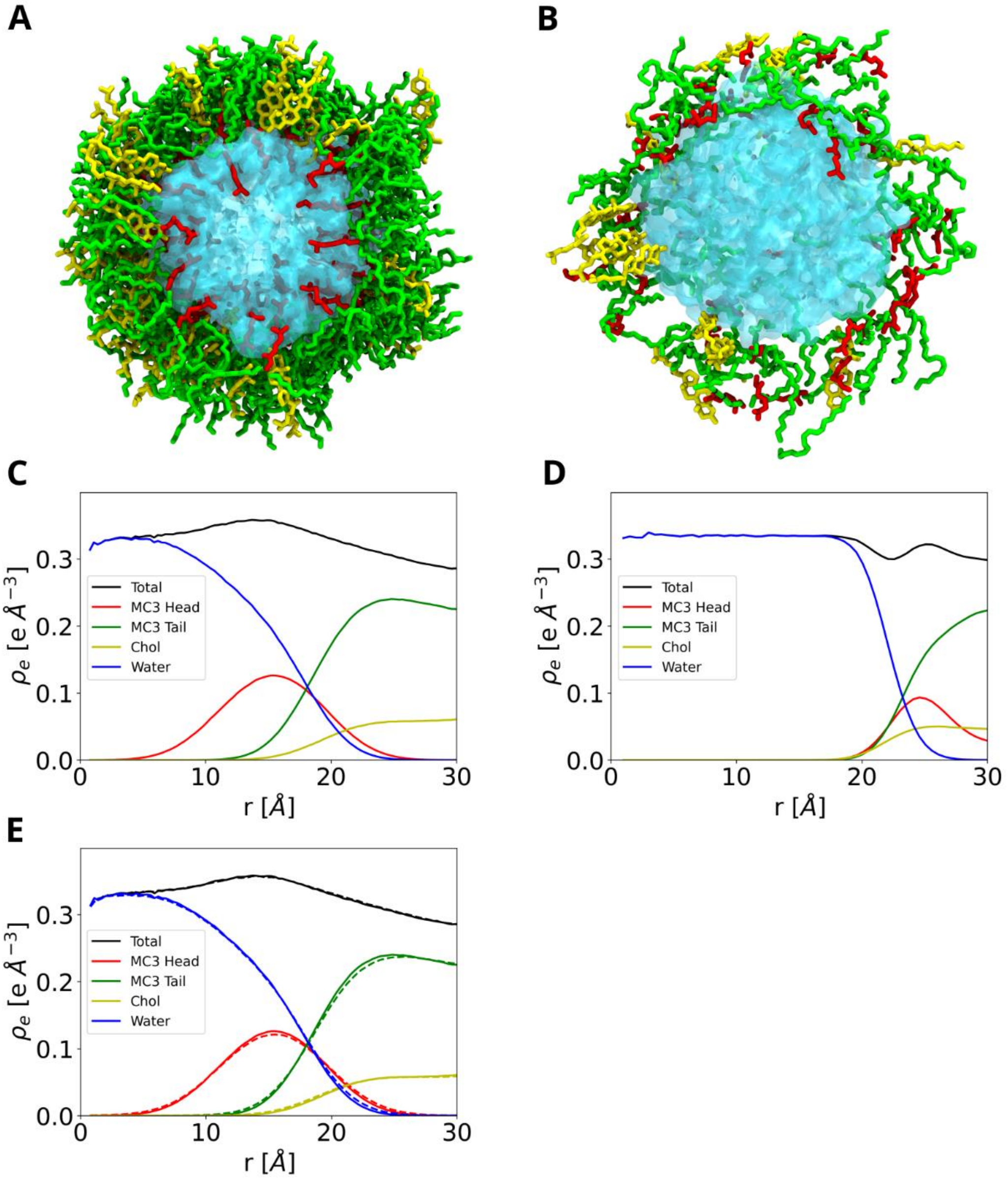

Figure S7. Simulation snapshots and electron densities for a single water column and a single inverse micelle. (A) Cross-section of the simulation box from the H_{II} phase (top view). (B) Cross-section of the simulation box for an inverse micelle from the L_{II} phase. Water is shown in blue, ionizable headgroups and tails of MC3 are shown in red and green, respectively. Cholesterol is shown in yellow. (C,D) Electron density profiles of the unit cell H_{II} including the contributions from neighboring micelles. Note that the headgroup of the protonated MC3 sticks into water in the H_{II} phase. The uncharged MC3 headgroup hides in the lipid region in the L_{II} phase. (E) To provide insights into the convergence of the H_{II} phase, the results after 200 ns (solid) and 1 µs (dashed) are shown.

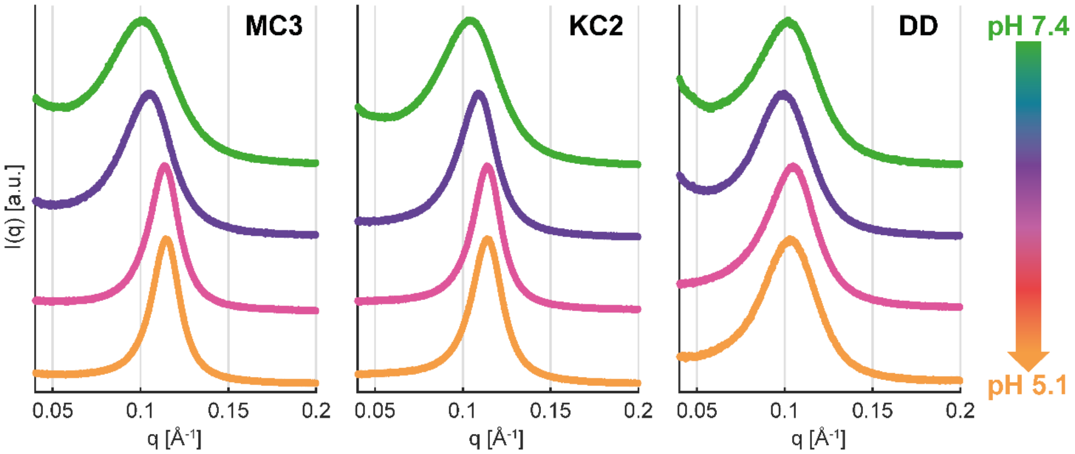

Figure S8. SAXS scattering curves of lipid nanoparticles containing eGFP mRNA. The plot shows a more significant pH-dependent peak position shift for LNPs with MC3 and KC2 compared to DD. The peak positions are plotted in **Fig.4E** of the main publication. Dispersions of LNPs (at 3-6 mg/mL mRNA concentration in McIlvaine buffer) were measured in quartz capillaries. The scattering background was subtracted using reference buffer measurements.

Fluorescence anisotropy measurements of DPH as a function of pH at 37 °C for LNPs

1,6-Diphenyl-1,3,5-hexatriene (DPH) was obtained from Fluka (lot 1054132). McIlvaine buffers of pH 3, 4, 5, 5.8, 6.6, 7.4 and 8 was prepared by mixing appropriate volumes of 0.05 M citric acid and 0.1 M Na_2HPO_4 followed by five times dilution with water and 1.5 M NaCl to obtain 0.15 M NaCl in the final solution. LNP samples in McIlvaine buffers were prepared at 40 μM lipid and 0.4 μM DPH and, also, corresponding samples without DPH for background correction. DPH/buffers were prepared by 1000-fold dilution of 0.5 mM DPH (acetonitrile) in each buffer. For each sample: 1600 μl DPH/buffer (or only buffer) +330 μl buffer +x μl LNP +(70-x) μl PBS. LNP/DPH samples were prepared and measured in triplicate while background samples were only measured once. The LNP samples were incubated over night at room temperature in the dark, followed by incubation at 37 °C for 8 minutes before measurements. The fluorescence intensity was measured with a PerkinElmer LS55 Luminescence Spectrometer at 37 °C with Ex/Em wavelengths= 360/430 nm. Fluorescence anisotropy, *r*, was calculated from the fluorescence intensities with polarizer settings HV (horizontal, vertical), HH, VV and VH as described in the supplementary information. The resulting r(pH) dependence was fitted by the Henderson-Hasselbalch equation.

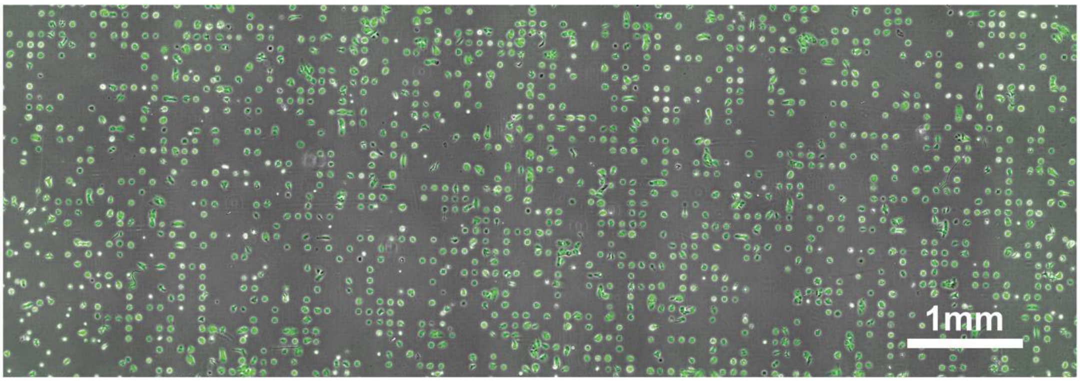

Figure S9. Expression kinetics and efficiency of CIL mediated transfection. (A) Individual cells expressing eGFP (green) on a micropatterned array 10 h after transfection (see also (6)).

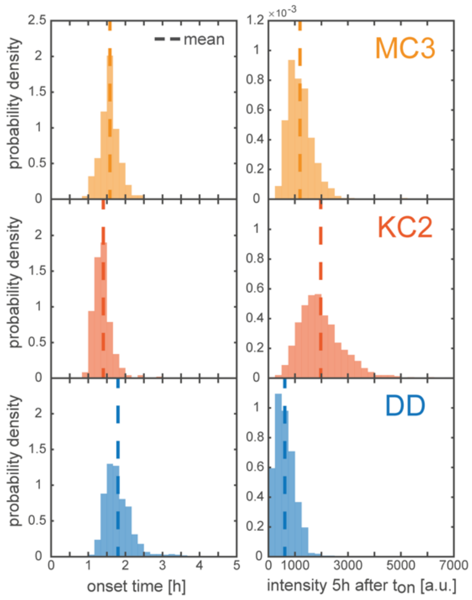

Figure S10. Onset time distribution and expression level after 5h Histograms of the eGFP onset time distribution of MC3 (orange) KC2 (red), and DD (blue) mediated transfection.

Lipid phase	Miller indices (hkl)	a/d_{hkl}	m_{hkl}
$Pn3m$	$(110),(111),(200),(211),(220),\ldots$	$\sqrt{h^2+k^2+l^2}$	$\sqrt{2},\sqrt{3},2,\sqrt{6},\sqrt{8},\ldots$
H_{II}	$(10),(11),(20),(21),(30),\ldots$	$\sqrt{h^2+k^2+hk}$	$1,\sqrt{3},2,\sqrt{7},\sqrt{9},\ldots$
$Fd3m$	$(111),(220),(311),(222),(400),\ldots$	$\sqrt{h^2+k^2+l^2}$	$\sqrt{3},\sqrt{8},\sqrt{11},\sqrt{12},\sqrt{16},\ldots$
$P6_3/mmc$	$(010),(002),(011),(012),(110),\ldots$	$\frac{4}{3}(h^2+k^2+hk)+\frac{3}{8}l^2$	$\sqrt{4/3},\sqrt{3/2},\sqrt{41/24},\sqrt{17/6},4,\ldots$

Table S1. Miller indices of the measured lipid phases.

Lipid Phase	a	d_{NN}
$Pn3m$	$\frac{2\pi\, m_{hkl}}{q_{hkl}}$	$\frac{a}{\sqrt{2}}$
H_{II}	$\frac{4\pi\, m_{hkl}}{\sqrt{3}\, q_{hkl}}$	a
$Fd3m$	$\frac{2\pi\, m_{hkl}}{q_{hkl}}$	$\frac{a}{\sqrt{8}}$
$P6_3/mmc$	$\frac{2\pi\, m_{hkl}}{q_{hkl}}$	a

Table S2. Formula of the lattice constant a and the nearest neighbor distance d_{NN} for the measured lipid phases.

Movie S1 (separate file). The video starts with a 90° round view of the inverse micellar phase (L_{II}) with 12 nearest neighbors. All ionizable MC3 lipids are neutral. Subsequently, the cross section of the L_{II} phase is shown. Mimicking the change in pH, the MC3 lipids are protonated and the molecular dynamics simulations start. The MC3 head groups (red) quickly enter the water phase. Subsequently, the topology changes from L_{II} to H_{II} and the water columns are formed. The dynamics stops and a 90° rotation of the inverse hexagonal phase (H_{II}) is shown. In the video, head and tail groups of the MC3 lipids are shown in red and green, respectively. Water is shown in cyan and cholesterol in yellow

SI References

1. M. Ramezanpour, *et al.*, Structural Properties of Inverted Hexagonal Phase: A Hybrid Computational and Experimental Approach. *Langmuir* **36**, 6668–6680 (2020).
2. S. Jo, T. Kim, V. G. Iyer, W. Im, CHARMM-GUI: A web-based graphical user interface for CHARMM. *J. Comput. Chem.* **29**, 1859–1865 (2008).
3. L. Martínez, R. Andrade, E. G. Birgin, J. M. Martínez, PACKMOL: A package for building initial configurations for molecular dynamics simulations. *J. Comput. Chem.* **30**, 2157–2164 (2009).
4. N. Michaud-Agrawal, E. J. Denning, T. B. Woolf, O. Beckstein, MDAnalysis: A toolkit for the analysis of molecular dynamics simulations. *J. Comput. Chem.* **32**, 2319–2327 (2011).
5. C. Vega, J. L. F. Abascal, Simulating water with rigid non-polarizable models: a general perspective. *Phys. Chem. Chem. Phys.* **13**, 19663 (2011).
6. A. Reiser, D. Woschee, S. M. Kempe, J. O. Raedler, Live-cell Imaging of Single-Cell Arrays (LISCA) - a Versatile Technique to Quantify Cellular Kinetics. *Jove-J. Vis. Exp.*, e62025 (2021).

5 Publication 2: Buffer Specificity of Ionizable Lipid Nanoparticle Transfection Efficiency and Bulk Phase Transition

Lipid nanoparticles (LNPs) are the gold-standard carriers for mRNA delivery, yet the apparent superiority of citrate buffer in their formulation has remained mechanistically obscure. To address this knowledge gap, we collaborated with Cristina Carucci, Drew Parsons, and Andrea Salis from the University of Cagliari in Italy to investigate buffer specificity.

Our initial in-vitro experiments, led by Judith Müller, analyzed the effect of different buffers (citrate, phosphate, and acetate) on the transfection efficiency of LNPs formulated with common ionizable lipids (MC3, SM-102, and ALC-315). Our key finding was that LNPs prepared with citrate exhibited a significantly earlier onset and stronger gene expression compared to those prepared with phosphate or acetate. Crucially, buffer type did not affect LNP encapsulation efficiency or particle size, indicating that its role is confined to the subsequent endosomal release mechanism and not the initial LNP structure.

To elucidate the structural basis for the superiority of citrate buffer, we utilized synchrotron small-angle X-ray scattering (SAXS) in collaboration with Cristina Carucci, Ekaterina Kostyurina, and Clement Blanchet, to study the mesophase structure of the ionizable lipid/cholesterol core material. Based on our previous work, we hypothesized that the crucial event for mRNA release is the pH-dependent phase transition from the inverse micellar to the inverse hexagonal phase.

The SAXS data revealed that in comparison to the acetate and phosphate buffers, the citrate buffer shifts this critical phase transition to a higher, less-acidic pH by approximately one pH unit. This pH shift is proposed to cause earlier endosomal escape within the endosomal pathway, thereby critically enhancing transfection efficiency.

We proposed that this effect is governed by specific ion adsorptions. To validate this mechanism, we performed all-atom molecular dynamics (MD) simulations in collaboration with Nadine Schwierz and Akhil Sudarsan from the University of Augsburg. The MD results confirmed that the citrate anion specifically interacts with the positively charged head group of the ionizable lipid. This specific interaction effectively reduces the area per lipid head group, consequently stabilizing the inverse hexagonal phase. Conversely, acetate and phosphate anions preferentially stabilized the inverse micellar phase, providing a complete molecular-level explanation for the observed differences in LNP performance.

For licensing reasons, the research paper below is the accepted manuscript instead of the final, properly formatted publication. The final version can be found as DOI 10.1021/acsnano.4c14098.

Buffer specificity of ionizable lipid nanoparticle transfection efficiency and bulk phase transition

Cristina Carucci[1,‡], Julian Philipp[2,‡], Judith A. Müller[2], Akhil Sudarsan[3], Ekaterina Kostyurina[2], Clement E. Blanchet[4], Nadine Schwierz[3], Drew F. Parsons[1,], Andrea Salis[1], Joachim O. Rädler[2,*]*

[1]Department of Chemical and Geological Sciences, University of Cagliari & Center for Colloid and Surface Science (CSGI),
Cittadella Universitaria, 09042 Monserrato, CA, Italy

[2]Faculty of Physics, Ludwig-Maximilians University,
Geschwister-Scholl-Platz 1, Munich, Germany.

[3]Institute of Physics, University of Augsburg, Augsburg 86159, Germany.

[4]European Molecular Biology Laboratory Hamburg Outstation c/o Deutsches Elektronen-Synchrotron, Hamburg 22607, Germany.

*Prof. Joachim O. Rädler, raedler@lmu.de
*Prof. Drew F. Parsons, drew.parsons@unica.it

ABSTRACT. Lipid nanoparticles (LNPs) are efficient and safe carriers for mRNA vaccines based on advanced ionizable lipids. It is understood that the pH dependent structural transition of the mesoscopic LNP core phase plays a key role in mRNA transfer. However, buffer specific variations in transfection efficiency remain obscure. Here we analyze the effect of buffer type on the transfection efficiency of LNPs. We find that LNPs formulated with the cationic ionizable lipids DLin-MC3-DMA (MC3), SM-102 and ALC-315 in citrate compared to phosphate and acetate buffers exhibit earlier onset and stronger mRNA-GFP expression in-vitro. Using synchrotron small angle X-ray scattering (SAXS) we determine the buffer specificity of the pH dependent structure of ionizable lipid/cholesterol/water mesophases that serve as model systems for the LNP core phase. The results show that the phase transition from inverse micellar to inverse hexagonal with decreasing pH is shifted to a lower transition pH for acetate and phosphate compared to citrate buffer. Based on continuum theory and ion specific adsorption obtained from all-atom MD simulations, we propose a mechanism for buffer specificity. Citrate stabilizes the inverse hexagonal phase thus shifting the formation of H_{II} to a higher pH. By contrast, phosphate and acetate stabilize L_{II}. It stands to reason that the inverse micellar to inverse hexagonal transition, which is facilitated in citrate buffer, enables a sensitized pH-response of the LNP core phase. This, in turn, enhances endosomal release efficiency and accounts for the earlier onset of gene expression observed in LNPs prepared with citrate buffer.

KEYWORDS. *Lipid Nanoparticles, Ionizable Lipids, Transfection efficiency, Dlin-MC3-DMA, pH transition, Specific Buffer Effects.*

Gene delivery carriers have been developed and improved for decades but reached an unprecedented breakthrough through successful, safe and efficient delivery of mRNA-based vaccination during the COVID-19 pandemic.[1–3] Specifically, lipid nanoparticle (LNP) formulations have been approved by the Food and Drug Administration (FDA) due to favorable properties such as colloidal stability, low toxicity, and controlled size. While early cationic lipoplexes proved toxic to human cells, LNPs based on ionizable lipids exhibit pH dependent lipid headgroup ionization and hence less toxic surface charge. Furthermore, once endocytosed, LNPs overcome endosomal entrapment via endosomal fusion in a pH dependent manner. LNPs are internalized at physiological pH and experience protonation during the time course of the early endosomal maturation with pH values decreasing to (6.5-5.0).[4,5] The process of charging ionizable lipid headgroups facilitates endosomal fusion, releasing mRNA into the cytosol. The exact process of how LNPs fuse with the endosome membrane is the subject of intense research. In cationic lipid based lipofection it has been rationalized that the mesoscopic bulk structure of lipoplexes affects fusogenicity, with the inverse hexagonal phase[6] and cubic phase[7] being particularly fusogenic compared to lamellar internal packing. LNPs are nanoscale particles with well-defined surface and core composition. The interior of LNPs consists of a cationic ionizable lipid/cholesterol moiety complexed with mRNA. The surface is composed of a monolayer that includes all lipid components specifically the stabilizing PEG-lipid/DSPC and cholesterol. The core of the LNP, structured by ionizable lipids, exhibits pH-dependent mesostructures, leading to multiple phases and structural transitions as the pH decreases.[8–10] The behavior of the core phase has been studied using binary ionizable lipid/cholesterol bulk phases as model systems.[9] This simplification to just two lipid components is feasible because both DSPC and PEG are largely absent from the LNP core.

It is generally understood that lyotropic mesophases depend on the lipid chain splay described by the Israelachvili shape factor.[11,12] Ionizable lipids with strongly conic shape form inverted phases, which with increasing headgroups size range from inverse micellar disordered, L_{II}, to disconnected inverse micellar cubic, I_{II}, to inverse hexagonal, H_{II} and bicontinuous cubic phases, Q_{II}. Thereby the (I_{II}-H_{II}) as well as (H_{II}-Q_{II}) transitions change connectivity of the lipid network.[13] In recent work, we showed that specifically the ionizable lipid MC3 shows a structural phase transition with decreasing pH from inverse micellar cubic phase with space group Fd3m to inverse hexagonal (denoted Fd3m-H_{II} transition in the following).[14] X-ray scattering from full LNPs also provide evidence that a similar structural transition occurs within the LNPs as a function of pH, assuming that the LNP core mesophase is predominantly formed by ionizable excess lipid and cholesterol. The pH-dependent lipid core transition has been suggested as a critical factor in inducing endosomal fusion and hence mRNA escape efficiency.[14] Therefore, further investigation of ionizable lipid/cholesterol bulk phases as LNP core mimics is valuable for gaining insight into the LNP-endosomal fusion mechanism.

The critical pH-value of the structural transition coincides with the pK_a value of the ionizable lipid. The regulation of pH in both chemical and biological systems is carried out by buffers, a mixture of a weak acid (HA) or base (B) with its conjugate base (A^-) or acid (BH^+). According to the Henderson-Hasselbalch equation, the only important parameter for the choice of buffer is the pK_a and the concentrations of the buffer components. Little attention has been paid to the chemical identity of the weak electrolytes and their conjugate species used to prepare the buffer.[15] However, starting from the pioneering work by Ninham and coworkers on restriction enzyme activities,[16] several studies have shown that the chemical nature of the buffer, even at the same nominal pH, can have important unexpected effects on the investigated biosystem. For example, buffers have been found to affect specifically the behavior of proteins, including lysozyme electrophoretic mobility[17] and adsorption,[18] Brownian motion of BSA,[19] and more recently, DNA thermal stability,[20] DNA interactions with lipid bilayers,[21] and the formation of a protein corona around nanoparticles.[22] In fact, "specific buffer effects" can be included in the wider classification of "ion specific effects" first observed by Hofmeister in 1888.[23] The "Hofmeister series" is an order based on ion induced protein precipitation (salting out) or solubilization (salting in). A conventional explanation of the Hofmeister series was proposed [24,25] invoking Jones and Dole's work [26] on the viscosity of aqueous salt solutions. Ions were classified as "kosmotropic" (order maker) or chaotropic (disorder maker) on the basis of their interaction with water quantified through the value (and the sign) of the Jones-Dole viscosity B coefficient. More recent theoretical and simulation work explains ion specificity as the result of a delicate interplay between electrostatic, hydration and ion-dispersion forces.[27,28] Whatever the details of the mechanisms explaining "Hofmeister phenomena", it must be considered that ions play an important role to modulate biological mechanisms in a way which is not fully understood. For example, Meulewaeter et al.[29] found that Tris and HEPES buffers improved cryoprotection and, more importantly, the transfection efficiency of mRNA-LNPs compared to PBS buffer. What emerges from previous studies is that the mechanism of transfection, based on bulk phase transitions, is controlled not only by pH but is also specifically affected by the buffer ions used to control pH.[30,31]

The present work aims to investigate the effect of the choice of preparation buffer solution (here, citrate, phosphate and acetate buffers) on the transfection efficiency of LNPs formulated with the ionizable lipid DLin-MC3-DMA (MC3), SM-102, and ALC-315, in combination with cholesterol, DSPC and DSPE-PEG2000, respectively. In order to explain the observed buffer specific transfection efficiency, we investigated the corresponding bulk phase composed of ionizable lipid/cholesterol model systems as a function of pH in different buffers, using synchrotron small angle X-ray scattering (SAXS). We present a mechanism for the observed buffer specific pH shift of the inverse micellar to inverse hexagonal bulk phase transition in terms of changes in the area per lipid headgroup affected by pH and by ion specific adsorption based on all-atom MD simulations. The study highlights the role of buffer ions on the pH-dependent structural transitions in ionizable lipid bulk phases. We propose that a similar pH-dependent structural transition might occur in the excess lipid region within the LNP core phase facilitating endosomal release and hence resulting in an earlier gene expression onset compared to phosphate and acetate buffer.

RESULTS AND DISCUSSION

Specific buffer effects on mRNA LNPs and transfection efficiency

LNPs are composed of an external layer composed of PEG polymer with DSPC and MC3 lipids, with an internal bulk phase composed of Dlin-MC3-DMA and cholesterol. MC3 is an ionizable lipid with a p*K*$_a$ of 6.44,[32] which makes it pH sensitive (Fig. 1A-B). The LNPs are internalized inside living cells at pH ~ 7 until reaching the endosome, where mRNA is released at pH ~ 6-6.5 (Fig. 1E). To study the buffer effects three common buffers were chosen (Fig. 1C-D).

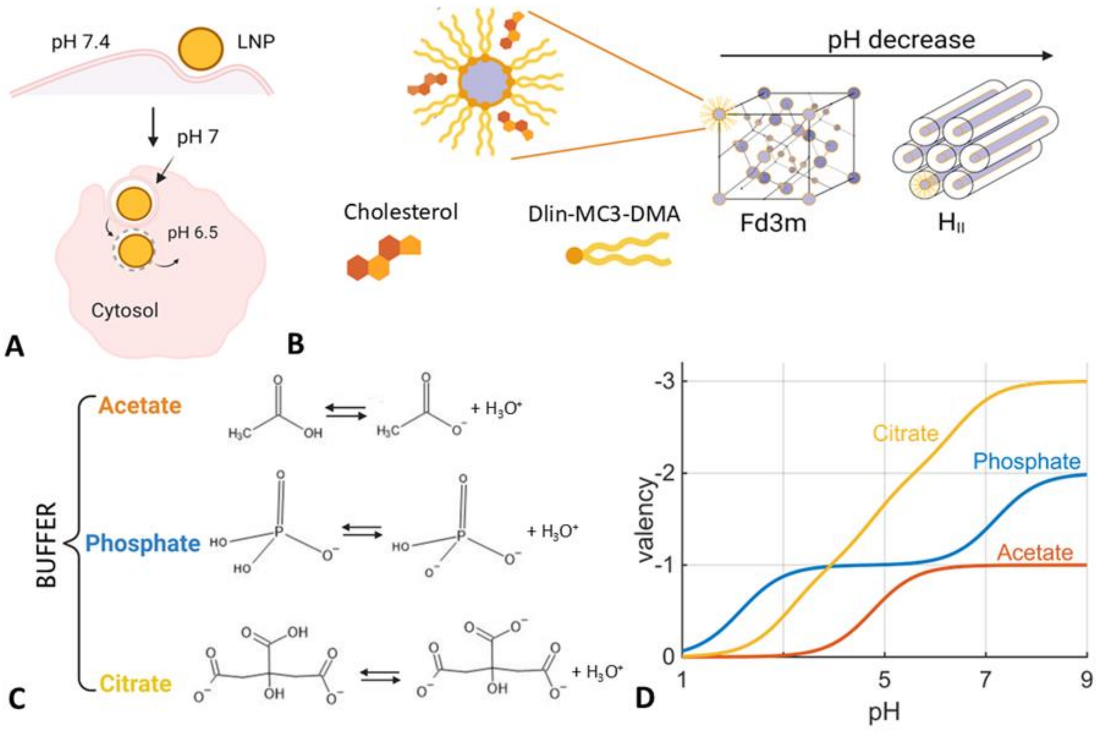

Figure 1. Buffer specificity of LNP mediated mRNA delivery. (A) Schematic drawing of internalization via endocytosis. Endosomal release of LNPs occurs as a consequence of acidification inside the endosome from pH 7 to about pH 6.5. Schematic drawing of bulk phase made by ionizable lipid Dlin-MC3-DMA and cholesterol together with bulk phase transition from Fd3m to H$_{II}$ as pH

decreases. (C) The buffer used during the dialysis process is chosen among a range of buffers, citrate (pK*a* 6.4), phosphate (pK*a* 7.2), and acetate (pK*a* 4.8). To evaluate the phase transition a wide range of pH values from 3.5 to 7.0 in a 0.5 pH unit has been studied. (D) Buffer valency at each pH depending on pK*a* values.

According to the Henderson-Hasselbalch equation (pH = p*K*a ± 1), citrate, phosphate and acetate with p*K*a of 6.40, 7.22 and 4.80, respectively, cover the whole pH range of the LNP route from internalization (pH 7) to mRNA release (pH 6). Sodium citrate buffer has been used in cationic lipid design for siRNA delivery,[1] and is by far the most used for LNP preparation at acidic pH. Sodium phosphate buffer was used with KCl and NaCl to store Pfizer's mRNA vaccine.[30] Sodium acetate buffer has been used to dilute mRNA for LNP encapsulation[33] and as dialysis buffer for ethanol removal after LNP preparation.[34]

To investigate buffer specific effects on transfection kinetics, we prepared eGFP-mRNA LNPs in citrate, phosphate or acetate buffer as described previously,[14] followed by dialysis into water. We performed live-cell imaging on single cell arrays (LISCA) after transfection and measured protein expression in a time resolved manner.[35] To this end, LNPs were preincubated in cell culture medium supplemented with serum, and transfected into the human liver carcinoma cell line (HuH7) seeded on a single-cell slide (Fig. 2A).

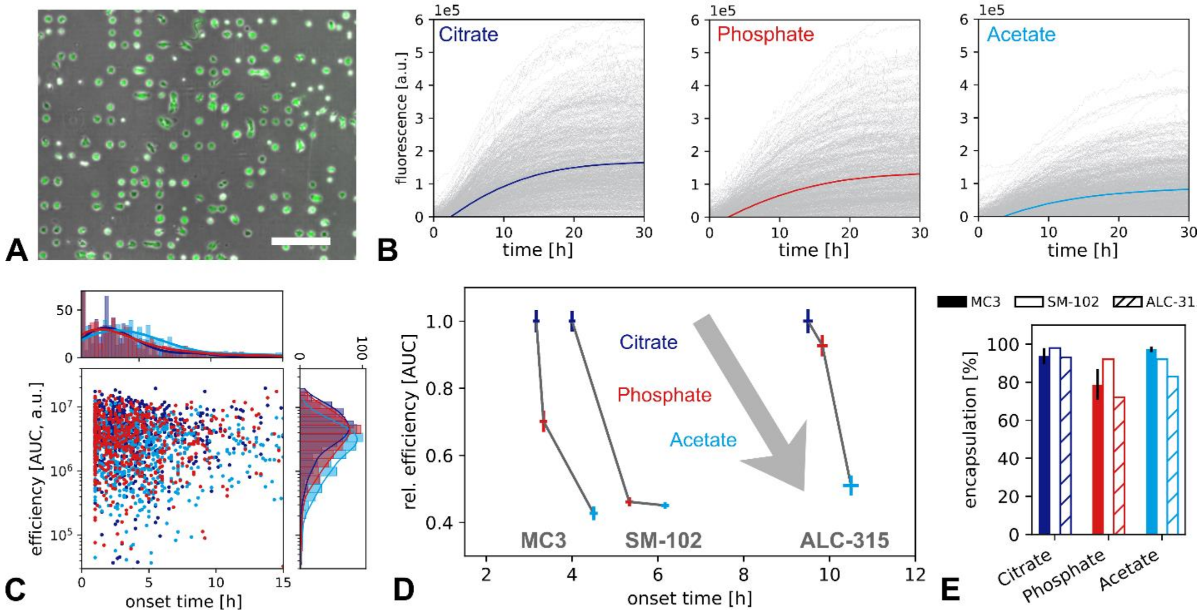

Figure 2. Single cell transfection experiments: (A) Culturing cells on microfabricated single-cell arrays allows recording of hundreds of single-cell fluorescence trajectories in parallel. (B) Single cell expression time courses of eGFP-mRNA/LNPs (gray lines) show different fluorescence kinetics for different preparation buffers (averaged time courses shown in color). (C) Scatter plot of single cell expression efficiencies, area under the curve (AUC), versus expression onset times (D) Relative efficiency in terms of AUC relative to efficiency of the LNP prepared in citrate buffer versus onset time of fluorescence. The three LNP buffer conditions exhibit an apparent Hofmeister ordering, showing earlier onset and higher protein expression for citrate compared to phosphate and acetate. Error bars indicate standard error of the mean. (E) Encapsulation efficiencies for LNPs prepared using three different buffers and three different ionizable lipids.

Observation of GFP expression kinetics of single cells resulted in a fluorescence trajectory for each cell (Fig. 2B). Distinct differences between the buffers were apparent from these traces. Averaging all traces revealed the highest overall GFP level for LNPs prepared in citrate buffer followed by those prepared in phosphate buffer and the lowest expression from the acetate LNPs. Single-cell resolution allowed for the calculation of the total protein amount per cell, expressed as the area under the curve (AUC) and the distinct onset of protein expression for every single cell (Fig. 2C). Protein expression varied depending on the buffer in which the LNP was prepared, with the highest eGFP expression for the citrate, followed by phosphate and lowest for the acetate buffer. Figure 2D shows the mean AUCs, in relative units normalized to the AUC in citrate, for all three ionizable lipids versus the mean expression onset. The buffer specific effect appears to follow a conventional Hofmeister series, with citrate > phosphate > acetate for the expression. The observed ordering in the onset times exhibits an inverse relation of expression efficiency and expression onset time (Fig. 2D). This confirms a correlation between fast onset and high protein expression levels as previously reported in time-resolved studies.[36] To rule out buffer specific effects on LNP preparation, LNP encapsulation (Fig. 2E) as well as particle size (Table S1) were measured as controls. Note the encapsulation efficiencies and sizes are not affected by buffers within the accuracy of the measurement. In the case of MC3 the eGFP-mRNA LNPs encapsulation efficiency in citrate, phosphate and acetate buffer, 50 mM at pH 3, were 94 ± 4, phosphate 79 ± 8 and acetate 97 ± 2 respectively.

In summary, these findings indicate that the underlying endosomal release mechanism but not the formulation is dependent on the LNP preparation buffer.

Specific buffer effects on bulk phase transitions

Next, we investigate the impact of buffers on the phase behavior of ionizable lipid/cholesterol bulk phases as a function of pH. These two-component bulk phases serve as a model for the inner core structure of LNPs, given that PEG and DSPC are restricted to the outer shell of the LNPs. As described in the methods section, the preparation of bulk phase samples consists of three dialysis steps to mimic the LNP production by replacing the ethanol with buffer. The buffer (citrate, phosphate or acetate) at the pH of choice comes into play in the third dialysis step. Figure 3A presents the SAXS scattering profiles for MC3/cholesterol/buffer phases in the presence of citrate, phosphate, and acetate buffers. In the following sections, we describe the pH-dependent structural transitions observed. As shown in Figure 3B decreasing the pH induces a phase transition from inverse micelles (L_{II})[37] to inverse hexagonal phase (H_{II}).[37] The inverse micellar phase undergoes ordering transitions from a disorder L_{II} through close-packed $P6_3/mcc$[37,38] towards an inverse cubic Fd3m phase.[39] This order of inverse phases as a function of pH has been reported before for MC3/cholesterol in citrate buffer.[10] Here we find that the same behavior is found also in phosphate and acetate buffer but with slightly shifted pH values of transitions. In citrate buffer $P6_3/mmc$ and Fd3m phases are formed at pH 7.0 and pH 6.5 respectively with decreasing pH. The same transitions are observed in the presence of acetate, but at a lower pH ($P6_3/mmc$ at pH 6.5 and Fd3m at pH 6.0). A bigger difference is observed for phosphate resulting in the L_{II} phase being found in the region from pH 7.5 to 6.0 and a mixed phase $P6_3/mmc$+Fd3m at pH 5.5.

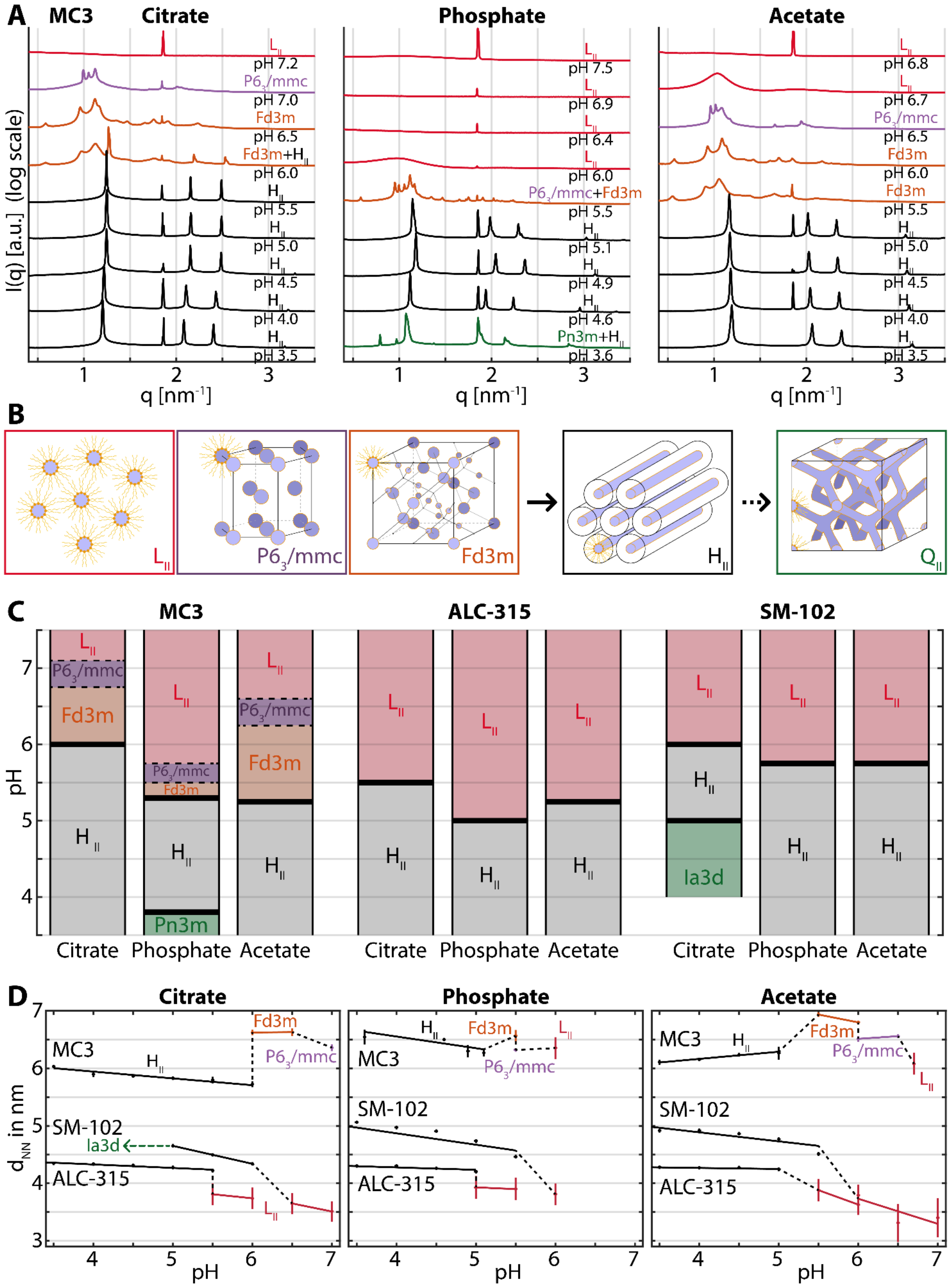

Figure 3. Buffer specific effects on ionizable lipid mesophases. (A) SAXS measurements of MC3-cholesterol bulk samples dialyzed in the presence of 50 mM citrate, acetate and phosphate buffer and NaCl 150 mM across a pH range of approximately 3.5 to 7.5. (B) Sequence of lipid phase symmetries with increasing protonation showing the order L_{II}, $P6_3/mcc$, Fd3m, H_{II} and Q_{II}. (C) Phase diagrams showing the buffer-specific pH dependence for MC3, ALC-315 and SM-102. (D) Nearest neighbor distance d_{NN} between centers of encapsulated water micelles/tubes for MC3, ALC-315 and SM-102 with H_{II}, Fd3m, $P6_3/mcc$ and L_{II} phases as a function of pH for the three different buffers.

This inverse cubic-to-inverse hexagonal (Fd3m - H_{II}) transition occurs at pH= 6.0 for citrate and at pH= 5.0 for acetate and phosphate (Fig. 3 A-C). Remarkably the critical pH value is shifted by one pH unit for acetate and phosphate compared to citrate. To demonstrate that the transition from inverse micellar (L_{II}) to inverse hexagonal phase (H_{II}) is a universal characteristic of clinically relevant ionizable lipid we also present the phase behavior of ALC-315/cholesterol and SM-103/cholesterol for all three buffers. We observe that the specific buffer effect on the L_{II}-H_{II} transition follows the trend pH (citrate)>pH (phosphate) = pH (acetate). This behavior can be explained by the common conic lipid shape factor which promotes inverse micellar phases at neutral pH.

Nearest neighbor distance (d_{NN})

The dimensions of the bulk phase are characterized by the nearest neighbor distance (d_{NN}), determined from extracting the lattice constants from SAXS measurements (Table S3). d_{NN} is defined as the smallest distance between neighboring water cores or channels. Significant differences in d_{NN} as a function of pH are seen in Fig. 3D. We observe a general trend of increasing d_{NN} with decreasing pH throughout all lipids and buffers. This general trend is caused by the increasing charge at the ionizable lipid's head group with decreasing pH. As described later in the theoretical section increasing electrostatic repulsion reduces the curvature of the lipid-water interface and causes an increasing lattice spacing. We find two distinct exceptions to this rule in the data. The first exception to this trend is the transition from Fd3m to H_{II} which is accompanied by a reduction of d_{NN}. This discontinuity is due to the packing symmetry of H_{II} in contrast to the face centered cubic Fd3m symmetry. We will come back to the associated energies in the inverse micellar to inverse hexagonal transition in the section on mechanism of the pH transition. The second exception is the anomalous behavior found in case of the HII phases of MC3 in acetate buffer, which appears to shrink with increasing protonation.

Effect of ionic strength and temperature on bulk phase

Charging of the lipid head groups, and consequently the geometric packing parameter of the lipids, is influenced by pH, temperature and salt concentration. In the following we examine these parameters in detail in the case of MC3 lipid. The previous experiments were carried out by using the fixed concentration of 50 mM for all buffers at the different pH values. However, the charge (z) and the concentration (c) ratio between the acidic and the basic component of the buffer depends on pH (Fig. 1 C-D). For instance, at pH 5.5, say, the ionic strength for the different 50 mM buffers is 151 mM for citrate, 52 mM for phosphate, and 42 mM for acetate. To understand if the observed buffer specificity (Fig. 2) could be ascribed to an ionic strength effect of the different 50 mM buffers, SAXS measurements were performed of the LNP bulk phases dialyzed in the presence of citrate and acetate at pH 5.5 and at a defined ionic strength (namely 160, 200, and 300 mM). pH 5.5 was chosen since all buffers showed a clearly ordered structure (Fd3m or H_{II}). Figure S1A shows that, for citrate buffer, the H_{II} is the only phase occurring at pH 5.5 for the three ionic strengths. In the case of acetate (Fig. S1B) Fd3m and H_{II} phases coexist at all ionic strengths, but an increase in ionic strength results in an increase in the signal of the inverse hexagonal structure compared to the Fd3m phase. The results indicate that electrostatic interactions play a role in driving the pH-dependent structural transition. It is known for triethanolamine buffer that an increase of ionic strength results in a shift in the equilibrium of $-NH^+ \Leftrightarrow -N + H^+$ towards the left, corresponding to a shift to higher effective pH (that is lower H^+ activity).[40] Similarly, in our system an increase of ionic strength would enhance the protonation of the MC3 headgroup which would stabilize H_{II} with respect to the Fd3m phase. We also investigated the effect of temperature at 22°C and 37°C under pH 5.5. It is important to examine whether the transitions of the inner bulk phase of LNPs, which we consider the driving mechanism of mRNA transfection, occur in the same pH range observed at lab temperature compared to body temperature. In Fig. S1B, we find the temperature increase favors the phase transition from inverse hexagonal H_{II} to Fd3m + H_{II} in the case of citrate and from Fd3m + H_{II} to Fd3m for acetate. That is, the temperature increase has the opposite effect to an increase in ionic strength (Fig.S1A), tending to stabilize F3dm and shifting the Fd3m-H_{II} transition to lower pH values. The temperature dependence is consistent with the trend we would expect from the van't Hoff equation for the temperature dependence of an acid equilibrium.[41] The $-NH^+ \Leftrightarrow -N + H^+$ equilibrium is pushed towards dissociation at higher temperatures, leaving the MC3 molecule uncharged. This can be interpreted as an equivalent to pushing the system towards the behavior that would be expected at lower pH. In summary, the effect of increasing ionic strength is to favor the inverse hexagonal phase, i.e. shift the phase transition to higher pH values, while that of increasing temperature is to favor the inverse micellar phases, i.e. pushing the phase transition to lower pH.

Mechanism of pH transition and buffer specificity

In the following we discuss the mechanism that drives the pH-dependent L_{II}-H_{II} transition in lipid mesophases. We then ask the question why this mechanism is buffer specific. Transfection efficiency measurements (Fig. 2D) showed a buffer specific effect that follows a (conventional) Hofmeister series, with citrate > phosphate > acetate. In SAXS measurements this ordering is also observed for the pH value of the MC3 bulk phase transitions Fd3m-H_{II}. The bulk phase transitions observed by changing pH and ionic strength involve the MC3 charge, but crucially also involve a change in the curvature and area per MC3 headgroup. The balance between these properties determines the phase transition pH. Then, buffer specificity introduces shifts to that transition pH via specific adsorption of buffer ions at the water-lipid interface (Fig. 4A). The formation of the charge on MC3 at low pH favors the H_{II} phase over the inverse micelle phases of the due to the higher mean curvature of the latter, which gives the inverse micelles phases a larger positive electrostatic energy. But at the same time, the curvature of the interface and area per headgroup affects the L_{II}-H_{II} transition via the elastic bending energy of the lipid layer,[28] favoring the inverse micelle phases over the inverse hexagonal phases.

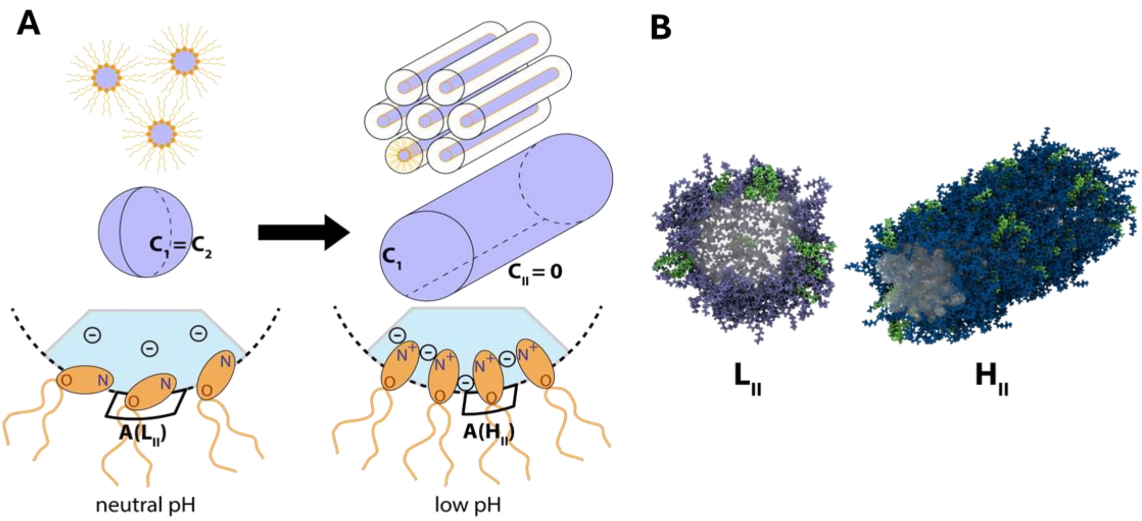

Figure 4. (A) Schematic drawing of lipid conformation and geometric curvature in the inverse micellar (L_{II}) and inverse hexagonal (H_{II}) phase. At low pH, the lipid headgroups become protonated and extend outward, reducing the area per headgroup. (B) Snapshots of MD simulations of the L_{II} and H_{II} phase of the MC3/cholesterol system. The area per lipid obtained from MD simulations are $A(L_{II}) = 0.53$ nm^2 and $A(H_{II}) = 0.45$ nm^2. The protonated and neutral MC3 lipids are represented by dark and light blue colors respectively, cholesterol is green, and water is shown in transparent grey.

In general energy is required if the lipid monolayer bends away from its preferred curvature. The bending energy is characterized by bending moduli κ and κ_G, and may be quantified via a Helfrich bending energy, $E_{bend} = \kappa\,(C_1 + C_2 - C_0)^2/2 + \kappa_G C_1 C_2$, where $C_1 = 1/R_1$ and $C_2 = 1/R_2$ are the curvatures associated with the radii R_1 and R_2 in perpendicular directions along the surface of the lipid layer layer and C_0 is the so-called spontaneous total curvature due to the conical lipid shape. Although spherical inverse micelles with $C_1=C_2$ have lower individual curvatures (larger radii, corresponding to larger d_{NN} values in the case of MC3), the cylinders of the inverse hexagonal phase have a lower total curvature $(C_1 + C_2)$ because of the flat dimension along the axis of the cylinders with $C_2 = 0$ (see also cartoon in Fig. 4A). Protonation of the ionizable lipid head group will decrease the spontaneous curvature and drive the system from L_{II} into the H_{II} phase. The exact transition point depends on the ratio κ_G/κ, i.e. the contribution of gaussian curvature and mean curvature to the total bending energy.[42,43] The electrostatic energy due to headgroup charge favors formation of the inverse hexagonal phase at low pH, while the higher spontaneous curvature favors formation of the inverse micelle phases at high pH. The balance between the two explains the broad trend of the MC3 phase transitions, with the transition point lying at a pH close to the MC3 pK_a inside the LNPs of 6.44.[44]

To explain the buffer specific order observed for bulk phase transitions, we propose a mechanism of specific ion adsorption with a consequent buffer-specific change in the area per headgroup. As illustrated in Fig. 4A, we identify near (charged N group) and far (O ester group) moieties within the headgroup. The N-moiety remains in contact with the aqueous phase whereas the O-moiety may not be in contact, depending on the headgroup orientation (Fig. 4A). The strength of interactions of buffer ions with the lipid surface, including the N-moiety, follows the conventional series citrate > phosphate > acetate, confirmed by our MD simulations (Fig. 5B). On the other hand, MD simulations (Fig. 5C), and evaluation of London dispersion coefficients of ions (Table S4) with the O-moiety, suggest that adsorption at the O-moiety would be stronger for acetate than other buffer ions. Adsorption of acetate at the O-moiety requires the ion to penetrate deeper into the lipid phase and therefore is expected to lead to an increase in the area per headgroup. In this way, acetate stabilizes L_{II}, consistent with SAXS data. At the same time, adsorption of negatively charged ions at the N-moiety is expected to reduce the repulsion between the positively charged MC3 headgroup and will therefore reduce the area per headgroup at low pH. Consequently, citrate anions with preferred adsorption at the (positively charged) N-moiety (Fig. 5B and Table 1) decrease the area per head group, increasing the bending modulus and shifting the Fd3m-HII transition to a higher pH by stabilizing H_{II}. Acetate ions with preferred adsorption at the O-moiety, likely involving London dispersion forces, increase the area per head group, decreasing the bending modulus and shifting the Fd3m-H_{II} transition to a lower pH by stabilizing Fd3m. This mechanism, involving two types of specific interactions between the buffer ions and the lipid headgroups, in particular with the positively charged N-moiety (via electrostatic interactions) and the neutral O-moiety (via nonelectrostatic dispersion forces) is in agreement with the results obtained by investigating the effect of ionic strength. Indeed, results in Fig. S1, showing different SAXS patterns for the same ionic strengths obtained with citrate and acetate, confirm the occurrence of different mechanisms for the two buffers. The inverse hexagonal HII phase observed for citrate at the three investigated ionic strengths suggests its preferential interaction with the positively charged MC3 headgroups. Contrarily, the coexisting Fd3m and H_{II} phases, observed for acetate at the three ionic strengths, are consistent with a partial stabilization of the neutral form of MC3 headgroup. In short, we can identify a direct buffer effect mediated via electrostatics and ion dispersion interactions, and an indirect effect via a consequent change in the area per head group.

All-atom MD simulations of interactions between buffer ions and MC3

To provide evidence of our hypothesis of specific ion adsorption at the lipid/water interface, we performed all-atom MD simulations in explicit water. To ensure the correct protonation degree of the ionizable MC3 lipid, we chose a MC3/POPC monolayer system (Fig. 5A) for which the area per lipid and protonation degree at pH 5.0 and 7.5 were determined consistently in previous work.[45] In the simulations, citrate buffer was represented by the trivalent citrate ion, phosphate buffer by HPO_4^{2-}, and acetate buffer by the monovalent acetate ion. The affinity of the ions in terms of the probability distribution perpendicular to the lipid/water interface at pH 5.0 and 7.5 is shown in Fig. 5B, C. The main adsorption peak at $z = 0$ nm corresponds to the interactions of the ions with the nitrogen moiety and follows a conventional Hofmeister ordering: citrate > phosphate > acetate. A second minor adsorption peak at $z = -2$ nm appears for acetate and corresponds to the interaction with the oxygen moiety. This peak is absent for the other ions and significantly smaller compared to the main adsorption peak. Further insights into the adsorption behavior at the interface can be gained from the local radial ion distributions $g(r)$ of the around the charged and uncharged MC3 molecules. Fig. 5D, E shows $g(r)$ for the buffer ions around the N and O-moieties (O1 representing the carbonyl O-moiety and O2 representing the ester O-moiety). For neutral MC3, the distributions at N- and O-moieties are similar (Fig. 5D).

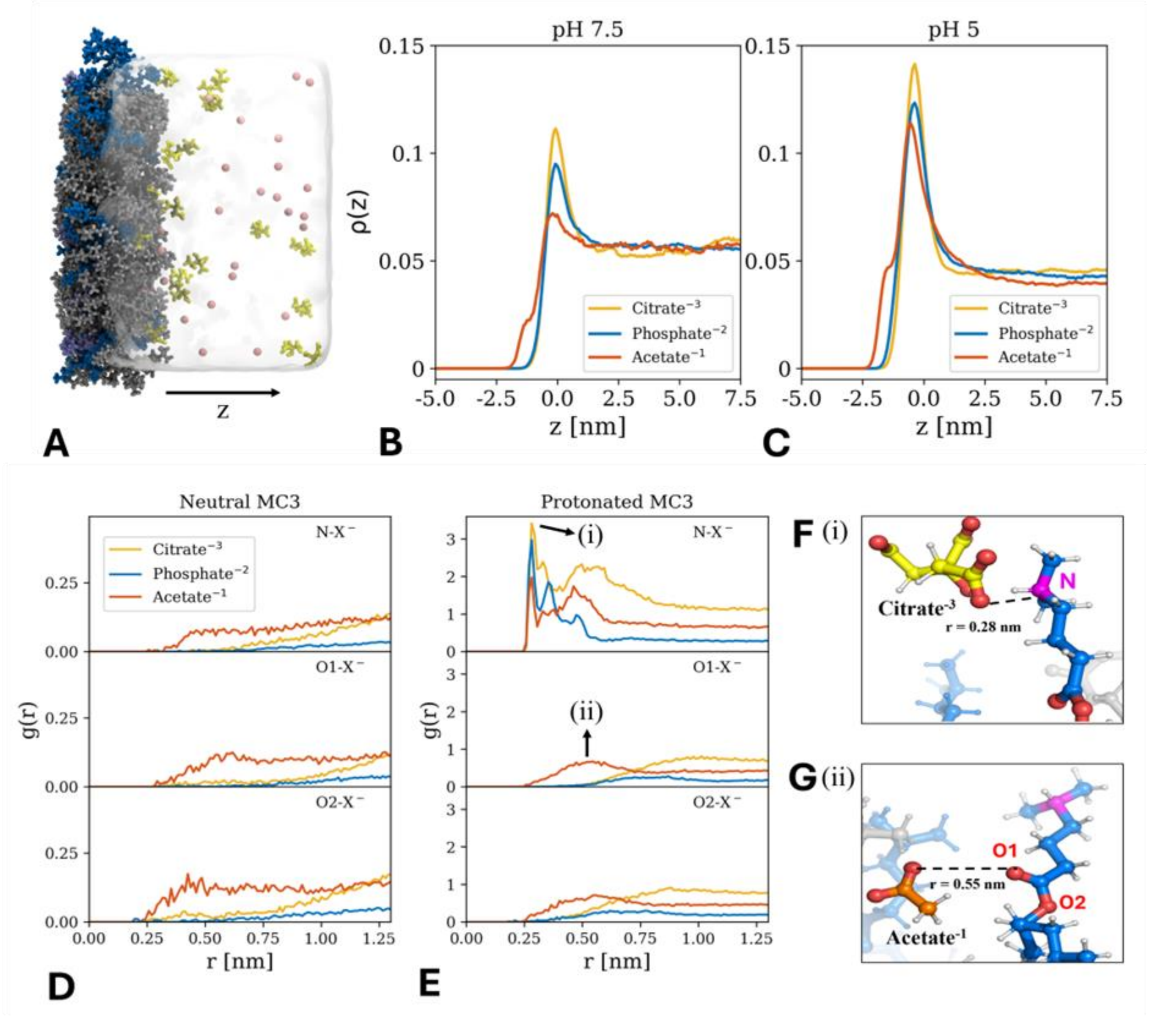

Figure 5. (A) Simulation snapshot of the lipid/water interface of the monolayer system at pH 5. Charged and uncharged MC3 lipids are shown in dark and light blue, respectively. POPC is shown in gray, citrate ions in yellow and sodium in pink. (B, C) Normalized probability distributions of the buffer ions for pH 7.5 and pH 5 along the z axis (perpendicular to the interface as indicated in A). (D, E) Radial distribution function g(r) of the different buffer ions around the nitrogen (N) and oxygen (O1, O2) atoms of an uncharged or charged MC3 molecule in the monolayer at pH 5. (F, G) Selected simulation snapshot of citrate and acetate at distances indicated by the arrows in panel E.

For charged MC3 (Fig. 5E), pronounced differences between the ions and the different binding sites can be observed. The results show that citrate ions have a higher affinity toward the N-atom in positively charged MC3 compared to the other buffer ions (as indicated by the highest peak in $g(r)$ at a radial distance $r = 0.28$ nm in Fig. 5E, top). Phosphate ions have the second highest affinity for the N-moiety followed by acetate. In the case of O-moieties, only acetate ions adsorb while citrate and phosphate are depleted (Fig. 5E, bottom). The simulation snapshots reveal that citrate ions are located at the lipid/water interface while the acetate ions penetrate deeper into the lipid phase (Fig. 5 F,G). In summary, the affinity of buffer ions toward a lipid layer containing MC3 follows the Hofmeister series: citrate > phosphate > acetate. However, the local distribution of the ions is much more complex. The adsorption of acetate and depletion of phosphate and citrate at the oxygen are likely the cause of ion specific buffer effects.

CONCLUSIONS

In this work mRNA-LNPs were prepared in three buffers, citrate, phosphate, and acetate. Transfection efficiency showed a dependence on the preparation buffer employed, in the order citrate > phosphate > acetate for all three ionizable lipids investigated. To rationalize the buffer-specific efficiency we recall that the core phase of LNPs exhibits a dense ordered lipid phase, which is predominantly formed by cationic ionizable lipid MC3 together with cholesterol and hence is pH responsive. Note that DSPC and PEG-lipid are unlikely to partition into inverse phases. To explore the effect of buffer on pH response, we studied ionizable lipid-cholesterol bulk mesophases as core phase mimicking systems using SAXS synchrotron measurements. We find that the critical phase transition from inverse micellar to inverse hexagonal, specifically Fd3m-HII in case of MC3 and LII -HII in case of SM-102 and ALC-315, is dependent on the buffer in the order citrate > phosphate ~ acetate. In case of MC3 lipid the pH value of the transition shifts by 1 pH unit in citrate (6.5-5.5) compared to acetate (5.5-4.5). In earlier work it was hypothesized that an analog structural transition occurs in the excess lipid regions inside LNPs and plays a critical role in the pH-dependent endosomal fusion process.[8,14] The hypothesis, that the structural transition of the LNP core induces endosomal fusion, is plausible as the inverse micellar-to inverse hexagonal transition causes defects destabilizing the surface monolayer of LNPs. A second mechanism associated with the pH-dependent structural transition involves the accumulation of the protonated ionizable lipid in the surface layer of LNPs at low pH. The resulting cationic surface charge consequently enhances the likelihood of endosomal fusion. A central question in our study is whether a theoretical explanation exists for the shift in the pH value of the Fd3m-H_{II} transition as a function of the specific buffer used. We propose that competition of elastic bending energy and charging of the ionizable lipid head group leads to the predicted shift. A surprising insight was that the protonated MC3 lipid exhibits a smaller headgroup area due to a conformational change in the headgroup as seen by MD simulations. The dependence of the phase transition on the buffer is explained by specific ion adsorption at the nitrogen (N) and oxygen (O) moieties of the ionizable lipid, with a consequent change in the area per headgroup. This view is consistent with the finding that increasing the ionic strength stabilizes the H_{II} phase, likely favoring an even smaller headgroup area. By contrast, increasing the temperature to 37°C stabilizes the Fd3m phase due to a decrease in the pK_a of MC3, which favors the neutral lipid species, pushing the phase transitions toward lower pH. There is scope for further work to confirm our interpretation that the area per headgroup varies with buffer ion adsorption. It seems likely that acetate adsorption at the O-moiety, with an associated increase in area per headgroup, is responsible for the swelling trend observed in the H_{II} phase with the nearest neighbor distance (d_{NN}) increasing with pH, while decreasing in the case of citrate and phosphate buffers.

The proposed mechanism presents a consistent structure-activity relation. The key assumption is that a pH dependent structural transition in the excess lipid regions of the LNP core phase leads to endosomal fusion. For the argument to be conclusive we must assume that the buffer ions used in the preparation of LNPs remain inside the LNPs and are not diluting out. A correlation of transfection efficiency and bulk phase transition has been demonstrated here for three ionizable lipids: MC3, SM-102 and ALC-315. To what extent the structure-activity relation can be extended to other ionizable lipids remains to be determined. In recent work it has been shown that the two mainstream COVID-19 vaccine ionizable ALC-315 and SM-102 lipids, show the same order of core phase changes as presented here.[8] The proposed mechanism involves a direct buffer effect via specific adsorption of buffers, but also an indirect effect via changes in the area per lipid headgroup consequent to buffer adsorption. In the case of MC3, a crucial finding is the role of buffer (acetate) adsorption at the O-moiety of the headgroup, distinct from interactions with the N-moiety carrying the headgroup charge. This suggests an avenue for engineering LNP behavior, manipulating the transition pH by functionalization of the headgroup beyond simply its ionizable character. Consistent with the notion of the lipid packing parameter,[11,39] controlling the area per headgroup, and thereby the strength of the lipid layer bending energy, is key to controlling the transition. To achieve rational design strategies to exploit the described buffer specific effects theoretical models are required that explain the specific ion adsorption mechanism using MD simulation as well as an elastic continuum description of the mesophases. The consistent buffer specific effects on LNP behavior demonstrate that understanding ionizable lipid mesophase transitions is useful for rationalizing mRNA transfection efficiencies and further advancement of lipid formulations for gene therapy.

METHODS

Materials

DLin-MC3-DMA(O-(Z,Z,Z,Z-heptatriaconta-6,9,26,29-tetraem-19-yl)-4-(N,N-dimethylamino) butanoate; (MC3, 99 %), ALC-315 ([(4-hydroxybutyl)azanediyl]di(hexane-6,1-diyl) bis(2-hexyldecanoate)) and SM-102 (9-Heptadecanyl 8-{(2-hydroxyethyl)[6-oxo-6-(undecyloxy)hexyl]amino}octanoate) were purchased by MedChemExpress. 1,2-distearoyl-sn-glycero-3-phosphocholine, (DSPC, 99%), 1,2-distearoyl-sn-glycero-3-phosphoethanolamine-N-[amino(polyethylene glycol) (DSPE-PEG2000, 99%), cholesterol, sodium citrate dihydrate (99 %), citric acid (99 %), monobasic sodium phosphate (99 %), disodium hydrogen phosphate (99 %), hydrochloric acid (37 %), sodium hydroxide (97 %), sodium acetate (99 %), acetic acid (99.8 %), and citric acid (99.5 %) were purchased by Avanti Polar lipid Sigma Aldrich.

Preparation of eGFP-mRNA LNPs

ARCA eGFP (Enhanced Green Fluorescent Protein) mRNA (APExBIO) was encapsulated in an LNP of four lipid components (DLin-MC3-DMA, DSPC, Cholesterol, DMPE-PEG2000) in a 50:10:38.5:1.5 molar ratio. mRNA and buffer (pH 3) were prepared in aqueous solution (0.075 mg/mL) while the lipid components (1.11 mg/mL MC3, 0.27 mg/mL DSPC, 0.52 mg/mL cholesterol, 0.15 mg/mL DSPE-PEG2k) were dissolved in ethanol. Concentrations were chosen to reach a final LNP concentration of 0.05 mg/mL mRNA concentration with an N/P ratio of 4 and a final buffer concentration of 50 mM. Microfluidic mixing was carried out with the NanoAssemblr^{TM} Spark^{TM} (Precision NanoSystems) at a volume ratio of aqueous:organic 2:1 ratio. Following mixing, LNPs were incubated 20 min at room temperature. To remove residual ethanol and buffers from the solution, LNPs were transferred to Slide-A-Lyzer™ MINI dialysis cups 3.5 kDa molecular weight cut-off (ThermoFisher Scientific) and dialysed into water for 18 h at room temperature. Size distribution was measured using a DynaPro® NanoStar™ (Wyatt) DLS device. Encapsulation efficiency was assessed using the Quant-it^{TM} RiboGreen RNA dye (Invitrogen).

LNPs transfection efficiency

Cells were cultured in RPMI 1640 Medium (ThermoFisher Scientific) supplemented with 10% (v/v) FBS (Fetal bovine Serum, ThermoFisher Scientific, #10270106), 5 mM HEPES (GibcoTM, Thermofisher Scientific, #15630080) and 1mM Na-Pyruvate (GibcoTM, Thermofisher Scientific, #11360070) at 37°C, 5% CO_2. For live-cell imaging, microstructures were prepared to allow single-cell culture. Therefore, 6-channel µ-slides (ibidi) coated with cell-repellent PVA were treated with PLPP N-(4-[benzoyl]benzyl)-N,N,N-triethylammonium bromide) (enamine) in an agarose and calcium peroxide solution and selectively illuminated with UV-light (365 nm). Selective illumination was facilitated with a photomask patterned with 20 × 20µm squares and a 80µm spacer. After illumination, the channels were rinsed with water and 0.5M HCl. The resulting squares were coated with laminin by incubation in a 20µg/mL laminin (BioLamina) working solution in PBS for 1h at 37°C.

Application of cells in medium for 1h led to self-assembly in a single cell pattern as depicted in Fig. 2A. eGFP-mRNA-LNPs were diluted in RPMI medium supplemented with FCS to a final concentration of 1ng/µL and incubated for 1h at room temperature to allow formation of a protein corona. Subsequently, LNP solution was applied for 1h and washed afterwards with L15-medium without phenol red (ThermoFisher Scientific). Cells were transferred to the microscope (Nikon TI Eclipse) and imaged over 30h with image acquisition every 10 min. Image analysis was then performed using our in-house python-based software including segmentation and background correction based on Schwarzfischer et al.[46] to generate fluorescence trajectories.

Bulk phase preparation: dialysis steps

MC3/cholesterol bulk phases were prepared at a range of pH conditions via three dialysis steps. First, the MC3 and cholesterol were dissolved in ethanol and mixed in a molar ratio of 3:1 (MC3: cholesterol) to a total lipid concentration of 56.1 mg/mL (MC3 46.7 mg/mL and cholesterol 9.4 mg/mL). The mixture was put into a dialysis cup with a molecular weight cut off of 3.5 kDa. Samples were first dialyzed against a 50 mM citrate buffer (pH 3) containing ethanol (at a volume ratio of 3:1, buffer: ethanol) for 48 hours. In the second dialysis step, the sample was dialyzed against PBS (1 mM KH_2PO_4, 155 mM NaCl, 3 mM Na_2HPO_4 0.7 H_2O, pH 7.4) for 48 hours. In the third step, the sample was dialyzed against NaCl 150 mM and the buffer of choice (citrate, acetate or phosphate 50 mM at pH 3.5, 4.0, 4.5, 5.0, 5.5, 6.0, 6.5, 7.0) with the required final pH for 48 hours. The samples at different ionic strengths (I) were prepared at different acetate, phosphate and citrate concentrations to reach I= 160 mM, I=200 mM, I=300 mM including the background salt NaCl 150 mM. The supernatant was removed from the cup and the solid precipitates were extracted for characterization by SAXS.

SAXS measurements

Synchrotron small-angle X-ray scattering (SAXS) was carried out at the P12 EMBL BioSAXS and P62 SAXSMAT beamlines, PETRA III, DESY (Hamburg, Germany). The beamline instrumentation has been described previously.[47,48] Further SAXS experiments were performed using an internal instrument at LMU. The crystallographic space groups of the liquid crystalline phases were determined from relative peak positions. All the measurements at P12 and P62 were performed in quartz capillaries. The scattering data background was subtracted by measuring empty capillaries.

Calculation of nearest neighbor distance d_{NN}

The nearest neighbor distance was calculated for each mesophase using the peak positions with as their respective miller indices following the formula shown in Table S2 and S3 (see Supporting information).[14]

All-atom molecular dynamics simulations

Ion specific adsorption simulation setup: To investigate the adsorption of acetate, phosphate and citrate at the lipid/water interface, we used a monolayer setup. The lipid monolayer contained MC3 and POPC lipids in a 1:4 molar ratio and was constructed using the Men-Gen web server[49] following the published procedure of our previous work.[45] Each leaflet of the monolayer contained 200 lipids, separated by a water column of approximately 15 nm. The reason for choosing this setup was that the protonation degree at two pH values was determined consistently from a combination of simulations and scattering experiments.[45] This was crucial since the protonation degree is inherently difficult to predict since it depends on the local lipid environment and is not directly accessible from experiments. Specifically, the lipid monolayer at pH 5 has a protonation degree of 67.5% ionizable MC3. At pH 7.5 the protonation degree is 14.5%. Both values significantly deviate from simple theoretical predictions. For each pH value, the monolayers were simulated at a buffer concentration of 50 mM. Sodium acetate (CH_3COONa), sodium phosphate (Na_2HPO_4), and sodium citrate ($Na_3C_6H_5O_7$) were used as in the experiments. Thus, a total of six simulations of the lipid monolayer were performed, covering two pH levels and three different buffers. Each simulation was repeated three times to improve the sampling statics.

The AMBER Lipid 17 force field was used to describe the POPC lipids. For the cationic and neutral MC3 molecules, we used recently developed force fields, which closely reproduce the experimental structure of lipid layers and are compatible with the AMBER force field family.[50] The TIP3P water model[51] along with Mamatkulov–Schwierz[52] force field parameters for Na^+ ions were also used. The citrate ion was described using the force field parameters obtained from Wright[53] while the acetate and phosphate ion force field parameters were obtained from Kashefolgheta.[54] The combination rule for the anion-cation interactions were modified to avoid crystallization artifacts. The resulting force field parameters are available at "*(https://git.rz.uni-augsburg.de/cbio-gitpub/force-fields-buffer-ions).*"

All-atom molecular dynamic simulations were performed using the GROMACS[55] package (v-2024). A gradient descent algorithm was used to minimize the energy of the system. The simulations were performed in the NVT ensemble to ensure the correct area per lipid.[50] The temperature was maintained at 293.15 K using the velocity rescale thermostat with a time constant of 1.0 ps. The Lennard-Jones potential was cut off and shifted to zero at 1.2 nm. Short-ranged electrostatic interactions were cut-off at 1.2 nm and the Particle Mesh Ewald (PME) method was used to evaluate long-range electrostatics. Hydrogen bonds were constrained using the LINCS algorithm and a time step of 2 fs was used. Each production run was performed for 70 ns. The first 20 ns of the simulation were discarded to account for equilibration and the rest of the trajectory was analyzed using GROMACS inbuilt modules and MDAnalysis.[56] The trajectories were visualized, and snapshots were generated using visual molecular dynamics (VMD).[57]

Area per headgroup of H_{II} and L_{II} phases: to obtain the area per headgroup, we used data from our previous work,[14] where we simulated the inverse hexagonal (H_{II}) and inverse micellar (L_{II}) phases. The H_{II} phase consisted of fully protonated Dlin-MC3-DMA (MC3) lipids combined with cholesterol in a 3:1 molar ratio, maintaining a water-to-lipid ratio (n_w) of 12 to match the experimental lattice spacing of 60 Å. The L_{II} phase consisted of fully uncharged MC3 lipids using also $n_w = 12$. Details on the calculation of the area per headgroup are provided in the supporting information.

AUTHOR INFORMATION

Corresponding Authors

*Prof. Joachim Radler, raedler@lmu.de

*Prof. Drew Parsons, drew.parsons@unica.it

Author Contributions

C.C.: Conceptualization; Formal analysis; Data curation; Investigation; Methodology; SAXS measurements; SAXS data acquisition; Validation; Visualization; Writing - original draft; Writing - review & editing. **J.P.**: Formal analysis; Data curation; Investigation; Methodology; SAXS measurements; SAXS data acquisition; Validation; Visualization; Writing - original draft. **J.M.**: Formal analysis; Data curation; Methodology; Investigation; Writing - review & editing. **Ak.Su**.: Validation; Formal analysis; Software; Methodology **E.K.** SAXS data acquisition; Validation; Visualization **C.E.B.** SAXS data acquisition **N.S.**: Validation; Formal analysis; Software; Methodology **D.F.P.**: Conceptualization; Formal analysis; Software; Investigation; Validation; Visualization; Writing - original draft, Writing - review & editing; Supervision. **A.S.**: Conceptualization; Formal analysis; Investigation; Methodology; Validation; Visualization; Funding acquisition; Writing - original draft, Writing - review & editing; Supervision. **J.R.**: Conceptualization; Formal analysis; Investigation; Methodology; Validation; Visualization; Resources; Funding acquisition; Writing - original draft, Writing - review & editing; Supervision.

The manuscript was written through contributions of all authors. All authors have given approval to the final version of the manuscript. ‡ CC and ‡ JP contributed equally to the work.

Notes

The authors declare no competing financial interest.

ASSOCIATED CONTENT

Supporting information

The following data are present in supporting information: SAXS measurements of the ionic strength and temperature effects in the presence of buffer citrate and acetate, DLS data of LNPs, Miller indices of the measured lipid phases together with formula of the lattice parameter, SAXS measurements of mesophase of MC3-cholesterol, ALC-315-cholesterol, SM-102-cholesterol samples with Miller indices in buffer citrate, phosphate and acetate, d_{NN} values for H_{II} and L_{II} phases for ALC-315-cholesterol and SM-102- cholesterol samples as a function of pH for buffer citrate, phosphate and acetate, Molecular simulations methods including adjustment of combination rules for the force field parameters, force field parameters, and calculation of area per lipid. London dispersion coefficients of buffer ions in water and in non-polar media (doc).

Content submitted to pre-print server bioRxiv, Authors: Cristina Carucci, Julian Philipp, Judith A. Müller Akhil Sudarsan, Ekaterina Kostyurina, Clement E. Blanchet, Nadine Schwierz, Drew F. Parsons, Andrea Salis, Joachim O. Rädler. Title: Buffer specificity of ionizable lipid nanoparticle transfection efficiency and bulk phase transition. 2025, DOI: 10.1101/2025.01.17.63350. Repository: bioRxiv, the preprint service for biology. https://doi.org/10.1101/2025.01.17.633509 (version accessed January 21, 2025).

ACKNOWLEDGMENT

C.C. thanks Mobilità Giovani Ricercatori (MGR) 2023 project from University of Cagliari (UniCA) and MIUR (PON-AIM Azione I.2–DD n. 407-27.02.2018, AIM1890410-2). AS thanks the Italian Center for Colloid and Surface Science (CSGI) and Fondazione di Sardegna - FdS 2022 (F73C23001600007) for financial support. NS thanks Ana Vila Verde for sharing the force field parameters, help on the partial charges and fruitful discussions. Deutsches Elektronen-Synchrotron (DESY) P12 BioSAXS EMBL and P62 SAXSMAT beamlines at PETRA III (Hamburg, Germany) and the beamline scientists Clement E. Blanchet and Xiao Sun are greatly acknowledged for synchrotron beamtime under the project's proposal SAXS-1247 and SAXS-1261. JR and NS were supported by the German Federal Ministry of Education and Research through BMBF Project 05K18WMA and 05K18EZA within the framework of the Swedish German research collaboration Röntgen-Ångström Cluster. DFP acknowledges financial support under the National Recovery and Resilience Plan (NRRP), Mission 4, Component 2, Investment 1.1, Call for tender No. 1409 published on 14.9.2022 by the Italian Ministry of University and Research (MUR), funded by the European Union – Next GenerationEU– Project Title Structure and flow dynamics of Concentrated AMphiphilic BIOmolecules (CAmBio): driving the change to eco-sustainable surfactant formulations – CUP F53D23008790001- Grant Assignment Decree No. n. 1386 adopted on 01/09/2023 by the Italian Ministry of Ministry of University and Research (MUR). We also acknowledge the CINECA award under the ISCRA initiative, for the availability of high-performance computing resources and support. The authors gratefully acknowledge the scientific support and HPC resources provided by the Erlangen National High Performance Computing Center (NHR@FAU) of the Friedrich-Alexander-Universität Erlangen-Nürnberg (FAU) under the NHR project b119ee.

REFERENCES

(1) Semple, S. C.; Leone, R.; Barbosa, C. J.; Tam, Y. K.; Lin, P. J. C. Lipid Nanoparticle Delivery Systems to Enable mRNA-Based Therapeutics. *Pharmaceutics* **2022**, *14* , 398.

(2) Sahin, U.; Karikó, K.; Türeci, Ö. mRNA-Based Therapeutics — Developing a New Class of Drugs. *Nat. Rev. Drug Discov.* **2014**, *13* , 759–780.

(3) Yin, H.; Kanasty, R. L.; Eltoukhy, A. A.; Vegas, A. J.; Dorkin, J. R.; Anderson, D. G. Non-Viral Vectors for Gene-Based Therapy. *Nat. Rev. Genet.* **2014**, *15* , 541–555.

(4) Paramasivam, P.; Franke, C.; Stöter, M.; Höijer, A.; Bartesaghi, S.; Sabirsh, A.; Lindfors, L.; Yanez Arteta, M.; Dahlén, A.; Bak, A.; Andersson, S.; Kalaidzidis, Y.; Bickle, M.; Zerial, M. Endosomal Escape of Delivered mRNA from Endosomal Recycling Tubules Visualized at the Nanoscale. *J. Cell Biol.* **2022**, *221*.

(5) Hu, Y.-B.; Dammer, E. B.; Ren, R.-J.; Wang, G. The Endosomal-Lysosomal System: From Acidification and Cargo Sorting to Neurodegeneration. *Transl. Neurodegener.* **2015**, *4*, 18.

(6) Koltover, I.; Salditt, T.; Rädler, J. O.; Safinya, C. R. An Inverted Hexagonal Phase of Cationic Liposome-DNA Complexes Related to DNA Release and Delivery. *Science,* **1998**, *281*, 78–81.

(7) Cheng, M. H. Y.; Leung, J.; Zhang, Y.; Strong, C.; Basha, G.; Momeni, A.; Chen, Y.; Jan, E.; Abdolahzadeh, A.; Wang, X.; Kulkarni, J. A.; Witzigmann, D.; Cullis, P. R. Induction of Bleb Structures in Lipid Nanoparticle Formulations of mRNA Leads to Improved Transfection Potency. *Adv. Mater.* **2023**, *35*, 1–11.

(8) Yu, H.; Angelova, A.; Angelov, B.; Dyett, B.; Matthews, L.; Zhang, Y.; El Mohamad, M.; Cai, X.; Valimehr, S.; Drummond, C. J.; Zhai, J. Real-Time pH-Dependent Self-Assembly of Ionisable Lipids from COVID-19 Vaccines and In Situ Nucleic Acid Complexation. *Angew. Chemie Int. Ed.* **2023**, *62* .

(9) Yanez Arteta, M.; Kjellman, T.; Bartesaghi, S.; Wallin, S.; Wu, X.; Kvist, A. J.; Dabkowska, A.; Székely, N.; Radulescu, A.; Bergenholtz, J.; Lindfors, L. Successful Reprogramming of Cellular Protein Production through mRNA Delivered by Functionalized Lipid Nanoparticles. *Proc. Natl. Acad. Sci.* **2018**, *115* , 3351–3360.

(10) Uebbing, L.; Ziller, A.; Siewert, C.; Schroer, M. A.; Blanchet, C. E.; Svergun, D. I.; Ramishetti, S.; Peer, D.; Sahin, U.; Haas, H.; Langguth, P. Investigation of PH-Responsiveness inside Lipid Nanoparticles for Parenteral mRNA Application Using Small-Angle X-Ray Scattering. *Langmuir* **2020**, *36*, 13331–13341.

(11) Seddon, J. M.; Templer, R. H. Polymorphism of Lipid-Water Systems. In *Handbook of Biological Physics*, Lipowsky R., Sackmann E., Eds.; Elsevier: North-Holland, 1995; pp 97–160.

(12) Kulkarni, C. V. Calculating the 'Chain Splay' of Amphiphilic Molecules: Towards Quantifying the Molecular Shapes. *Chem. Phys. Lipids* **2019**, *218*, 16–21.

(13) Xu, Z.; Seddon, J. M.; Beales, P. A.; Rappolt, M.; Tyler, A. I. I. Breaking Isolation to Form New Networks: pH-Triggered Changes in Connectivity inside Lipid Nanoparticles. *J. Am. Chem. Soc.* **2021**, *143*, 16556–16565.

(14) Philipp, J.; Dabkowska, A.; Reiser, A.; Frank, K.; Krzysztoń, R.; Brummer, C.; Nickel, B.; Blanchet, C. E.; Sudarsan, A.; Ibrahim, M.; Johansson, S.; Skantze, P.; Skantze, U.; Östman, S.; Johansson, M.; Henderson, N.; Elvevold, K.; Smedsrød, B.; Schwierz, N.; Lindfors, L.; Rädler, J. O. pH-Dependent Structural Transitions in Cationic Ionizable Lipid Mesophases Are Critical for Lipid Nanoparticle Function. *Proc. Natl. Acad. Sci.* **2023**, *120*, 2017.

(15) Salis, A.; Monduzzi, M. Not Only pH. Specific Buffer Effects in Biological Systems. *Curr. Opin. Colloid Interface Sci.* **2016**, *23*, 1–9.

(16) Kim, H.-K.; Tuite, E.; Nordén, B.; Ninham, B. W. Co-Ion Dependence of DNA Nuclease Activity Suggests Hydrophobic Cavitation as a Potential Source of Activation Energy. *Eur. Phys. J. E* **2001**, *4*, 411–417.

(17) Medda, L.; Salis, A.; Magner, E. Specific Ion Effects on the Electrochemical Properties of Cytochrome C. *Phys. Chem. Chem. Phys.* **2012**, *14*, 2875–2883.

(18) Cugia, F.; Sedda, S.; Pitzalis, F.; Parsons, D. F.; Monduzzi, M.; Salis, A. Are Specific Buffer Effects the New Frontier of Hofmeister Phenomena? Insights from Lysozyme Adsorption on Ordered Mesoporous Silica. *RSC Adv.* **2016**, *6*, 94617–94621.

(19) Salis, A.; Cappai, L.; Carucci, C.; Parsons, D. F.; Monduzzi, M. Specific Buffer Effects on the Intermolecular Interactions among Protein Molecules at Physiological pH. *J. Phys. Chem. Lett.* **2020**, *11* , 6805–6811.

(20) Mura, M.; Carucci, C.; Marincola, F. C.; Monduzzi, M.; Parsons, D. F.; Salis, A. The Melting Curves of Calf Thymus-DNA Are Buffer Specific. *J. Colloid Interface Sci.* **2023**, *630*, 193–201.

(21) Mura, M.; Humphreys, B.; Gilbert, J.; Salis, A.; Nylander, T. Cation and Buffer Specific Effects on the DNA-Lipid Interaction. *Colloids Surfaces B Biointerfaces* **2023**, *223*, 113187.

(22) Mura, M.; Carucci, C.; Caddeo, E.; Sovová, Š.; Piludu, M.; Pekař, M.; Jachimska, B.; Parsons, D. F.; Salis, A. Specific Buffer Effects on the Formation of BSA Protein Corona around Amino-Functionalized Mesoporous Silica Nanoparticles. *J. Colloid Interface Sci.* **2025**, *677*, 540–547.

(23) Lo Nostro, P.; Ninham, B. W. Hofmeister Phenomena: An Update on Ion Specificity in Biology. *Chem. Rev.* **2012**, *112*, 2286–2322.

(24) Collins, K. D. Charge Density-Dependent Strength of Hydration and Biological Structure. *Biophys. J.* **1997**, *72*, 65–76.

(25) Collins, K. D. The Behavior of Ions in Water Is Controlled by Their Water Affinity. *Q. Rev. Biophys.* **2019**, *52*, 11.

(26) Jones, G.; Dole, M. The Viscosity of Aqueous Solutions of Strong Electrolytes with Special Reference to Barium Chloride. *J. Am. Chem. Soc.* **1929**, *51*, 2950–2964.

(27) Boström, M.; Parsons, D. F.; Salis, A.; Ninham, B. W.; Monduzzi, M. Possible Origin of the Inverse and Direct Hofmeister Series for Lysozyme at Low and High Salt Concentrations. *Langmuir* **2011**, *27*, 9504–9511.

(28) Parsons, D. F.; Carucci, C.; Salis, A. Buffer-Specific Effects Arise from Ionic Dispersion Forces. *Phys. Chem. Chem. Phys.* **2022**, *24*, 6544–6551.

(29) Meulewaeter, S.; Nuytten, G.; Cheng, M. H. Y.; De Smedt, S. C.; Cullis, P. R.; De Beer, T.; Lentacker, I.; Verbeke, R. Continuous Freeze-Drying of Messenger RNA Lipid Nanoparticles Enables Storage at Higher Temperatures. *J. Control. Release* **2023**, *357*, 149–160.

(30) Binici, B.; Borah, A.; Watts, J. A.; McLoughlin, D.; Perrie, Y. The Influence of Citrate Buffer Molarity on mRNA-LNPs: Exploring Factors beyond General Critical Quality Attributes. *Int. J. Pharm.* **2025**, *668*, 124942.

(31) Cheng, F.; Wang, Y.; Bai, Y.; Liang, Z.; Mao, Q.; Liu, D.; Wu, X.; Xu, M. Research Advances on the Stability of mRNA Vaccines. *Viruses* **2023**, *15*, 668.

(32) Carrasco, M. J.; Alishetty, S.; Alameh, M.-G. G.; Said, H.; Wright, L.; Paige, M.; Soliman, O.; Weissman, D.; Cleveland, T. E.; Grishaev, A.; Buschmann, M. D. Ionization and Structural Properties of mRNA Lipid Nanoparticles Influence Expression in Intramuscular and Intravascular Administration. *Commun. Biol.* **2021**, *4*, 956.

(33) McKenzie, R. E.; Minnell, J. J.; Ganley, M.; Painter, G. F.; Draper, S. L. mRNA Synthesis and Encapsulation in Ionizable Lipid Nanoparticles. *Curr. Protoc.* **2023**, *3,* 898.

(34) Li, S.; Hu, Y.; Li, A.; Lin, J.; Hsieh, K.; Schneiderman, Z.; Zhang, P.; Zhu, Y.; Qiu, C.; Kokkoli, E.; Wang, T.-H.; Mao, H.-Q. Payload Distribution and Capacity of mRNA Lipid Nanoparticles. *Nat. Commun.* **2022**, *13*, 5561.

(35) Reiser, A.; Woschée, D.; Kempe, S. M.; Rädler, J. O. Live-Cell Imaging of Single-Cell Arrays (LISCA) - a Versatile Technique to Quantify Cellular Kinetics. *J. Vis. Exp.* **2021**, No. 169.

(36) Reiser, A.; Woschée, D.; Mehrotra, N.; Krzysztoń, R.; Strey, H. H.; Rädler, J. O. Correlation of mRNA Delivery Timing and Protein Expression in Lipid-Based Transfection. *Integr. Biol. (Camb).* **2019**, *11*, 362–371.

(37) Shearman, G. C.; Tyler, A. I. I.; Brooks, N. J.; Templer, R. H.; Ces, O.; Law, R. V.; Seddon, J. M. A 3-D Hexagonal Inverse Micellar Lyotropic Phase. *J. Am. Chem. Soc.* **2009**, *131* (5), 1678–1679.

(38) Zeng, X.; Liu, Y.; Impéror-Clerc, M. Hexagonal Close Packing of Nonionic Surfactant Micelles in Water. *J. Phys. Chem. B* **2007**, *111*, 5174–5179.

(39) Yaghmur, A.; Rappolt, M. The Micellar Cubic Fd3m Phase. Recent Advances in the Structural Characterization and Potential Applications. In *Advances in Planar Lipid Bilayers and Liposomes*; Elsevier, 2013; pp 111-145.

(40) Voinescu, A. E.; Bauduin, P.; Pinna, M. C.; Touraud, D.; Ninham, B. W.; Kunz, W. Similarity of Salt Influences on the pH of Buffers, Polyelectrolytes, and Proteins. *J. Phys. Chem. B* **2006**, *110*, 8870–8876.

(41) Olofsson, G. Thermodynamic Quantities for the Dissociation of the Ammonium Ion and for the Ionization of Aqueous Ammonia over a Wide Temperature Range. *J. Chem. Thermodyn.* **1975**, *7*, 507–514.

(42) Shearman, G. C.; Ces, O.; Templer, R. H.; Seddon, J. M. Inverse Lyotropic Phases of Lipids and Membrane Curvature. *J. Phys. Condens. Matter* **2006**, *18,* 1105-24.

(43) Templer, R. H.; Khoo, B. J.; Seddon, J. M. Gaussian Curvature Modulus of an Amphiphilic Monolayer. *Langmuir* **1998**, *14*, 7427–7434.

(44) Jayaraman, M.; Ansell, S. M.; Mui, B. L.; Tam, Y. K.; Chen, J.; Du, X.; Butler, D.; Eltepu, L.; Matsuda, S.; Narayanannair, J. K.; Rajeev, K. G.; Hafez, I. M.; Akinc, A.; Maier, M. A.; Tracy, M. A.; Cullis, P. R.; Madden, T. D.; Manoharan, M.; Hope, M. J. Maximizing the Potency of SiRNA Lipid Nanoparticles for Hepatic Gene Silencing in Vivo. *Angew. Chemie - Int. Ed.* **2012**, *51*, 8529–8533.

(45) Grava, M.; Ibrahim, M.; Sudarsan, A.; Pusterla, J.; Philipp, J.; Rädler, J. O.; Schwierz, N.; Schneck, E. Combining Molecular Dynamics Simulations and X-Ray Scattering Techniques for the Accurate Treatment of Protonation Degree and Packing of Ionizable Lipids in Monolayers. *J. Chem. Phys.* **2023**, *159*, 154706.

(46) Schwarzfischer, M.; Marr, C.; Krumsiek, J.; Hoppe, P. S.; Schroeder, T.; Theis, F. J. Efficient Fluorescent Image Normalization for Time Lapse Movies. *Proc. Microsc. Image Anal. with Appl. Biol.* **2011**.

(47) Blanchet, C. E.; Spilotros, A.; Schwemmer, F.; Graewert, M. A.; Kikhney, A.; Jeffries, C. M.; Franke, D.; Mark, D.; Zengerle, R.; Cipriani, F.; Fiedler, S.; Roessle, M.; Svergun, D. I. Versatile Sample Environments and Automation for Biological Solution X-Ray Scattering Experiments at the P12 Beamline (PETRA III, DESY). *J. Appl. Crystallogr.* **2015**, *48*, 431–443.

(48) Haas, S.; Sun, X.; Conceição, A. L. C.; Horbach, J.; Pfeffer, S. The New Small-Angle X-Ray Scattering Beamline for Materials Research at PETRA III: SAXSMAT Beamline P62. *J. Synchrotron Radiat.* **2023**, *30*, 1156–1167.

(49) Knight, C. J.; Hub, J. S. MemGen: A General Web Server for the Setup of Lipid Membrane Simulation Systems. *Bioinformatics* **2015**, *31*, 2897–2899.

(50) Ibrahim, M.; Gilbert, J.; Heinz, M.; Nylander, T.; Schwierz, N. Structural Insights on Ionizable Dlin-MC3-DMA Lipids in DOPC Layers by Combining Accurate Atomistic Force Fields, Molecular Dynamics Simulations and Neutron Reflectivity. *Nanoscale* **2023**, *15*, 11647–11656.

(51) Jorgensen, W. L.; Chandrasekhar, J.; Madura, J. D.; Impey, R. W.; Klein, M. L. Comparison of Simple Potential Functions for Simulating Liquid Water. *J. Chem. Phys.* **1983**, *79*, 926–935.

(52) Mamatkulov, S.; Schwierz, N. Force Fields for Monovalent and Divalent Metal Cations in TIP3P Water Based on Thermodynamic and Kinetic Properties. *J. Chem. Phys.* **2018**, *148*, 74504.

(53) Wright, L. B.; Rodger, P. M.; Walsh, T. R. Aqueous Citrate: A First-Principles and Force-Field Molecular Dynamics Study. *RSC Adv.* **2013**, *3*, 16399.

(54) Kashefolgheta, S.; Vila Verde, A. Developing Force Fields When Experimental Data Is Sparse: AMBER/GAFF-Compatible Parameters for Inorganic and Alkyl Oxoanions. *Phys. Chem. Chem. Phys.* **2017**, *19*, 20593–20607.

(55) Abraham, M. J.; Murtola, T.; Schulz, R.; Páll, S.; Smith, J. C.; Hess, B.; Lindahl, E. GROMACS: High Performance Molecular Simulations through Multi-Level Parallelism from

Laptops to Supercomputers. *SoftwareX* **2015**, *1–2*, 19–25.

(56) Michaud-Agrawal, N.; Denning, E. J.; Woolf, T. B.; Beckstein, O. MDAnalysis: A Toolkit for the Analysis of Molecular Dynamics Simulations. *J. Comput. Chem.* **2011**, *32*, 2319–2327.

(57) Humphrey, W.; Dalke, A.; Schulten, K. VMD: Visual Molecular Dynamics. *J. Mol. Graph.* **1996**, *14*, 33–38.

TOC graphic

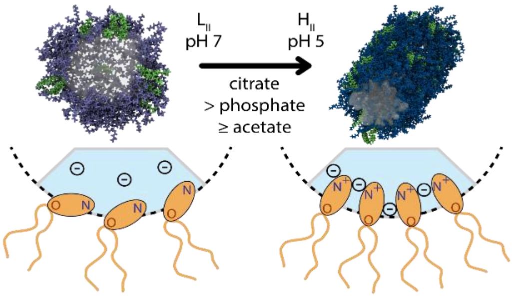

Supporting Information

Buffer specificity of ionizable lipid nanoparticle transfection efficiency and bulk phase transition

Cristina Carucci[1,‡], *Julian Philipp*[2,‡], *Judith A. Müller*[2], *Akhil Sudarsan*[3], *Ekaterina Kostyurina*[2], *Clement E. Blanchet*[4], *Nadine Schwierz*[3], *Drew F. Parsons*[1,*], *Andrea Salis*[1], *Joachim O. Rädler*[2,*]

[1]Department of Chemical and Geological Sciences, University of Cagliari & Center for Colloid and Surface Science (CSGI),
Cittadella Universitaria, 09042 Monserrato, CA, Italy

[2]Faculty of Physics, Ludwig-Maximilians University,
Geschwister-Scholl-Platz 1, Munich, Germany.

[3]Institute of Physics, University of Augsburg, Augsburg 86159, Germany.

[4]European Molecular Biology Laboratory Hamburg Outstation c/o Deutsches Elektronen-Synchrotron,

Hamburg 22607, Germany.

‡ CC and ‡ JP contributed equally to the work.

*Prof. Joachim Radler, raedler@lmu.de

*Prof. Drew Parsons, drew.parsons@unica.it

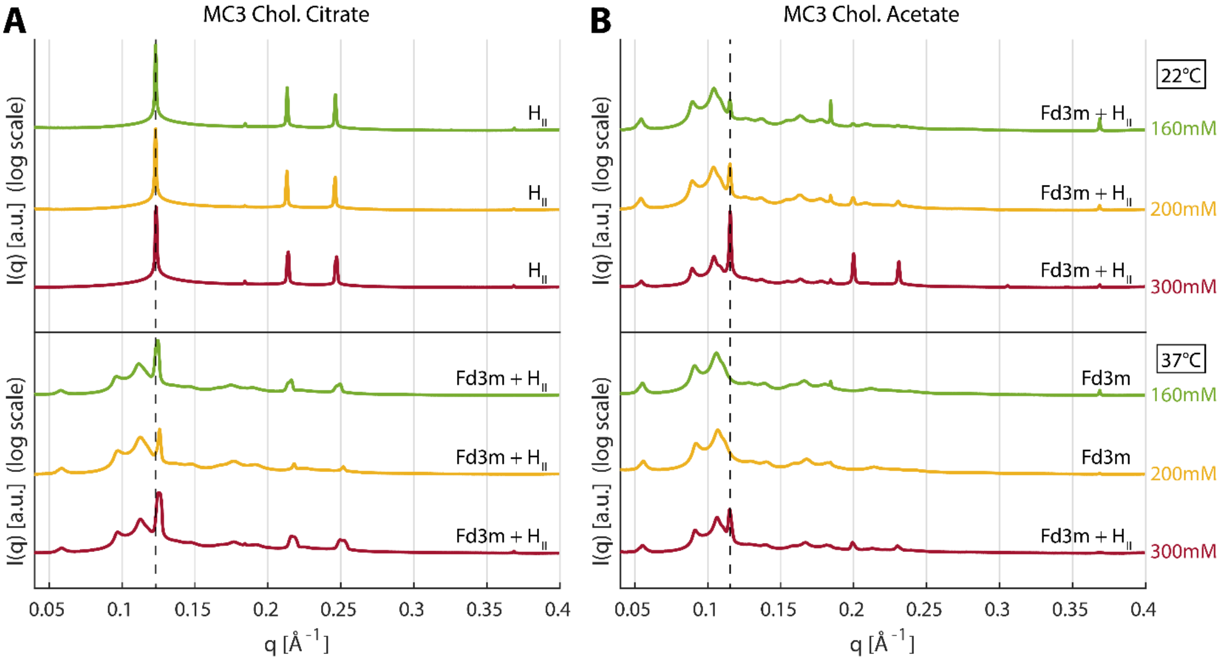

Figure S1. SAXS measurements of MC3-cholesterol dialyzed in the presence of 160-, 200-and 300-mM ionic strength citrate (A) and acetate (B) buffer at 22 °C and 37 °C at pH 5.5. Measurements of ionic strength (*I*) include the presence of NaCl 150 mM as background salt.

Table S1. Hydrodynamic diameter d_H, polydispersity index (PDI) as indication of the size measurements quality associated to the size distribution and zeta potential measurements of MC3 LNPs prepared in acetate 155 mM, phosphate 100 mM, and citrate 50 mM buffers at pH 4.5.

Buffer	d_H (nm)	PdI	pH*
Citrate	76 ± 7	0.330	5.75 ± 0.25
Phosphate	70 ± 1	0.304	5.3 ± 0.5
Acetate	73 ± 2	0.324	5.25 ± 0.25

*pH of Fd3m-H_{II} transition

Table S2. Miller indices of the measured lipid phases. a is the lattice parameter and d_{hkl} the corresponding real-world distance. This table is taken from reference [1].

Lipid phase	**Miller indices** (hkl)	a/d_{hkl}	m_{hkl}
H_{II}	$(10), (11), (20), (21), (30), \ldots$	$\sqrt{h^2+k^2+hk}$	$1, \sqrt{3}, 2, \sqrt{7}, \sqrt{9}, \ldots$
$Fd3m$	$(111), (220), (311), (222), (400),$	$\sqrt{h^2+k^2+l^2}$	$\sqrt{3}, \sqrt{8}, \sqrt{11}, \sqrt{12}, 4, ..$
$P\,6_3/mmc$	$(010), (002), (011), (012), (110),$	$\frac{4}{3}(h^2+k^2+hk)+\frac{3}{8}l^2$	$\sqrt{\frac{4}{3}}, \sqrt{\frac{3}{2}}, \sqrt{\frac{41}{24}}, \sqrt{\frac{17}{6}}, 4$

Table S3. Formula of the lattice constant a and the nearest neighbor distance d_{NN} for the measured lipid phases using the peak positions q_{hkl} as well as m_{hkl} from Table 2. This table is taken from reference [1].

Lipid phase	a	d_{NN}
H_{II}	$\frac{4\pi m_{hk}}{\sqrt{3}q_{hk}}$	a
$Fd3m$	$\frac{2\pi m_{hkl}}{q_{hkl}}$	$\frac{a}{\sqrt{8}}$
$P6_3/mmc$	$\frac{2\pi m_{hkl}}{q_{hkl}}$	a

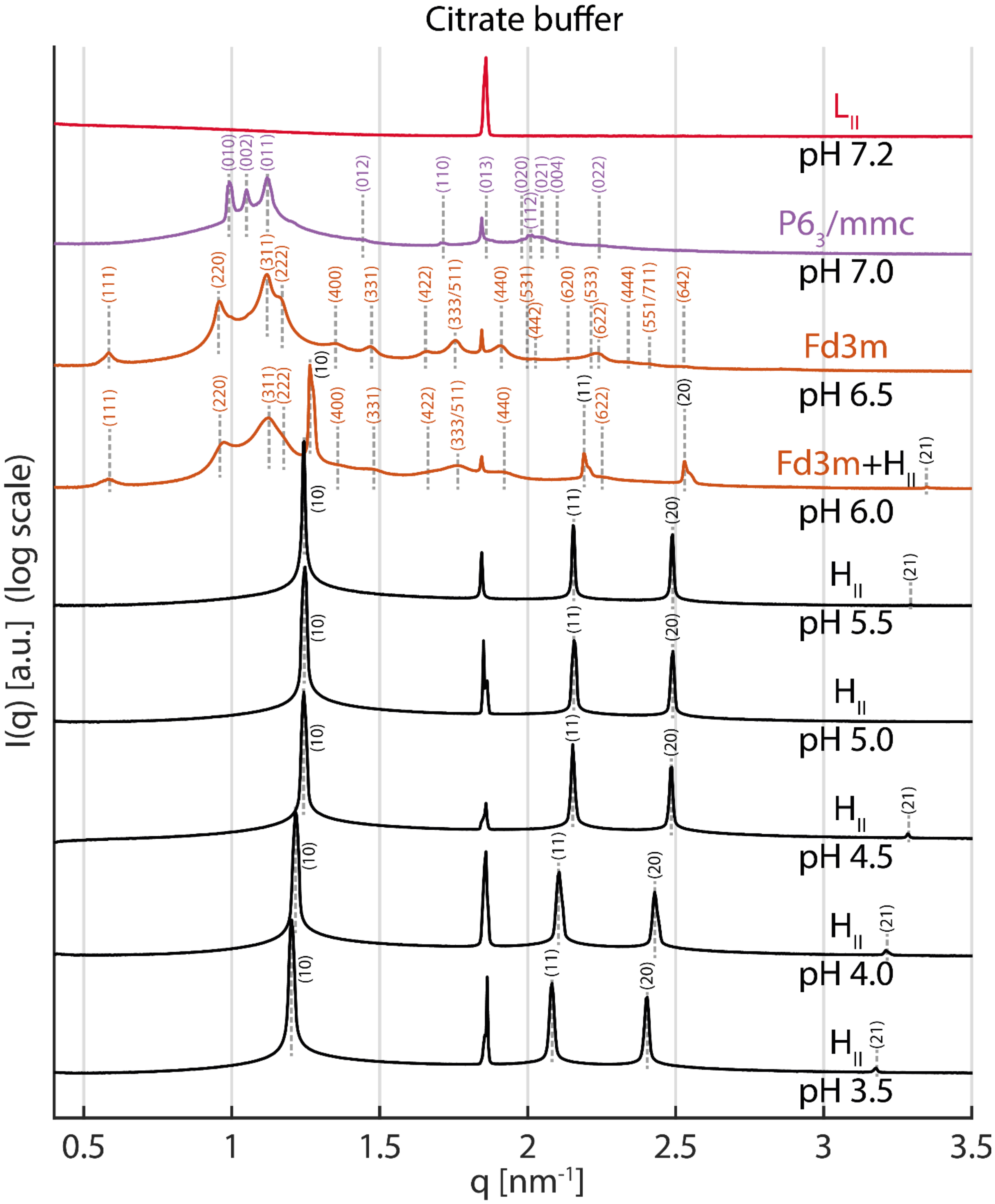

Figure S2. SAXS measurements and Miller indices of the mesophase of MC3-cholesterol samples dialyzed in the presence of 50 mM citrate buffer and NaCl 150 mM in a range of pH 3.5 - 7.2.

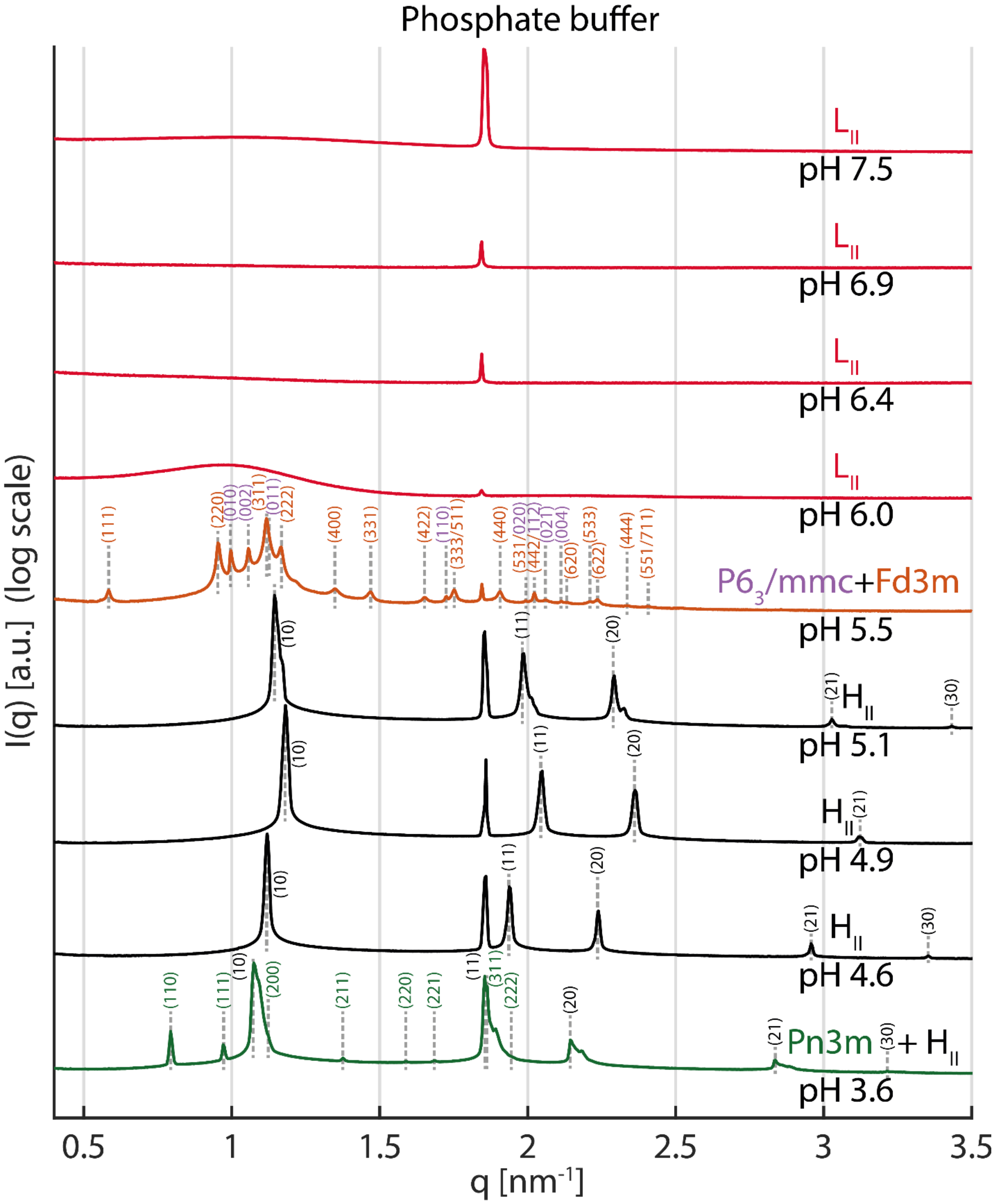

Figure S3. SAXS measurements and Miller indices of the mesophase of MC3-cholesterol samples dialyzed in the presence of 50 mM phosphate buffer and NaCl 150 mM in a range of pH 3.6 - 7.5.

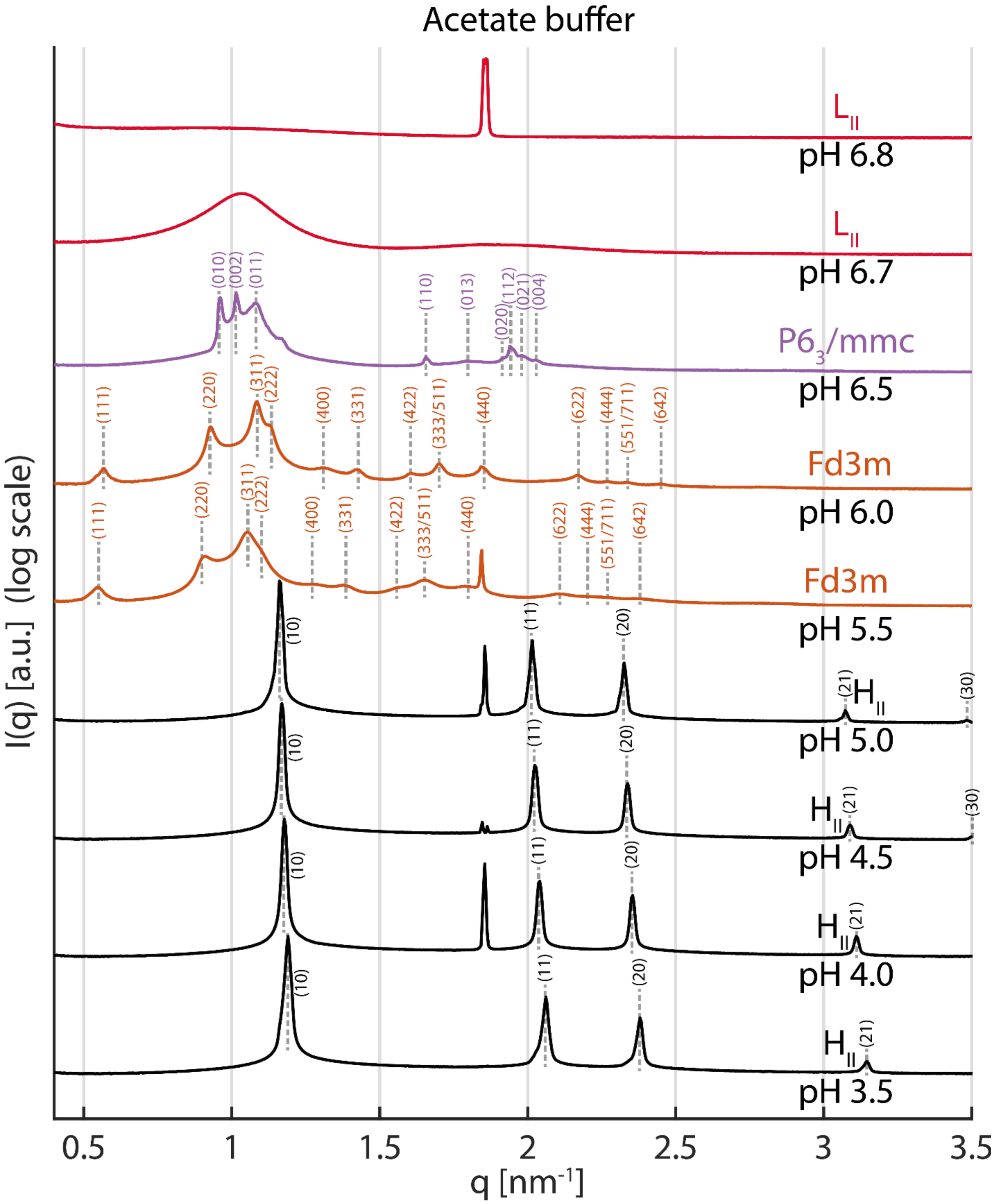

Figure S4. SAXS measurements and Miller indices of the mesophase of MC3-cholesterol samples dialyzed in the presence of 50 mM acetate buffer and NaCl 150 mM in a range of pH 3.5 - 6.8.

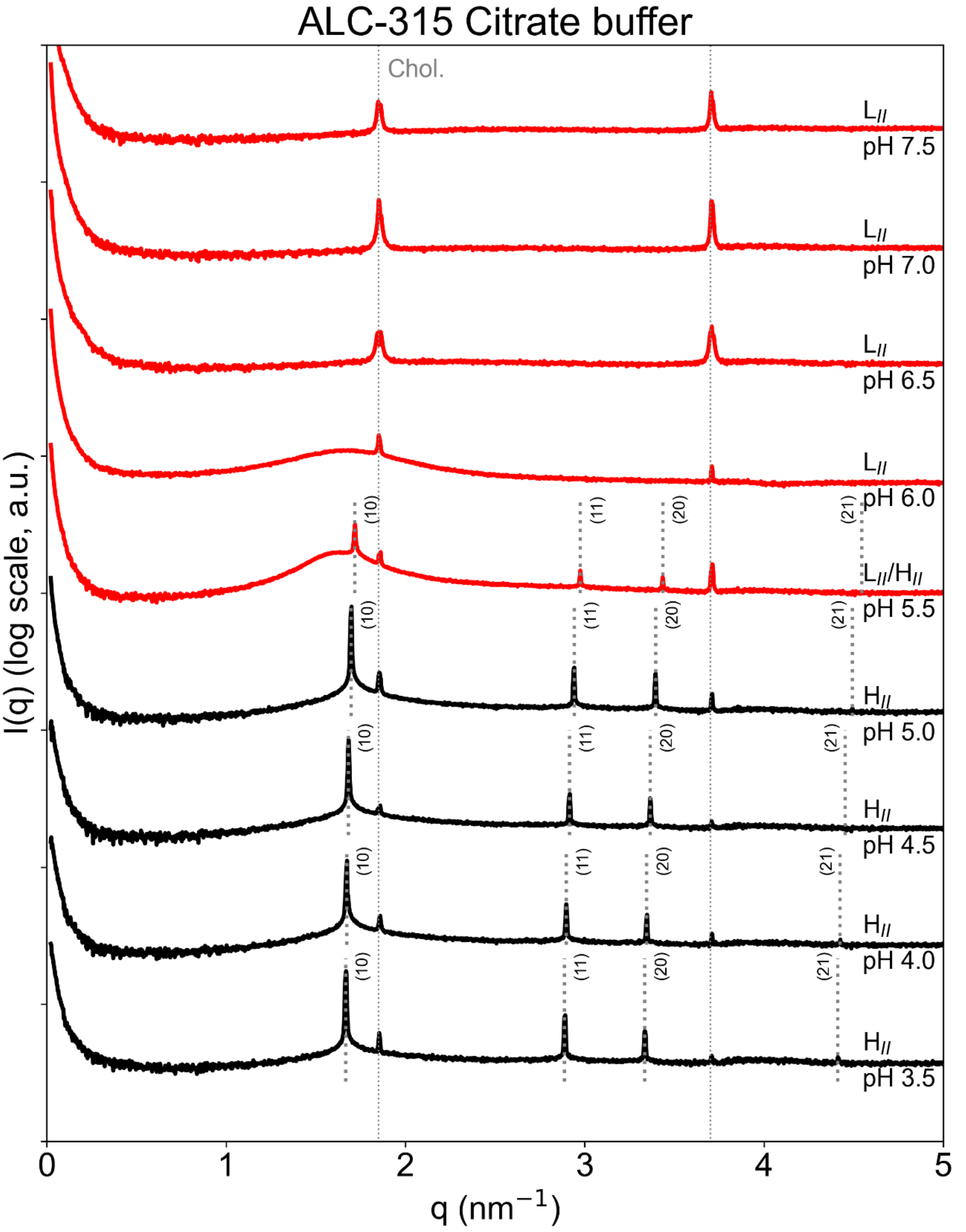

Figure S5. SAXS measurements of the mesophase of ALC315-cholesterol samples dialyzed in the presence of 50 mM citrate buffer and NaCl 150 mM in a range of pH 3.5- 7.5.

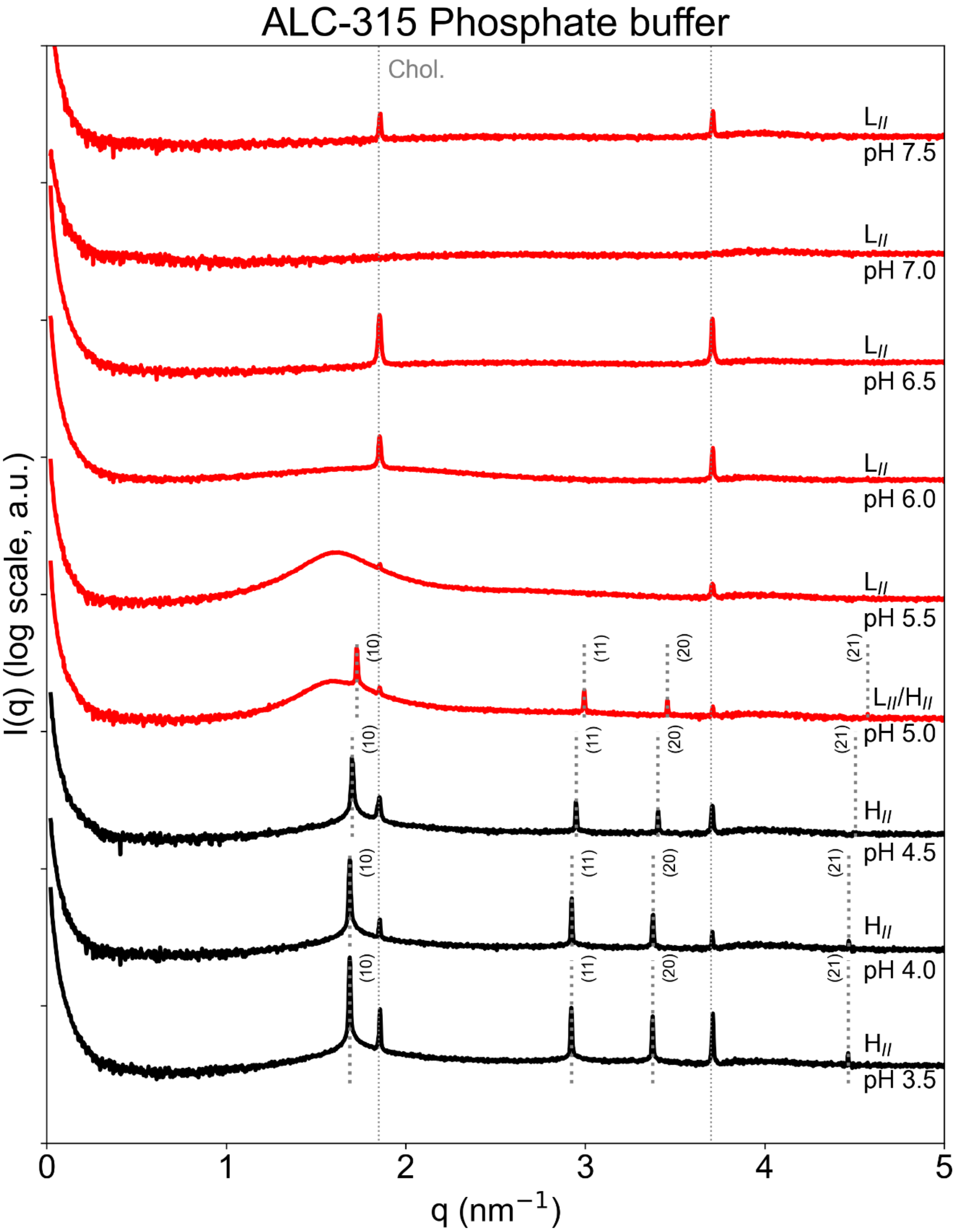

Figure S6. SAXS measurements of the mesophase of ALC315-cholesterol samples dialyzed in the presence of 50 mM phosphate buffer and NaCl 150 mM in a range of pH 3.5- 7.5.

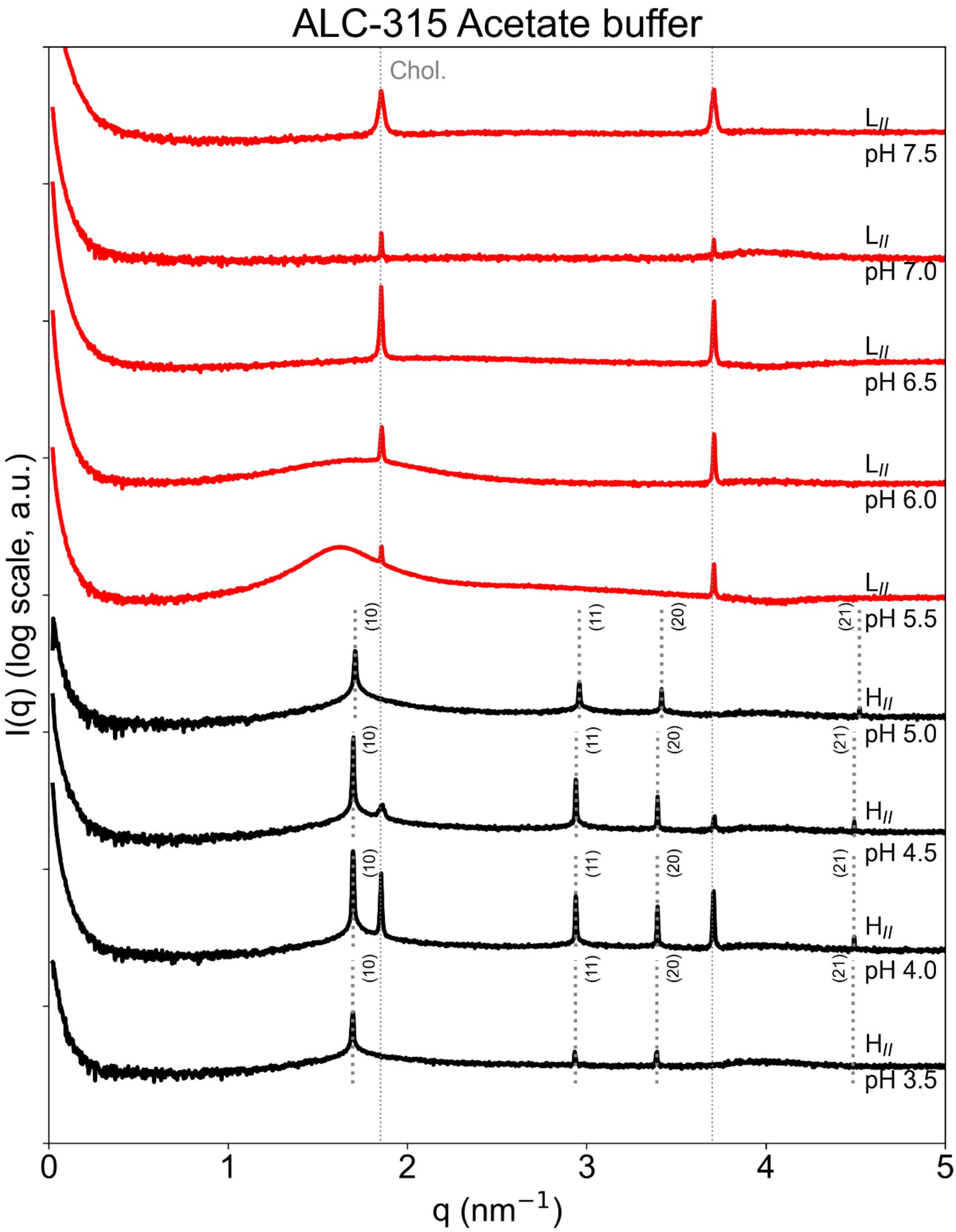

Figure S7. SAXS measurements of the mesophase of ALC315-cholesterol samples dialyzed in the presence of 50 mM acetate buffer and NaCl 150 mM in a range of pH 3.5- 7.5.

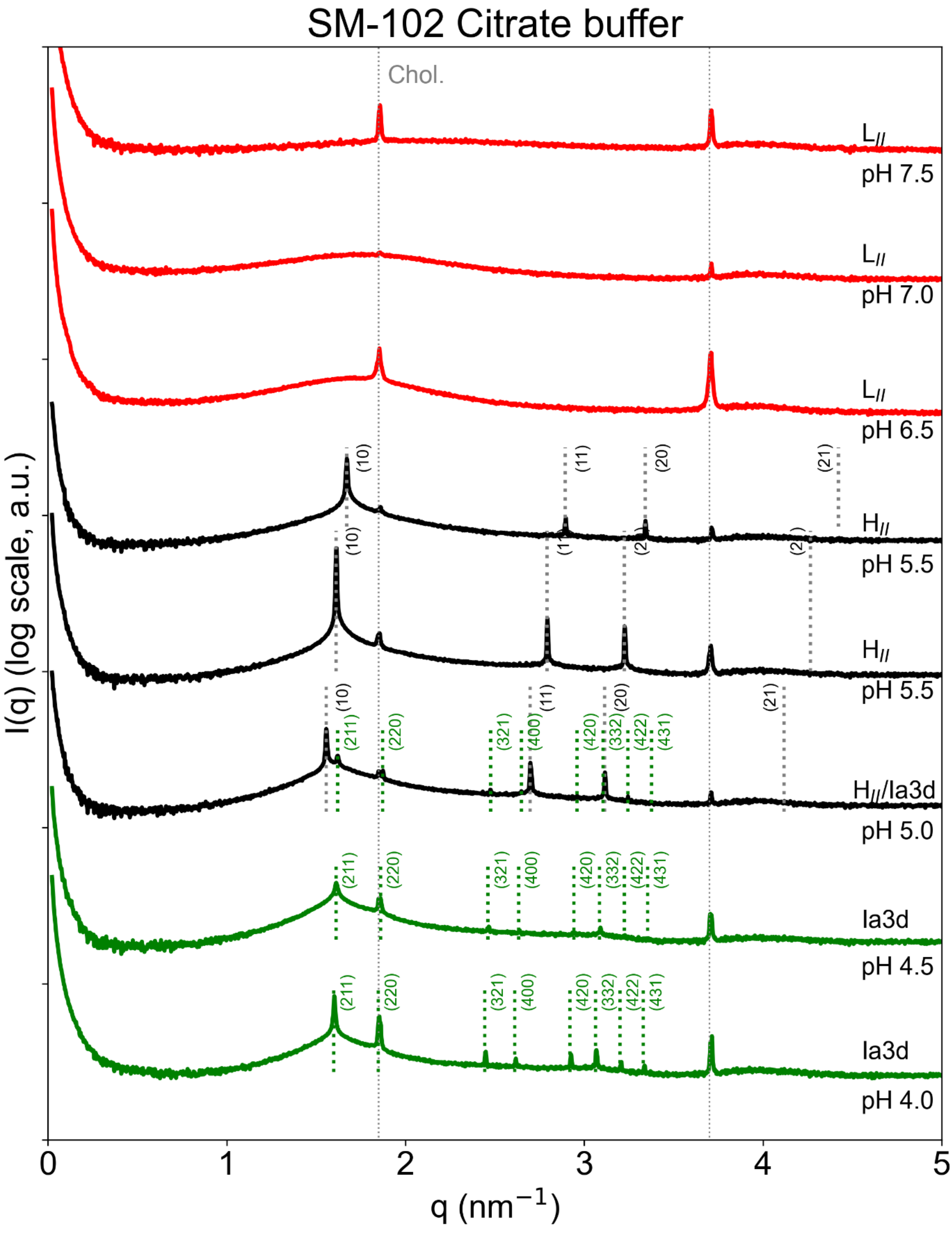

Figure S8. SAXS measurements of the mesophase of SM102-cholesterol samples dialyzed in the presence of 50 mM citrate buffer and NaCl 150 mM in a range of pH 4.0 - 7.5.

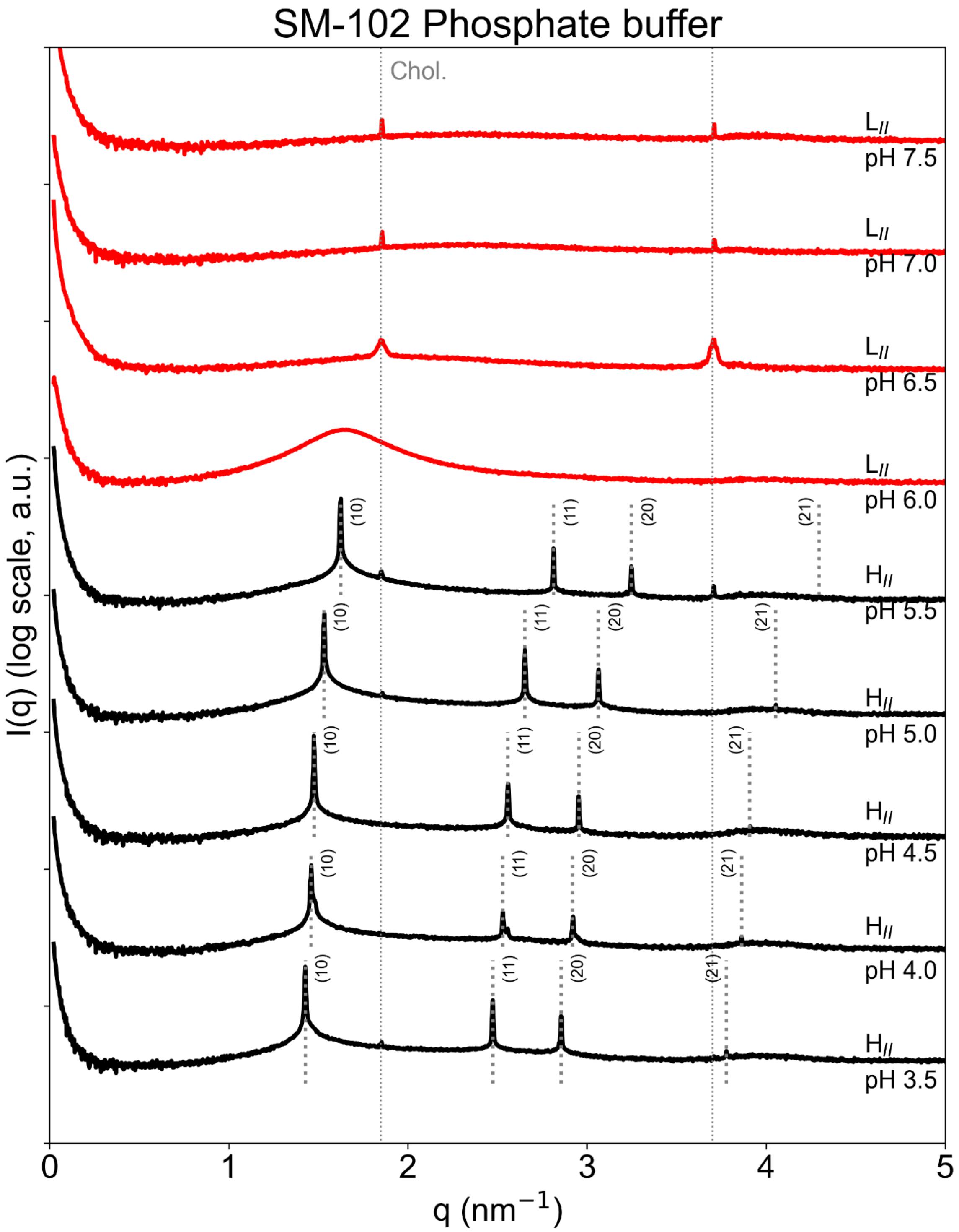

Figure S9. SAXS measurements of the mesophase of SM102-cholesterol samples dialyzed in the presence of 50 mM phosphate buffer and NaCl 150 mM in a range of pH 3.5 - 7.5.

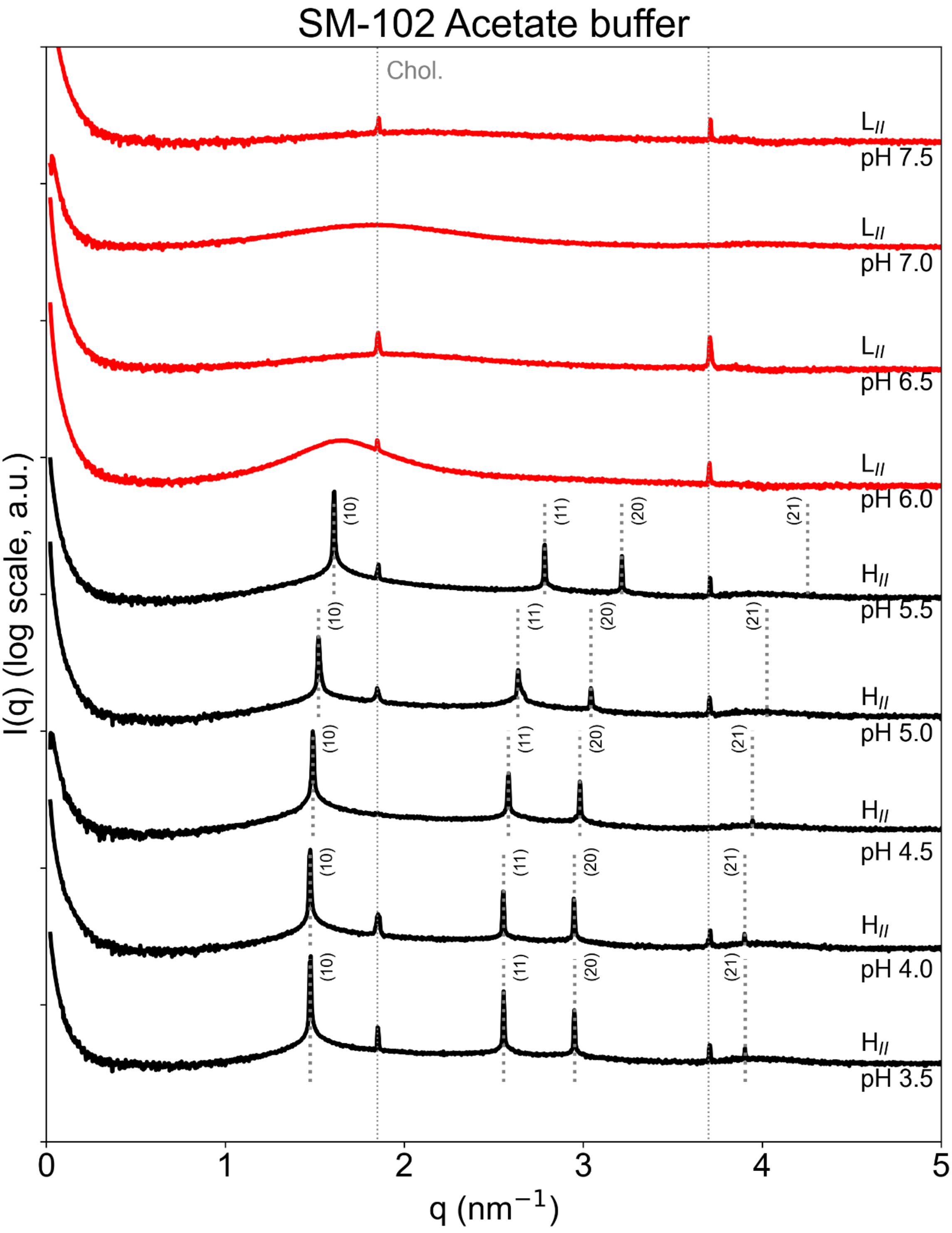

Figure S10. SAXS measurements of the mesophase of SM102-cholesterol samples dialyzed in the presence of 50 mM acetate buffer and NaCl 150 mM in a range of pH 3.5 - 7.5.

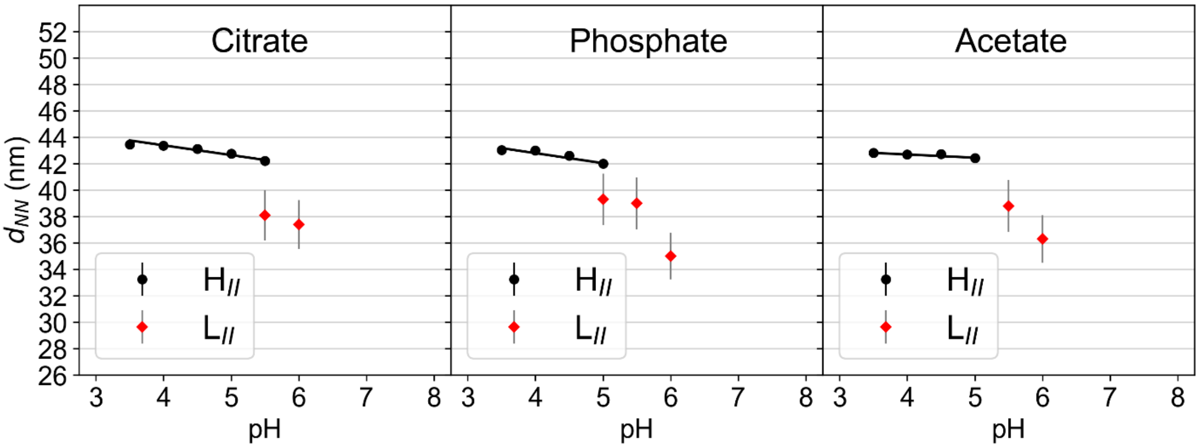

Figure S11. d_{NN} values for H_{II} and L_{II} phases for ALC315-cholesterol samples as a function of pH for buffer citrate, phosphate and acetate.

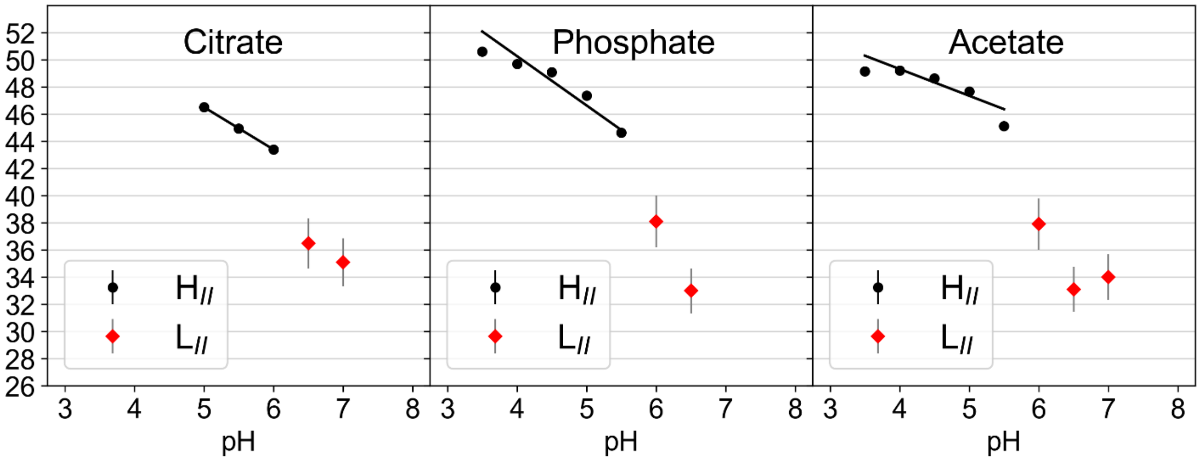

Figure S12. d_{NN} values for H_{II} and L_{II} phases for SM102-cholesterol samples as a function of pH for citrate, phosphate and acetate.

Molecular simulation methods

Adjustment of combination rules for the force field parameters

In MD simulations, the non-bonded interaction potential of the ions has the following form:

$$V(r_{ij}) = \frac{q_i q_j}{4\pi\epsilon_o r_{ij}} + 4\epsilon_{ij}\left[\left(\frac{\sigma_{ij}}{r_{ij}}\right)^{12} - \left(\frac{\sigma_{ij}}{r_{ij}}\right)^{6}\right] \qquad (1)$$

The first term describes the electrostatic interactions via a Coulomb potential. The last two terms describe the Van-der-Waal interactions via a Lennard-Jones (LJ) interaction potential. q_i and q_j are the charges of atoms i and j respectively, r_{ij} is the interatomic distance, σ_{ij} describes the LJ diameter at which the potential is zero and ϵ_{ij}accounts for the interaction strength. MD simulations of citrate and phosphate ions at finite concentrations resulted in crystallization of the ions. This effect was observed for different Na^+ force fields including the ones from ref. 50, 52 of the main manuscript. To avoid this artifact, we systematically increased the anion-cation LJ diameter by introducing a scaling factor in the corresponding Lorentz-Bertholot combination rule:

$$\sigma_{ij} = \lambda_{ij}\frac{\sigma_i + \sigma_j}{2} \qquad (2)$$

The value of λ_{ij} was increased until no more clustering was observed as judged by the anion-cation radial distribution functions. The final values are $\lambda=2$ for the citrate-sodium scaling and the phosphate-sodium interaction. Only the interaction of the sodium ions with the oxygen atoms of the phosphate and citrate ions were scaled. Note that in a more rigorous approach, the experimental activity derivative could be used to further optimize the anion-cation interactions as in previous work in reference 2.

Force Field parameters for phosphate

The Lennard-Jones force field parameters for the phosphate ions (HPO_4^{2-}) were taken from $H_2PO_4^-$ in ref 3. The partial charges were obtained from RESP fitting.

Calculation of area per lipid

The area per lipid of both the L_{II} and H_{II} phases were calculated for the system with $n_w = 12$. In the H_{II} phase, which is enclosed within a triclinic unit cell characterized by a lattice spacing d_H and height h, we assume that the water column is an equally long cylinder with a radius R_H. The water volume fraction (H) of the H_{II} phase is obtained by dividing the volume of the water column by the total volume of the system. The total volume of the system in the H_{II} phase is the volume of the triclinic unit cell which is given by $d_H^2 h$ sin(60°). The water volume fraction ϕ_H is given by:

$$\varphi_H = \frac{\pi R_H^2 h}{d_H^2 h \, Sin(60°)} \qquad (3)$$

From this equation, the radius R_H of the cylindrical water column can be derived as

$$R_H = d_H \sqrt{\frac{\sqrt{3}}{2\pi}\phi_H} \qquad (4)$$

The value of H = 0.24 and d_H = 60 Å is taken from ref. 1. The area per lipid *(A)* of the f the H_{II} phase is obtained by dividing the surface area of the water column by the total number of lipids *N*.

$$A = \frac{2\pi R_H h}{N} \qquad (5)$$

Similarly, for the $\mathrm{L_{II}}$ phase simulated in a rhombic dodecahedron box of lattice spacing *dL*, we assume a water sphere of radius R_L surrounded by lipids. The water volume fraction (L) of the $\mathrm{L_{II}}$ phase is obtained by dividing the volume of the water sphere by the total volume of the system. For a rhombic dodecahedron box of length *dL*, the volume of the box is 0.707 $d_L{}^3$ (i.e. $d^3/\sqrt{}2$). The water volume fraction ϕ_L is given by

$$\phi_L = \frac{(4/3)\pi R_L^3}{0.707\ d_L^3} \qquad (6)$$

The radius of the water sphere R_L can be obtained from the above equation by:

$$R_L = 0.55\ d_L(\phi_L)^{\frac{1}{3}} \qquad (7)$$

Corresponding area per lipid of the $\mathrm{L_{II}}$ phase,

$$A_L = \frac{4\pi {R_L}^2}{N} \qquad (8)$$

Calculation of probability distributions

The probability distributions for the ions perpendicular to the interface were calculated as

$$P(z) = \frac{\rho(z)}{\int_{-D/2}^{D/2} \rho(z) dz} \tag{9}$$

where D is the distance between the monolayers and $\rho(z)$ is the number density of the ions. The probability distributions are normalized such that $\int_{-D/2}^{D/2} \rho(z) dz = 1$.

Calculation of radial distribution function

The radial distribution function $g(r)$ provides insights into the local distribution of the ions around the protonated and neutral MC3 lipids. The radial distribution functions were obtained from the following equation:

$$g(r) = \frac{n(r)}{N_R \rho 4\pi r^2 dr} \tag{10}$$

n(r) is the count of buffer ions around the reference atoms at distance r, N_R is the number of reference atoms, and $\rho = N_I/V_w$ is the bulk density of the ions. N_I is the total number of anions in the system minus the anions used for neutralization and V_w is the volume of water obtained by multiplying the theoretical molecular volume of a water molecule with the total number of water molecules in the system. In a bulk solution, $g(r)$ gives the number of ions at distance r relative to the number of ions in an ideal solution. At an interface, such as the lipid water interface investigated here, equation (8) gives the number of buffer ions at distance r relative to a uniform ion distribution in the same slab geometry. The MD analysis python module (reference 4) was used to count the number of anions around the reference atoms (N, O1 and O2) of the charged and uncharged MC3 lipid head group using the simulation setup at pH 5.

London dispersion interactions and the O-moiety

Acetate ion binding to the O-moiety of the MC3 headgroup can be understood in part from direct London dispersion interactions, $U(d) = -C/d^6$, where d is the distance between the ion and the O-moiety. The London dispersion coefficient may be evaluated from quantum mechanical electronic polarizabilities of the species by applying quantum electrodynamics methods as reported in reference 5,6. Table S4 presents calculated London dispersion coefficients of buffer ions with a neutral acetic molecule representing the O-moiety (i.e. representing with O-moiety via a simple bound carbonyl group). London coefficients are evaluated in aqueous medium, and in nonpolar medium (tetradecane).

Table S4. London dispersion coefficients of buffer ions with acetic acid (representing the MC3 O-moiety) in aqueous media and in non-polar medium

Buffer ion	***C*, aqueous (Å^6 kJ/mol)**	***C*, in tetradecane**
acetate	5414	3752
$H_2PO_4^-$	5635	4473
HPO_4^{2-}	4188	1722
PO_4^{3-}	-2069	-8693
H_2-citrate$^-$	2182	149
H-citrate^{2-}	1456	-1347
citrate^{3-}	-258	-4635

The London coefficient is significantly more attractive for acetate ion than any of the citrate species. Curiously, trivalent citrate even has a negative coefficient, indicating a repulsive interaction pushing citrate away from the representative O-moiety. The aqueous London coefficient for phosphate is similar to acetate, indicating that this mechanism does not solely control the binding of acetate to the O-moiety observed in MD simulations. The O-moiety is located deeper inside the headgroup layer, such that the environment of the interaction is not purely aqueous. The reduced polar environment deep inside the head group is more unfavorable to phosphate than to acetate, which is surface active (partially oleophilic) due to its short hydrocarbon group. Indeed, the London coefficient of acetate in a nonpolar environment (tetradecane) is much stronger (more attractive) than all phosphate and citrate species apart from $H_2PO_4^-$.

REFERENCES

(1) Philipp, J.; Dabkowska, A.; Reiser, A.; Frank, K.; Krzysztoń, R.; Brummer, C.; Nickel, B.; Blanchet, C. E.; Sudarsan, A.; Ibrahim, M.; Johansson, S.; Skantze, P.; Skantze, U.; Östman, S.; Johansson, M.; Henderson, N.; Elvevold, K.; Smedsrød, B.; Schwierz, N.; Lindfors, L.; Rädler, J. O. PH-Dependent Structural Transitions in Cationic Ionizable Lipid Mesophases Are Critical for Lipid Nanoparticle Function. *Proc. Natl. Acad. Sci.* **2023**, *120*, 2017.

(2) Fyta, M.; Netz, R. R. Ionic Force Field Optimization Based on Single-Ion and Ion-Pair Solvation Properties: Going beyond Standard Mixing Rules. *J. Chem. Phys.* **2012**, *136*.

(3) Kashefolgheta, S.; Vila Verde, A. Developing Force Fields When Experimental Data Is Sparse: AMBER/GAFF-Compatible Parameters for Inorganic and Alkyl Oxoanions. *Phys. Chem. Chem. Phys.* **2017**, *19*, 20593–20607.

(4) Michaud- Agrawal, N.; Denning, E. J.; Woolf, T. B.; Beckstein, O. MDAnalysis: A Toolkit for the Analysis of Molecular Dynamics Simulations. *J. Comput. Chem.* **2011**, *32*, 2319–2327.

(5) Fiedler, J.; Thiyam, P.; Kurumbail, A.; Burger, F. A.; Walter, M.; Persson, C.; Brevik, I.; Parsons, D. F.; Boström, M.; Buhmann, S. Y. Effective Polarizability Models. *J. Phys. Chem. A* **2017**, *121*, 9742–9751.

(6) Bergström, S.; Olofsson, G. Thermodynamic Quantities for the Acid Dissociation of Alkylammonium Ions in Water over a Wide Temperature Range. *J. Solution Chem.* **1978**, *7*, 497–513.

6 Publication 3: Combining SAXS Analysis and MD Simulation to Determine Structure and Hydration of Ionizable Lipid Hexagonal Phases

In our latest publication, we present an integrated methodology combining SAXS experiments, all-atom molecular dynamics (MD) simulations, and a novel continuum model to quantitatively determine the structure and hydration of inverse hexagonal (H_{II}) phases. The H_{II} mesophase, formed by cationic ionizable lipids (CILs) in lipid nanoparticles (LNPs), is critical for mediating mRNA release.

Building on our prior work (Section 4), we complemented our SAXS dataset with new measurements for the ionizable lipid SM-102 (collected by Ekaterina Kostyurina). We utilized a Fourier analysis method based on the work of Michael Rappolt and colleagues[41] to reconstruct high-resolution 2D electron density maps of the H_{II} phase. A key technical innovation in our SAXS analysis was that, unlike previous work that used the height of fitted peak functions as intensity values, we integrated the areas under the peaks. This approach made our analysis independent of the exact peak shape, significantly increasing the robustness and accuracy of our structural determination.

These 2D maps were used to calibrate MD simulations created by Nadine Schwierz and Akhil Sudarsan, which in turn allowed us to discern the individual spatial distributions of all molecular components (lipid head groups, tails, water, and ions). A further innovation for validation was developing a novel method to correct for periodic boundary artifacts in the calculated MD scattering profiles, ensuring quantitative agreement with the experimental data.

To generalize our findings, and due to a lack of validated force field data for most CILs, we constructed a generalized continuum model with Jan Westergren and Lennart Lindfors, which was parameterized by the calibrated MC3 MD results, to extend structural prediction to other CILs. Using this model, we successfully calculated the water content for MC3, KC2, DD, and SM-102 across different pH values. While the water content of MC3, KC2, and SM-102 was found to be largely invariant with respect to pH, the DD system suggested a pH-dependence, albeit with larger associated error bars. Most importantly, we found a negative correlation between the H_{II} phase water content and the corresponding transfection efficiency. This finding provides a structural basis for LNP performance, suggesting that a lower H_{II} water content is linked to increased therapeutic efficacy, which in turn allows for rational LNP design.

Soft Matter

ROYAL SOCIETY OF CHEMISTRY

PAPER

View Article Online
View Journal

Check for updates

Cite this: DOI: 10.1039/d5sm00666j

Combining SAXS analysis and MD simulation to determine structure and hydration of ionizable lipid hexagonal phases

Julian Philipp, †[a] Akhil Sudarsan,†[b] Ekaterina Kostyurina,[a] Viktoriia Meklesh,[c] Monica Berglund,[c] Michael Rappolt, [d] Jan Westergren,[e] Lennart Lindfors,[c] Nadine Schwierz [b] and Joachim O. Rädler *[a]

Cationic ionizable lipids (CILs) are fundamental components of inverse hexagonal (H_{II}) lipid assemblies, which mediate the encapsulation and release of negatively charged mRNA through a pH-dependent mechanism. Since variations in the structure and composition of the H_{II} phases can significantly impact the biological efficacy of the mRNA-carrying lipid nanoparticles (LNP), a comprehensive understanding of the ionizable lipid H_{II} phases is necessary. We present an integrated approach combining small-angle X-ray scattering (SAXS) experiments, molecular dynamics (MD) simulations and a continuum model to elucidate lipid distribution and water content within H_{II} phases. Our results indicate strong agreement between structures derived from MD simulations and SAXS data. To this end, we introduce a method to correct for periodic boundary artifacts when computing scattering profiles from MD simulations. This enables direct, model-free comparisons between experimental and simulated data, enhancing the reliability of structural interpretations, specifically the water content of the H_{II} phases. Next, we developed a continuum model to extend structural analysis to CIL H_{II} phases for which MD data is unavailable. This integrative framework not only provides molecular-level insights into the ionizable lipid H_{II} mesophase but also enables the prediction of hydration properties across different CIL compositions. The different approaches consistently yield water contents that seem to correlate with the lipids' transfection efficiencies. By bridging experimental and simulation data, our approach offers a powerful tool for the rational design and optimization of lipid nanoparticles, potentially linking a lower water content with an increased therapeutic performance.

Received 27th June 2025,
Accepted 20th September 2025

DOI: 10.1039/d5sm00666j

rsc.li/soft-matter-journal

1 Introduction

Lipid nanoparticles (LNPs) have emerged as powerful RNA delivery vehicles in modern medicine, with recent applications demonstrating their effectiveness in a wide range of drugs and vaccines. A critical component of efficient LNPs is the cationic ionizable lipid (CIL), which carries a pH-dependent charge at its head group. Although the optimal pK_a range for CILs in LNPs is well established (pH 6–7), *in vivo* transfection efficiencies can vary by up to two orders of magnitude, even among structurally similar CILs. This discrepancy highlights the importance of a deeper understanding of LNP structure to elucidate their intracellular release mechanisms, particularly during endosomal escape.[1–5]

LNPs are known to exhibit distinct mesophases depending on the local pH environment.[5–7] Among these, the inverse hexagonal (H_{II}) phase plays a key role in membrane fusion and cargo release. Although different CILs can form similar mesophases, subtle variations in structure can have a profound impact on transfection efficiency. In our previous work,[5] we demonstrated that bulk lipid phases composed of DLin-MC3-DMA (MC3), DLin-KC2-DMA (KC2), and DLinDMA (DD), in combination with cholesterol and water, undergo a pH-dependent structural transition from an inverse cubic micellar phase ($Fd3m$) to an inverse hexagonal (H_{II}) phase at approximately pH 6.0. Despite this shared transition point, significant differences in lattice spacing were observed between DD and the MC3/KC2 systems, suggesting distinct packing or hydration characteristics.

This underscores the need for a deeper analysis of these mesophases, with a particular focus on their water content, as

---

[a] *Faculty of Physics, Ludwig-Maximilians University, Geschwister-Scholl-Platz 1, Munich, Germany. E-mail: raedler@lmu.de*
[b] *Institute of Physics, University of Augsburg, Augsburg 86159, Germany*
[c] *Pharmaceutical Sciences, BioPharmaceuticals R&D, AstraZeneca, Gothenburg, Sweden*
[d] *School of Food Science and Nutrition, University of Leeds, Leeds LS2 9JT, UK*
[e] *Wendelsbergs beräkningskemi AB, Kyrkvägen 7B, 435 35 Mölnlycke, Sweden*

† JP and AS contributed equally to this work.

water content is relevant in RNA mobility, curvature energies as well as disruption occurring in pH-dependent structural transitions.

To gain a comprehensive understanding of lipid organization and hydration within LNPs, small-angle X-ray scattering (SAXS) experiments can be combined with molecular dynamics (MD) simulations. SAXS has significantly advanced our knowledge of lipid phase structures, particularly the inverted hexagonal H_{II} phase, which has been extensively studied as a model system.[8–10] Traditional SAXS data interpretation often relies on simplified models, such as Lorentzian peak-based structure factors and box model form factors. In contrast, more advanced Fourier-based analysis that reconstructs two-dimensional electron density maps, offer a more accurate and detailed view of the phase architecture.[11]

MD simulations have achieved significant progress in modeling large molecular systems like lipid mesophases and lipid nanoparticles. However, quantitative results rely heavily on the calibration of force fields and system parameters through experimental validation.[12–15] Previous studies on LNPs using coarse-grained force fields such as SPICA, which were meticulously optimized for lipid and nucleic acid systems, were able to closely reproduce experimental observations while providing molecular level insights into the pH-dependent structure of LNPs, thereby underscoring the importance of employing a rigorously validated force field.[16,17] Integrating experimental data not only refines and validates the simulations but also provides atomic-scale insights regarding water content,[5] ion interactions,[18] lipid structure[19] and lipid protonation.[20]

For easier interpretation, it is useful to describe the H_{II} phase using continuum models that describe the electron density profiles. Continuum models are characterized by interpretable parameters such as water content and area per lipid head group. A central challenge in developing such models is to minimize the number of free parameters while maintaining sufficient accuracy to capture the key structural features of the system. Simple models typically partition the phases into distinct, non-overlapping regions of water, lipid head groups, and lipid tails. More sophisticated approaches allow for overlapping Gaussian distributions to represent the spatial extent of each molecular component.[21,22]

In this study, we introduce a systematic methodology for structural analysis that integrates experimental SAXS data, MD simulations, and continuum model representations. Through an iterative refinement process, we align experimental and simulation data to produce a consistent and quantitative interpretation of lipid organization and hydration. Using this framework, we determine the water content of the inverse hexagonal phase formed by MC3, and extend our analysis to assess water content across a range of pH values and for additional ionizable lipids, including KC2, DD, and SM-102.

Our results reveal two key trends. First, the water content within the hexagonal phase appears to be largely invariant with respect to pH, indicating structural stability of hydration across physiologically relevant conditions. Second, we observe substantial differences in hydration among the different lipids: DD exhibits significantly higher water content than MC3 and KC2, while SM-102 shows a notably lower water content. This trend suggests a potential correlation between the hydration properties of CIL mesophases and their transfection efficiency when used in LNP formulations.[3,5] By offering a unified framework that links mesophase structure with functional performance, our approach provides valuable insights for the rational design and optimization of next-generation lipid nanoparticles.

2 Methods and model

2.1 Data analysis small angle X-ray scattering

Lipid bulk phase samples were prepared following the same procedure as explained in detail in our previous research.[5] In order to mimic the inner lipid phase of lipid nanoparticles, we mixed the cationic ionizable lipid (MC3/KC2/DD) with cholesterol at a 3 : 1 molar ratio in ethanol. The lipid mixture was filled into a dialysis cup together with a 50 mM citrate buffer at pH 3 creating a ethanol to water ratio of 2 : 1. Following dialysis steps first reduced the ethanol to water ratio to 1 : 3, then replaced the citrate–ethanol mixture with PBS buffer (1 mM KH_2PO_4, 155 mM NaCl, and 3 mM Na_2HPO_4, pH 7.4) and finally replaced it again with McIlvaine buffer (citric acid and disodium phosphate) at the desired final pH. For SM-102 we instead used citrate buffer (citric acid and sodium citrate) to adjust the pH. Each of these dialysis steps took 48 h to make sure that all the buffers in the dialysis cup were replaced and to give the sample material enough time to equilibrate to its new environment. These dialysis steps resulted in white precipitation that was extracted from the dialysis cup and sealed in quartz capillaries with 1.5 mm diameter together with an excess of the final buffer below and above the sample.

Small angle X-ray scattering (SAXS) patterns of the ionizable lipid bulk phases were recorded at the P12 EMBL BioSAXS[23] and the P62 SAXSMAT[24] beamlines at DESY. The angular calibration of the detector was performed with a silver-behenate reference sample. The resulting scattering patterns were radially integrated and background scattering was subtracted with reference measurements of empty capillaries.

For the inverted hexagonal H_{II} phase we found up to seven peaks (Fig. 1A). In order to get 2D electron density maps and radial scattering density profiles we closely followed the procedure described by Michael Rappolt and colleagues[11] but with a slight adjustment. Since the peaks were sharp and spaced out enough that there was no overlap between neighboring peaks, two distinct optimizations to the procedure were possible. Firstly we adjusted the background subtraction by calculating the background at each peak position individually. For each peak the background was determined with the measured intensity on both sides of the peak. Secondly, instead of fitting the peaks with Lorentz peak shapes first, we integrated the peaks above the background directly (grey area in insert of Fig. 1A). This way we could sum up all the scattering around a certain angle independent of the measured peak shape, which generally differs from an ideal Lorentz peak due to the

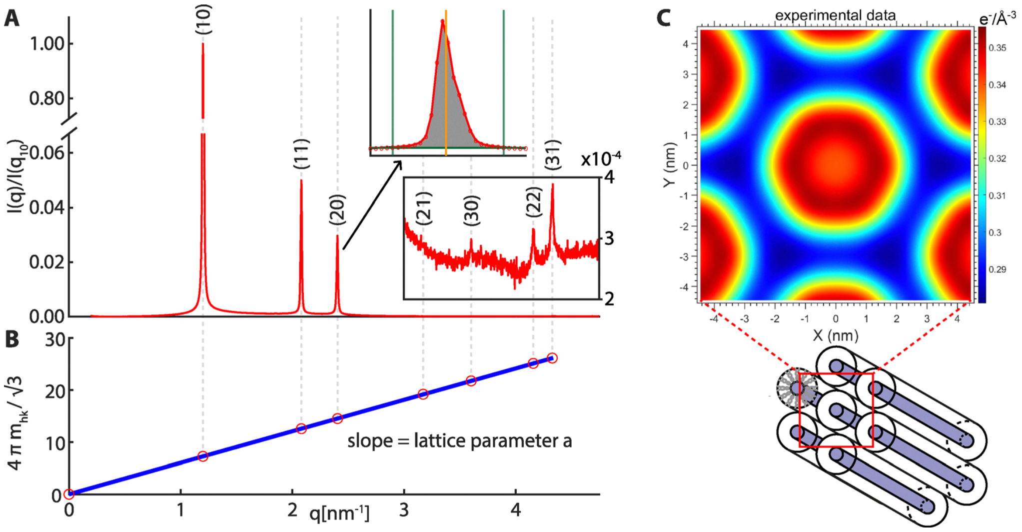

Fig. 1 Analysis of experimental SAXS data. (A) SAXS profile of the inverted hexagonal phase, normalized with the first peak height. Up to seven peaks could be measured and integrated for further analysis, although the later peaks are several magnitudes of order smaller than the first one. The insert shows the individual peak analysis. We define the peak intensity as the peak integral, independent of its exact shape. This is possible because the peaks are sharp enough not to overlap each other. The peak position is then the half-point of the integral, indicated by the orange line. (B) For each measurement the peak positions on the q scale are plotted against $\frac{4\pi}{\sqrt{3}}m_{hk}$. The slope of the linear fit through all points including the origin is the inverse hexagonal lattice parameter a. (C) The analysis of the lattice parameter and all peak intensities allows for the calculation of detailed 2D electron density maps of the inverse hexagonal lipid structure.

convolution of the direct beam profile (Gaussian distribution) with the diffraction peak contribution, arising from the inverse hexagonal phase.

After integrating each peak individually, we defined their positions to be where 50% of their total area is reached (orange line in insert of Fig. 1A). The lattice parameter a is determined as the slope when fitting $q_{hk} = \frac{4\pi}{\sqrt{3}}m_{hk}$ with $m_{hk} = \sqrt{h^2 + hk + k^2}$ and q_{hk} as the measured peak positions (Fig. 1B). The integrated peak areas were normalized regarding their multiplicity and a Lorentz correction was applied by multiplying each peak area by its corresponding $m_{hk}{}^2$. Finally, the square root of the corrected peak area was used to determine the form factor F of each peak. The electron density contrast was calculated by the same Fourier analysis as described by Michael Rappolt and colleagues:[11]

$$\Delta\rho(x,y) = \sum_{h,k\neq 0,0}^{h,k\,\max} \alpha_{h,k}\cdot F_{h,k}\cdot\cos(q_x(h,k)x)\cdot\cos\left(q_y(h,k)y\right). \quad (1)$$

$F_{h,k}$ is the peak amplitude (area) at position $q(h,k)$ with h and k as its respective Miller indices. The phase $\alpha_{h,k}$ for each peak is either +1 or 1. In order to find the right phase combination, we calculated the fourth moment of each phase combination following this formula from Mariani *et al.*:[25]

$$\left\langle(\Delta\rho)^4\right\rangle = (1/A)\int_A [\Delta\rho(r)]^4 \mathrm{d}r \quad \text{with} \quad \Delta\rho(r) = \rho(r) - \langle\Delta\rho\rangle. \quad (2)$$

A is the unit cell area, $\rho(r)$ the electron density at position r and $\langle\Delta\rho\rangle$ the average electron density. The correct peak phase combination generally has the lowest fourth moment. For almost all of our measurements (76 of 86) this is (+1, −1, −1, +1, +1, +1, +1) for the seven observed peaks. Only in a few cases either (+1, −1, −1, −1, +1, +1, +1) or (+1, −1, −1, −1, +1, +1, −1) had a slightly lower fourth moment. Those two alternatives can be disregarded since the resulting electron density maps show a 30° rotated hexagonal phase, which contradicts the assumption of an even tail region band between neighboring lipid tubes (Fig. S1). Therefore we used (+1, −1, −1, +1, +1, +1, +1) for all measurements, which is also in agreement with literature.[26,27] The result is a 2D electron density map (Fig. 1C), but without additional assumptions the electron density is not on an absolute scale.

2.2 MD simulations

All-atom MD simulations of inverse hexagonal H_{II} phases were performed for 1 μs using the GROMACS[28] software package. The starting structures for the simulation were generated using the CHARMM-GUI[29] web server and consisted of cationic MC3 lipids and cholesterol in a 3 : 1 molar ratio. The water content of the H_{II} phase was adjusted iteratively to match the experimental lattice spacing of 60 Å as reported in our previous work,[5] resulting in a ratio of 12 water molecules per lipid (Fig. 2A). A salt concentration of 0.15 M was introduced and additional ions were added to neutralize the system. A triclinic box with a length of 60 Å and a height of 91.4 Å was used to reproduce the symmetry of the H_{II} phase with the water column

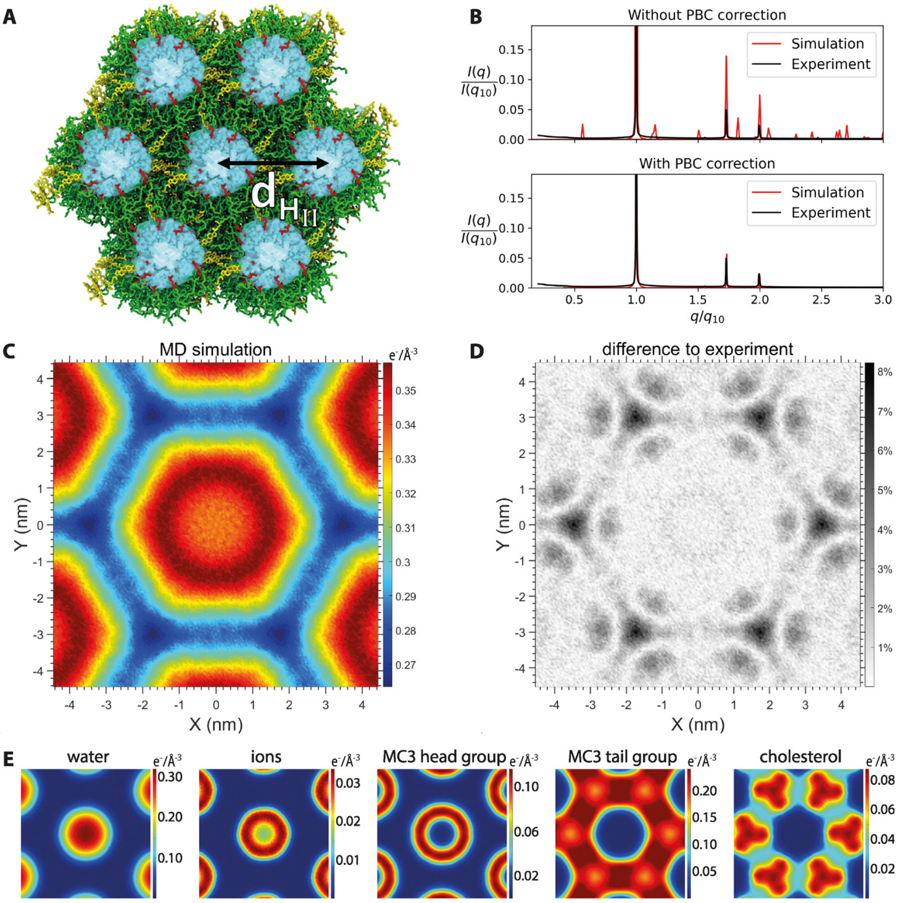

Fig. 2 Comparison of MD simulations and experimental data. (A) Simulation snapshot of the H_{II} phase. Water is shown in light blue, charged MC3 head groups in red, MC3 tails in green and cholesterol in yellow. $d_{H_{II}}$ indicates the distance between water columns. (B) Comparison of the scattering profiles obtained from MD simulations (red) and experiments (black) without periodicity corrections (top). After applying the methodology to correct scattering artifacts from periodic boundary conditions the simulated and experimental scattering profiles are in quantitative agreement (bottom) (C) 2D electron density profiles obtained from MD simulations. (D) Difference between the 2D electron density maps from simulations and experiments. (E) 2D electron density maps of the individual components obtained from the MD simulations. Higher resolution images are available in SI Fig. S4.

oriented along the *z*-axis. For the ionizable MC3 lipids, we used force field parameters, that were previously validated by neutron reflectometry and rigorously tested across multiple lipid phases, therefore the simulations focus exclusively on MC3 bulk phases.[19] For cholesterol, AMBER parameters derived from the lipid 17 force field[30] were used in combination with the TIP3P water model[31] and ion parameters from S. Mamatkulov & N. Schwierz.[32]

Following a steepest descent minimization, a 2 ns equilibration was performed to generate velocities and maintain the system at the desired temperature and pressure. The temperature was kept at 298 K using the Nose–Hoover thermostat with a time constant of 1.0 ps. The pressure was coupled semi-isotropically and maintained at 1.0 bar using the Berendsen barostat with a time constant of 1.0 ps. After equilibration a 1 μs production run was performed with a time step of 2 fs, keeping the former thermostat and employing the Parrinello–Rahman barostat with a time constant of 5.0 ps. van der Waals interactions and electrostatic interactions were cut-off at 1.2 nm and long-range electrostatics were evaluated using the particle Mesh Ewald method. The LINCS algorithm was used to constrain all bonds involving hydrogens. To correct for periodic boundary effects in the calculated scattering intensities, additional NVT simulations were carried out, which maintained a constant lattice spacing of 60 Å, as well as simulations of a multi-column system composed of 9 H_{II} columns in parallel, also simulated in the NVT ensemble. These simulations were 0.2 μs and 0.5 μs long respectively. The multi-column system was generated by extracting snapshots from the trajectory of a single H_{II} column at different time frames and combining them together in a 3 × 3 hexagonal lattice. A triclinic unit cell of length 180 Å and height 91.4 Å was used to define the periodic boundaries of the multi-column system. To avoid overlapping contacts and steric clashes, the larger system was energy minimized, equilibrated and simulated for 500 ns. A comprehensive list of all simulations performed in this study is provided in the SI (see Table S1). VMD[33] was used to visualize and generate snapshots of the trajectory, while MDAnalysis[34,35] was employed to analyze the trajectory. Generation of 2D electron density maps perpendicular to the Z-axis (*i.e.* the water column orientation) from the simulation trajectory (discarding the first 100 ns for equilibration) for the whole system and the individual components were done by MDAnalysis scripts.

2.2.1 Scattering intensity from MD. Molecular dynamic simulations provide a detailed temporal and spatial mapping of atomic coordinates, enabling a direct and straightforward computation of the theoretical scattering profiles from atomic positions. Mercury CCDC (Cambridge Crystallographic Data Centre) was used to calculate the X-ray scattering profiles from the MD simulations. The simulated X-ray scattering profiles were generated using the Cu-K$_\alpha$ radiation source of wavelength λ = 1.54056 Å for a 2θ range of 0.7–7°. Here, the scattering angle θ is related to the momentum transfer vector q *via* $q = \frac{4\pi}{\lambda}\sin(2\theta/2)$. The simulated H$_{\text{II}}$ phases were assumed to have a crystalline size of 1130 nm by fixing the broadness of the scattering peaks to 0.00781°. The peak width, defined by the full width at half maximum (FWHM), is related to the crystal domain size by the Scherrer equation. The random orientation of individual crystals are taken into account by using the powder diffraction technique.

However, additional peaks in the theoretical scattering profiles are observed due to the periodicity of the molecular system. MD simulations are typically performed using finite nanometer sized simulation boxes with periodic boundary conditions to mimic macroscopic systems. By construction, the initial system is identical to its periodic images. However, the periodic repetition leads to constructive interference at q values inversely proportional to the size of the simulation box. These scattering artifacts appear as additional peaks in the scattering profile (Fig. 2B). To remove these artifacts, a methodology tailored to the H$_{\text{II}}$ lipid phase was formulated and is presented below.

2.2.2 Removal of scattering artifacts from periodic boundary conditions. Given that periodic boundary conditions are applied along x, y and z directions in the 3D lattice, it is necessary to correct for the scattering artifacts arising in all three directions. We start by defining the Z axis as the direction parallel to the water column. To remove the additional interference peaks due to the periodicity along the Z direction, scattering profiles are calculated from the same NVT simulations but with a reduced box size of 5, 10 and 15% of the original system respectively. For a reduced box size, the position of the peaks shift to higher q values (*e.g.* for $L' = (9/10)L$ the peak at q will appear at $q' = (10/9)q$, see Fig. S2A). By contrast, the position of the peaks reflecting the hexagonal symmetry (q_{10}, q_{11} and q_{20}) remain at the same position. The corrected intensity profile is obtained by removing the shifting peaks and taking the minimum intensity at the symmetry peaks.

Artifacts arising from the periodicity in the XY plane are addressed by tiling the system along the XY plane, resulting in the creation of a multi-column H$_{\text{II}}$ phase. Since the first three peaks of the H$_{\text{II}}$ system appear at $q/q_{10} = 1, \sqrt{3}$ and 2, the box size has to be tripled to avoid overlap of the artifact peaks with the symmetry peaks. We calculate the scattering profile for the full 3 × 3 system and for a single subsystem. For the multi-column system with $L' = 3L$, the symmetry peaks split. For example, the q_{11} peak is shifted to lower q values with $q' = 1/3q$ (see Fig. S2B). The corrected intensity profile is again obtained by removing the shifting peaks and taking the minimum intensity at the symmetry peaks. Note that the q_{30} peak will still contribute to the q_{10} peak after tripling the system. However, since its intensity is very low the contribution is neglected. Finally, the scattering profiles were calculated for 20 distinct molecular snapshots sampled from the NVT simulation trajectory (Fig. S3).

2.3 Continuum model of the lipid–water interface

With the MD simulations we are able to calculate the water content of the MC3 bulk phase but for many different ionizable lipids there is no force field data available, so at the moment it is impossible to extend the MD simulations to those as well. In order to generalize the model without the need for extensive and lipid specific MD simulations, we developed a numerical continuum model that can be easily extended to different ionizable lipids as well. The model uses parameters calculated with ACD ChemSketch from literature data and fits radial scattering length density (SLD) distributions of water molecules as well as the lipid head- and tail-groups to a total SLD profile. The radial electron density curves can be converted to SLD profiles because for X-rays the SLD is proportional to the electron density. This generally enables the calculation of water content in inverse hexagonal lipid phases without the need for associated MD simulations.

The parameters calculated with ACD ChemSketch[36] are the molecular volumes of the lipid head group V_{head} and tail group V_{tail}. The scattering length density SLD$_{\text{tail}}$ was calculated using SasView 6[37] (see Table 1).

The SLD of water is taken from literature (SLD$_{\text{water}}$ = 9.45 × 10^{-4} nm^{-2}).[38] This continuum model assumes smooth distributions for water and lipid tail groups of a distinct shape based on the distributions observed in our MD simulations. The head group distribution is defined so that at each radius the volume fractions of all components add to one.

In detail the distribution base function of the water core is defined as

$$f_{\text{water,base}}(r) = \exp\left(-\ln(2)\left(\frac{r}{b_{\text{w}}}\right)^{\alpha_{\text{w}}}\right), \quad 0 < r < \frac{d}{2} \qquad (3)$$

Table 1 Continuum model parameters calculated with ACD ChemSketch[36] and SasView 6[37]

CIL	V_{head}[a] [nm^3]	V_{tail}[b] [nm^3]	SLD$_{\text{tail}}$[b] [10^{-4} nm^2]
SM-102	0.411	0.862	7.46
MC3	0.183	1.019	8.02
KC2	0.184	1.019	8.02
DD	0.123	1.039	7.70

[a] Head group definitions: SM-102 $C_{16}H_{29}NO_5$, MC3 $C_6H_{13}NO_2$, KC2 $C_7H_{15}NO_2$, DD $C_5H_{13}NO_2$. [b] Tail group definitions: SM-102 $C_{28}H_{60}$, MC3 $C_{37}H_{68}$, KC2 $C_{37}H_{68}$, DD $C_{36}H_{68}$.

with r as the radial variable, d as the center-center distance of two neighboring water cylinders and both b_w and α_w as fitting parameters. Similarly the distribution base function of the lipid tail groups is defined as

$$f_{\text{tail,base}}(r) = \exp\left(-\ln(2)\left(\frac{r-d/2}{b_t}\right)^{\alpha_t}\right), \quad 0 < r < \frac{d}{2} \tag{4}$$

with α_t as an additional fitting parameter. b_t is not a free parameter but is used to adjust the ratio of volume fractions of head groups and tail groups to the same ratio as their molecular volumes in order to have the same number of head and tail groups.

These base functions have to be stretched depending on the angle θ up to $r = \frac{d}{\sqrt{3}}$ to account for the hexagonal shape of the unit cell. The stretched functions are then integrated over θ to get back to a pure radius dependency. Refer to the SI for more details. Since the distribution functions must add to unity everywhere, the stretched radial distribution of the head groups is then defined as

$$\begin{aligned} &f_{\text{h,stretched}}(r) = 1 - \left(f_{\text{w,stretched}}(r) + f_{\text{t,stretched}}(r)\right) \\ &\text{with} \quad 0 < r < \frac{d}{\sqrt{3}} \end{aligned} \tag{5}$$

The stretched distribution functions are then multiplied by their respective molecular SLD and added together for all three components. By adjusting the fitting parameters b_w, α_w, α_t as well as the molecular SLD of the lipid head group SLD_{head}, the model can be fitted to SLD profiles and allows for the calculation of the volume fractions of its components like the water volume fraction ϕ_w. SLD_{head} could also be calculated by ACD ChemSketch, but the model only fits properly if SLD_{head} is left as a fitting parameter. This is a slight imperfection of the model, but might be caused by the changing charge of the head group depending on the pH and buffer.

Additionally the area per head group S can be calculated according to M. W. Tate & S. M. Gruner[39] using

$$S = \frac{2V_{\text{lip}}\phi_w}{b_w(1-\phi_w)} \tag{6}$$

V_{lip} is the lipid volume ($V_{\text{lip}} = V_{\text{head}} + V_{\text{tail}}$, see Table 1) and b_w is the radius at which the water distribution reaches 50% of its maximum value (see eqn (3)).

2.4 Dynamic vapor sorption

To validate the water contents derived from the combined continuum model/SAXS approach we aim to determine water content using an alternative experimental technique. Dynamic vapor sorption (DVS) is a gravimetric technique used to measure the amount of water absorbed or desorbed by a sample. The technique involves suspending the sample on a highly sensitive microbalance in a temperature-controlled chamber followed by systematic regulation of the relative humidity (%RH) by a mass flow controller. The %RH is changed once the sample reaches a state of equilibrium moisture content (EMC) where there is no longer any change in the amount of water absorbed/desorbed by the sample. EMC is defined as the ratio of water weight to dry weight of the sample and is plotted against %RH to obtain vapor sorption isotherms. Empty bulk phases of DLin-MC3-DMA, DLin-KC2-DMA and DLinDMA at pH 5.5 were prepared using the sequential buffers: 50 mM citrate pH 3.0, PBS pH 7.4 and Mcllvaines buffer 5.5. DVS analysis was performed using an instrument from surface measurement system, DVS resolution. A bulk phase sample (approximately 15–25 mg) was transferred to a tared sample holder. The instrument was purged with nitrogen, 200 mL min^{-1}, at 25 °C and data was collected at different %RH. Starting at 95%RH and going stepwise down to 80%RH, using 2.5%RH steps and finally to 0%RH to obtain the dry weight of the sample. The %RH was changed manually when the equilibrium was reached and the signal showed no drift. From the measure weights and the dry weight together with density of each lipid the water volume fraction was calculated against %RH. The extrapolation to 100%RH was carried by deriving eqn (7) below.[40]

$$\phi_w(a_w) = \frac{a_w\phi_w}{a_w\phi_w + \dfrac{(1-\phi_w)(1-a_wq)(1+a_w(q_i-q))}{(1-q)(1+q_i-q)}} \tag{7}$$

in which a_w = water activity (%RH/100), ϕ_w = water volume fraction at $a_w = 1$, and q_1 and q, from the statistical weights of the first layer (a_wq_1) and all other layers (a_wq), were treated as fitting parameters.

This extrapolation generally exhibits large margins of error but it is necessary since going beyond 95%RH could cause condensation on the sample. Additionally, obtaining data for a single point on the isotherm requires a significant amount of time, making this approach impractical for a large number of samples. While DVS is not a flawless technique, it can serve as a useful experimental tool to validate and complement the results obtained from the combined MD-SAXS approach.

3 Material

DLin-MC3-DMA (*O*-(*Z*,*Z*,*Z*,*Z*-heptatriaconta-6,9,26,29-tetraem-19-yl)-4-(*N*,*N*-dimethylamino) butanoate; $C_{43}H_{79}NO_2$; mw 642.09 g mol^{-1}; >99% purity), DLin-KC2-DMA (2,2-dilinoleyl-4-(2-dimethylaminoethyl)-[1,3]-dioxolane; $C_{43}H_{79}NO_2$; mw 642.09 g mol^{-1}; >99% purity), and DLinDMA (1,2-dilinoleyloxy-3-dimethylaminopropane; $C_{41}H_{77}NO_2$; mw 616.06 g mol^{-1}; >99% purity) were synthesized at AstraZeneca.

Cholesterol ($C_{27}H_{45}OH$; 386.66 g mol^{-1}; >98% purity), potassium phosphate monobasic (KH_2PO_4; >99% purity), sodium chloride (NaCl; >99% purity), disodium phosphate (Na_2HPO_4; >99% purity), citric acid ($C_6H_8O_7$; >99.5% purity), sodium citrate dihydrate ($C_6H_5Na_3O_7\cdot 2H_2O$; >99% purity), and ethanol (C_2H_6O; >99.5% purity) were purchased from Sigma-Aldrich.

4 Results

4.1 Validation of the MD simulations

To validate and test the reliability of the MD simulations, we compare the water content obtained from the MD simulations with the experimental water content and the spatial distribution of the ionizable lipids and cholesterol around the water column.

4.1.1 Volume fraction of water. The water content in our MD simulations were calculated using three different methods. The first method involved calculating the water volume fraction ϕ_w from the radial distributions as described in our previous work.[5] The second method assumes an empirical water volume of 30 Å^3 to calculate the volume fraction based on the number of water molecules in the simulation box.

The third method utilizes the procedure developed by Petrache *et al.*[41] to generate the volume fractions and molecular volumes of the components that make up the H_{II} system (see SI Section S4 for further details). The resulting molecular volumes obtained for the individual components MC3, cholesterol and water are 1190 Å^3, 632.7 Å^3 and 28.7 Å^3 respectively. Using a three component splitting (MC3, cholesterol, water + ions) resulted in the water + ions component having a molecular volume of 29.9 Å^3. Based on these molecular volumes, the volume fraction of individual components were calculated and are listed in Table 2.

The computationally derived water content aligns closely with the experimental measurement as we show below, suggesting that the MD simulations provide an excellent representation of the system.

4.1.2 Electron densities and scattering profiles from MD simulations. To further validate the molecular model employed in the MD simulations, we directly compared the scattering intensities (Fig. 2B) and the two-dimensional (2D) electron density maps obtained from simulations and experiments (Fig. 2C and D). The corrected theoretical scattering profiles exhibit excellent quantitative agreement with the experimental data, accurately reproducing the measured intensities within the experimental errors (Fig. 2B, bottom). It is important to note, however, that this level of agreement is only achieved after correcting for scattering artifacts introduced by the periodic boundary conditions inherent to the MD simulations (see Section 2 for details).

The 2D electron density maps from the simulations and the experiments exhibit a characteristic hexagonal symmetry, with a prominent ring of highest electron density surrounding the central water tube (Fig. 2). The differences between the simulated and experimental electron density maps are minimal, indicating strong agreement in the 2D spatial distributions. This concordance is consistent with the previously observed similarity in the scattering intensities (Fig. 2B). Note that the noise level in the experimental electron density map is lower compared to the simulations due to the smooth interpolation used. The electron densities obtained from the MD simulations can be split into electron densities of the individual components (Fig. 2E and Fig. S5). Interestingly the distribution of dissolved ions does not completely follow the distribution of water, but forms a ring of highest density close to the MC3 head groups, attracted by its charges. Most of the distributions are radially symmetric except cholesterol and the MC3 tails. In order to fill the gaps between three water channels, the MC3 tails have to stretch, causing a shift from a round to a hexagonal shape in the total electron density. Additionally in our experiments we see that the excess of cholesterol in our system phase separates as large crystals of cholesterol monohydrate. These are both often visible in our SAXS data as a sharp peak at $q = 1.85$ Å^{-1} and as quadrangular platelets in microscopy data. In the MD simulations this effect is not taken into account and the cholesterol content is therefore likely overestimated. Here, the cholesterol accumulates in the corners between three water cylinders, which probably causes the difference between MD simulation and experimental data at this location (Fig. 2D).

In addition to the 2D electron density maps, generation of theoretical X-ray scattering profiles from MD simulation achieves direct comparison with the experimental scattering profiles. However prior correction of scattering artifacts are necessary as per the procedure described in the Methods section. The corrected theoretical scattering profiles exhibit excellent quantitative agreement with the experimental scattering profiles, reproducing the experimental intensities within the error of the simulations (Fig. 2B).

In summary, the scattering intensities (Fig. 2B) and 2D electron density maps (Fig. 2C and D) derived from simulations and experiments show remarkably good agreement, highlighting recent advancements in molecular modeling[5,19] and underscoring the importance of direct, quantitative comparisons between simulated and experimental data. To model the low pH conditions that favor the H_{II} phase, we assumed full protonation of the ionizable lipid residues. However, it is possible that the actual protonation degree in the complex lipid environment is lower.[20] Despite this simplification, the close agreement between simulated and experimental scattering profiles and electron densities supports the accuracy and robustness of the molecular model.

Table 2 Volume fractions of different components of the system obtained using three different approaches

Component	ϕ_w (method 1)	ϕ_w (method 2)	ϕ_w (method 3)
MC3	63.0%	—	62.3%
Cholesterol	12.3%	—	11.1%
Water	24.0%	25.1%	24.0%
Water + ions	24.6	—	26.5%

4.2 Validation of the continuum model

Validation of our continuum model was realized in two independent ways. The first one is by applying the model to total SLD profiles from MD simulations for MC3 bulk phases at different water contents (see Table 3). To obtain meaningful and controlled validation, the MC3 bulk phase in the MD simulations was assumed to be fully protonated, given that

Table 3 Validation of continuum model against different MD simulations by comparing the water content. Adjusting the MD simulation to the lattice spacing of our experimental data led to 12 water molecules per CIL[5]

Water molecules/CIL	ϕ_w (MD simulation) (%)	ϕ_w (continuum model) (%)
12	24.6	25.5
13	25.3	25.6
18	32.6	32.7

the exact protonation states of MC3 in lipid mesophases at specific pH conditions remain unknown. In order to avoid differences caused by cholesterol in the three channel corner in the range $d/2 < r < d/\sqrt{3}$, we took the SLD profiles in the direction towards the nearest neighboring water channel center. Here the radial electron density profiles of experimental data and MD simulation match quantitatively. From the MD simulations we are able to split the total electron density profile into three distinct components: the water including its dissolved ions, the MC3 head group and the MC3 tails including cholesterol (Fig. 3). Both water contents agreed in all three comparisons with less than one percent difference.

We then applied the continuum model to the total SLD profiles from our experimental data as shown in Fig. 4A. The continuum model fits the SLD profile extracted from experimental data almost perfectly by adding the shown distributions of water molecules, lipid head groups and lipid tail groups together. This allows us to calculate the water content for MC3 bulk phases at different pH values as well as for three additional ionizable lipids: DLin-KC2-DMA (KC2), DLinDMA (DD) and SM-102.

According to our continuum model, DD has the highest water content of 32.0 ± 2.5%, followed by KC2 (24.7 ± 1.1%) and MC3 (24.7 ± 1.0%). The water content of MC3 was consistent with the value obtained from MD simulations (24.6%). SM-102 has the lowest water content with only 16.2 ± 2.0%. The calculated water contents are independent of pH within the margins of error. There is a small trend of reducing water content with increasing pH for DD, but the margins of error are too big for the trend to be significant.

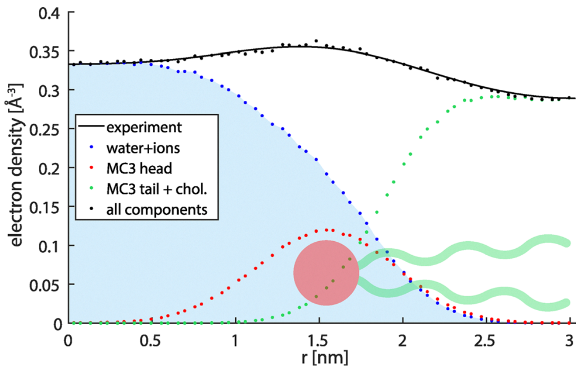

Fig. 3 Total scattering length density (SLD) and splitting into components. Radial electron density profile in the direction towards a neighboring water channel, starting from the center of the water tube at r = 0. The electron densities are split further into individual components.

The second approach to validate our continuum model is by comparing these results to DVS measurements. The extrapolated water volume fractions from DVS measurements for MC3, KC2 and DD lipids are 22.8 ± 1.7%, 24.6 ± 0.9% and 25.4 ± 0.8% as shown in Fig. 4B. Even though the observed trends in water content are consistent with the continuum model, minor deviations in magnitude with the expected water volume fractions are observed. This may be due to the reliance on extrapolation to 100%RH from a limited number of data points obtained from the time-intensive DVS measurements, further highlighting the importance of integrating multiple computational and experimental methodologies to achieve reliable and consistent outcomes. An overview of the calculated water content for all four lipids as well as the results from DVS and MD are presented in Fig. 4C.

The average area per head group over our pH range, weighted by their inverse errors, is for SM-102 0.57 ± 0.5 nm^2, followed by MC3 (0.54 ± 0.2 nm^2), KC2 (0.53 ± 0.2 nm^2) and DD (0.51 ± 0.3 nm^2) (see Fig. 4D). The area per head group is mostly pH independent for MC3 and KC2 within their margins of error. SM-102 seems to have a decreasing area per head group with decreasing pH, but a constant area is also possible within the margins of error. Only DD has an increasing area per head group with decreasing pH.

The average hexagonal lattice spacing is the lowest for SM-102 with only 4.50 ± 0.13 nm, followed by MC3 with 6.01 ± 0.07 nm, KC2 with 6.10 ± 0.06 nm and DD with 7.62 ± 0.22 nm.

5 Discussion and conclusions

The combination of experimental SAXS data and MD simulations enables the determination of water content in inverse hexagonal bulk phases containing MC3. With the addition of the proposed continuum model and additional SAXS measurements the water content of different inverse hexagonal bulk phases is estimated. We find a defined order of water content as a function of CIL with DLinDMA (DD) > DLin-MC3-DMA (MC3), DLin-KC2-DMA (KC2) > SM-102. The order is inversely correlated to the reported transfection efficiencies[3,5] that follow DLinDMA (DD) < DLin-KC2-DMA (KC2), DLin-MC3-DMA (MC3) < SM-102. The observed systematic trend hints towards a possible functional link between both properties. In general, our combined structural analysis allows for measurement of the water content of any CIL bulk phase that exhibits H_{II} bulk phase based on SAXS data and the proposed continuum model. Following the proposed structure–function relation, water content together with a pH-sensitive phase transition could possibly prove to be a reliable indicator of transfection efficiency.

The continuum model developed here should be useful as a close proxy of the electron density profile for the lipid and water moiety. However, while the model shows good agreement with MD simulations it does still exhibit slight imperfections. The necessity to use the head group scattering length density

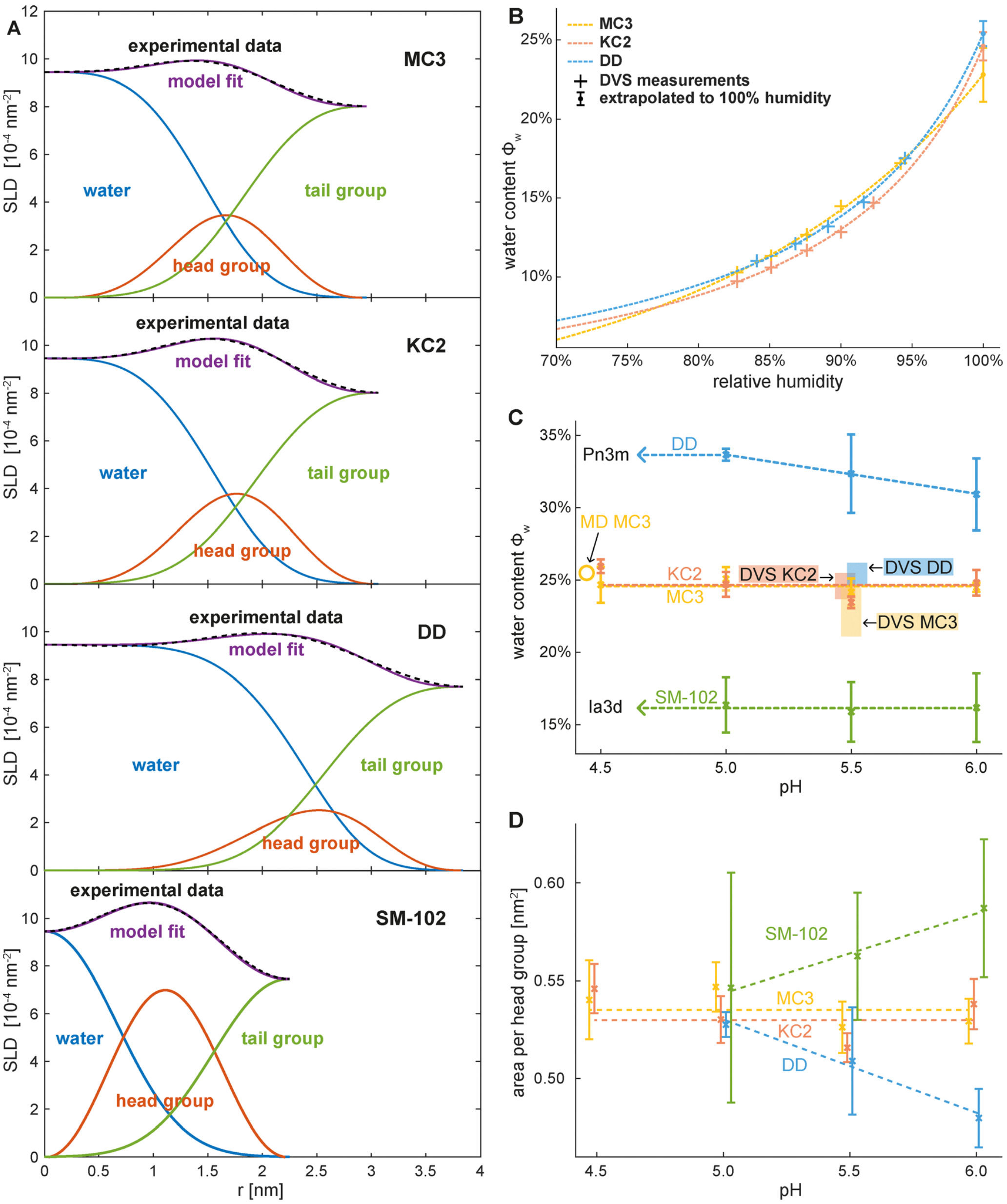

Fig. 4 Application of continuum model on SLD profiles of experimental data and results. (A) Radial SLD profiles from experimental data of MC3, KC2, DD, and SM-102, here shown as a dashed black lines, are fitted by continuum model (purple) which consists of the water distribution (blue), head group distribution (red) and tail group distribution (green). (B) Dynamic vapor sorption (DVS) measurements of MC3, KC2 and DD at pH 5.5 are extrapolated to 100% relative humidity resulting in estimated water contents for MC3 (22.8 ± 1.7%), KC2 (24.6 ± 0.9%) and DD (25.4 ± 0.8%). (C) Summarized results from the continuum model, DVS measurements and MD simulations. The DVS measurements of DD do not agree with our continuum model within their margins of error which might be due to the reliance on extrapolation to 100%RH from a limited number of DVS data points. According to our continuum model SM-102 has the lowest water content with 16.2 ± 2.0%, followed by MC3 (24.7 ± 1.0%) and KC2 (24.7 ± 1.1%). DD has the highest water content and is the only lipid that increases its water content with decreasing pH. The MD simulation with fully ionized MC3 was calibrated to 24.6% water content. Below pH 5.0 the bulk phases of SM-102 and DD transition from the H_{II} phase to bicontinuous phases (*Ia3d* and *Pn3m*). (D) The area per lipid head group within the H_{II} phase was calculated with our continuum model. Dotted lines are added as a guide to the eye. Within their margins of error the area per head group is independent of pH for MC3 and KC2. For SM-102 it displays an increasing area per head group with increasing pH and for DD the area is decreasing.

SLD_{head} as a fitting parameter although it could instead be calculated with ACD ChemSketch indicates inaccuracies of the fit. Our MD simulations themself show also slight differences compared to experimental data coming from the cholesterol distribution. From experiments we know that excessive cholesterol forms large cholesterol monohydrate crystals that grow orders of magnitude larger than the lipid structure unit cells making it impossible to be accurately simulated. Although these cholesterol crystals are probably not part of the actual bulk phase inside lipid nanoparticles, its obvious excess makes it difficult to predict the correct amount of cholesterol for the simulations.

Initially, we expected to observe an electrostatically driven swelling of the ionizable mesophases at lower pH, caused by the increasing charge of the head groups. Such behavior is well documented for ionizable lamellar phases. However, swelling of the hexagonal phases was barely detectable and only observed for DD. In contrast, SM-102 even showed the opposite trend, though within large margins of error. Furthermore, the bulk phase water content of all lipids except DD appeared to be independent of pH. For DD, a slight increase in water content with decreasing pH was observed, which can be explained by the reduced absolute curvature resulting from the increasingly charged head groups.

We propose that the spacing of hexagonal phases is largely insensitive to pH because the elastic curvature energy of the lipid tail region dominates over electrostatic contributions of the head group. In other words, the energetic cost of lipid deformation prevents electrostatic swelling of the hexagonal phase. This interpretation aligns with our hypothesis that the micellar-to-hexagonal phase transition of the excess lipid fraction in LNPs is critical in the initial endosomal fusion process. In this context, it is noteworthy that the elastic energy depends strongly on curvature, which would explain why ionizable lipid mesophases with high curvature, *i.e.* small hexagonal lattice spacing or low water content, are more potent to drive fusion than those with lower curvature (larger spacings), such as DD.

Compared with DD, all the other tested lipids form denser structures; notably SM-102 has the lowest water content and highest transfection efficiency. We speculate that the micellar-to-hexagonal transition at decreasing pH values initiates the onset of fusion due to the rearrangements in topological discontinuous structures. Note that, while fusion disrupts the endosomal compartment, it does not necessarily coincide with the release of mRNA from its hexagonal complexed phase. The mRNA–lipid salt complex is likely to dissolve more gradually once released into the cytosol.

In summary, SAXS analysis combined with MD simulations and a newly derived continuum model has proven to be a reliable method to determine the water content of inverse hexagonal bulk phases. The approach can be extended to other ionizable lipids that show H_{II} bulk phase signatures in SAXS. The bulk phase water content, along with the pH-dependent phase transition behavior of ionizable lipids, are critical parameters for estimating their transfection efficiency in future applications.

Author contributions

L. L., N. S. and J. O. R. designed research; J. P., E. K., V. M., and M. B. performed research; A. S. and N. S. performed simulations; J. P., A. S., E. K., V. M., M. B., and J. W. analyzed data and J. P., A. S., N. S., M. R., J. W., L. L., N. S., and J. O. R. wrote the paper.

Conflicts of interest

V. M., M. B., and L. L. are employed by AstraZeneca R&D Gothenburg.

Data availability

Raw SAXS data can be accessed *via* DOI: **10.5282/ubm/data.689**.

Additional information and high resolution images can be found in the supplementary information (SI). Supplementary information is available. See DOI: **https://doi.org/10.1039/d5sm00666j**.

Acknowledgements

This work was supported by the German Federal Ministry of Education and Research through BMBF Project 05K18WMA and 05K18EZA within the framework of the Swedish–German research collaboration Röntgen-Ångström Cluster as well as by the Deutsche Forschungsgemeinschaft (Project No. 201269156, SFB1032-B01). The authors gratefully acknowledge the scientific support and HPC resources provided by the Erlangen National High Performance Computing Center (NHR@FAU) of the Friedrich-Alexander-Universität Erlangen-Nürnberg (FAU) under the NHR project b119ee and b253ee. NHR funding is provided by federal and Bavarian state authorities. NHR@FAU hardware is partially funded by the German Research Foundation (DFG) – 440719683. Deutsches Elektronen-Synchrotron (DESY) P12 BioSAXS EMBL and P62 SAXSMAT beamlines at PETRA III (Hamburg, Germany), and the beamline scientists Clement E. Blanchet and Xiao Sun are greatly acknowledged for synchrotron beamtime. M. R. is particularly grateful for the support provided by Gerome Vancuylenberg in the initial analysis of the electron density maps, who has been supported by the EPSRC scholarship grant (EP/S023631/1). This work also benefited from the use of the SasView application, originally developed under NSF award DMR-0520547. SasView contains code developed with funding from the European Union's Horizon 2020 research and innovation programme under the SINE2020 project, grant agreement no 654000. This manuscript is dedicated to Erich Sackmann, who pioneered lipid membrane biophysics and advised structural research on biological systems using X-ray and neutron scattering.

Notes and references

1 P. R. Cullis and M. J. Hope, *Mol. Ther.*, 2017, **25**, 1467–1475.
2 M. Jayaraman, S. M. Ansell, B. L. Mui, Y. K. Tam, J. Chen, X. Du, D. Butler, L. Eltepu, S. Matsuda, J. K. Narayanannair, K. G. Rajeev, I. M. Hafez, A. Akinc, M. A. Maier, M. A. Tracy,

P. R. Cullis, T. D. Madden, M. Manoharan and M. J. Hope, *Angew. Chem., Int. Ed.*, 2012, **51**, 8529–8533.

3 K. J. Hassett, K. E. Benenato, E. Jacquinet, A. Lee, A. Woods, O. Yuzhakov, S. Himansu, J. Deterling, B. M. Geilich, T. Ketova, C. Mihai, A. Lynn, I. McFadyen, M. J. Moore, J. J. Senn, M. G. Stanton, Ö. Almarsson, G. Ciaramella and L. A. Brito, *Mol. Ther.–Nucleic Acids*, 2019, **15**, 1–11.

4 G. Tesei, Y.-W. Hsiao, A. Dabkowska, G. Grönberg, M. Y. Arteta, D. Ulkoski, D. J. Bray, M. Trulsson, J. Ulander, M. Lund and L. Lindfors, *Proc. Natl. Acad. Sci. U. S. A.*, 2024, **121**, e2311700120.

5 J. Philipp, A. Dabkowska, A. Reiser, K. Frank, R. Krzysztoń, C. Brummer, B. Nickel, C. E. Blanchet, A. Sudarsan, M. Ibrahim, S. Johansson, P. Skantze, U. Skantze, S. Östman, M. Johansson, N. Henderson, K. Elvevold, B. Smedsrød, N. Schwierz, L. Lindfors and J. O. Rädler, *Proc. Natl. Acad. Sci. U. S. A.*, 2023, **120**, e2310491120.

6 Z. Xu, J. M. Seddon, P. A. Beales, M. Rappolt and A. I. I. Tyler, *J. Am. Chem. Soc.*, 2021, **143**, 16556–16565.

7 J. M. Seddon, *Cells*, 2025, **14**, 716.

8 M. Rappolt, A. Hickel, F. Bringezu and K. Lohner, *Biophys. J.*, 2003, **84**, 3111–3122.

9 B. Kollmitzer, P. Heftberger, M. Rappolt and G. Pabst, *Soft Matter*, 2013, **9**, 10877.

10 Š. Perutková, M. Daniel, M. Rappolt, G. Pabst, G. Dolinar, V. Kralj-Iglič and A. Iglič, *Phys. Chem. Chem. Phys.*, 2011, **13**, 3100–3107.

11 G. Vancuylenberg, A. Sadeghpour, A. I. I. Tyler and M. Rappolt, *Soft Matter*, 2023, **19**, 8519–8530.

12 M. F. Trollmann and R. A. Böckmann, *Biophys. J.*, 2022, **121**, 3927–3939.

13 W. Wang, S. Feng, Z. Ye, H. Gao, J. Lin and D. Ouyang, *Acta Pharm. Sin. B*, 2022, **12**, 2950–2962.

14 A. Hardianto, Z. S. Muscifa, W. Widayat, M. Yusuf and T. Subroto, *Molecules*, 2023, **28**, 4836.

15 X. Fernandez-Luengo, J. Camacho and J. Faraudo, *Nanomaterials*, 2017, **7**, 461.

16 A. P. Singh, H. Tanaka, Y. Miyazaki, S. Nagano and W. Shinoda, *J. Chem. Theory Comput.*, 2025, **21**, 6226–6238.

17 A. P. Singh, H. Tanaka, Y. Miyazaki and W. Shinoda, *J. Phys. Chem. B*, 2025, **129**, 7939–7950.

18 C. Carucci, J. Philipp, J. A. Müller, A. Sudarsan, E. Kostyurina, C. E. Blanchet, N. Schwierz, D. F. Parsons, A. Salis and J. O. Rädler, *ACS Nano*, 2025, **19**, 10829–10840.

19 M. Ibrahim, J. Gilbert, M. Heinz, T. Nylander and N. Schwierz, *Nanoscale*, 2023, **15**, 11647–11656.

20 M. Grava, M. Ibrahim, A. Sudarsan, J. Pusterla, J. Philipp, J. O. Rädler, N. Schwierz and E. Schneck, *J. Chem. Phys.*, 2023, **159**, 154706.

21 M. P. K. Frewein, M. Rumetshofer and G. Pabst, *J. Appl. Crystallogr.*, 2019, **52**, 403–414.

22 G. Pabst, M. Rappolt, H. Amenitsch and P. Laggner, *Phys. Rev. E: Stat. Phys., Plasmas, Fluids, Relat. Interdiscip. Top.*, 2000, **62**, 4000–4009.

23 C. E. Blanchet, A. Spilotros, F. Schwemmer, M. A. Graewert, A. Kikhney, C. M. Jeffries, D. Franke, D. Mark, R. Zengerle, F. Cipriani, S. Fiedler, M. Roessle and D. I. Svergun, *J. Appl. Crystallogr.*, 2015, **48**, 431–443.

24 S. Haas, X. Sun, A. L. C. Conceição, J. Horbach and S. Pfeffer, *J. Synchrotron Radiat.*, 2023, **30**, 1156–1167.

25 P. Mariani, V. Luzzati and H. Delacroix, *J. Mol. Biol.*, 1988, **204**, 165–189.

26 M. Rappolt, A. Hodzic, B. Sartori, M. Ollivon and P. Laggner, *Chem. Phys. Lipids*, 2008, **154**, 46–55.

27 P. E. Harper, D. A. Mannock, R. N. Lewis, R. N. McElhaney and S. M. Gruner, *Biophys. J.*, 2001, **81**, 2693–2706.

28 M. J. Abraham, T. Murtola, R. Schulz, S. Páll, J. C. Smith, B. Hess and E. Lindahl, *SoftwareX*, 2015, **1–2**, 19–25.

29 S. Park, Y. K. Choi, S. Kim, J. Lee and W. Im, *J. Chem. Inf. Model.*, 2021, **61**, 5192–5202.

30 C. J. Dickson, B. D. Madej, Å. A. Skjevik, R. M. Betz, K. Teigen, I. R. Gould and R. C. Walker, *J. Chem. Theory Comput.*, 2014, **10**, 865–879.

31 W. L. Jorgensen, J. Chandrasekhar, J. D. Madura, R. W. Impey and M. L. Klein, *J. Chem. Phys.*, 1983, **79**, 926–935.

32 S. Mamatkulov and N. Schwierz, *J. Chem. Phys.*, 2018, **148**, 074504.

33 W. Humphrey, A. Dalke and K. Schulten, *J. Mol. Graphics*, 1996, **14**, 33–38.

34 R. J. Gowers, M. Linke, J. Barnoud, T. J. E. Reddy, M. N. Melo, S. L. Seyler, J. Domański, D. L. Dotson, S. Buchoux, I. M. Kenney and O. Beckstein, Proceedings of the 15th Python in Science Conference, 2016, pp. 98–105.

35 N. Michaud-Agrawal, E. J. Denning, T. B. Woolf and O. Beckstein, *J. Comput. Chem.*, 2011, **32**, 2319–2327.

36 ChemSketch, version 2022.1.2, Advanced Chemistry Development, Inc. (ACD/Labs), Toronto, ON, Canada, **https://www.acdlabs.com**, 2022.

37 SasView, version 6.0.0, **https://www.sasview.org**, accessed 24 October 2024.

38 B. Nagy, M. Campana, Y. N. Khaydukov and T. Ederth, *Langmuir*, 2022, **38**, 1725–1737.

39 M. W. Tate and S. M. Gruner, *Biochemistry*, 1989, **28**, 4245–4253.

40 D. Marsh, *Biophys. J.*, 2011, **101**, 2704–2712.

41 H. Petrache, S. Feller and J. Nagle, *Biophys. J.*, 1997, **72**, 2237–2242.

Electronic Supplementary Information

Combining SAXS Analysis and MD Simulation to Determine Structure and Hydration of Ionizable Lipid Hexagonal Phases

Julian Philipp, Akhil Sudarsan, Ekaterina Kostyurina, Viktoriia Meklesh,
Monica Berglund, Michael Rappolt, Jan Westergren,
Lennart Lindfors, Nadine Schwierz, Joachim O. Rädler

1 Experimental 2D Electron Density Maps

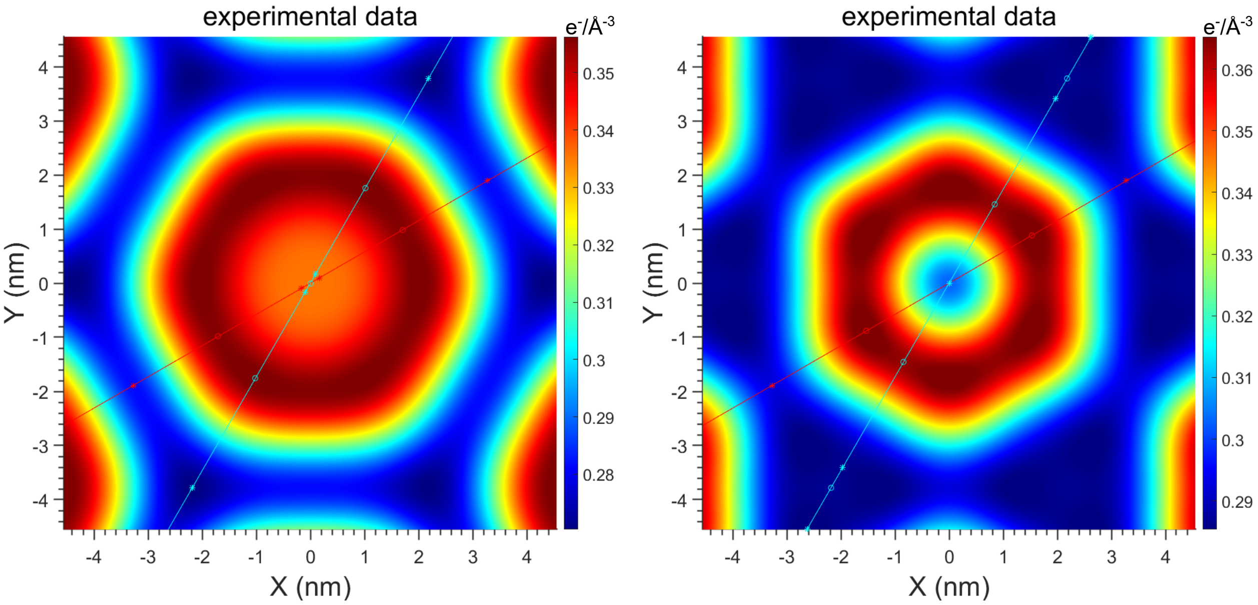

Figure S1 Electron density maps of DLin-DMA at pH 5.0 calculated with either (+1,-1,-1,+1,+1,+1,+1) (left side) or (+1,-1,-1,-1,+1,+1,+1) (right side). For (+1,-1,-1,-1,+1,+1,+1) this results in a 30° rotated hexagonal lipid tube with an unreasonable low electron density in the middle. The rotated hexagon also creates large voids between three tubes which would be energetically unfavorable.

2 Correction of Scattering Artifacts in MD Simulations

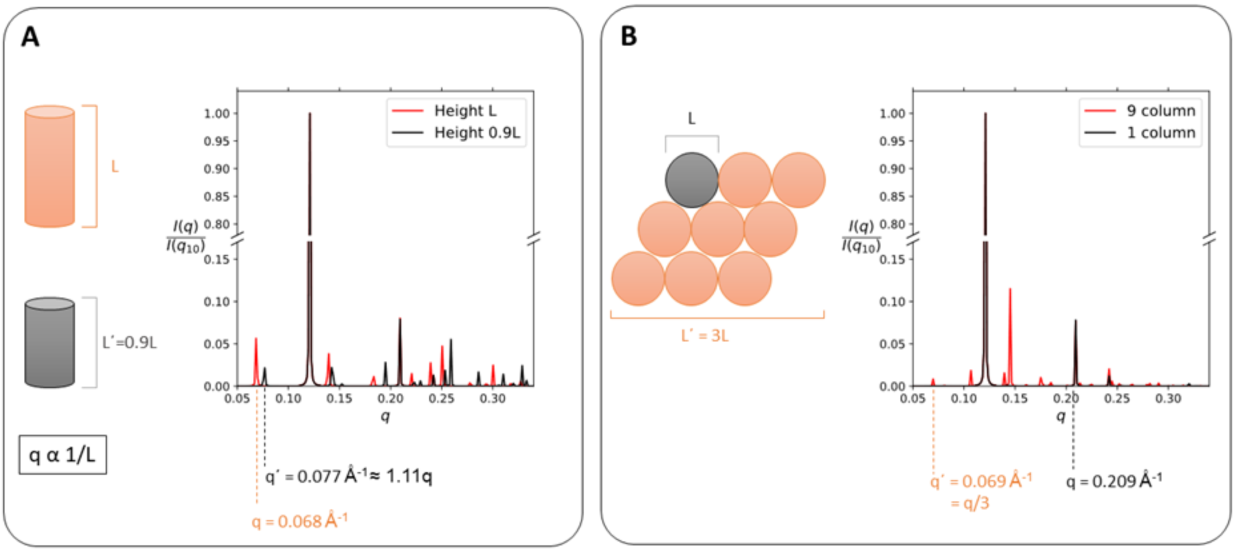

Figure S2 The methodology to remove scattering artifacts arising from periodic boundary conditions in MD simulations involves correcting for the periodicity along the z and the xy directions. (**A**) To remove the additional peaks along the z direction, scattering profiles were generated for the same system but with a reduced box size along z ($L' = 0.9L$). This shifts the additional peak at q for the original system to $q' = 1.11q$ for the reduced system, while preserving the symmetry-related peaks. The corrected intensity profile was obtained by removing the shifted peaks and taking the minimum intensity at the symmetry peak position. (**B**) Periodicity in the xy plane was corrected by tiling the system along the xy plane, creating a multi-column H_{II} phase with an extended box length of $L' = 3L$. Comparison of the scattering profiles for the single and multi-column H_{II} phase show that the symmetry peaks shift from q for the former to a lower value of $q' = 0.33q$ for the latter. The corrected intensity profile is obtained by removing the shifting peaks and taking the minimum intensity at the symmetry peaks.

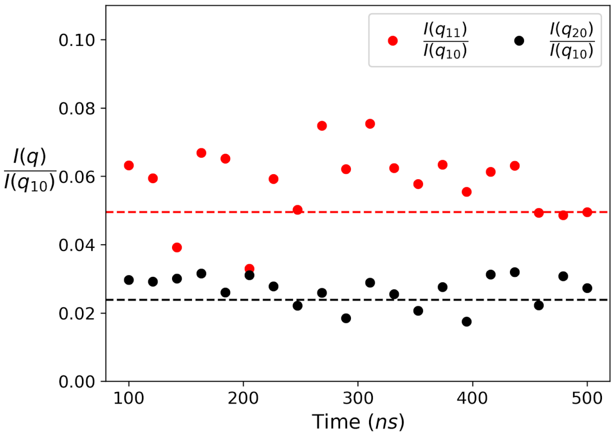

Figure S3 Comparison of the intensity ratios of q_{11} (red circles) and q_{20} (black circles) peaks relative to the primary q_{10} peak, computed for 20 snapshots over the course of the MD simulation after applying the correction procedure for artifacts arising from periodic boundary conditions. The experimentally derived intensity ratios for the q_{11} and q_{20} peaks relative to the q_{10} peak are represented as red and black dotted lines respectively.

3 2D Electron Density Maps from MD Simulations

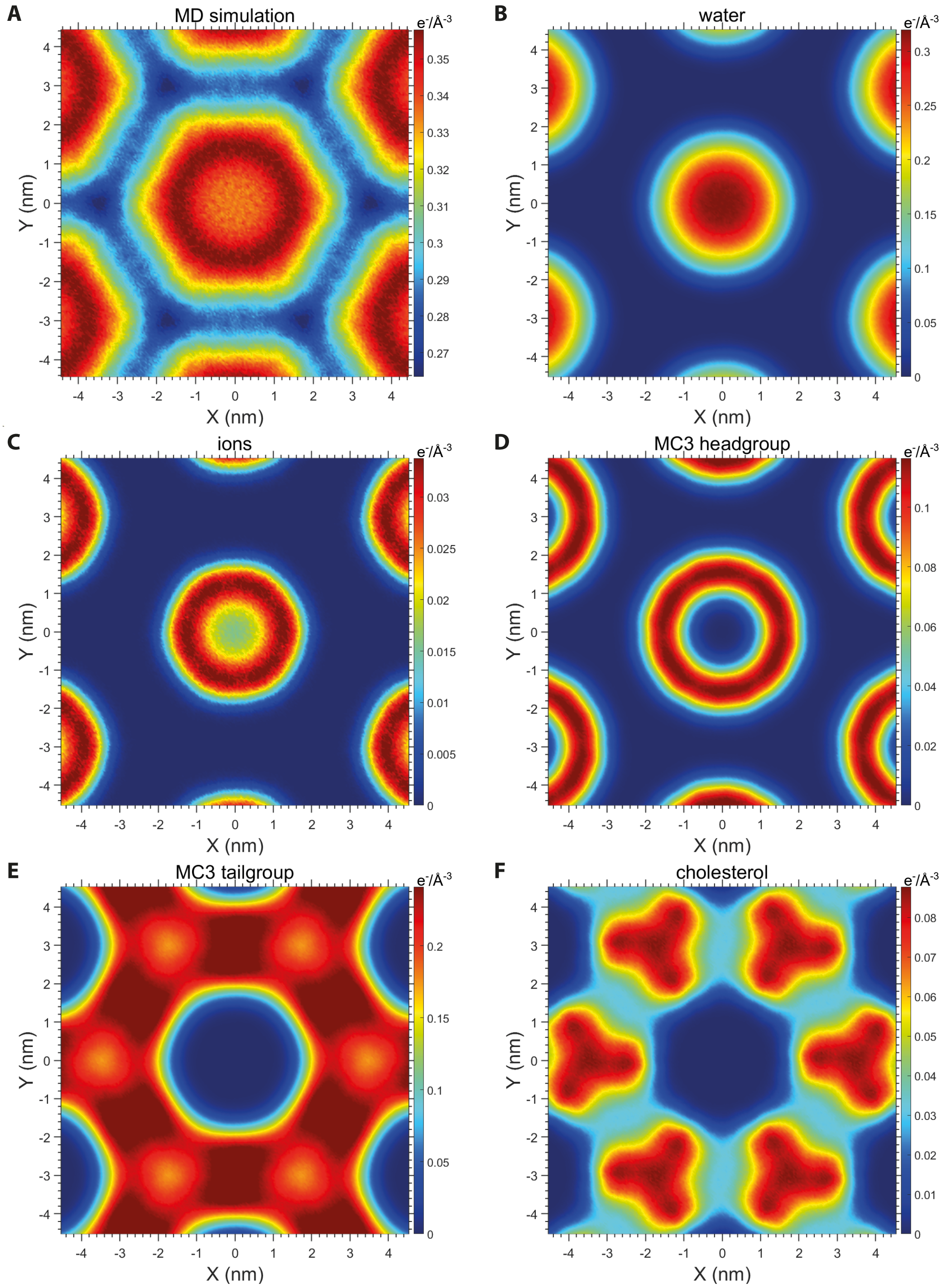

Figure S4 Higher resolution 2D electron density maps of different components from the MD simulations. (**A**) shows the total electron density of the whole system, followed by the split images of its components: (**B**) water, (**C**) ions dissolved in water, (**D**) MC3 head group, (**E**) MC3 tail group and (**F**) cholesterol.

4 Volume Fraction of Water

4.1 From the Radial Distribution of Water

The water volume fraction ϕ_w is calculated from the radial distributions by:

$$\phi_w = \frac{\int_0^\infty \rho_w(r) d^3r}{\int_0^\infty \rho_t(r) d^3r} \tag{S1}$$

where ρ_w and ρ_t are the number densities of the water along the radial coordinate using the simulation setup with a single water column (see Philipp et al.[1] for further details).

4.2 According to the method by Petrache et al.[2]

We followed the method described by Petrache et al.[2] to calculate the molecular volumes. The system was divided into four components: MC3, cholesterol, water, and ions. It was then partitioned into a series of slices along the Z-axis. The number density of the MC3 component in a slice at height z is given by:

$$n_{MC3}(z) = \frac{N_{MC3}(z)}{V_s} \tag{S2}$$

where V_s is the volume of the slice and N_{MC3} is the number of molecules of MC3 in that particular slice. Similar number densities can be generated for the other components, too. The volume of the slice V_s can be expressed as the sum of the volumes occupied by each component in the slice. The volume occupied by each component in slice z can be obtained by the product of the number of molecules of the component and the molecular volume of the component. Hence V_s can be obtained by:

$$V_{MC3}N_{MC3}(z) + V_{chol}N_{chol}(z) + V_{water}N_{water}(z) + V_{ion}N_{ion}(z) = V_s \tag{S3}$$

Where V_{MC3}, V_{chol}, V_{water}, V_{ion} are the molecular volumes of MC3, cholesterol, water and ions respectively. If we divide the above equation by V_s, we get

$$V_{MC3}n_{MC3}(z) + V_{chol}n_{chol}(z) + V_{water}n_{water}(z) + V_{ion}n_{ion}(z) = 1 \tag{S4}$$

We can define the probability of finding the component MC3 in slice z as

$$P_{MC3}(z) = V_{MC3}n_{MC3}(z) \tag{S5}$$

And we can rewrite the Eq.S4 as

$$P_{MC3}(z) + P_{chol}(z) + P_{water}(z) + P_{ion}(z) = P_{total}(z) = 1 \tag{S6}$$

Combining Eq.S4 and Eq.S6, we can find the molecular volumes of the components by minimizing the function:

$$F(V_{MC3}, V_{chol}, V_{water}, V_{ion}) = \sum_i (P_{total}(z_i) - 1)^2 \tag{S7}$$

The probabilities of the individual components and the total probability can be obtained by substituting the values of the molecular volumes in Eq.S4 and are shown in Fig.5.

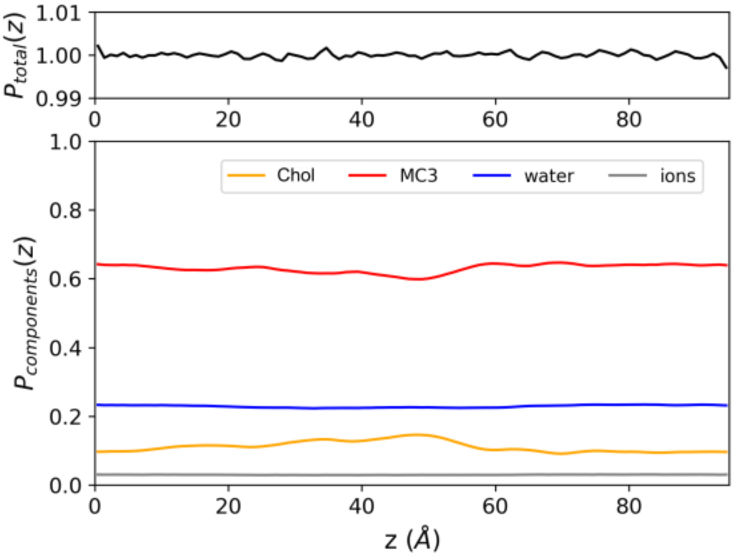

Figure S5 Volume probabilities of different components along the height of the column. The probabilities for MC3 and cholesterol fluctuate slightly, implying that in some volume slices, they are not uniformly distributed. The black line describes the total probability of finding an atom in the system and the value is around 1 with minor fluctuations.

5 Detailed Derivation of our Continuum Model

In this model, the core of an LNP is assumed to be built of parallel hexagonal domains where each hexagonal cylinder consists of a central water channel which is surrounded by a lipid region. There is no variation in composition along the cylinder axis, z, and thus the system may be described by two dimensions. The composition in a single hexagonal cylinder is not a function by the radius r from the central axis only, but varies with angle θ as well (Fig.S6).

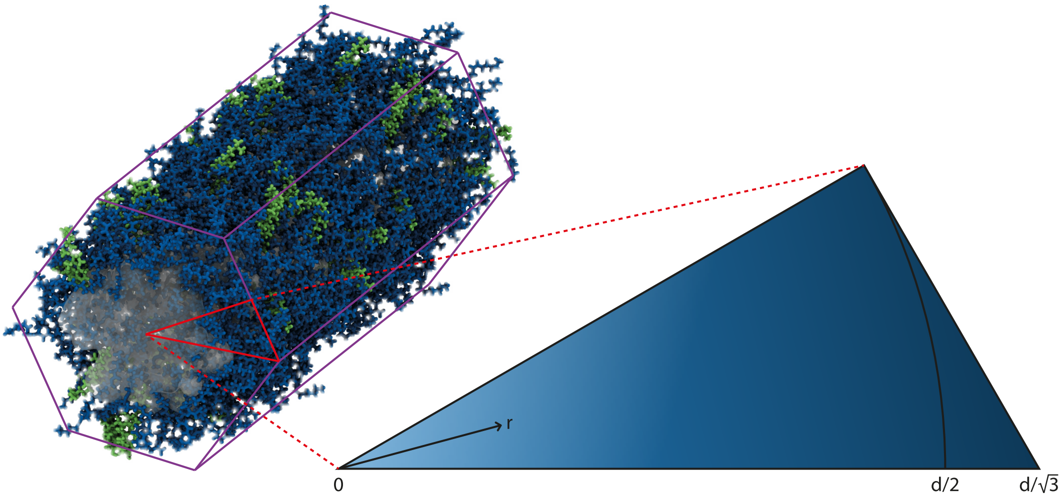

Figure S6 MD Simulation of the inverse hexagonal phase (H_{II}) with MC3 in blue, cholesterol in green and water in grey. The unit triangle is marked in red. The radius is measured from the middle point of the hexagonal tube.

However, it would be useful to find a formalism describing average properties at radius r. Let us imagine a physically correct function $g_{xy}(x, y)$ defined over the domain D_{tri} which is the triangle in Fig.S6 and the red triangle in Fig.S7. The function $g_{xy}(x, y)$ could for instance be the volume fraction of water inside the triangle.

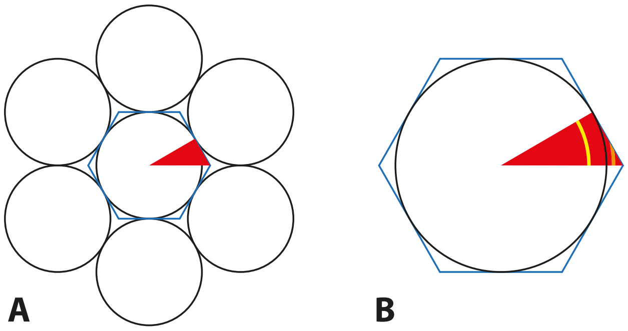

Figure S7 (**A**) In the inverse hexagonal phase (H_{II}), every tube is surrounded by six identical tubes. (**B**) Each hexagon can be divided in twelve unit triangles (shown in red). In contrast to the yellow shell inside the black ring, the orange shell does not cover the entire angle range.

We now want to define a radial function $g_r(r)$ that is an average of $g_{xy}(x,y)$ in a circular shell within $[r, r+dr]$.
Inside the circle ($0 \leq r < d/2$), any circular shell is given by

$$D_{shell}(r) = \left\{(x,y), r \leq \sqrt{x^2+y^2} \leq r+dr\right\} \tag{S8}$$

and is drawn as a yellow area in Fig.S7B. The intersection between the triangle and the shell is denoted as

$$D_{tri\cap shell}(r) = D_{tri} \cap D_{shell}(r) \tag{S9}$$

The area of the intersection is

$$A_{tri\cap shell}(r) = \frac{\pi}{6} r dr \tag{S10}$$

The radial function $g_r(r)$ is now defined as

$$\begin{aligned} g_r(r) &= \lim_{dr\to 0} \frac{\iint_{D_{tri\cap shell}(r)} g_{xy}(x,y) dx dy}{A_{tri\cap shell}(r)} \\ &= \lim_{dr\to 0} \frac{\iint_{D_{tri\cap shell}(r)} g_{xy}(x,y) r dr d\theta}{\frac{\pi}{6} r dr} \\ &= \frac{\int_{\theta=0}^{\pi/6} g_{xy}(x,y) d\theta}{\frac{\pi}{6}} \end{aligned} \tag{S11}$$

Outside the inscribed circle, i.e. where $d/2 < r < d/3$, the intersection between the triangle and the circular shell does not cover the entire angle range $0° < \theta < 30° \cdot \theta_{frac}(r)$ where the arc fraction $\theta_{frac}(r) \leq 1$. This intersection is shown in orange in Fig.S7B. The radial function $g_r(x,y)$ is again defined as the average of $g_{xy}(x,y)$ over the arc area

$$g_r(r) = \frac{\int_{\theta=0}^{\frac{\pi}{6}\theta_{frac}(r)} g_{xy}(x,y) d\theta}{\frac{\pi}{6}\theta_{frac}(r)} \tag{S12}$$

The arc fraction θ_{frac} is the ratio between the length of the orange and the green arcs in Fig.S8. Both arcs have the radius r to the origin (left corner of the triangle). A line is drawn from the origin to the point (a,b) where the orange arc intersects with the boundary of the triangle. The line defines an angle θ. Outside the inscribed circle the arc factor θ_{frac} equals the ratio between the angle θ and 30° with $\theta = \arctan(\frac{b}{a})$.

The point of intersection between the shell and the baseline of the triangle is given by the equations of the arc and the baseline, respectively

$$x^2 + y^2 = r^2 \quad \text{and} \quad y = d - \sqrt{3}x \tag{S13}$$

The point of intersection is

$$a = \frac{\sqrt{3}d + \sqrt{4r^2 - d^2}}{4} \quad \text{and} \quad b = \frac{d - \sqrt{12r^2 - 3d^2}}{4} \tag{S14}$$

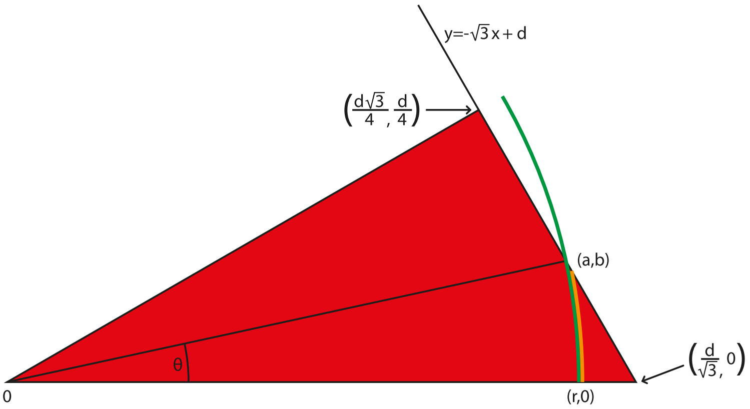

Figure S8 Sketch of the unit triangle to illustrate the arc fraction and intersection between shells (green and orange) with the hexagon.

This means that

$$\theta_{frac}(r) = 1 \qquad \text{for} \quad r \leq \frac{d}{2} \text{(in the inscribed circle)} \tag{S15}$$

and

$$\theta_{frac}(r) = \frac{\theta}{\pi/6} = \frac{\arctan\left(\frac{d-\sqrt{12r^2-3d^2}}{\sqrt{3}d+\sqrt{4r^2-d^2}}\right)}{\pi/6} \quad \text{for} \quad \frac{d}{2} < r \leq \frac{d}{\sqrt{3}} \text{(in the wedge)} \tag{S16}$$

5.1 Base, Intermediate and Stretched Functions

Until now we have considered functions $g_{xy}(x,y)$ being totally general or being already radial in character. Now we are to consider the volume fraction functions for various components in the LNP hexagon. Each hexagon is considered to consist of water as well as the head and tail groups of a lipid.

The volume fraction functions seem to be radial in the water channel. Outside the water channel the lipid stretches in the wedges to fill them up. In order to model the volume fraction functions for the two component water and tail, distribution functions along the short radius ($\theta = 30^\circ$, along green line in Fig.S9) have been proposed. These functions are called base functions. For water and lipid tails, the base functions are

$$f_{w,base} = \exp\left[-\ln(2)\left(\frac{r}{b_w}\right)^{a_w}\right] \qquad \text{for} \quad 0 < r < \frac{d}{2} \tag{S17}$$

$$f_{t,base} = \exp\left[-\ln(2)\left(\frac{r-d/2}{b_t}\right)^{a_t}\right] \qquad \text{for} \quad 0 < r < \frac{d}{2} \tag{S18}$$

While a_w, b_w and a_t are free parameters, b_t is used to get a correct relation between the volume fractions ϕ_h and ϕ_t (see further down). The volume fraction of the lipid head groups will be calculated from the constraint that all volume fractions must everywhere add to unity.

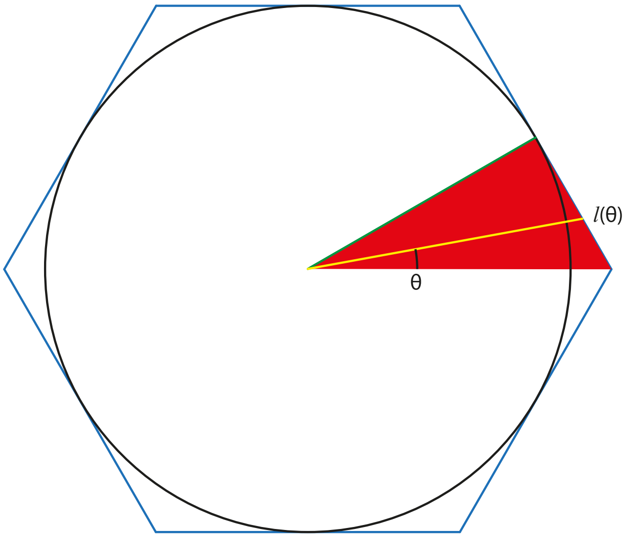

Figure S9 The hexagon (blue) with its inscribed circle (black) and the unit triangle (red) as well as the angle dependent effective radius $l(\theta)$ in orange.

The "effective radius" $l(\theta)$ is illustrated as a yellow line in Fig.S9. The triangle above that line is a right triangle and gives

$$\cos(30^\circ - \theta) = \frac{d/2}{l(\theta)} \Rightarrow l(\theta) = \frac{d}{2\cos(30^\circ - \theta)} \tag{S19}$$

Especially we find that

$$l(0^\circ) = \frac{d}{\sqrt{3}} \qquad \text{and} \qquad l(30^\circ) = \frac{d}{2} \tag{S20}$$

We want to define intermediate functions $f_{intermediate}(r,\theta)$ describing the stretching of the base functions for each angle θ. At $\theta = 30^\circ$ the base function is not stretched at all, i.e.

$$f_{intermediate}(r, 30^\circ) \equiv f_{base}(r) \tag{S21}$$

but at $\theta = 0^\circ$ it is stretched, so that at the hexagon boundary

$$f_{intermediate}\left(\frac{d}{\sqrt{3}}, 0^\circ\right) = f_{base}\left(\frac{d}{2}\right) \tag{S22}$$

In general the stretching $L(r,\theta)$ is defined as

$$r \cdot L(r,\theta) = r \qquad \text{for} \quad r < b_w \tag{S23}$$

$$r \cdot L(r,\theta) = \frac{\frac{d}{2} - b_w}{l(\theta) - b_w}(r - b_w) + b_w \qquad \text{for} \quad b_w < r < l(\theta) \tag{S24}$$

The intermediate functions for water and tail are now defined as

$$f_{w,intermediate}(r,\theta) = f_{w,base}(r \cdot L(r,\theta)) \qquad \text{for} \quad 0 < r < \frac{d}{\sqrt{3}} \tag{S25}$$

$$f_{t,intermediate}(r,\theta) = f_{t,base}(r \cdot L(r,\theta)) \qquad \text{for} \quad 0 < r < \frac{d}{\sqrt{3}} \tag{S26}$$

Finally, the intermediate functions are converted into stretched distribution functions, denoted $f_{w,stretched}(r)$ and $f_{t,stretched}(r)$, following Eq.S12,

$$f_{w,stretched}(r) = \frac{\int_{\theta=0}^{\frac{\pi}{6}\theta_{frac}(r)} f_{w,intermediate}(r,\theta)d\theta}{\frac{\pi}{6}\theta_{frac}(r)} \tag{S27}$$

$$f_{t,stretched}(r) = \frac{\int_{\theta=0}^{\frac{\pi}{6}\theta_{frac}(r)} f_{t,intermediate}(r,\theta)d\theta}{\frac{\pi}{6}\theta_{frac}(r)} \tag{S28}$$

Since the distribution functions must add to unity everywhere, the stretched distribution function for the lipid head group must be

$$f_{h,stretched}(r) = 1 - f_{w,stretched}(r) - f_{t,stretched}(r) \tag{S29}$$

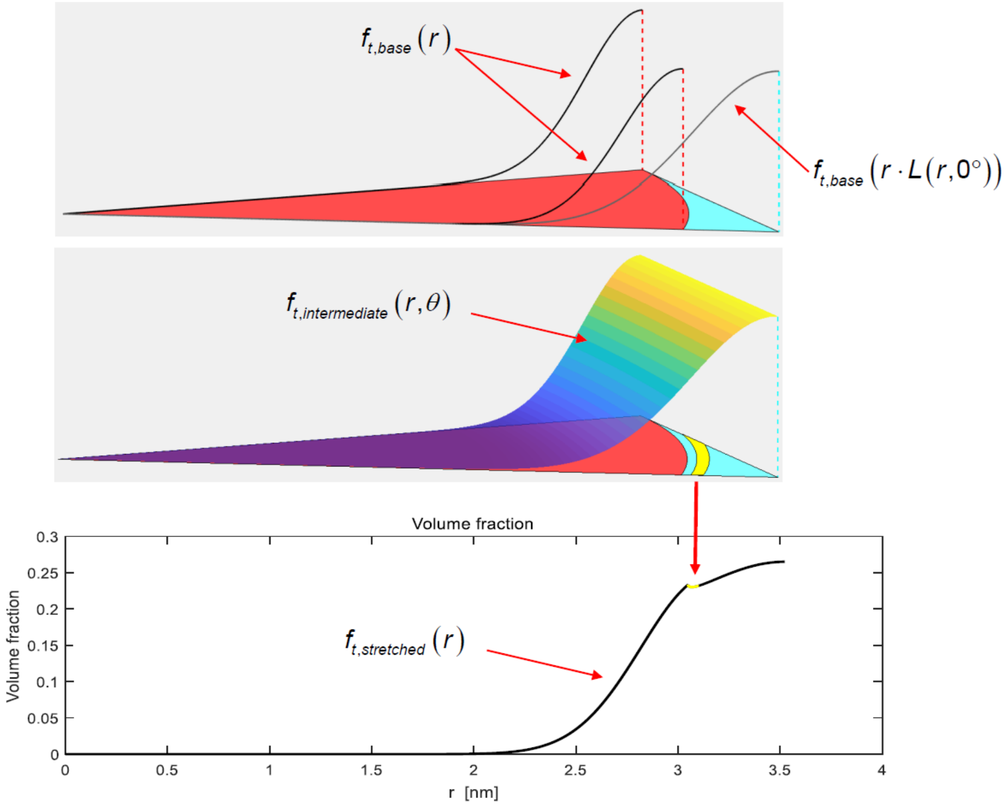

Figure S10 In order to account for the difference between circle and hexagon, the tail group distribution base function $f_{t,base}(r)$ has to be stretched depending on the angle θ to $f_{t,intermediate}(r,\theta)$ before it is radially integrated to the stretched distribution function $f_{t,stretched}(r)$. Similarly the water distribution function $f_{w,stretched}(r)$ can also be constructed.

5.2 Normalization

The base function for water is already normalized to $f_{w,base}(0) = 1$.

The total volume fraction of water ϕ_w is found by integrating the stretched function $f_{w,stretched}(r)$ and dividing by the total hexagon area:

$$\phi_w = \frac{\int_0^{d/\sqrt{3}} f_{w,stretched}(r) \cdot 2\pi r \cdot \theta_{frac}(r) dr}{\int_0^{d/\sqrt{3}} 2\pi r \cdot \theta_{frac}(r) dr} = \frac{4\pi\sqrt{3}}{3d^2} \cdot \int_0^{d/\sqrt{3}} f_{w,stretched}(r) \cdot r \cdot \theta_{frac}(r) dr \tag{S30}$$

The base function for the lipid tail group is already normalized to $f_{t,base}(d/2) = 1$.

The total volume fraction of the lipid tail group ϕ_t is

$$\phi_t = \frac{4\pi\sqrt{3}}{3d^2} \cdot \int_0^{d/\sqrt{3}} f_{t,stretched}(r) \cdot r \cdot \theta_{frac}(r) dr \tag{S31}$$

and the total volume fraction of the lipid head group ϕ_h is

$$\phi_h = \frac{4\pi\sqrt{3}}{3d^2} \cdot \int_0^{d/\sqrt{3}} f_{h,stretched}(r) \cdot r \cdot \theta_{frac}(r) dr \tag{S32}$$

Since the number of head and tail groups has to be the same, a relation between the molecular volumes of head $V_{m,h}$ and tail $V_{m,t}$ group as well as ϕ_h and ϕ_t is set up:

$$\frac{\phi_h}{\phi_t} = \frac{V_{m,h}}{V_{m,t}} \tag{S33}$$

The parameter b_t should be adjusted so that Eq.S33 is satisfied.

5.3 Scattering Length Density

The radial SLD functions are proportional to the volume distribution functions

$$SLD_w(r) = SLD_{w,0} \cdot f_{w,stretched}(r) \tag{S34}$$

$$SLD_h(r) = SLD_{w,0} \cdot f_{h,stretched}(r) \tag{S35}$$

$$SLD_t(r) = SLD_{w,0} \cdot f_{t,stretched}(r) \tag{S36}$$

The total SLD function is the sum of the components:

$$SLD_{tot}(r) = SLD_w(r) + SLD_h(r) + SLD_t(r) \tag{S37}$$

6 Molecular Dynamics Simulation Details

n_w	Composition		Column	Ensemble	Simulation Duration	Initial Structure
12	Chol MC3 Water Na$^+$ Cl$^-$	50 150 2400 7 157	Single	NPT	1 μs	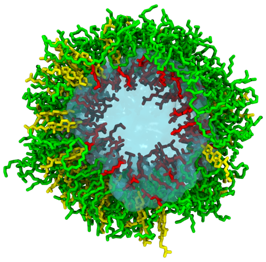
12	Chol MC3 Water Na$^+$ Cl$^-$	50 150 2400 7 157	Single	NVT	0.2 μs	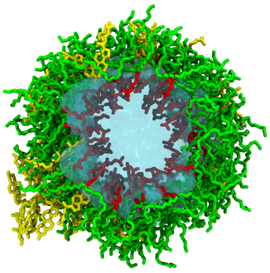
12	Chol MC3 Water Na$^+$ Cl$^-$	450 1350 21600 63 1413	Multi	NVT	0.5 μs	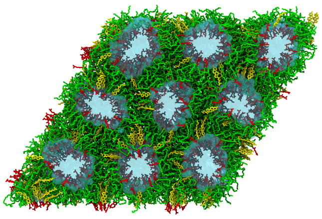

Table S1 Comprehensive details of the MD simulation of the H$_{II}$ phase. The first column lists the number of water molecules per lipid (n_w). The second column provides the names and number of the various components in each simulated system. The third column specifies whether the simulation contains a single H$_{II}$ column or multiple H$_{II}$ columns within the simulation box. The fourth column indicates the ensemble used for the simulation, while the fifth column shows the total simulation time. The sixth column describes the initial structure used for the production run of each simulation.

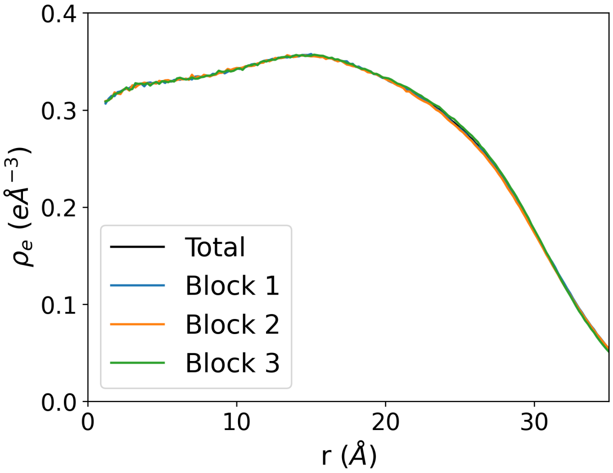

Figure S11 Comparison of the total radial electron density profiles of the H_{II} MD system over the full trajectory (black line) and at equally spaced time intervals (Blocks 1-3) shows complete overlap of the curves, confirming the convergence of the system.

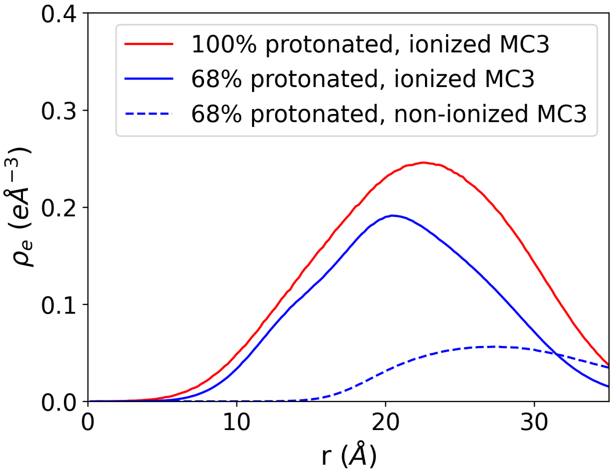

Figure S12 Radial electron density profiles of the ionizable MC3 lipids around the water column in the simulated HII MD system at two protonation states: 100% protonated (red) and 68% protonated (blue). Ionized MC3 lipids are shown as solid lines, while non-ionized MC3 lipids are shown as dotted lines.

Notes and references

[1] J. Philipp, A. Dabkowska, A. Reiser, K. Frank, R. Krzysztoń, C. Brummer, B. Nickel, C. E. Blanchet, A. Sudarsan, M. Ibrahim, S. Johansson, P. Skantze, U. Skantze, S. Östman, M. Johansson, N. Henderson, K. Elvevold, B. Smedsrød, N. Schwierz, L. Lindfors and J. O. Rädler, *Proceedings of the National Academy of Sciences*, 2023, **120**, e2310491120.

[2] H. Petrache, S. Feller and J. Nagle, *Biophysical Journal*, 1997, **72**, 2237–2242.

7 Conclusions and Future Outlook

7.1 Synthesis of Key Findings and Broader Implications

Our research was motivated by the open question about connections between structure and pharmaceutical performance of LNPs, the current state-of-the-art delivery vehicles for mRNA therapeutics. We focused on the nanoscale architecture of the LNP core under physiologically relevant conditions and its critical connection with functional efficacy. The primary objective was to move beyond empirical screening by establishing definitive structure-function correlations to link the molecular organization within the LNP core to the resulting in-vitro and in-vivo efficiency. This could then inform rational design principles for next-generation mRNA carriers.

Our structural analysis, primarily employing small-angle X-ray scattering (SAXS), clearly showed that the internal organization of the LNP core is highly sensitive to the ambient pH, which is a critical parameter during endocytosis. This responsiveness is central to the LNP mechanism, as we observed a distinct phase transition from the kinetically trapped inverse micellar (L_{II}) phase to the highly fusogenic inverse hexagonal (H_{II}) phase. Crucially, this transition is systematically triggered at mildly acidic conditions, specifically around early endosomal pH values ($\sim$ pH 6). The formation of the H_{II} phase is thus established as a physical prerequisite for efficient endosomal escape of the mRNA payload, a process facilitated by the intrinsic negative curvature stress and membrane destabilization properties of this phase.

Additional research progressed beyond a simple dependence on the bulk pH gradient to reveal that the chemical identity of the buffer during LNP preparation is an equally potent modulator of LNP function. Specifically, the second publication in this dissertation demonstrated that the chemical nature of the buffer ions significantly influences LNP transfection efficiency by modulating these critical pH-dependent structural transitions. We observed that LNPs prepared with citrate buffer exhibited a significantly earlier onset and stronger gene expression compared to those prepared with phosphate or acetate buffers. This effect was found to be entirely confined to the endosomal release mechanism, as the buffer type did not significantly affect initial characteristics like LNP encapsulation efficiency or particle size. Structurally, we showed that specific anion adsorption at the lipid-water interface directly alters the effective area per headgroup of the ionizable lipid. This specific ion effect fundamentally shifts the bulk phase transition pH, thereby tuning the LNP's responsiveness to the endosomal environment and ultimately impacting endosomal release efficiency. This finding elevates the understanding of LNP design from a one-dimensional focus on pH dependence to a multi-dimensional strategy incorporating the choice of the formulation buffer.

Furthermore, our investigation elucidated a critical and often overlooked physico-chemical parameter: the LNP core hydration state. LNP formulations exhibiting the lowest core water content consistently demonstrated the highest in-vitro endosomal escape efficiency and subsequent cellular protein expression. This high efficiency can be directly rationalized by the molecular geometry of the ionizable lipid, specifically the broadness of the hydrophobic tail region. The remarkable clinical success of ionizable lipids deployed in

SARS-CoV-2 vaccines, such as SM-102 and ALC-315, which exhibit significantly broader hydrophobic tail regions compared to the prior industry benchmark like MC3, provides compelling evidence for this structure-activity relationship.

Taken together, the cumulative structural and functional correlation presented herein provides a biophysical basis for the superior efficacy of contemporary clinical lipids. We rationalize the structure-activity relationship for optimal ionizable lipids and delineate two main, interdependent physico-chemical requirements for achieving superior mRNA delivery performance: pH-triggered L_{II}-H_{II} phase transitions and minimized core hydration.

pH-triggered L_{II}-H_{II} phase transition: The ionizable lipid must possess the chemical and geometric characteristics to undergo a pH-triggered phase transition from the inverse micellar to the inverse hexagonal phase specifically within the pH range of the early endosomal compartment ($\sim$ pH 6).

Minimized core hydration: The molecular geometry (broad hydrophobic tail region leading to high curvature stress) must be optimized to promote the formation of the H_{II} phase with an inherently low internal core hydration state.

These findings establish a clear, testable framework for the future rational design of highly potent ionizable lipids, enabling the systematic optimization of LNPs beyond empirical formulation screening and accelerating the development of the next generation of mRNA therapeutics.

7.2 Future Research Directions

Building upon the structural insights and methodological framework established in this dissertation, future research will focus on advancing both the computational and experimental understanding of LNPs, ultimately paving the way for superior therapeutic delivery systems. A primary computational challenge lies in scaling up MD simulations to capture increasingly complex and realistic systems. While modeling only a few nanometer has already proven invaluable for characterizing LNP core components, the ultimate goal is to simulate an entire LNP. Achieving this holistic view will require significant increases in computing power and breakthroughs in parametrization. The development of AI-driven machine learning models is anticipated to be transformative in this regard, enabling the accurate and rapid derivation of force fields for novel ionizable lipids.

Experimentally, a key remaining bottleneck is the direct visualization of the LNP's mechanism of action in-vitro or even in-vivo. Specifically, the critical and transient process of endosomal escape remains poorly understood in real-time. Future studies must leverage techniques like super-resolution microscopy, potentially in combination of sophisticated fluorescent probes and live-cell imaging, to directly observe the interaction between LNP and endosome. This direct observation might provide the definitive link of the structural features investigated here with the functional outcomes of delivery.

Finally, while structural understanding enhances LNP stability and cellular uptake, their therapeutic potential is directly linked to their ability to reach the desired physiological target. Consequently, a major research direction involves developing sophisticated targeting techniques. This includes engineering the LNP surface with specific ligands (e.g. peptides, aptamers, antibodies) to achieve active targeting to specific cell types or tissues, such as cancer or other localized diseases. Future work will bridge the gap between fundamental structural science and applied pharmacology, using detailed LNP architecture knowledge to rationally design delivery vehicles that are both highly effective and precisely targeted.

List of Publications

Publications that are part of this thesis

1. **Julian Philipp**, Aleksandra Dabkowska, Anita Reiser, Kilian Frank, Rafał Krzysztoń, Christiane Brummer, Bert Nickel, Clement E. Blanchet, Akhil Sudarsan, Mohd Ibrahim, Svante Johansson, Pia Skantze, Urban Skantze, Sofia Östman, Marie Johansson, Neil Henderson, Kjetil Elvevold, Bård Smedsrød, Nadine Schwierz, Lennart Lindfors, and Joachim O. Rädler
   pH-dependent structural transitions in cationic ionizable lipid mesophases are critical for lipid nanoparticle function
   Proc. Natl. Acad. Sci. U.S.A. (2023). 120 (50) e2310491120.

2. Cristina Carucci*, **Julian Philipp***, Judith A. Müller, Akhil Sudarsan, Ekaterina Kostyurina, Clement E. Blanchet, Nadine Schwierz, Drew F. Parsons, Andrea Salis, and Joachim O. Rädler
   Buffer Specificity of Ionizable Lipid Nanoparticle Transfection Efficiency and Bulk Phase Transition
   ACS Nano (2025). 19, 10829-10840.
   * Equal contribution

3. **Julian Philipp***, Akhil Sudarsan*, Ekaterina Kostyurina, Viktoriia Meklesh, Monica Berglund, Michael Rappolt, Jan Westergren, Lennart Lindfors, Nadine Schwierz, and Joachim O. Rädler
   Combining SAXS analysis and MD simulation to determine structure and hydration of ionizable lipid hexagonal phases
   Soft Matter (2025). 21, 8049-8059.
   * Equal contribution

Other publications

1. Tamara Ehm, **Julian Philipp**, Martin Barkey, Martina Ober, Achim Theo Brinkop, David Simml, Miriam von Westphalen, Bert Nickel, Roy Beck, and Joachim O. Rädler
   3D-printed SAXS chamber for controlled in situ dialysis and optical characterization
   J Synchrotron Radiat. (2022). 29(Pt 4):1014-1019.

2. Bingru Zhang, Linh Nguyen, Kevin Martens, Amelie Heuer-Jungemann, **Julian Philipp**, Susanne Kempter, Joachim O. Rädler, Tim Liedl, and Heinz-S. Kitzerow
   Luminescent DNA-origami nano-rods dispersed in a lyotropic chromonic liquid crystal
   Liquid Crystals (2023). 50(7–10), 1243–1251.

3. Miriam Grava, Mohd Ibrahim, Akhil Sudarsan, Julio Pusterla, **Julian Philipp**, Joachim O Rädler, Nadine Schwierz, and Emanuel Schneck
   Combining molecular dynamics simulations and x-ray scattering techniques for the accurate treatment of protonation degree and packing of ionizable lipids in monolayers
   J Chem Phys. (2023). 159(15):154706.

Bibliography

[1] Tim Hwang. *Progress Deferred: Lessons from mRNA Vaccine Development.* `https://ifp.org/progress-deferred-lessons-from-mrna-vaccine-development/`. Article Last Updated Date: February 20th 2024. 2024.

[2] Jon A. Wolff et al. "Direct Gene Transfer into Mouse Muscle in Vivo". In: *Science* 247.4949 (1990), pp. 1465–1468. DOI: `10.1126/science.1690918`. URL: `https://www.science.org/doi/abs/10.1126/science.1690918`.

[3] Elie Dolgin. "The tangled history of mRNA vaccines". In: *Nature* 597 (7876 Sept. 2021), pp. 318–324. ISSN: 0028-0836. DOI: `10.1038/d41586-021-02483-w`.

[4] Enrico Iaccino et al. "The aftermath of the Merck's HIV vaccine trial". In: *Retrovirology* 5 (1 Dec. 2008), p. 56. ISSN: 1742-4690. DOI: `10.1186/1742-4690-5-56`.

[5] Rafick-Pierre Sekaly. "The failed HIV Merck vaccine study: a step back or a launching point for future vaccine development?" In: *The Journal of Experimental Medicine* 205 (1 Jan. 2008), pp. 7–12. ISSN: 1540-9538. DOI: `10.1084/jem.20072681`.

[6] Blake Forman and Yizhou Dong. *The Future of RNA Therapeutics, From Design to Delivery.* `https://www.technologynetworks.com/biopharma/articles/the-future-of-rna-therapeutics-from-design-to-delivery-397775`. Article Last Updated Date: March 28, 2025. 2025.

[7] Feryal Alhamadani et al. "Adverse Drug Reactions and Toxicity of the Food and Drug Administration–Approved Antisense Oligonucleotide Drugs". In: *Drug Metabolism and Disposition* 50 (6 June 2022), pp. 879–887. ISSN: 00909556. DOI: `10.1124/dmd.121.000418`.

[8] David Adams et al. "Patisiran, an RNAi Therapeutic, for Hereditary Transthyretin Amyloidosis". In: *New England Journal of Medicine* 379 (1 July 2018), pp. 11–21. ISSN: 0028-4793. DOI: `10.1056/NEJMoa1716153`.

[9] Phei Er Saw and Erwei Song. "Historical Overview of RNA Therapeutics". In: *RNA Therapeutics in Human Diseases.* Springer Nature Singapore, 2025, pp. 1–22. DOI: `10.1007/978-981-96-3041-7_1`.

[10] Katalin Karikó et al. "Suppression of RNA Recognition by Toll-like Receptors: The Impact of Nucleoside Modification and the Evolutionary Origin of RNA". In: *Immunity* 23 (2 Aug. 2005), pp. 165–175. ISSN: 10747613. DOI: `10.1016/j.immuni.2005.06.008`.

[11] David Alvaro. *Beyond mRNA Vaccines: The Expanding World of RNA-Based Therapeutics.* `https://www.pharmasalmanac.com/articles/beyond-mrna-vaccines-the-expanding-world-of-rna-based-therapeutics`. Article Last Updated Date: March 21, 2025. 2025.

[12] Nojoud Al Fayez et al. "Recent Advancement in mRNA Vaccine Development and Applications". In: *Pharmaceutics* 15 (7 July 2023), p. 1972. ISSN: 1999-4923. DOI: `10.3390/pharmaceutics15071972`.

[13] Ugur Sahin, Katalin Karikó, and Özlem Türeci. "mRNA-based therapeutics — developing a new class of drugs". In: *Nature Reviews Drug Discovery* 13 (10 Oct. 2014), pp. 759–780. ISSN: 1474-1776. DOI: `10.1038/nrd4278`.

[14] Han Na Jung et al. "Lipid nanoparticles for delivery of RNA therapeutics: Current status and the role of in vivo imaging". In: *Theranostics* 12 (17 2022), pp. 7509–7531. ISSN: 1838-7640. DOI: `10.7150/thno.77259`.

[15] Rumiana Tenchov et al. "Lipid Nanoparticles - From Liposomes to mRNA Vaccine Delivery, a Landscape of Research Diversity and Advancement". In: *ACS Nano* 15 (11 Nov. 2021), pp. 16982–17015. ISSN: 1936-0851. DOI: `10.1021/acsnano.1c04996`.

[16] Camilla Hald Albertsen et al. "The role of lipid components in lipid nanoparticles for vaccines and gene therapy". In: *Advanced Drug Delivery Reviews* 188 (Sept. 2022), p. 114416. ISSN: 0169409X. DOI: `10.1016/j.addr.2022.114416`.

[17] Jialiang Wang et al. "Recent Advances in Lipid Nanoparticles and Their Safety Concerns for mRNA Delivery". In: *Vaccines* 12 (10 Oct. 2024), p. 1148. ISSN: 2076-393X. DOI: `10.3390/vaccines12101148`.

[18] Kaitlin Mrksich, Marshall S. Padilla, and Michael J. Mitchell. "Breaking the final barrier: Evolution of cationic and ionizable lipid structure in lipid nanoparticles to escape the endosome". In: *Advanced Drug Delivery Reviews* 214 (Nov. 2024), p. 115446. ISSN: 0169409X. DOI: `10.1016/j.addr.2024.115446`.

[19] Sean C. Semple et al. "Efficient encapsulation of antisense oligonucleotides in lipid vesicles using ionizable aminolipids: formation of novel small multilamellar vesicle structures". In: *Biochimica et Biophysica Acta (BBA) - Biomembranes* 1510 (1-2 Feb. 2001), pp. 152–166. ISSN: 00052736. DOI: `10.1016/S0005-2736(00)00343-6`.

[20] James Heyes et al. "Cationic lipid saturation influences intracellular delivery of encapsulated nucleic acids". In: *Journal of Controlled Release* 107 (2 Oct. 2005), pp. 276–287. ISSN: 01683659. DOI: `10.1016/j.jconrel.2005.06.014`.

[21] Tracy S. Zimmermann et al. "RNAi-mediated gene silencing in non-human primates". In: *Nature* 441 (7089 May 2006), pp. 111–114. ISSN: 0028-0836. DOI: `10.1038/nature04688`.

[22] Sean C Semple et al. "Rational design of cationic lipids for siRNA delivery". In: *Nature Biotechnology* 28 (2 Feb. 2010), pp. 172–176. ISSN: 1087-0156. DOI: `10.1038/nbt.1602`.

[23] Muthusamy Jayaraman et al. "Maximizing the Potency of siRNA Lipid Nanoparticles for Hepatic Gene Silencing In Vivo**". In: *Angewandte Chemie International Edition* 51 (34 Aug. 2012), pp. 8529–8533. ISSN: 1433-7851. DOI: `10.1002/anie.201203263`.

[24] Kimberly J. Hassett et al. "Optimization of Lipid Nanoparticles for Intramuscular Administration of mRNA Vaccines". In: *Molecular Therapy - Nucleic Acids* 15 (Apr. 2019), pp. 1–11. ISSN: 21622531. DOI: `10.1016/j.omtn.2019.01.013`.

[25] Manuel J. Carrasco et al. “Ionization and structural properties of mRNA lipid nanoparticles influence expression in intramuscular and intravascular administration”. In: *Communications Biology* 4 (1 Aug. 2021), p. 956. ISSN: 2399-3642. DOI: `10.1038/s42003-021-02441-2`.

[26] Michele Schlich et al. “Cytosolic delivery of nucleic acids: The case of ionizable lipid nanoparticles”. In: *Bioengineering & Translational Medicine* 6 (2 May 2021). ISSN: 2380-6761. DOI: `10.1002/btm2.10213`.

[27] Jessica Anindita et al. “The Effect of Cholesterol Content on the Adjuvant Activity of Nucleic-Acid-Free Lipid Nanoparticles”. In: *Pharmaceutics* 16 (2 Jan. 2024), p. 181. ISSN: 1999-4923. DOI: `10.3390/pharmaceutics16020181`.

[28] Mohamed Ibrahim et al. “Investigation of anti-PEG antibody response to PEG-containing cosmetic products in mice”. In: *Journal of Controlled Release* 354 (Feb. 2023), pp. 260–267. ISSN: 01683659. DOI: `10.1016/j.jconrel.2023.01.012`.

[29] Sushmita Chatterjee et al. “Endosomal escape: A bottleneck for LNP-mediated therapeutics”. In: *Proceedings of the National Academy of Sciences* 121 (11 Mar. 2024). ISSN: 0027-8424. DOI: `10.1073/pnas.2307800120`.

[30] Jean-Paul Behr. “The Proton Sponge: a Trick to Enter Cells the Viruses Did Not Exploit”. In: *CHIMIA* 51 (1-2 Feb. 1997), p. 34. ISSN: 2673-2424. DOI: `10.2533/chimia.1997.34`.

[31] Liza Malong et al. “A CRISPR/Cas9 screen reveals proteins at the endosome-Golgi interface that modulate cellular anti-sense oligonucleotide activity”. In: *Nature Communications* 16 (1 June 2025), p. 5378. ISSN: 2041-1723. DOI: `10.1038/s41467-025-61039-y`.

[32] Bowen Li et al. “Combinatorial design of nanoparticles for pulmonary mRNA delivery and genome editing”. In: *Nature Biotechnology* 41 (10 Oct. 2023), pp. 1410–1415. ISSN: 1087-0156. DOI: `10.1038/s41587-023-01679-x`.

[33] Sarah Lindsay et al. “Exploring the Challenges of Lipid Nanoparticle Development: The In Vitro–In Vivo Correlation Gap”. In: *Vaccines* 13 (4 Mar. 2025), p. 339. ISSN: 2076-393X. DOI: `10.3390/vaccines13040339`.

[34] Avi S. Patel and N. Sanjeeva Murthy. “SAXS Investigation of Hierarchical Structures in Biological Materials”. In: *Applied Sciences* 15 (8 Apr. 2025), p. 4472. ISSN: 2076-3417. DOI: `10.3390/app15084472`.

[35] Melissa Gräwert and Dmitri Svergun. “A beginner’s guide to solution small-angle X-ray scattering (SAXS)”. In: *The Biochemist* 42 (1 Jan. 2020), pp. 36–42. ISSN: 0954-982X. DOI: `10.1042/BIO04201036`.

[36] Ch. Broennimann et al. “The PILATUS 1M detector”. In: *Journal of Synchrotron Radiation* 13 (2 Mar. 2006), pp. 120–130. ISSN: 0909-0495. DOI: `10.1107/S0909049505038665`.

[37] G C Shearman et al. “Inverse lyotropic phases of lipids and membrane curvature”. In: *Journal of Physics: Condensed Matter* 18 (28 July 2006), S1105–S1124. ISSN: 0953-8984. DOI: `10.1088/0953-8984/18/28/S01`.

[38] Xiangbing Zeng, Yongsong Liu, and Marianne Impéror-Clerc. “Hexagonal Close Packing of Nonionic Surfactant Micelles in Water”. In: *The Journal of Physical Chemistry B* 111 (19 May 2007), pp. 5174–5179. ISSN: 1520-6106. DOI: `10.1021/jp0687955`.

[39] Gemma C. Shearman et al. “A 3-D Hexagonal Inverse Micellar Lyotropic Phase”. In: *Journal of the American Chemical Society* 131 (5 Feb. 2009), pp. 1678–1679. ISSN: 0002-7863. DOI: `10.1021/ja809280r`.

[40] Anan Yaghmur and Michael Rappolt. “The Micellar Cubic Fd3m Phase”. In: *Advances in Planar Lipid Bilayers and Liposomes*. Elsevier Science, 2013, pp. 111–145. DOI: `10.1016/B978-0-12-411515-6.00005-9`.

[41] Gerome Vancuylenberg et al. “From angular to round: in depth interfacial analysis of binary phosphatidylethanolamine mixtures in the inverse hexagonal phase”. In: *Soft Matter* 19 (44 2023), pp. 8519–8530. ISSN: 1744-683X. DOI: `10.1039/D3SM01029E`.

[42] Marianna Yanez Arteta et al. “Successful reprogramming of cellular protein production through mRNA delivered by functionalized lipid nanoparticles”. In: *Proceedings of the National Academy of Sciences* 115.15 (Mar. 2018). ISSN: 1091-6490. DOI: `10.1073/pnas.1720542115`. URL: `http://dx.doi.org/10.1073/pnas.1720542115`.

Acknowledgments

First of all, I really need to thank my supervisor Joachim Rädler. I originally did not plan to extend my time at the LMU with a PhD thesis. However during my Master thesis in your group, I became fond of the relaxed and friendly atmosphere at your chair and when you proposed this research topic, you piqued my interest and quickly convinced me. Little did I know that only a few months later, the topic of mRNA LNPs would suddenly blow up like this. It was the ultimate test of whether mRNA LNPs could prove their efficiency in the real world, and they even exceeded everyone's expectations. So thank you for putting me on this hot topic at exactly the right time, and thank you for all your support and encouragements during my time in your group. It was extremely helpful to have such a well-connected professor as my supervisor, which enabled all those collaborations.

Fortunately, I was not researching alone on this vast topic but could be part of the Swedish-German research collaboration, the Röntgen-Ångström Cluster, which included AstraZeneca as well. Here, I got to know Lennart Lindfors, who supported me so immensely during our joint research that he felt like a second supervisor to me. Thank you Lennart for our countless meetings and your humble praise of my work, even when things often proceeded way slower than I had hoped. You kept me motivated during all of my research and even invited me for a week at AstraZeneca. I was deeply honored by this invitation, and it provided me with invaluable insights in your fantastic work.

Thanks to Joachim's connections with seemingly everyone, I was also able to cooperate with Nadine Schwierz and her PhD student Akhil Sudarsan. Thank you both for this amazing and extremely fruitful cooperation. Every time we had a meeting, it felt like we took another big step forwards, and I enjoyed every second of it. We would have never achieved such conclusive results without your stunning MD simulations.

Next, I really have to thank Cristina Carucci, who was part of our cooperation with the group of Andrea Salis. Even though we encountered many difficulties during our joint research (including our endless train ride to Hamburg), I always had fun working with you.

Although I worked mostly alone on my topic at our chair for most of my PhD, Ekaterina Kostyurina joined us in 2023 and now continues my research at our group. You already achieved so much in this short time and I am truly impressed by your amazing work!

Finally, thank you Nadine Schüler for always being there for me. You never fail to light up my mood and support me in countless ways. So thank you for everything!